CORTICAL SHIFT CHARACTERIZATION USING A LASER RANGE SCANNER FOR NEUROSURGERY

By

Tuhin Kumar Sinha

Dissertation

Submitted to the Faculty of the

Graduate School of Vanderbilt University

in partial fulfillment of the requirements

for the degree of

DOCTOR OF PHILOSOPHY

in

Biomedical Engineering

December, 2004

Nashville, Tennessee

Approved by:

Benoit M. Dawant

Robert L. Galloway

Michael I. Miga

Terry M. Peters

Reid C. Thompson

Robert J. Weil

ACKNOWLEDGEMENTS

This dissertation is the work of more than just one person. Many people have helped me through the years required to complete this work.

I would like to thank the various members of the SNARL and BML laboratories for their friendship, help, and patience through the years. I would like to specifically like to thank Andy Bass, Mark Bray, Dave Cash, Richard Chen, Logan Clements, Prashanth Dumpuri, Steve Hartmann, Jao Ou, Jim Stefansic, John Warmath, and Chad Washington for their individual contributions during my tenure in the lab.

This work would largely be incomplete were it not for the effort of my committee members in guiding my research. I thank Dr. Benoit M. Dawant, Dr. Terry M. Peters, Dr. Reid C. Thompson, and Dr. Robert J. Weil for their help with this work.

My tenure in graduate school would have been very brief, i.e. non-existent, if Dr. Robert L. Galloway did not work his omnipresent magic. I owe every moment in graduate school to his faith in my abilities. I hope this work demonstrates some retribution for his gamble on my promise.

Dr. Michael I. Miga is the sole reason this work is of any merit. His relentless, tenacious, and precise guidance was exactly what I needed to get this dissertation together. Over the years I have know Dr. Miga, he has taught me how to step into the role of a good researcher and, more importantly, he has shown me the value of being a good mentor. My time spent in his office discussing ideas, issues, and everything else under the sun was some of the most enjoyable time I spent in graduate school.

Outside of school, there are many people that have directly impacted my life for the better. Without the aid of these people, I probably would not have had the stamina to complete the work required for this dissertation. They are: Ashnil Chopra, Dolly Devgan, Chad Grout, Agnella Izzo, Faizel Kassam, Aziz Khanifar, Dax Lopez, Bryan Martin, Neal Massand, Dana Powers, and Sandy Rathor.

I would like to thank my family for their past and continued support. My parents, to a large extent, contributed to my decision to go into graduate school, and I am glad that they

are able to share the fruits of my labor.

Finally, I must thank my ultimate inspiration through the years. His undying love and support are comforting in times of need, and his own performances in and out of school are the driving force for my own achievements. I dedicate this work to my better half, my little brother, Tanoy Sinha.

TABLE OF CONTENTS

LIST OF TABLES

LIST OF FIGURES

NOMENCLATURE

$H(x)$ Shannon entropy for signal x

$H(x, y)$ Joint Shannon entropy for signals x and y

$T_{x \to y}$ Transformation from coordinate frame x to y

ABA Adaptive bases algorithm

CT Computed Tomography

DLT Direct-linear transform

FOV Field-of-view

FRE Fiducial registration error

ICP Iterative closest point transforms

iCT Intraoperative Computed Tomography

IGNS Image-guided neurosurgery

IGS Image-guided surgery

iMR Intraoperative Magnetic Resonance Imaging

IRED Infrared light emmitting diode

iUS Intraoperative Ultrasound

LRS Laser range scanning

MI Mutual information

MR Magnetic resonance

MUIGNS Model-updated image-guided neurosurgery

MUIGS Model-updated image-guided surgery

NMI Normalized mutual information

PBR Point-based registration

POI Point-of-interest

ROI Region-of-interest

SFOV Surgical field-of-view

SMI SurfaceMI registration

STE Shift tracking error

TRE Target registration error

US Ultrasound

CHAPTER I

PURPOSE AND SPECIFIC AIMS

This dissertation provides information regarding brain shift tracking during neurosurgery using a laser range scanning device. Brain shift, an important phenomena within the field of image-guided surgery, compromises the accuracy of current surgical guidance systems. Recently, there has been considerable effort towards quantifying intraoperative brain shift for the purpose of developing compensation algorithms for image-guided surgery systems. One, intuitive, method for brain shift correction is to generate tomographic images which reflect the intraoperative state of surgery; two strategies, intraoperative imaging and computational modeling, are being explored for this purpose. The latter method provides the umbrella under which the goals of this research are outlined. Specifically, a computational framework to update images during surgery requires intraoperative sparse-data. Sparse-data, in this context, is defined as data with limited intraoperative information or extent. A requirement of the sparse-data is that it must provide accurate "boundary constraints" to ensure realistic modeling of the underlying soft-tissue deformation. Thus, an important area of research is the accurate and efficient acquisition of intraoperative sparse-data for computational modeling.

The goals of this research involve: using a laser-range scanner (LRS) within the operating room to acquire cortical surface data, registering the LRS data to preoperative images, and using serial LRS datasets to measure intraoperative brain shift. These shift measurements can then be applied to a computational model to predict deep tissue shift. The results and application of these research goals are important to the development of a computational framework for image-guided surgery. Thus, to limit the scope of this dissertation but still encompass the breadth of this important issue within image-guided surgery, the following specific aims for research were outlined:

Specific Aim 1. Acquire intraoperative laser range scan data of the cortical surface and rigidly register it to preoperative image sets.

- Develop an algorithm to register the intensity-encoded points clouds from the LRS to preoperative images.
- Verify the robustness and accuracy of the registration algorithm in computational, phantom, and *in vivo* studies.

Specific Aim 2. Deformably register, and measure shift using serial intraoperative laser range scan data.

- Develop an algorithm to deformably register serial range scans.
- Verify the robustness and accuracy of the registration algorithm in computational, phantom, and *in vivo* studies.

Specific Aim 3. Investigate new strategies to enhance the rigid and non-rigid registration of LRS data for the purpose of patient-to-image alignment and brain shift measurement.

- Analyze results of the aforementioned registration algorithms given alternative frameworks for registration.
- Optimize the shift tracking protocol given the results of the investigative studies.

CHAPTER II

BACKGROUND

Over the past century, image-guided neurosurgery (IGNS) has developed into a standard operating room protocol for invasive therapy of the brain. Critical to any IGNS system is the ability to relate intraoperative surgical conditions to preoperative patient data. In the '80's and '90s great strides were taken to ensure accurate correlation of the patient's intraoperative position to their preoperative tomographic datasets. Recently, however, research has shown that limitations, related to accuracy, exist in the current protocol for IGNS. The work described in this dissertation presents possible causes of the inaccuracies and outlines a potential method for compensating for them.

A brief introduction to image-guided neurosurgery

The discussion for future research in this dissertation must be prefaced with a brief introduction outlining the development of IGNS to its current state. The history of IGNS begins at the turn of the century with discovery of X-ray imaging [1, 2] and subsequently the first image-guided surgical procedure [3]. The benefits of using preoperative images during surgery were immediately apparent. With image-guided surgery the surgeon did not have to operate within the confines of generic anatomy. They could use patient-specific cues to target therapy. Since then, the impetus for image-guided surgery and, specifically, for IGNS research has been sustained by this desire to provide as much patient-specific information as possible during surgery.

Within this context, one problem garners quite a bit of attention as it dictates (to a large extent) the overall effectiveness of any IGNS implementation. In short, the problem is to align the patient in the operating room and the patient's preoperative datasets within a common frame of reference. For the remainder of the document, this problem will be referred to as *registration*. Initially the registration was provided in a qualitative fashion

by the surgeon based on their training. By aligning landmark structures, such as bones and tendons, in the patient-specific image to their respective locations based on their gross anatomy training, a surgeon could get a sense of where they were operating.

However, within a formal definition of IGNS[1], qualitative registrations do not provide the quantitative accuracy required. Initial attempts at determining a quantitative registration were provided using stereotactic[2] frames for surgical guidance. In 1908, Horsley and Clarke were the first to experiment with the design of stereotactic frames for animal surgery [6]. In the late '40's and early '50's, Horsley and Clarke's frame evolved for use in humans through designs offered by Spiegel & Wycis, Leksell, Reichert & Wolff and Talaraich [7, 8, 9, 10]. A common theme in each of these designs was to provide a mapping from locations within a patient's preoperative images to real world positions during surgery. Thus, the direction of information flow is from *image-space* to *physical-space*. *Image-space* is defined as the coordinate frame used in the patient's preoperative image sets, and is emphasized to indicate its mathematical nature. A typical *image-space* coordinate frame for an image is shown in Figure 1(a); this may be extended to three dimensions, as seen in Figure 1(b). *Physical-space* defines similar axes within a "real-world" localization system, i.e. a stereotactic frame. For brevity in the remainder of the document, *image-space* and *physical-space* will be denoted as S_S and S_P, respectively.

A paradigm shift in the direction of information flow was observed with the advent of computers and computerized imaging modalities capable of creating tomographic[3] image sets. Researchers quickly realized the potential of transforming S_P locations to S_I in real-time and providing this feedback to the surgeon(s). Three things are needed for this feedback process (also called interactive, image-guided surgery [11]) to occur in the operating room: a method of acquiring three-dimensional location and orientation in S_P, a method of registering the S_P location to S_I, and a method of presenting the S_I location to the surgeon. The

[1]Image guided surgery can be defined as the quantitative use of preoperative images during surgery [4].

[2]Greek: *stereo* – solid (representing three-dimensions) and Greek: *tassien* – to arrange or Latin: *tact* – to sense in touch. Originally used by Horsley and Clarke in 1908 in Brain [5].

[3]Greek: *tomos* – to slice or section, *graphos* – to write. Originally quoted in the British Journal of Radiology in 1935 [5].

marriage of stereotactic data with tomographic data in a real-time fashion was explored by many people [12, 13, 14, 15]. One of the first implementations of interactive, image-guided surgery was proposed by Kelly et al. [16]. In that paper, Kelly used an arc quadrant stereotactic frame for positional feedback of an ablative CO_2 laser. The positional changes of the laser tip were displayed to the surgeon in real-time on a computer monitor displaying the preoperative CT images. In retrospect, Kelly's paper was years ahead of its time because it also described a method to compensate for brain shift during surgery which will be revisited later in this document.

A feature of all of these systems were their use of a stereotactic frame for localization, which resulted in highly accurate S_P localizations. Subsequently, researchers aimed at providing the same accuracy in localization using *frameless* systems. One of the first devices to do this was described by Roberts et al. in 1986 [17]. In that paper, an operating microscope was retrofitted with an acoustical localization system for use in the OR. Roberts system provided localization accuracies on the order to 1-2 millimeters. Concurrently, a group from Japan approached the localization problem from a robotics standpoint [18, 19]. They demonstrated the use of an articulated arm for surgical localization. Galloway et al. also demonstrate the use of a mechanical linkage system for intraoperative localization [11]. Further work in this field has lead to the use of highly accurate optical and magnetic localization systems for IGNS [20, 21, 22, 23, 24, 25, 26]. These localization systems provide accurate positional data, while reducing the hardware requirement near the area of surgery. In optical systems, such as the OPTOTRAK and POLARIS systems from Northern Digital (www.ndigital.com), active (emitting) or passive (reflecting) markers are coupled with (infra-red) light sensitive cameras to triangulate three-dimensional position; multiple markers allow the calculation of orientation (see Figure 2). Similarly, magnetic systems use electromagnetic interference to probe the position and orientation of a device. Some of these systems, specifically the optical systems, have demonstrated localization accuracies rivaling those found in the frame based navigation systems, and are therefore the *de facto* method for commercial surgical navigation solutions (e.g. StealthStation, Medtronic Inc, Boulder,

CO).

The second hurdle for frameless systems is the accurate registration of S_P to S_I. With framed systems the registration was provided via "N" bar localization on the frames [27] across spaces. Since this method is not possible without frames, alternative methods had to be developed. Fundamentally, the process of registration using frames aligned a set of three dimensional points in one space to their corresponding locations in another space. Given at least three non-collinear points, the registration of these points across spaces implicitly maps *all* points from one space to another [28]. Thus, all that is needed is a set of corresponding, uniquely identifiable points (markers) in each space for registration. Initial attempts at finding corresponding markers in S_P and S_I for frameless systems utilized the bony anatomy of a patient, for example the bridge of the nose [29, 30]. However, repeatability in accurate localization of anatomic markers proved to be difficult. As a result, synthetic markers were developed to ensure accurate and precise marker localization across spaces. Both skin and implantable markers have been developed and are used for current image-guided neurosurgical procedures [31, 32, 33, 34, 35]. Skin markers are favored for their non-invasive nature, while bone implantable markers have the advantage of high accuracy due to their rigid application [36].

Given the accurate localization and registration provided by marker-based system, many interactive surgical navigation suites have been developed [37]. The implementation details of these complex programs are beyond the scope of this dissertation, however their objective for providing accurate feedback is intimately tied to purposes of this dissertation.

In conclusion, the current *state-of-the-art* method for IGNS involves the use of either optical or magnetic localization in physical space, a rigid-registration between physical- and image-space using fiducials and point-based registrations, and combination 2D/3D computer graphics for feedback. Galloway et al. provide an excellent review of the development of both framed and frameless stereotactic surgery in [27] and [4].

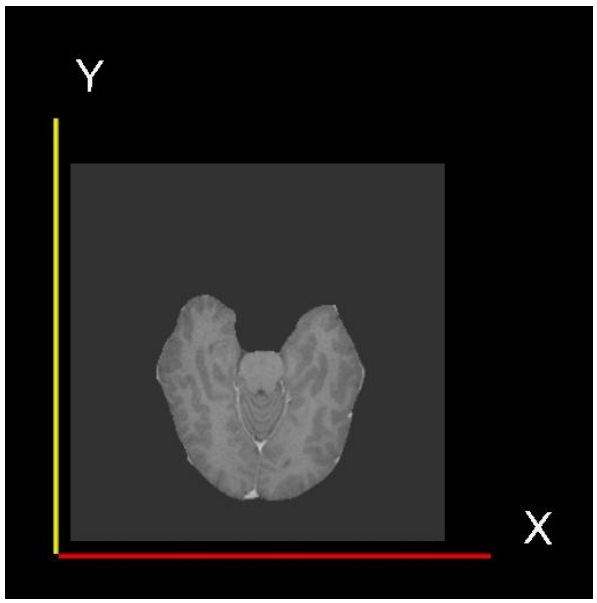

1(a) Typical image coordinate frame for single slice images.

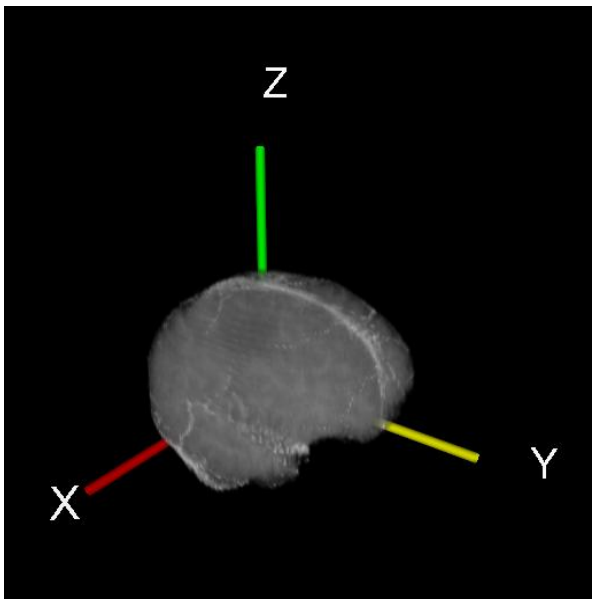

1(b) Typical image coordinate frame for volumetric image sets. This volume represents the stacking of individual slices in the X-Y plane on top of one another along the positive Z axis.

Figure 1: Typical image space (S_I) coordinate frames.

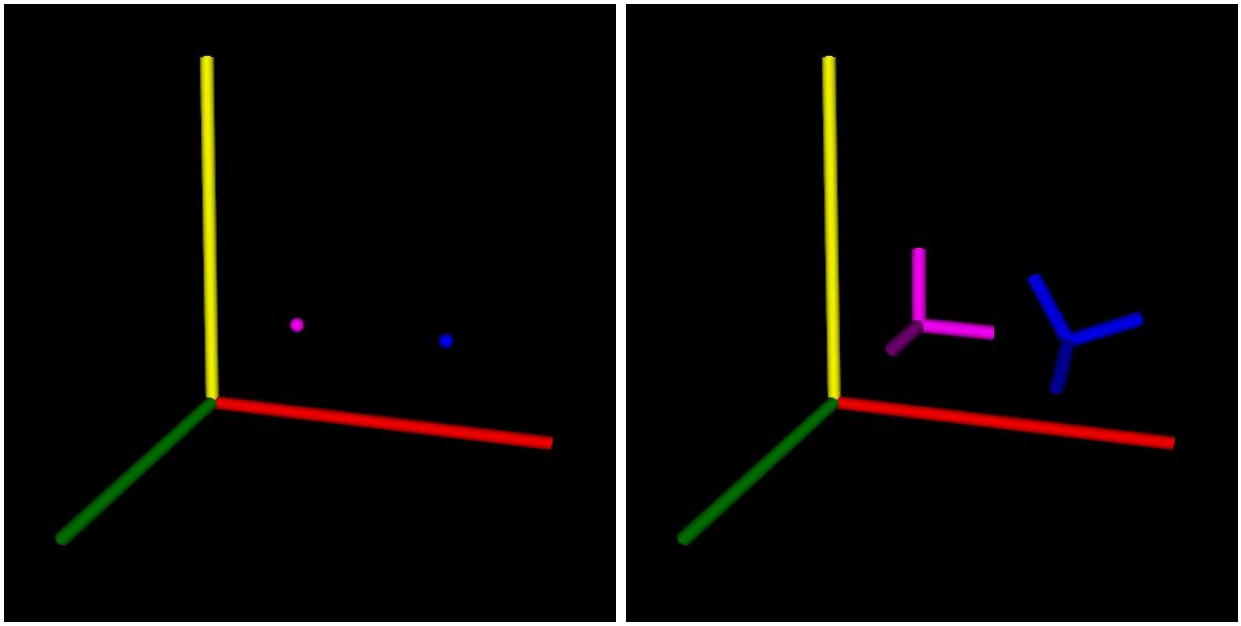

Figure 2: Representation of position and orientation in three dimensional space. On the left are 2 points in three dimensional space with different positions. On the right are two coordinate frames, defined by 4 points, with different position and orientation.

Brain shift during current IGNS

An assumption within the aforementioned method for IGNS is that the brain is rigid. Rigidity is defined mathematically such that relative distances and angles between corresponding points in the brain do not change spatially or temporally across different coordinate frames (or modalities). Thus, when using current IGNS systems one must assume that the brain maintains its shape and position before and during surgery. However, the brain, being soft tissue, is mobile during surgery and its mobility compromises the accuracy of current IGNS systems. A qualitative example of this effect on IGNS is shown in Figure 3.

One of the first quantitative reports of brain shift, or post-imaging brain distortion, during surgery was by Nauta et al. [38]. In that paper, two stereotactic localization systems (CRW frame and ISG wand) were used simultaneously to quantify brain shift in a patient undergoing resection therapy for "an extremely small" tumor. The size of the tumor, Nauta hypothesized, made it ideal to quantify brain shift due to the lack of motion with respect to resection. The CRW target localization of the center the tumor was used as the ground-truth reference. After resection, the ISG wand was localized manually at the center of the shifted tumor. The difference in localizations, attributed to brain shift, was recorded to be approximately 5 millimeters. Nauta, reports this number as support for a method of more accurate image-guidance during surgery.

In 1997, a preliminary report by Hill et al. measured brain surface shift in 5 patients, with serial measurements (showing the time-course of deformation) in 2 of the 5. The method outlined in that paper began with OPTOTRAK localization of a surface points intraoperatively; the mean number of surface points across all acquisitions was 25.57 ± 27.96. Corresponding surface points were then found in the preoperative images using a nearest neighbor search, and the difference between the corresponding points were recorded as shift. In the five patients, the lowest quartile of shift measurements indicated a sinking of at least 3 millimeters. However, in two patients the lowest quartile indicated shift on the order of a centimeter. The results also indicated that brain shift increased over the course of the

surgery in the two patients with serial surface localizations. Hill et al. revisit this experiment in a more thorough study published in 1998, expanding the patient population size to 21 patients and recording time-course measurements[4] in each patient [39]. The expanded results indicated that a mean surface (sinking-)shift of 3 millimeters, with a max of 8 millimeters, was seen before the dura was removed. Furthermore, the surface of the brain in the 21 patients sank on average 10 millimeters, *even before resection began.* Hill also comments that the shift results were surprising and is evidence for the development of enhancements to current image-guided surgery systems.

One of the first intraoperative ultrasound (iUS) imaging measurements of brain shift was performed by Bucholz et al. [40] For the shift measurement, an optically tracked and calibrated ultrasound probe was used to capture cross-sectional images of the brain. Corresponding features in serial ultrasound images, such as the depths of sulci, were measured to quantify shift. Bucholz applied this technique of brain shift measurement to 23 patients undergoing a variety of procedures. The largest average shifts observed occurred during a procedure to address a intracerebral hematoma (mean shift = 9.5 millimeters). For tumor resection procedures, the average post-resection shift observed was 7.3 millimeters with a standard deviation of 5.8 millimeters. Bucholz also demonstrates an increasing trend in shift over the duration of surgery, similar to Dorward's and Hill's results. Finally, he comments that the osmotic drug, Mannitol, affects brain shift by increasing it on average 0.5 millimeters. The results of the shift analysis provide Bucholz with evidence to support the development of an iUS neuroimaging method to compensate for brain shift that will be discussed later.

Subsequently, Dorward et al. demonstrated measurements of brain shift for not only surface points but also deep tissue points for 48 patients [41]. To do this, Dorward localized five points during surgery: on the surface of the skull at the center of the craniotomy, on the dura at the center of the craniotomy, at the deep tumor margin after resection, and on the

[4]Surface points were recorded in each patient before dural opening, before functional mapping, and after functional mapping but before resection.

surface of the cortex adjacent to the tumor before and after resection. Upon localization, the image-guidance system was inactivated and the distance between localized point and the actual point on the images was calculated. Another feature of Dorward's paper was the quantification of shift as a function of 5 different tumor groups: vault meningiomas, cerebral gliomas, nonglial intraaxial lesions, and skull base lesions. The mean surface tissue shift for all patients at opening and at closing were 4.6 and 6.7 millimeters, respectively. The deep tissue shift for all patients averaged 5.1 millimeters. The results also demonstrated that the meningioma tumor group produced the largest shifts. Furthermore, according to Dorward's observations, the time-course effects of brain shift show bulging of the brain at dural opening and at depth after resection, and infalling of the surface occurring in late stages of the surgery. This seems to be contrary to Hill's findings, however, Dorward's surface shift calculation comes from 1 point very close to the tumor resection boundary. Hill's data represents surface shift averaged over the area of the craniotomy, and thus reflects gross movement of the brain's surface during the course of surgery. Dorward's and Hill's results are, in fact, quite complementary and provide insight into the complex deformations of the brain shift phenomenon.

Maurer et al. were one of the first to demonstrate the effects of brain shift using an intraoperative magnetic resonance imaging (iMR) [42]. In five cases performed at the University of Minnesota, intraoperative MR images of patients undergoing resection therapy for brain tumors were recorded. Retrospective analysis of the intraoperative tomograms with respect to corresponding preoperative images were then carried out. Little quantitative information was presented in this paper, however, Hartkens et al. extended Maurer's experimental procedure to 24 patients in a subsequent paper published in 2003 [43]. In order to quantify the brain shift in serial iMR images, a deformable volumetric image registration algorithm was employed. Much like the registrations of S_P to S_I in IGNS, the deformable registration provides a mapping of image points in the preoperative image to corresponding points in serial iMR images, while taking into account the non-linear motion of any shift. This mapping allowed Hartkens to measure 3 dimensional shift of the whole brain, as well as volumetric

change over the course of surgery. The results of the deformation measurements highlighted shifts occurring in both the ipsi-lateral and contra-lateral hemispheres[5], with deformations generally being larger in the ipsi-lateral hemisphere. Furthermore, shift magnitudes were observed to be greater in deep tissue than on the surface of the brain near the area of resection. This result has implications for shift correction which will be discussed later. Finally, Hartkens's results complement findings of other studies that show gross brain shift mainly occurs in the direction of gravity.

Dr. David Roberts, a pioneer in the field of IGNS, and his research team at Dartmouth were one of the first to demonstrate that the majority of brain shift in the OR is due to gravitational sag [44]. In his paper, a tracked surgical microscope was used to localize points on the surface of brain during surgery in 28 patients. For three dimensional shift measurements, a laser focus system was used to localize surface points during the course of surgery. Roberts also used a memory feature of the microscope to capture serial images of a given surgical field-of-view (SFOV). This allowed for the tracking of 2-dimensional motion between images. The two dimensional shift could be extrapolated to 3-dimensions given the relative orientation of the patient during surgery. The results of both 3D and 2D measurements, the largest direction of shift was parallel to the gravitational vector. Roberts, hypothesizes the inadvertent loss of CSF fluid (and concomitant loss of buoyancy in the brain tissue) is the cause of this gravitational sag. Roberts goes on to categorize statistical analysis of the observed deformations as a function of: the type of surgery, the size of the craniotomy, the location of the tumor, the effect of osmotic drugs, and the time-course effects of brain shift. With respect to the type of surgery, Roberts found that resection therapies resulted in larger shifts when compared to other types of surgeries (i.e. electrode placement). This result fits the intuitive expectations of shift in different types of neurosurgical procedures. For results categorized according to craniotomy size, Robert's found no statistical significance. Thus, from a brain shift standpoint, the size of the craniotomy does not promote or hinder the error in IGNS due to brain shift. Roberts also found that left frontal and interhemispheric

[5]Ipsi-lateral and contra-lateral with respect to the craniotomy.

tumors caused significantly higher shifts when compared to tumors in other locations (i.e. right temporal, left temporal, right frontal, right parietal, and left occipital). However, the small and disparate sample sizes used in this analysis call into question the bias in the results. In a counter-intuitive result, Roberts demonstrated no significant relationship between the use of Mannitol (an osmotic drug) and brain shift. However, he comments that the experimental procedure used in his paper does not resolve the difference in brain shift due to gravity or osmotic drugs. In fact, the effects of the Mannitol may be overwhelmed or obscured by gravitational sag. In terms of time-course analysis, Roberts supports the results found by Hill and Dorward by demonstrating increasing shift over the duration of surgery. Further, Roberts states that the time effects of shift are greatest at the beginning of surgery and plateau as the surgery proceeds.

In efforts to implement iMR systems to update neuronavigational systems, Nimsky and Nabavi, in separate reports, revisit the idea originally explored by Maurer et al. of measuring intraoperative brain shift using iMR systems [45, 46]. However, Nimsky and Nabavi calculate brain shift concurrent to surgery and not in a retrospective manner as outlined by Maurer. In the study by Nimsky et al., 64 patients undergoing cortical resection therapy were imaged preoperatively and intraoperatively using 0.2T scanner [45]. Image sets were rigidly registered to each other using a point-based registration of implanted bone markers near the craniotomy. Nimsky recorded sinking (in the direction of gravity) shifts of the cortical surface between 0 to 23.8 millimeters, with a mean of 8.4 millimeters. The shifts observed at the deep tissue tumor margins indicated sinking shifts of up to 8.0 millimeters and bulging (against the direction of gravity) shifts up to 31 millimeters, with a mean of shift of 4.4 millimeters in the sinking direction. Using a classification system proposed by Bucholz et al. [40], Nimsky observed high cortical shifts in 63% of all cases. Furthermore, Nimsky reports a complex shift pattern of infalling of the cortical surface in 83% of the cases and swelling of the deep tumor margin in 69% of the cases. Nimsky also comments that: "The direction of brain shift was influenced primarily by patient and head positioning, i.e., gravity." Nabavi et al. also used an iMR system (0.5T) to measure shifts in 25 patients, while focusing on the

time-course of brain shift during surgery. To do this, each patient was subject to at least 4 serial iMR scans during surgery. The program 3DSlicer (www.slicer.org) was then used for quantitative analysis of brain shift. The time-course results of Nabavi's study indicated a general sinking of the brain during the course of surgery. Nabavi reports surface shifts as large at 5 *centimeters* in some cases. Nabavi states that the sinking due to gravitational sag generated subsurface compression which was relieved as tissue was removed. The reduction in compressive force, via resection, caused the deep tissue to expand towards the surgical site over the course of the operation, hence the bulging of deep tissue margins. In some cases, the expansion resulted in "obliteration of the surgical site." This observation is congruent to earlier findings, i.e. Dorward's, of swelling at the deep tumor margins. Nabavi's results also resonate with earlier findings from Roberts et al., showing a plateau in the rate of increase of surface shift towards the end of surgery. Finally, in a somewhat counter-intuitive finding, the results of all 25 patients showed a general *increase* in brain volume between the end of resection and dural closure. Nabavi attributes this finding to edemic effects as well as expansion of compressed subsurface tissue.

The results of these papers highlight the major factors and effects of brain shift during IGNS. Although the individual measurements of brain shift vary from paper to paper, the general trend is surface shifts on the order of centimeters and deep tissue shifts on the order of 5 millimeters. Also, the direction of shift is generally parallel to the gravitational vector, with expansive shifts near the resection boundary bulging towards the surgical site. Furthermore, the shift phenomena is time dependent and the gravitational sag generally increases over the course of surgery. Although, the rate of increase tapers towards the end of surgery. Finally, the specific methods of each paper demonstrate the complex patterns of brain shift. A conclusion that can be made from all of these papers is that the correction of brain shift is important for current IGNS systems. However, a solution to the brain shift problem will not have generic properties, as the underlying phenomena are quite intricate and patient-specific.

Brain shift compensation methods

The previous section showed that the brain shift phenomena has been extensively researched, and there is no question that it compromises the accuracy of current IGNS systems. As a result of these findings, current research has been aimed at providing a more accurate representation of the brain during surgery. The dominant methods to provide consistent representation of the brain's intra-surgical state can be split into two categories: intraoperative imaging, and computational methods for shift compensation. Each method has its strengths and weaknesses which will be highlighted in the next two sections.

However, before exploring the current methods, one should revisit some of the more "manual" methods to brain shift correction for perspective. Patrick Kelly was one of the first to describe a qualitative compensation for neurosurgery in a paper that was highlighted in an earlier section[16]. His method was to place 1 millimeter stainless steel balls, 5 millimeters apart, along the surgeon's viewing axis of the craniotomy. Kelly would then acquire projective images normal to the viewing axes during surgery. Any positional shifts of the balls seen in the projection images was attributed to brain shift and was accounted for. In 1991, Hassenbusch et al. demonstrated a marker based method to account for brain shift during resection [47]. The method outlined used surgical micropatties with string tails tethered to them. A series of patties were placed under stereotactical guidance around the tumor margin. The string tethers were then used as guides which helped demarcate the tumor boundary even in the presence of brain shift. Even though this method is very clever and simple it has not seen widespread use for unknown reasons. The following sections describe two, more "automatic", methods currently under heavy investigation as possible strategies for brain shift compensation.

Intraoperative imaging for IGNS

Even before brain shift was identified as a source of error within IGNS, researchers found an intuitive benefit to having updated images during surgery. As early as 1979, and again in 1982, Shalit et al. demonstrated the use of an intraoperative CT (iCT) scanner during

neurosurgery [48, 49]. Shalit's explicit reason for using iCT was to help in the determination of tumor margins during surgery, implicitly, however, his method helped account for brain shift. During surgery, when serial iCT images showed no tumor contrast, Shalit extrapolated that the tumor had been effectively excised, and he terminated resection. Much like the first image-guided surgeries, Shalit's method for shift correction was very qualitative. In a more quantitative exercise, L. Dade Lunsford explored the use of iCT and stereotactic frames in the early '80's [50, 51, 52, 53, 54, 55, 56]. Lunsford's contribution to iCT included the development of a clinical OR around an CT machine. Lunsford also researched CT compatible stereotactic frame developed from plexiglass and aluminum. The modified frame allowed the surgeon to maintain the position of the targeting probe as it passed through the CT machine. A limitation of Lunsford's protocol was that the surgeon was required to perform surgery on the CT gantry. Okudera et al. noticed this limitation and promoted the development of a novel CT scanner for use in the OR [57]. Working with the Toshiba corporation, Okudera developed a detachable gantry that could be moved up to 10 meters from the scanner's frame. A digital control mechanism was also introduced to allow precise reattachment of the gantry table to the X-ray generator unit. Furthermore, Okudera's design allowed for greater flexibility in the patient's position, e.g. the design allowed for surgeries while the patient was in the prone position. Okudera used the scanner in transsphenoidal surgeries, highlighting the ability of the scanner to demarcate tumor margins in three-dimensions [58]. Compared to projective images of operating microscopes and radiofluoroscopes used at that time for surgery, the iCT method provided greater level of resection margin refinement during surgery. Even with the remarkable advancements made by Okudera, Lunsford, and Shalit , a common limitation in all of the iCT systems is the dedication of entire rooms to the intraoperative imaging system. In 1998, Butler et al. made another fundamental advancement in the use of CT during surgery by demonstrating a mobile iCT system [59]. Butler's iCT system can be wheeled into an OR when needed and then can be removed when not in use. As a result the, system can be shared among multiple OR's and thus spread the expense and use among multiple operating theaters, unlike Lunsford's and Shalit's systems. Research and use of iCT

continues to this day; Lunsford comments that over 3000 surgeries have been performed in their dedicated iCT OR through 1998 [60]. However, general adoption of iCT as a method to correct for brain shift has not occurred. This is probably due to dose considerations related to repeated exposure to X-ray radiation.

Another, more "dose friendly", intraoperative tomographic scanning method currently being investigated is iMR. As stated earlier, Maurer, Hill, Nimsky and Nabavi have all demonstrated the use of iMR as a shift measurement tool. However, the underlying reason to develop iMR is to produce an accurate and safe method of enhancing current IGNS. Peter Black had exposed the idea of using MR within the operating room as early as 1993 and in 1995, his group at Harvard (Brigham and Women's Hospital) published one of the first reports on the development and use of iMR [61, 62]. Subsequently, a flurry of papers have been published demonstrating the technical and practical solutions needed to implement iMR use during surgery, as well as it use [63, 64, 65, 66, 67, 68, 69, 70, 71, 72, 73, 74, 75, 76, 45, 77, 78, 79, 80, 81, 82, 83, 84, 85, 86, 87, 88]. These reports indicate that iMR can successfully be used to compensate for the shift seen during IGNS. However, there are still many concerns with iMR, such as: field inhomogeneities during scanning and their causes, false-positive readings caused by the leaking contrast agents and bleeding, the logistical requirements of surgery within or near an MR system, and the total cost of operation (TCO) of an iMR system given that actually very few cases benefit greatly from iMR updating. Current research in this field is addressing these issues, and their results may reduce the impact of or eliminate many of these concerns. However, currently iMR does not present itself as an completely efficient method of providing accurate IGNS.

In light of the TCO concerns of current iMR systems, intraoperative ultrasound (iUS) has gathered quite a bit of attention as a cheap and safe alternative to both iMR and iCT. This comes as no surprise, since iUS has been investigated and developed almost concurrently with modern stereotactic procedures and is found in almost all OR's [89, 90, 91, 92, 93, 94, 95, 96, 97, 98, 99, 100, 101, 102, 103, 104]. In 1989, in a paper that almost resembles a quantification of brain shift, LeRoux et al. measure the difference in tumor volumes predicted

by preoperative CT and iUS [105]. LeRoux's paper demonstrated the use of ultrasound to enhance the selection of resection margins during surgery using iUS, a method he revisits in a subsequent paper [106]. A more refined and explicit approach to iUS as a method to correct for brain shift was presented by in 1997 Bucholz et al. [40]. In that report, Bucholz demonstrated the ability to capture, register, and quantify brain shift using iUS [40]. The results in that paper were found using 2-dimensional iUS images. Bucholz went on to predict future research in iUS would be geared towards 3D acquisition, reconstruction and shift correction. In keeping with Bucholz's prediction, Gronningsaeter et al. have developed a 3 dimensional ultrasound system called SonoWand for iUS image acquisition [107, 108, 109, 110, 111]. They demonstrate the ability to acquire iUS images and then provide the iUS data to the surgeon for therapy planning. A group from Canada has also demonstrated the ability to acquire 3-dimensional iUS images [112, 113, 114], however, they extend the paradigm for brain shift correction by incorporating image warping in order to register intraoperative data to preoperative images. A process which will be discussed in the next section. By themselves, however, current iUS systems suffer from low signal-to-noise ratio (SNR), limiting their effectiveness in demarcating tumor regions during surgery. Furthermore, the SNR diminishes over the course of surgery, further limiting the effective use of iUS to the initial stages of surgery. Although brain shift stabilizes over the course of surgery, there is no evidence of that the stabilization of brain shift coincides with the diminishing SNR. With these limitations, iUS does not present itself as a complete intraoperative solution to the brain shift phenomena.

Overall, the intraoperative protocols described in this section do not provide quantitative compensation for brain shift by themselves. Rather, the brain shift correction comes from the surgeon's expertise and is performed in a qualitative manner. In light of this fact, David Roberts, building on the ideas presented by Bucholz, presented a novel framework for image-guided surgery aimed at providing quantitative shift compensation, called model-updated image guided neurosurgery (MUIGNS) [115].

Model-updated image guided neurosurgery

The idea behind MUIGNS is that intraoperative data acquisition methods can be combined algorithmically with preoperative images to provide accurate feedback of the brain's position during surgery. Roberts's method called for the use of a computational model that predicted the soft tissue motion of the brain under loading conditions seen in the OR. Since Robert's report there has been quite a bit of research on computational modeling of the brain [116, 117, 118, 119, 120, 121, 122, 123, 124, 125, 126, 127, 128, 129, 130, 131, 132, 133]. However, other mathematical methods may be used for the algorithmic matching of the intraoperative and preoperative datasets, such as atlas based statistical modeling of the shift [134] or interpolation of shift [135]. In terms of computational models, one of the most accurate models for brain shift has been demonstrated by a group at Dartmouth. The model is based on Biot's theory of consolidation mechanics and likens the behavior of the brain to a sponge. As CSF is removed from the brain, the tissue begins to sag in the direction of gravity. The consolidation mechanics mimic the empirical observations made by Roberts during surgery. In fact, *in vivo* studies of the model on a porcine brain demonstrate the ability to predict 70-80% of the manually induced shift. However, the finite-element method used to solve the equations of consolidation mechanics are computationally expensive and, at high resolutions, are not tractable for real-time[6] application in the OR. However, advances in computer technology are likely to invalidate this constraint. In lieu of current computer limitations, researchers have also looked at (computationally) simpler methods to model brain deformation. Skrinjar et al. at Yale, evaluate both spring-mass and linear stress-strain continuum models for brain shift. Gobbi et al., have also demonstrated a simple spline based warping of preoperative images to match intraoperative ultrasound volumes [136]. These models benefit from easier computation at the cost of accurate modeling of the brain tissue.

Regardless of the method to compute shifts, the output of each of these computational methods takes the form of a 3-dimensional deformation field that describes the motion of the

[6]Skrinjar et al. define real-time for MUIGNS as being faster than the rate of brain deformation [131]. That is, if the MUIGNS framework can measure, calculate, and correct for the the deformation faster than it occurs, then it will seem like real-time for the surgeon.

brain between its preoperative and intraoperative states. For the MUIGNS framework, this deformation field is used to update preoperative images to make them reflect the effects of the brain shift. Ideally, after the model updating has been performed, S_P localization of the brain would be displayed in the corresponding position on the surgical guidance system. Compare this with the erroneous presentation seen in Figure 13 of current IGNS systems. Furthermore, the MUIGNS framework is iterative and can be executed in a serial manner during surgery to follow brain deformation over the course of the operation. A schematic of MUIGNS is shown in Figure 4. As one can see from the figure, a key component to any MUIGNS implementation is the accurate acquisition of intraoperative data. The intraoperative data, or sparse-data, is used to drive and constrain the computational model's prediction of brain shift. Sparse, in this context, means data with limited information or extent. The sparsity of the data collected for modeling purposes is reflected by the fact that, usually, the data cannot reflect the total deformation of the brain by itself. Each of the intraoperative imaging methods described earlier, as well as S_P localization devices (i.e. pen-probes, etc.) can be used for sparse-data data acquisition. However, the concerns outlined earlier for each intraoperative method limit their potential as sparse-data acquisition systems, save iUS because of its ubiquity most OR's. Also, the ability for iUS to safely and accurately acquire subsurface data, which provides critical data for most computational models, may play a critical role in the development of a standard MUIGNS framework. Nonetheless, iUS by itself may not be enough and must therefore be coupled with a complementary sparse-data acquisition system. An efficient method to generate this complementary data is non-contact range-sensing of the cortical surface. The tandem of surface and limited deep tissue information is hoped to provide computational models with enough information to correct for brain shift over the course of surgery.

Range sensing of the cortical surface for sparse-data

The impetus for the research in this dissertation is geared towards providing some of the sparse-data required for MUIGNS. Specifically, the accurate and efficient localization of

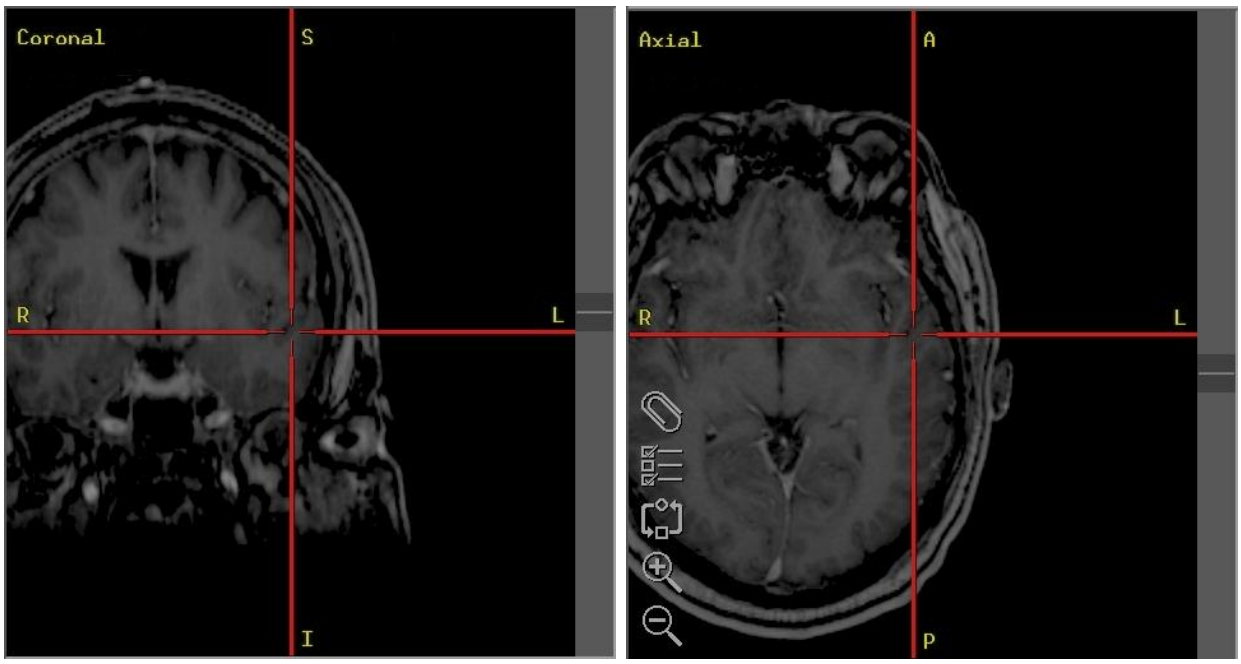

Figure 3: Intraoperative brain shift observed at Vanderbilt University. The images show the location of a surgical probe in S_I to be within the parenchyma of the brain. In fact, the surgical probe is located in S_P on the surface of the brain near the superior temporal gyrus.

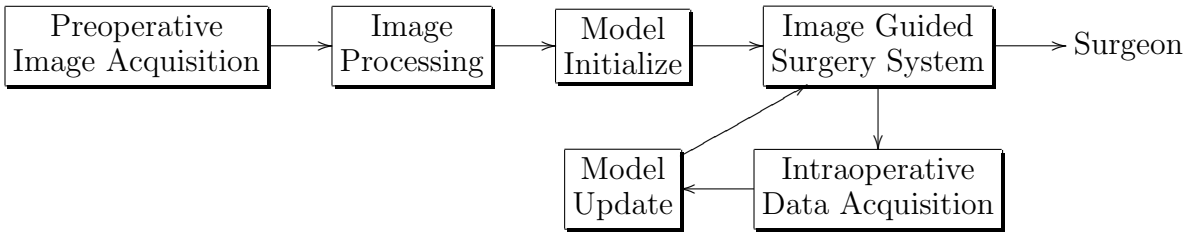

Figure 4: Schematic for model updated image guided neurosurgical procedures (MUIGNS).

cortical surface data. The goal of characterizing the cortical surface accurately is shared by other research groups as well. A group at Yale are considering gathering cortical surface data using photogrammetric range sensing methods. Photogrammetry[7] dates back to the middle of the 19th century when Aim*é* Laussadat originally proposed using cameras for map-making [137]. More recently, Paul Debevec and George Borshukov, who have helped usher photogrammetry into Hollywood as a method of virtual cinematography[8], have defined photogrammetry as a method of 3-dimensional object reconstruction using images [138, 139]. A subset of this broad concept is range sensing using only two images, i.e. stereo-pair photogrammetric range sensing. This method of range-sensing provides 3-dimensional geometry measurement in a non-contact fashion, using a pair of calibrated still cameras. Photogrammetry and stereo-pair imaging has been used in medicine for a number of applications [140, 141, 142, 143, 144, 145, 146, 147, 148, 149, 150]. Skrinjar and Duncan at Yale have demonstrated the use of stereophotogrammetry to determine cortical surface data [129, 130, 131]. More recently, Hai Sun et al. from Dartmouth have used stereoscopic images from an operating microscope to generate 3-dimensional data for MUIGNS [151, 152]. Photogrammetry has the benefit of over a century of research and development. As a result, the photogrammetric algorithms resolve three-dimensional position from calibrated images highly accurately.

Another highly accurate method for range sensing is laser range sensing (LRS). LRS uses monochromatic (narrow band), collimated light and the principle of triangulation to resolve geometry, see Figure 5 and Equation 1 [153].

$$r = \frac{d * \sin b}{a} \tag{1}$$

Because of its high precision in controlled environments, LRS has seen application in CAD modeling as well as machine vision [154, 155, 156, 157]. LRS has also been used as a non-

[7]Greek: *foto* – light, and Greek: *metria* – to measure. Originally proposed by Meyenbauer and referenced in Vogel's Chem. Light in 1875 [5].

[8]Highlighted in the stunning visual effects seen in the Warner Bros. Pictures "Matrix" movies.

contact deformation measurement tool in industry [158]. However, LRS is still in its infancy relative to photogrammetric range sensing and therefore demonstrates some limitations that current methods of photogrammetry do not. Specifically, laser range scanning is intimately tied to the linewidth (or frequency range) of the laser light. This means that objects that do not reflect the linewidth of the laser light do not permit range scanning. Furthermore, since the distance calculation is made based on reflected angles, highly specular[9] objects tend to confuse or prevent LRS. Finally, laser range scanning suffers from over- and under-estimation of the distances of curved surfaces. However, these limitations are systematic and thus surmountable in future generation LRS systems [159, 160, 161].

Despite its lack of refinement, LRS systems have already seen use in medicine. Many of the applications that have enjoyed success using photogrammetry are also possible using LRS [158]. In neurosurgery, LRS systems were first used for surface registration of patients' foreheads to align S_P to S_I[162]. Surface registration, which will be discussed in detail later in this document, is a complementary system to the standard registration provided by markers. Subsequent use of lasers for S_P-$S_I$registration was also reported by Rabbe et al. [163]. With respect to MUIGNS, Michel Audette, while a graduate student with Terry Peters, was one of the first to describe the use of LRS systems to characterize the cortical surface [164, 165]. However, Audette did not perform any quantification of intraoperative LRS. In many respects, this dissertation picks up where Audette left off. That is, the critical evaluation of LRS of the cortical surface during surgery, the registration of the LRS data to preoperative images, and algorithmic investigation of the optimal method for both. The umbrella under which the goals of this dissertation are outlined are within MUIGNS. Thus, the research for using LRS in neurosurgery will be extended in this dissertation to allow critical insight for the computational modeling pipeline. Specifically, the tracking of cortical shift using the LRS will be investigated as a method to provide boundary constraints for a

[9]Light reflection can be split into two basic categories: specular and diffuse. Diffuse reflectance occurs when incident light is reflected in all angles equally. The piece of paper this dissertation is printed on (if printed) is a good example of a diffuse reflector. Specular reflection is when the incident light is preferentially reflected at a certain angle. In general, "shiny" objects exhibit specular reflectance.

computational model. With these ideas in mind, let me divest some of the results of this research.

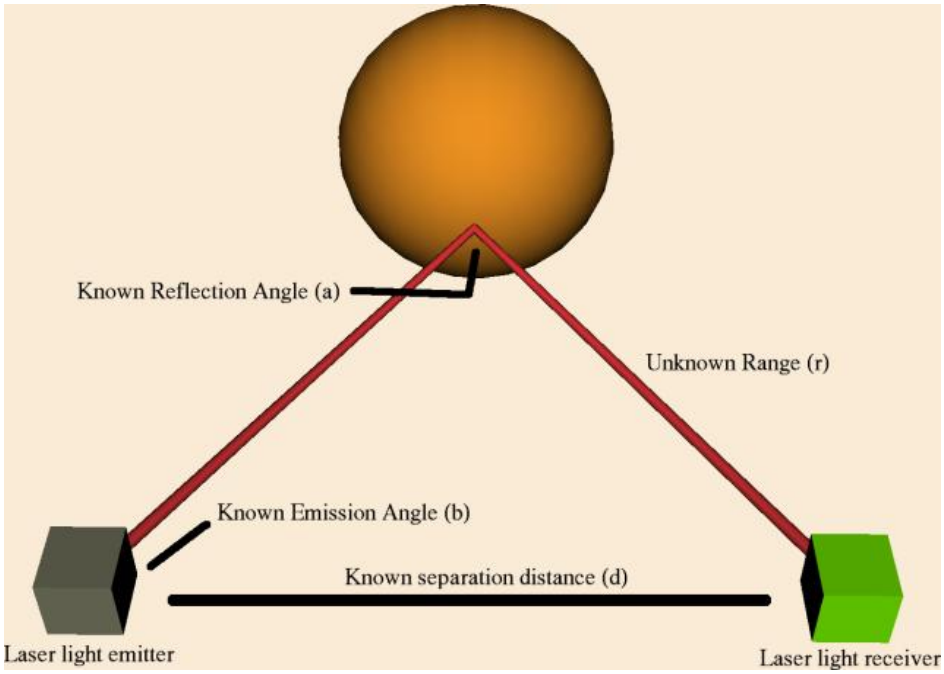

Figure 5: Laser range scanning for 3-dimensional geometry measurement. The unknown distance r can be calculated given the angles a and b and the distance d with the relationship in Equation 1.

CHAPTER III

MANUSCRIPT 1 - CORTICAL SURFACE REGISTRATION USING TEXTURE MAPPED POINT CLOUDS AND MUTUAL INFORMATION

Original form of manuscript appears in LNCS: Medical Image Computing and Computer Assisted Intervention: 2002, 2489: 533, 2002.

Abstract

An inter-modality registration algorithm that uses textured point clouds and mutual information is presented within the context of a new physical-space to image-space registration technique for image-guided neurosurgery. The approach uses a laser range scanner that acquires textured geometric data of the brain surface intraoperatively and registers the data to grayscale encoded surfaces of the brain extracted from gadolinium enhanced MR tomograms. Intra-modality as well as inter-modality registration simulations are presented to evaluate the new framework. The results demonstrate alignment accuracies on the order of the resolution of the scanned surfaces (i.e. submillimetric). In addition, data are presented from laser scanning a brain's surface during surgery. The results reported support this approach as a new means for registration and tracking of the brain surface during surgery.

Introduction

Understanding the geometric characteristics and the impact of intraoperative surgical events upon the cortical brain surface has important implications in the development of image-guided surgery (IGS) systems. In recent studies [45], the need for brain shift compensation strategies to prevent compromising IGS navigation has become an important area of research [115]. When using a computational approach to correct for brain shift [121], capturing the geometric and visual changes of the brain surface due to deformation may be a valuable source of intra-operative data. To achieve this end, a laser range scanning system capable of capturing textured surfaces with sub-millimetric accuracy will be used.

Using features from the cortical surface to register does have precedent. Nakajima et al. demonstrated an average of 2.3 $\pm$ 1.3 mm fiducial registration error (FRE) using cortical vessels for registration [166]. More recently, Nimsky et al. reported a deformable surface approach to quantify surface shifts using a variation on the iterative closest point (ICP) algorithm [45]. Also, some preliminary work utilizing a scanning based system for cortical surface registration has been reported but a systematic evaluation has not been performed to date [164]. The novelty of the approach reported here is that both vessel information and three-dimensional topography will be used as the basis of alignment. Furthermore, the scanner provides a highly accurate method for tracking the brain surface that can be used in the model-updating framework.

As an initial step, an implementation has been developed using an iterative closest point (ICP) [167] framework with mutual information (MI) [168]. Although ICP and MI have been used extensively [169, 170], previously published registration frameworks do not entirely apply to the unique data provided by the scanner or this particular registration approach. The data acquired by the scanner provides a one-to-one correspondence between contour point and image intensity. However, intensity correspondence between a three-dimensional MR surface and an intraoperatively acquired laser-scanned cortical surface is somewhat more elusive. The most similar work relating to this registration framework is that by Johnson and Kang [171] in which these investigators used an objective function for registration based on a combined Euclidean distance and color difference metric. Used primarily in a landscape alignment application, this technique would not be amenable to the alignment process here, since the intensity distribution between scanner and MR image data is fundamentally very different. To our knowledge, no registration algorithm has been developed that will register textured three-dimensional surfaces from two different imaging modalities within the context of cortical surface registration.

Methods

In the realization of this approach, a laser range scanning system (RealScan 3D, 3D Digital Corporation, Danbury, CT) capable of capturing three-dimensional textured surfaces to sub-millimeter accuracy has been utilized (see Figure 6). The scanner is lightweight, compact and has a standard tripod mount. The scanning field consists of 500 horizontal by 494 vertical points per scan and is accomplished in approximately 5 seconds. Extensive calibration and characterization has been performed by Cash et al. and has demonstrated the fidelity at which surface data can be acquired [172]. Additionally, the device is approved for use in neurosurgery by the Vanderbilt University Medical Center Institutional Review Board.

The registration framework involves two primary steps in its execution. The first step involves acquisition and preparation of the registration surfaces. With respect to laser scanned surfaces, the scanner is currently placed approximately 1-2 feet from the surface of interest (achieved either by passive arm or monopod for intraoperative use). The horizontal range of the scanner is established and a vertical laser stripe passes over the surface in approximately 5 seconds. The data acquired consists of a three-dimensional point cloud with each Cartesian coordinate color-encoded via texture mapping into a digital image that is acquired just after scanning. The texture-space to scanner-space registration is calibrated by the manufacturer. The MR-generated point cloud is prepared by segmenting the brain volume, followed by ray-casting to find surface points, and averaging subsequent voxels to generate gray-scale values for each surface point (Analyze AVW - Biomedical Imaging Resource).

The final step in our approach is to perform surface registration using a two-stage process. An iterative closest point (ICP) algorithm is performed initially to align the point clouds of interest (i.e. laser-scanned surface and/or MR surface). The second stage is a constrained intensity-based registration. The constraint requires the alignment transformation to only operate in spherical coordinates with known radius R; the radius is provided by sphere-fitting the target surface [173]. By enforcing this restriction on the transformation, the degrees of

geometric freedom are reduced from six to three, i.e. elevation ϕ, azimuthal θ, and roll ψ. For the method of intensity-based registration, a maximization of normalized mutual information (NMI) [174] approach is conducted using Powell's optimization algorithm [175]. Referred to as Surface MI in this work, the method aligns textured surfaces only and does not use volumetric image data. The results presented here do not reflect true cross-modality registration (i.e. scanner to MR).

Registration Experiments

To evaluate robustness and accuracy of Surface MI, an initial series of experiments was conducted using a spherical phantom with a heterogenous intensity pattern on the surface. The range scanned surface acquired for registration experiments occupied a solid angle of $\Omega = 1.2\pi$ steradians[1] and contained 67257 points (see Figure 7). A known transformation was then applied to the target surface to generate the floating surface. The limits for elevation, azimuthal and roll angle perturbations were ± 13, ± 13, and ± 25 degrees, respectively (the radius of the spherical phantom was approximately 110 mm). The floating and target surfaces are then re-registered using Surface MI. Five hundred randomly distributed combinations of ϕ, θ, and ψ were tested for registration accuracy.

The second series of experiments employed the point clouds generated from surface projections of the MR volume. The target surface that was generated using a clipping plane had a solid angle of approximately $\Omega = .38533\pi$ steradians and contained 48429 points (see Figure 8). Similar to the spherical phantom experiments, perturbations in ϕ, θ, and ψ were applied to the MR surface over 500 trials. The range for the parameters ϕ, θ, and ψ were the same as those for the previous experiment with similar radius (R=105 mm).

The last series of experiments evaluated the efficacy of the developed algorithm in registering surfaces across modalities. Inter-modality surfaces were simulated by inverting the texture of the point cloud. Five hundred trials registering a texture-inverted region of interest (ROI) to the original MR brain surface were performed with initial misregistrations

[1]The solid angle of a unit sphere $\Omega = 4\pi$ steradians.

Figure 6: Laser scanner used to acquire textured point clouds.

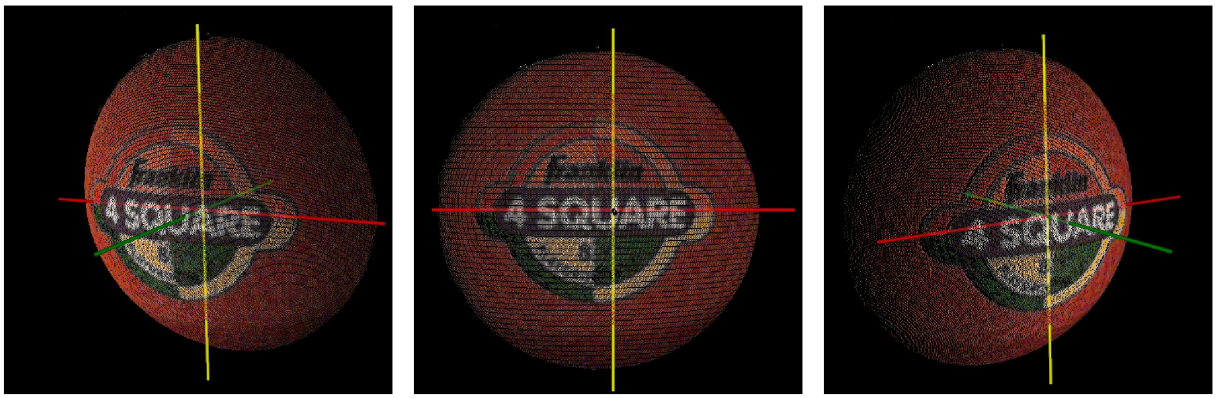

Figure 7: Sample textured point cloud generated using a laser range scanner.

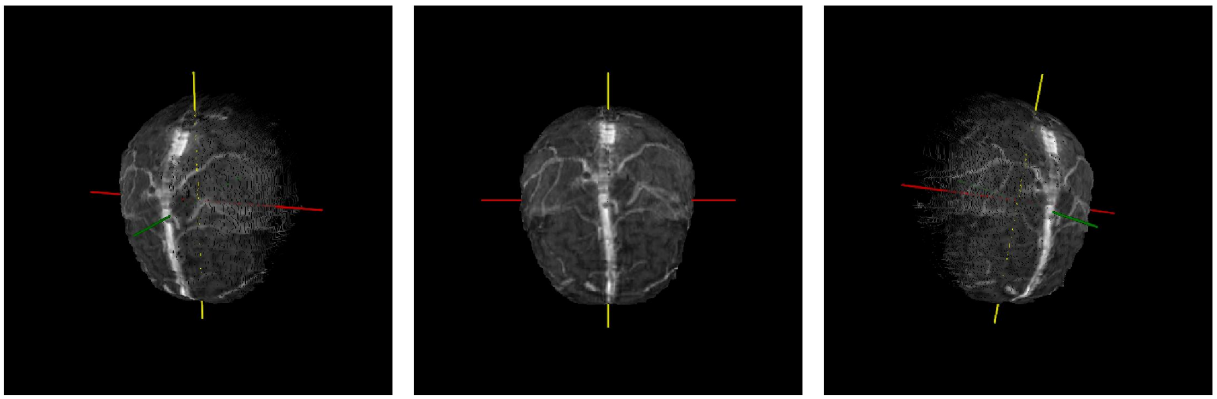

Figure 8: Sample textured point cloud generated using surface projection on a gadolinium enhanced MR volume.

comparable to the spherical phantom experiments. The ROIs were generated by varying the normal of the clipping plane used to create the target surface between ± 0.1 cm in the sagittal and coronal axis while holding the axial value at 1 cm (see Figure 9). To create the misregistration between the float and target surface, each surface was re-centered about it's geometric centroid.

Registration Results and Discussion

Since the same scan was used for both target and floating surfaces in the registrations process, the one-to-one correspondence in points was known. This allowed calculation of the mean target registration error (TRE) between point clouds as well as the global maximum for NMI. Sample registration results are presented for each experiment series (i.e. spherical phantom, intra-modality MR, simulated inter-modality MR) in Figure 10. In addition, a distribution of TREs for each series of experiments can be seen in Figure 11.

Registration results from the 500 trials using the spherical phantom yielded a mean TRE of $11.38 \pm 28.75mm$ (min.=0.04, max.=$127.61mm$). Although this result is less than remarkable, it should be noted that 70% of the trials achieved a mean TRE of $0.20 \pm 0.05mm$ (min.=0.04, max.=$0.31mm$). Furthermore, the misalignment range during surgery is expected to be ± 5 degrees within each angular coordinate. Within this range, the registration process achieved a 100% success rate (i.e. NMI optimization reached it's global maximum).

With respect to the intra-modality MR experiments, all 500 trials resulted in an ideal value of NMI. The mean TRE for the 500 trials was $0.14 \pm 0.04mm$ (min.=0.04, max.=$0.27mm$). The increased success rate of this series of experiments as compared to the previous trials is likely due to the differences in the geometric structure of the intensity information. Most of the intensity information of the spherical phantom is contained in the central region of the surface. In some cases, when the initial mis-registration of the spherical phantom caused sufficient non-overlap of the central area, the algorithm did not register the surfaces correctly. For the brain, the intensity pattern of the vessel structure occupies most of the surface. Thus, even though the brain's surface occupies a smaller solid angle than that of the ball,

the distribution of the intensity pattern allows the alignment of more severely misregistered surfaces.

The last series of experiments simulating inter-modality registration generated a mean TRE of $3.38 \pm 7.18mm$ (min.=0.07, max.=$53.75mm$). Similar to the spherical phantom, 67% of these trials produced a mean TRE of $0.37 \pm 0.19mm$ (min.=0.07, max.=$1.00mm$). Analysis of the failed trials indicated that the spherical constraint prevented accurate registration. In general, the algorithm failed to register surfaces clipped from or containing the periphery of the surface projection, which contained a much higher surface curvature as compared to the target surface. This discrepancy in surface curvatures between target and floating surfaces caused the sub-optimal registrations. In general, the occurrence of curvature discrepancies intra-operatively will be limited since vessel landmarks will be used to provide an initial alignment for the Surface MI.

Conclusions and Future Work

The results of this paper show that the ICP and MI framework is a useful tool for cortical surface registration. Results of both intra- and inter-modality surface registration show sub-millimetric accuracies using a phantom. This paper outlines preliminary steps taken with the laser range scanner and the Surface MI algorithm. *In vivo* analysis of the registration results is currently in progress. Figure 12 shows intra-operative data of the cortical surface acquired by the laser range scanner. More quantitative studies of the laser range scanner and registration algorithm are also planned using an optical tracking system. Algorithmically, the ability to track and register cortical deformations is also being studied.

Acknowledgements

The authors acknowledge Dr. Hill for his correspondence on MI. VTK (Kitware Inc.) and Analyze AVW (Mayo Clinic) provided software. A grateful acknowledgement to the VUMC Neurosurgical staff. This project is supported in part by the Vanderbilt University Discovery Grant Program.

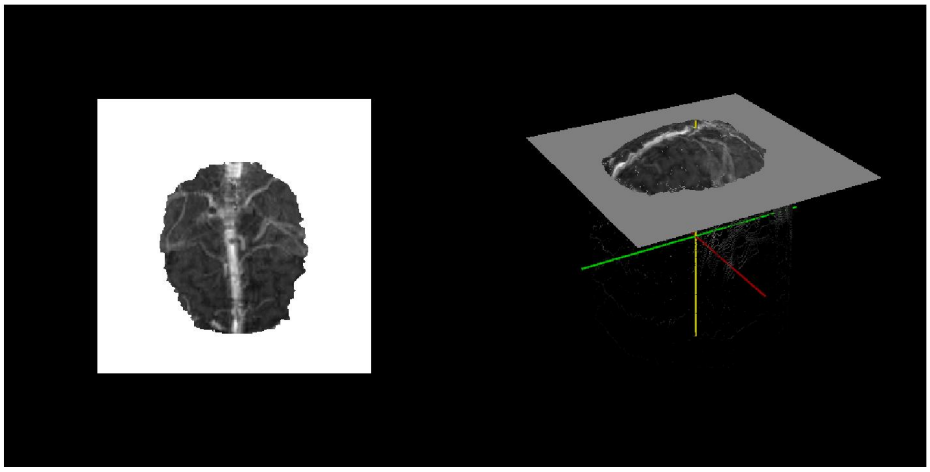

Figure 9: Use of a clipping plane to select a region of interest in the surface projection.

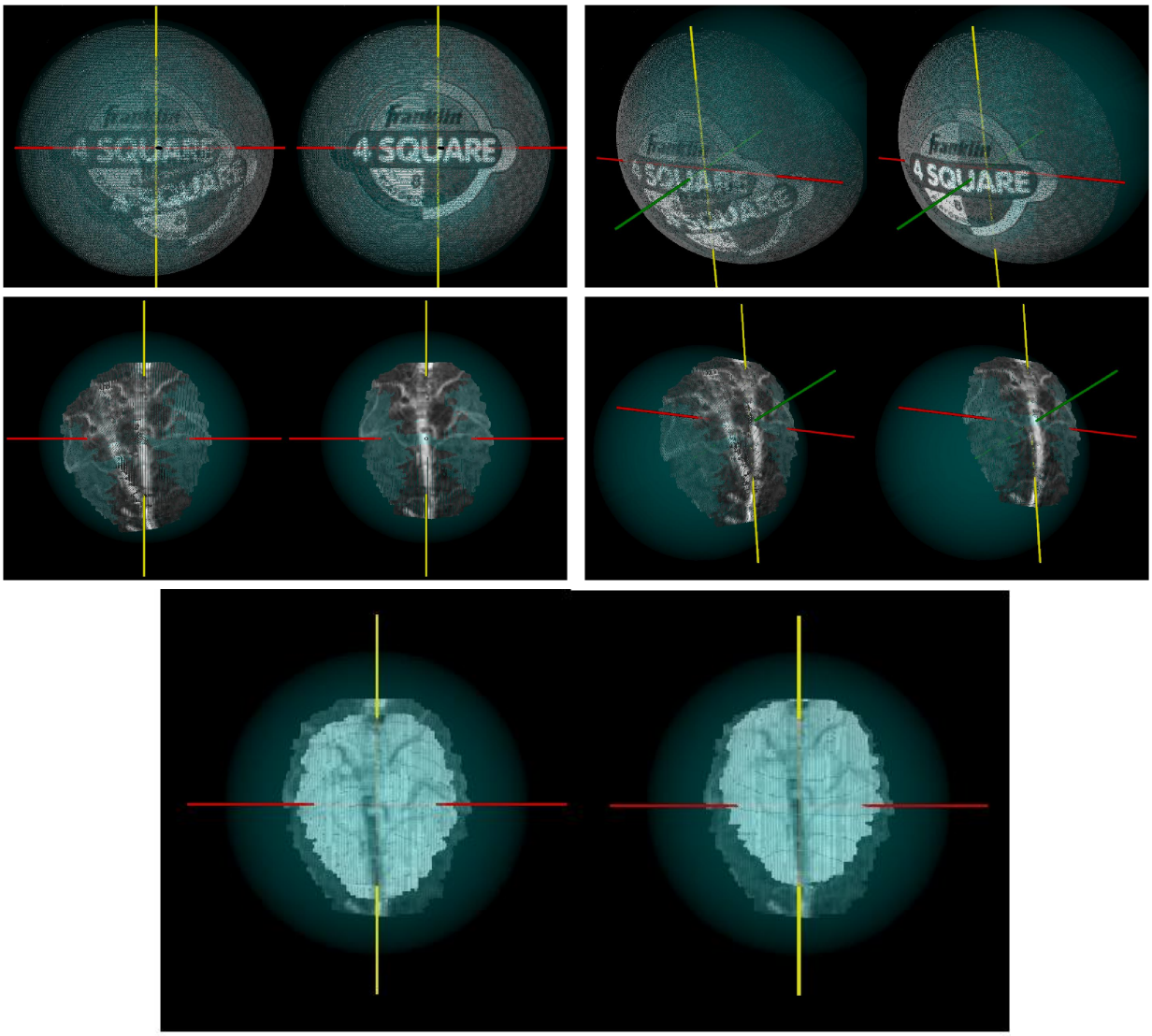

Figure 10: Sample registration results. Top row, from left to right: on-axis view of misregistered and registered surfaces of the spherical phantom, off-axis view of misregistered and registered surfaces. Middle row: sample results of the intra-modality registration, presented similar to the top row. Bottom row from left to right: misregistered and registered surfaces from simulated inter-modality experiments.

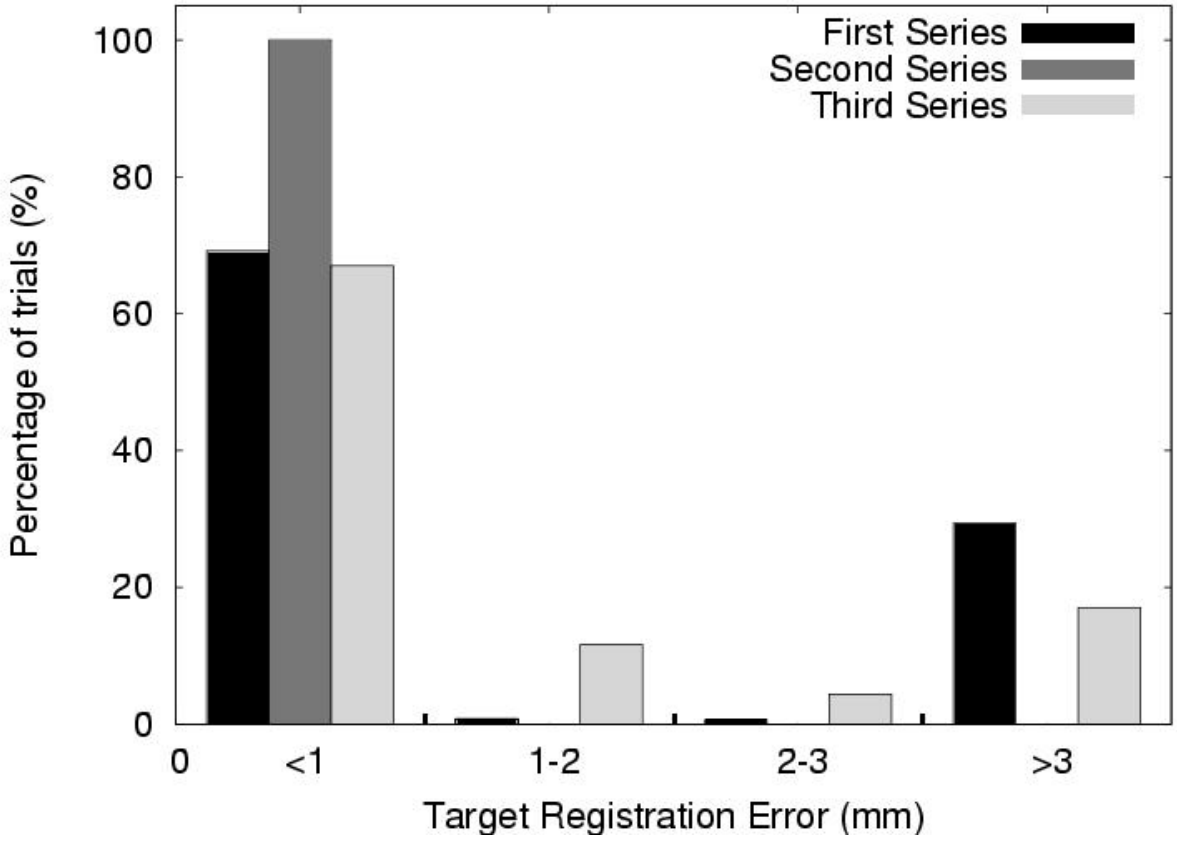

Figure 11: Distribution of Target Registration Error (TRE) for each series of experiments

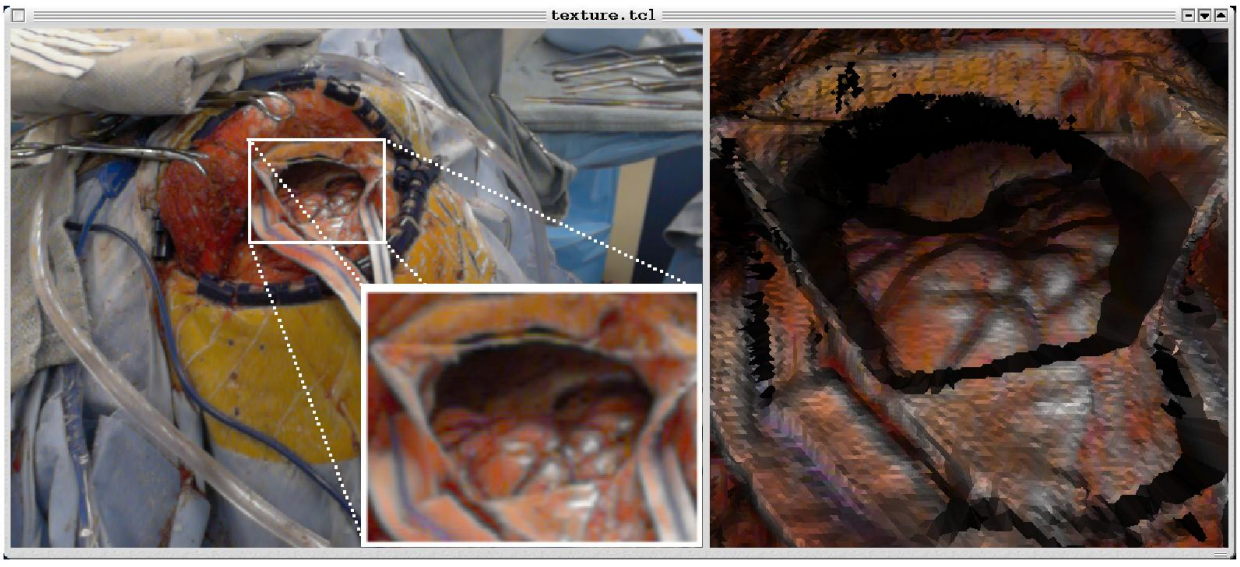

Figure 12: Example dataset taken with the laser range scanner in the operating room. Left, a CCD image of the surgical area. Right, a tessellated point cloud with texture mapped points on the right.

CHAPTER IV

MANUSCRIPT 2 - CORTICAL SURFACE REGISTRATION FOR IMAGE-GUIDED SURGERY USING LASER-RANGE SCANNING

Original form of manuscript appears in IEEE Transactions on Medical Imaging, 22(8): 973-985, August 2003

Abstract

In this paper, a method of acquiring intra-operative data using a laser range scanner (LRS) is presented within the context of model-updated image guided surgery. Registering textured point clouds generated by the LRS to tomographic data is explored using established point-based and surface techniques as well as a novel method that incorporates geometry and intensity information via mutual information (SurfaceMI). Phantom registration studies were performed to examine accuracy and robustness for each framework. In addition, an *in vivo* registration is performed to demonstrate feasibility of the data acquisition system in the operating room. Results indicate that SurfaceMI performed better in many cases than point-based (PBR) and iterative closest point (ICP) methods for registration of textured point clouds. Mean target registration error (TRE) for simulated deep tissue targets in a phantom were 1.0 ± 0.2, 2.0 ± 0.3, and 1.2 ± 0.3 millimeters for PBR, ICP, and SurfaceMI, respectively. With regard to *in vivo* registration, the mean TRE of vessel contour points for each framework was 1.9 ± 1.0, 0.9 ± 0.6, and 1.3 ± 0.5 for PBR, ICP, and SurfaceMI, respectively. The methods discussed in this paper in conjunction with the quantitative data provide impetus for using LRS technology within the model-updated image guided surgery framework.

Introduction

Image-guided neurosurgery (IGS) requires the accurate alignment of the preoperatively acquired diagnostic image series to a coordinate system that is specific to the intraoperative

patient's neuroanatomy, a process often referred to as registration. Once the registration has been provided, all preoperative planning and acquired data relevant to the patient's neuroanatomy can be displayed to the neurosurgeon intraoperatively and used for assistance in guidance and treatment. This process to a large extent has become routine within medical centers across the country. Additionally, the methods of localization within image-space (establishment of coordinate system within the diagnostic image series) and physical-space (coordinate system relevant to patient features) have been investigated to a great extent. For example, the necessary shape and volume of synthetic image landmarks, i.e. fiducials, has been rigorously analyzed and has resulted in design constraints that optimize localization within conventional imaging modalities [36][176]. Regarding localization in physical-space, various optical, acoustic, electromagnetic, or mechanical devices have been developed to characterize the intraoperative environment for the registration process.

With respect to mathematical aspects of image-to-patient alignment, the most common approach used is a point-based registration (PBR) whereby landmarks, either natural or synthetic, are localized in the patient's image series and aligned with corresponding landmarks digitized in physical-space intraoperatively. The geometric transformation is generated based on the minimization of the squared distance error between corresponding points [28]. Further analysis on the configuration of fiducial markers, the optimum number, and the effects on target localization error have also been forthcoming [176]. Apart from the point-based approach, another common technique for registration is the use of matching geometric surfaces. The ability to acquire surface data using optical/electromagnetic/ultrasound probes and lasers [177][178][164][179][163] in conjunction with surface extraction algorithms applied to imaging data have led to new robust methods of registration [170]. Surface-based alignment techniques have two distinct advantages: (1) point correspondence is not required, and (2) an averaging-effect serves to reduce uncorrelated localization error generated during the acquisition of spatially well-resolved surface data. However, some disadvantages are present in that the scalp in general lacks geometric specificity, and the skin surface may deform due to intraoperative drugs or procedural retraction [4]. A third registration technique, less

commonly used for IGS purposes, is the intensity-based or volume registration approach [176]. Usually applied for the alignment of image volumes, the predominant use for these techniques in IGS has been within the intraoperative magnetic resonance (iMR) environment where serial image volumes are acquired during surgery.

One common assumption in all of the above methods is that the skull and brain can be characterized by rigid body mechanics; and, in general, many of these techniques have achieved accuracy measures that are clinically useful. However, with the growing experience in applying these enhancements in surgical navigation, design characteristics for the next generation of surgical guidance systems are slowly emerging. More specifically, one of the most challenging problems to IGS development is the realization that rigid body assumptions are in many cases inadequate. Identified as early as 1986 by Kelly et al. [16], the potential problem of "brain shift", i.e. deformation, during surgery has given rise to concerns regarding the fidelity of current IGS systems. The earliest assessments of error from brain shift using IGS were on the order of 5 millimeters [38]. Subsequent investigations measuring intraoperative brain surface movements have reported an average deformation of 1 centimeter. An example of intraoperative brain shift experienced by our group can be seen in Figure 13.

Insightful relationships regarding the predisposition for brain movement in the direction of gravity have also been reported [39][44]. In addition, with the advent and use of iMR systems, more detailed studies measuring both surface and subsurface shift have been performed [45][46]. The general conclusion from these studies is that brain deformation during surgery needs to be accounted for to maximize the effectiveness of IGS systems.

The approaches to accounting for brain shift can be generally placed into two categories: (1) intraoperative imaging, and (2) intraoperative non-rigid registration frameworks. Intraoperative imaging would include the use of computed tomography (iCT), magnetic resonance (iMR), and/or ultrasound (iUS) imaging. In the 80's, there was a significant effort to introduce iCT, but concerns over patient radiation, the need for radiological staffing of the OR, and the cumbersome lead protection seemed to adversely affect the adoption of this technique [53]. Several medical centers are now deploying iMR imaging capabilities [180][80] and

have developed elegant and sophisticated methods for visualization in the operating room (OR) [177][181][81]. Although conceptually appealing, the exorbitant cost and cumbersome nature of such systems (e.g. need for an MR compatible OR) have left their widespread adoption unclear at this time. In addition to these logistical concerns, recent reports have illustrated potential problems related to surgically-induced contrast enhancement which can be often confused with contrast-enhancing residual tumor [182]. Other reports have illustrated "image distortions from susceptibility and/or eddy current artifacts" related to the presence of MRI-compatible Yasargil clips for aneurysm clipping procedures [86]. Although this did not compromise this particular procedure, the question regarding the degree of distortion from other MR compatible instruments (e.g. retractors) must be studied further . It should be noted, however, that researchers have also shown significant benefits with iMR by increasing patient survival times and decreasing patient complications [68]. Appropriately, investigators are still determining the efficacy of iMR in order to identify its most important uses. An interesting alternative to iCT and iMR also under consideration is co-registered intraoperative ultrasound (iUS) [40][113][109][110]. Although not capable of whole-brain imaging, many advocate that the locally reconstructed volumes provided by iUS can provide real-time guidance feedback. However, the clarity of iUS images is limited and using this technique as the sole source of feedback may not be the best approach. Often the images become less valuable as the procedure continues since the contrast between tumor and normal brain begins to diminish. This is not to say that iUS does not have a role in image-guided neurosurgery; but rather, its role could be as one source of data within the mechanics of building an intraoperative updating system.

The second category of solutions to intraoperative brain shift represent a more minimally invasive approach to the OR environment whereby non-rigid registration methods would be used to register preoperative data to the intraoperative environment. This strategy as highlighted by Roberts et al. [115] uses computational models in conjunction with non-intrusive intraoperative data acquisition as a means for deforming high resolution preoperative-based images to reflect intra-surgical conditions. Detailed work regarding the fidelity of such com-

putations within animal and human systems has been reported [121][123]. One advantage of this framework is that all forms of preoperative data can be simultaneously updated (i.e. positron emission tomography, electroencephalography data, functional MR imaging, and MR spectroscopy) whereas iMR/iCT/iUS systems will still require a non-rigid registration method for the effective utilization of all preoperatively acquired data. In addition, computational techniques to non-rigidly register image data via modeling methods have a long precedent in the neurosurgical community. Elastic matching has been a technique employed by many to register multi-modality images [183][184]. Deformable templates for large deformation warping of images has also been utilized [185]. With respect to the model-updating paradigm, other investigators have also been pursuing variants of this approach [132][186][128]. Although computational models may not be able to predict the extent of tumor margins as well as iMR or iCT, it must be recognized that alternative localized imaging techniques are rapidly being developed for this task (e.g. such as optical spectroscopy [187][188]). Within this vision of IGS, neurosurgeons will have a collection of minimally invasive tools to aid in navigation, visualization, and demarcation of diseased tissue. The work reported within this paper subscribes to this shift compensation strategy.

Rapidly acquiring minimally invasive data that describes changes in brain geometry during surgery is necessary to develop a computational approach that accounts for brain deformations. In this paper, preliminary work using a laser range scanner (LRS) is presented within the context of a new image-to-patient registration framework that is inherently sensitive to the brain shift problem. The registration method employs both geometric and intensity data acquired from the laser range scanner to align the patient's intraoperative cortical surface to the MR image counterpart. Since the LRS captures both geometric and color-intensity information from the intraoperative brain surface, a feature-rich source of data is provided for registration and the eventual tracking of deformation. In this work, a detailed set of phantom experiments is performed to illustrate the method, and the paper concludes with a clinical example. To our knowledge, these results represent the first clinical illustration of an image-to-patient registration between an MR tomogram and a laser range

scanned cortical surface. It should be noted that using features from the cortical surface to register images does have some precedent. Nakajima et al. demonstrated an average of 2.3 ± 1.3 millimeters fiducial registration error using cortical vessels for registration [166]. Also, some preliminary work using a scanning based system for cortical surface geometric registration has been reported but a systematic evaluation has not been performed to date [164]. In addition to LRS work, efforts by Skrinjar et al. have been reported for the use of a stereo-pair camera systems to capture and characterize the brain surface during surgery [130][129]. The work presented here represents an initial step in developing OR compatible equipment designed to capture brain shift systematically for the eventual use in a model-updating paradigm.

Methods

Laser Range Scanner

One critical component in developing a model-updating strategy for compensating for shift is the rapid acquisition of geometric data that describes the deforming nature of the brain during surgery. For this task, we have employed a LRS (RealScan 3D, 3D Digital Corporation, Bedford Hills, NY) that is capable of capturing three-dimensional topography as well surface texture mapping to sub-millimeter accuracy (Figure 14(a)).

The LRS is lightweight, compact and has a standard tripod mount (L9.5" x W12.5" x H3.25", 4.5 lbs). For clinical use, the LRS has been equipped with a customized vibration-damping monopod (Figure 14(b)) or can be attached to a surgical arm within the operating room (Figure 14(c)). The scanning field consists of 512 horizontal by 500 vertical points per scan and is accomplished in approximately 5-7 seconds. The laser used is a Class I "eye safe" 6.7 mW visible laser. The laser stripe generator has an adjustable fan-out angle (maximum fan-out is 30 degrees) and acquires each stripe at approximately 60 hertz. The scanner accuracy is 300 microns at 30 centimeters from the object of interest and approximately 1000 microns at 80 centimeters.

For the experimental and clinical data reported herein, the scanner was brought to be-

tween $30 - 45cm$ of the target. The complete process of moving the scanner into the field of view (FOV), acquiring a scan, and exiting from the FOV takes approximately 1-1.5 minutes (this includes laser light adjustments and LRS fan-out-angle). In general, the surgical staff has considered the impact of the LRS in the OR to be negligible. Also, the Institutional Review Board at the Vanderbilt University Medical Center has approved the laser range scanner for use on human patients and patient consent was acquired for all clinical data.

Registration

With respect to the alignment of image space to patient space, several standard registration methodologies have been used with the addition of a novel registration strategy custom-developed for the unique data acquired by the scanner. The distinction between this last approach and the more traditional methods is that the feature-rich intraoperative brain surface as acquired by a laser range scanner and the MR grayscale encoded brain surface derived from the image volume are used for patient registration. One advantage of cortical surface registration over rigid cranium-based techniques is that the method is inherently sensitive to brain shifts occurring in the early stages of surgery. For example, often during clinical cases involving tumor resection, the brain will swell upon opening of the cranium and dura. By registering with respect to the shifted brain surface, one could argue that a more accurate and spatially consistent registration can be achieved (even when using rigid body assumptions). In addition, the surface of the brain could be registered dynamically during surgery to account for some portion of shift or be used to track non-rigid deformations for use in a model-updating shift compensation strategy.

The new registration approach (SurfaceMI) begins with the segmentation of the region of interest, i.e. brain, from the MR image volume. From this segmented volume, a point cloud representation of the brain surface geometry is extracted. Using the preoperative plan, the location of the resection surface is identified on the CT/MR images and positioned orthogonal to a ray-casting source. A ray-casting algorithm combined with voxel intensity averaging (averages 3-5 voxel intensities along ray) is employed to grayscale encode the point

cloud. At the conclusion of this process, the patient's cortical image surface is rendered into a textured point cloud that contains intensity patterns representing sulcal-gyrus differences as well as contrast-enhanced vasculature (Figure 15). These unique tissue patterns of intensity will be central to the alignment process. For the point clouds used in this paper generated via ray-casting, the mean and median point-to-point distances were 0.7 and 0.6 millimeters, respectively. With respect to the intraoperative acquisition of data, a calibration object is routinely scanned prior to registration to ensure operational fidelity of the laser scanner. At select times during the surgery, after durotomy, the laser range scanner is positioned over the exposed brain surface and a range scan is acquired. Triangulating between the laser light source and the captured laser light pattern on a CCD digital camera, the three-dimensional location of each illuminated point can be determined. In addition, each three-dimensional point is color encoded by a second digital camera on the scanner that captures an image of the surgical field of view. The mean and median point-to-point distances for the range scan point clouds used in this paper were 0.65 and 0.6 millimeters, respectively.

The intensity and geometric data acquired by the laser-scanner coupled with the image processing of the segmented brain surface provides a novel avenue for developing a new registration framework. The process begins with an initial guess based on aligning natural fiducials using a traditional point-based framework. Following this process, an iterative closest point (ICP) algorithm is used to further align the laser range scanner point cloud to the CT/MR counterpart. The disparity function, d, used within this minimization algorithm is,

$$d = \frac{1}{N} \sum_{j}^{N} ||y_j - T(x_j)||_2 \tag{2}$$

where $T(x_j)$ represents a rigid transformation of N points on the source surface to corresponding points on the target surface, y_j. Given that one-to-one point correspondence does not exist with surface-based registrations, correspondence is established by pairing points according to a closest distance metric. Following the determination of correspondence, a point-based registration can be executed and subsequently followed by an update to the

closest point operator. This sequence of steps proceeds iteratively until the disparity function shown in Equation (1) satisfies a specified tolerance. Although excellent at aligning geometrically unique surfaces, ICP in general may have difficulty with the intraoperative environment if relied upon solely. In our experience, not all regions of the brain surface express a unique geometry with respect to visible sulcal/fissure features of the intraoperatively exposed brain. Pathology, such as a tumor, can also influence the initial shape of the brain surface dramatically. In addition, the fidelity of image segmentation can also become a potential source of misalignment. There is some research that addresses these problems and relates to our work. Specifically the work of Feldmar et al. [189] and Johnson et al. [171] attempts to register using both geometry and intensity, by adding intensity differences to the disparity function in Equation 2. These methods, although effective, are not applicable to our situation due to the contrasting colormaps of the two point clouds. Thus we employ an optimization of normalized mutual information, as reported by Studholme et al. [174], between the two textured point clouds. Normalized mutual information is written here,

$$NMI(x, y) = \frac{H(x) + H(y)}{H(x, y)} \tag{3}$$

where, $H(x)$, and $H(x, y)$ are the marginal and joint entropies of the point clouds, respectively. Although extensively used within image-to-image alignment [169, 190, 191], there are no readily apparent means for calculating mutual information in this context. The difficulty arises in determining correspondence among point cloud intensity distributions. For this initial work, the closest point metric determined from the initial geometric registration is used to determine proper intensity correspondence among source and target surfaces. To further constrain the approach, a spherical geometry was fitted to the target surface and was used to reduce the registration degrees of freedom from six to three angular references in spherical coordinates about the fitted center and radius. The method of optimization employed for the mutual information-based registration was Powell's iterative method [175]. Results regarding the implementation of SurfaceMI on intra-modal and simulated inter-modal phantom data

are presented in [192].

In addition to this new registration approach, more traditional methods of cortical surface registration were performed for the purposes of comparison and feasibility. The second method used for registration was based on the approach by Nakajima et al. where cortical features such as vessel bifurcations were localized in both MR and scanner image space and a rigid point-based registration (PBR) was performed between the two. A third registration framework based on iterative closest point transforms (ICP) was used where the registration targets became vessel and sulcal contours visible on the MR and laser-scanned cortical surface. This suite of registration approaches provides multiple avenues to pursue for determining an optimal cortical surface alignment under varying surgical conditions.

Experimental Setup

A set of experiments using a watermelon phantom was utilized to test the algorithm's ability to register intermodality surfaces. In this experiment, Omnipaque (Amersham Health plc.) soaked twine was laid into the watermelon surface to simulate the appearance of contrast enhanced vasculature on the brain surface (Figure 16(a)) in CT.

In addition, CT/MR visible rigid markers (Acustar®, Z-Kat, inc.) were also implanted into the watermelon surface for use as an alternate digitization technology (Figure 16(b)). The phantom was imaged in the CT imager (Mx8000, Philips Medical Systems), scanned by the laser scanner and digitized by a Northern Digital Optotrak® 3020 (RMS accuracy of 0.1 mm, *www.ndigital.com*) (Figure 16(c)).

Several registrations were performed and fiducial registration and target localization errors were reported. The first registration aligned the image space coordinate system, *img*, to the Optotrak coordinate system, *opto*, using the Acustar markers in each modality, i.e. find $T_{img \rightarrow opto}$. Fiducial registration errors (FRE) and target registration errors (TRE), as defined by Mandava and Fitzpatrick [193][194], were calculated for this registration to provide the optimal registration for physical-space to image-space. Figure 17(a) shows the location of the 6 fiducial markers (letters) and 15 manually identified points (numbers). Having estab-

lished this registration optimum, corresponding sets of manually identified points at vessel bifurcations in *img* and *opto* were registered to provide quantitative validation of Nakajima's method of using cortical features for registering physical-space to image-space. Additionally, 10 visible bifurcation points in LRS space, lrs, corresponding to those in *img* and *opto* were localized (Figure 17(b)) and used for PBR registration as a verification of Nakajima's method applied to the LRS data. FRE was calculated and reported for all registrations (i.e. $T_{img \rightarrow opto}$, $T_{img \rightarrow lrs}$ and $T_{opto \rightarrow lrs}$). The manually identified points in each space were localized three (3) times and averaged to minimize localization error.

The other candidates for intraoperative registration were also examined within the context of phantom experiments. ICP registrations were performed using phantom vessel contours extracted (using simple thresholding) from the LRS and CT data. In addition, the segmented surface was aligned using the SurfaceMI framework. For each registration, a reduced region of the watermelon LRS surface was extracted to simulate the approximate size of the surgical field-of-view (FOV). For both registration methods (ICP and Surface MI), initial alignment of the surfaces was provided by using 3 manually localized targets visible in the segmented surface. TRE was calculated in both registration frameworks using 7 novel surface targets (i.e. those landmarks that were not in the surgical FOV) and was compared to the TRE provided by the PBR alignment of vessel landmarks.

Robustness studies for the registration frameworks were carried out by perturbing initial landmarks uniformly along the surface of a sphere fitted to the target point cloud, i.e. perturbing the landmarks in spherical coordinates: ϕ, θ, and ψ at the fitted radius r. The perturbations were independently and uniformly sampled from -2.5 to 2.5 degrees (simulates approximately $1cm$ fiducial localization error, i.e. perturbation arc length: $r\Theta = 9.29mm$) in each spherical axis for each trial, and each framework was subject to 500 perturbation trials. The results of this experiment provide insight as to the efficacy of the registration frameworks given sub-optimal initial conditions.

Accuracy of the registration frameworks with regard to deep tissue targets was also investigated. For this experiment deep tissue targets were sampled within a 5 centimeter radius of

the centroid of the manually localized surface points. The sampling was constrained to only deep tissue targets, i.e. sample points which lie within both the sphere and melon (Figure 18). "True" positions of the deep tissue targets were found in LRS space by transforming targets from image space using the rigid-body transformation $T_{img \rightarrow lrs}$ (based on identifying vessel points in both modalities). These same tissue targets within image space were also registered to LRS using transformations based on SurfaceMI which when compared served as an estimate of TRE.

Clinical Setup

In addition to phantom experiments, a preliminary clinical example has been achieved. The patient was a 37-year old man with a six-week history of focal motor seizures. Magnetic resonance (MR) imaging revealed a hypointense, non-enhancing mass in the posterior, superior left frontal lobe, abutting the motor strip. He underwent awake resection, with motor and speech mapping. Intra-operatively, he was placed in the supine position, with the vertex of the head elevated 15 degrees and the head turned 30 degrees to the right. A fronto-temporal-parietal craniotomy was performed and the tumor was localized using ultrasound and frameless stereotaxy. The vein of Trolard coursed superiorly to the superior sagittal sinus, immediately behind the posterior extent of the tumor and directly in front of the motor gyrus. After mapping of the speech and motor regions of the face and arm, gross total resection of the tumor was accomplished. The patient tolerated the procedure without neurological sequelae. Intraoperatively, following durotomy, the scanner was moved into position via the customized monopod (Figure 14(b)) above the craniotomy site at approximately 30-45 centimeters from the brain's surface. The scanner was activated and acquired approximately 20,000 points in 5-7 seconds. Following retrieval of the scanner data, registration between the patient's intraoperative data and the MR tomogram were performed retrospectively. Figure 19 shows the surgical FOV as well as the textured range scan of the FOV acquired during surgery.

Results

The registration results achieved with implantable markers were comparable to previously published data [36]. Using the Acustar marker system, a mean FRE of $0.3 \pm 0.1mm$ was attained using six markers. The mean TRE for this registration was $1.7 \pm 0.3mm$ using fifteen target landmarks. These results demonstrate the accuracy associated with implantable fiducial markers and provides a baseline for comparison with subsequent registrations.

The registration results for studies concerned with the alignment of the cortical surface using vessel-based landmarks show excellent correlation with the previously published studies of Nakajima et al. [166]. FRE using 10 manually localized landmarks in all three spaces (i.e. *opto*, *img*, lrs) were $1.3 \pm 0.5mm$ and $1.7 \pm 0.6mm$ for $T_{img \rightarrow opto}$ and $T_{img \rightarrow lrs}$, respectively. In addition, a second PBR was calculated using a subset of the vessel markers within a focal cortical region (to simulate vessel fiducials within a craniotomy). The remaining vessel bifurcations were used as targets and the TRE is reported in Table 1.

As an aside, a measure of localization precision was calculated since each set of landmarks (i.e. in *img*, *opto*, and lrs) was identified three times. Precision was measured as the mean standard deviation for each measurement (x,y,z) in corresponding landmarks across the three trials. For the landmarks selected in *img* the mean standard deviations in x, y, and z were 0.27, 0.28, and 0.31 millimeters, respectively. In *opto* the mean standard deviation in x, y, and z are 0.35, 0.22, 0.13 millimeters, respectively. For the 10 landmarks chosen in lrs the mean standard deviations in x, y, and z were 0.71, 0.58, and 1.14 millimeters.

In addition to FRE studies, the histogram and mean TRE for simulated deep tissue targets is provided in Figure 20 with a spatial distribution of TRE overlaying the melon image volume shown in Figure 21. The results suggest that SurfaceMI may predict deep tissue targets more accurately then the PBR and ICP registration methods. Also, the three dimensional distribution of TRE demonstrates that SurfaceMI predicts deeper targets more accurately than either PBR or ICP for this registration case.

In addition to reporting registration results based on a routine application of each align-

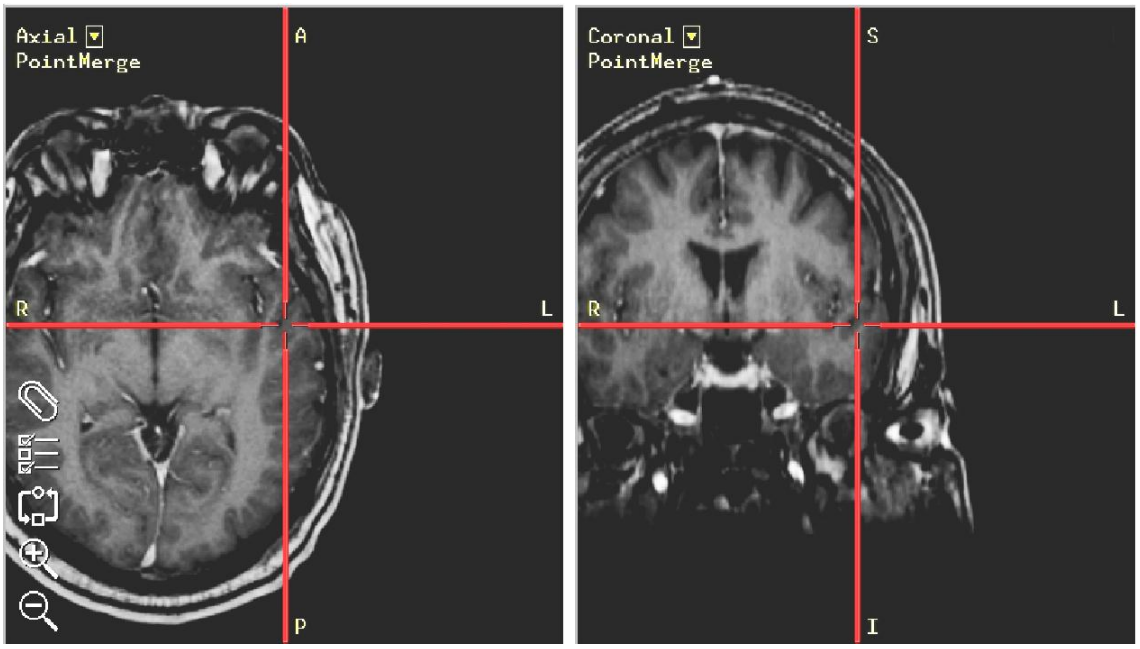

Figure 13: An example of brain shift seen using an intraoperative image guided surgery system. The crosshairs indicate the location of the surgical probe in image space, in this case inside the brain. In reality, the probe is touching the surface of the brain near the superior temporal gyrus.

Table 1: TRE for the three registration protocols in melon experiment: PBR, ICP, and SurfaceMI, on an LRS surface that approximates a surgical FOV. Three landmarks were used as fiducials and 7 targets were used to calculate TRE.

Registration Method	Mean TRE (mm)
PBR	2.6 ± 0.7
ICP	2.4 ± 0.8
SurfaceMI	2.5 ± 0.7

14(a) Close up of the scanner showing the laser emit window in the middle and the CCD and laser receive cameras on the right.

14(b) LRS in the operating room covered with sterile isolation bag and mounted on custom built vibration damping monopod.

14(c) LRS in the OR, covered in sterile bag, and mounted to overhead swing arm.

Figure 14: The 3D Digital RealScan USB and its use in the operating room.

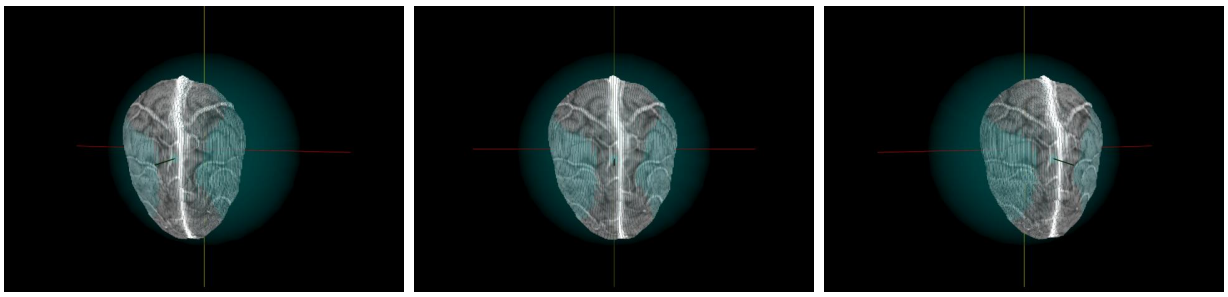

Figure 15: Three views of the surface extracted from a patient-specific gadolinium enhanced MR volume.

16(a) Watermelon with Omnipaque soaked twine laid into carved vessel grooves.

16(b) Acustar® imaging marker filled with CT/MR contrast enhancement fluid.

16(c) Acustar® divot caps for localization using Optotrak®.

Figure 16: The watermelon phantom used in this paper for registration accuracy experiments.

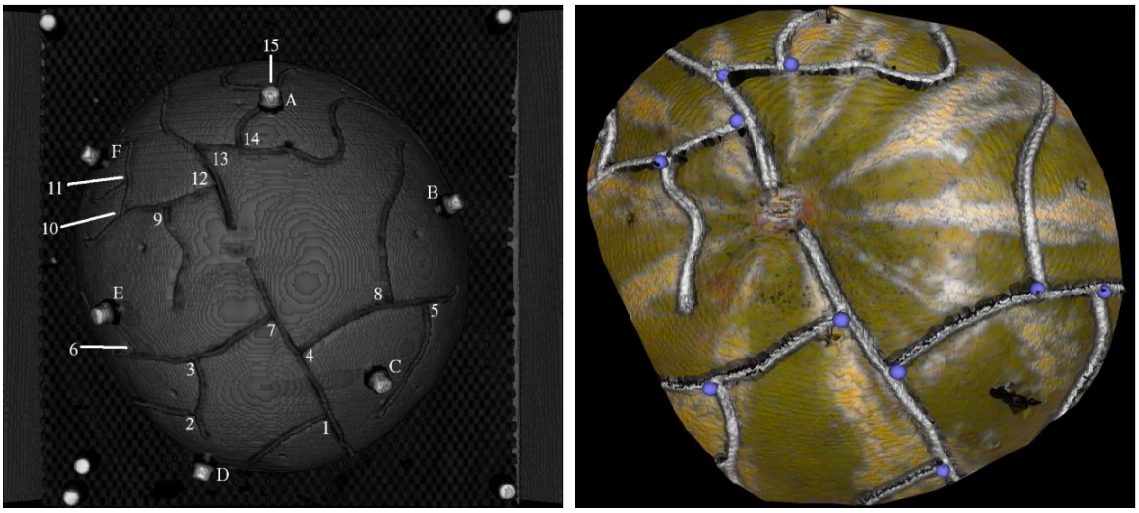

17(a) Volume rendering of image data showing markers (letters) and manually localized landmarks (numbers) in *opto* and *img*.

17(b) Landmarks localized in lrs space.

Figure 17: Localized points in *img*, *opto*, and lrs.

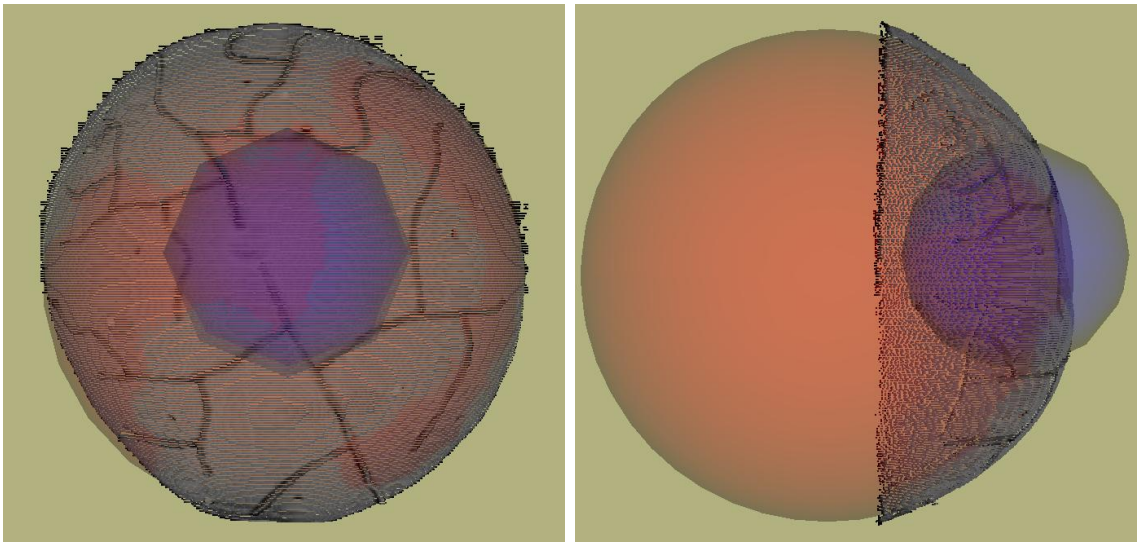

Figure 18: Simulated deep tissue sampling. The larger sphere demonstrates the geometric sphere fit of the point cloud. The smaller sphere represents a sampling region with radius of 50 millimeters, centered about the centroid of the localized fiducials. The volume of overlap demonstrates the deep tissue sampling region.

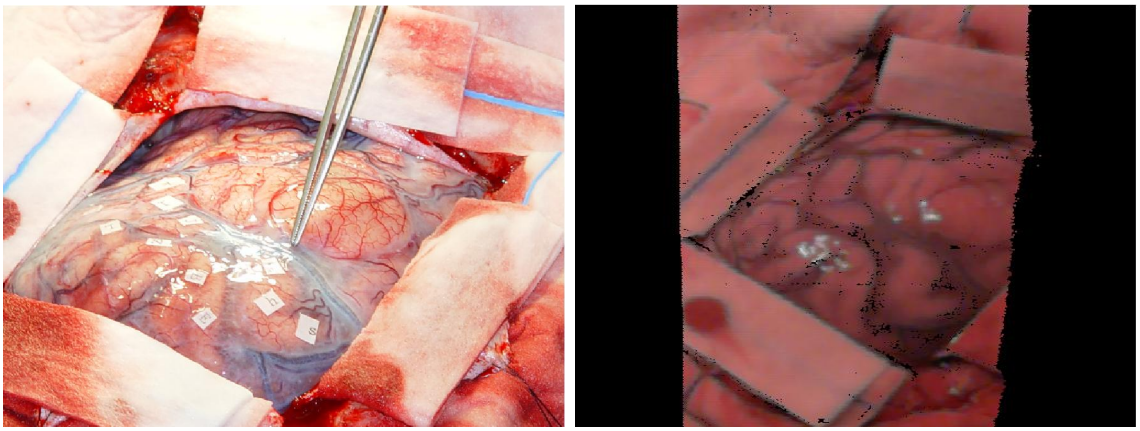

Figure 19: Intra-operative field-of-view. On the left is a digital photograph with the surgeon highlighting the Vein of Trolard, a significant vessel in the area of therapy. On the right is a textured point cloud generated intra-operatively using our LRS.

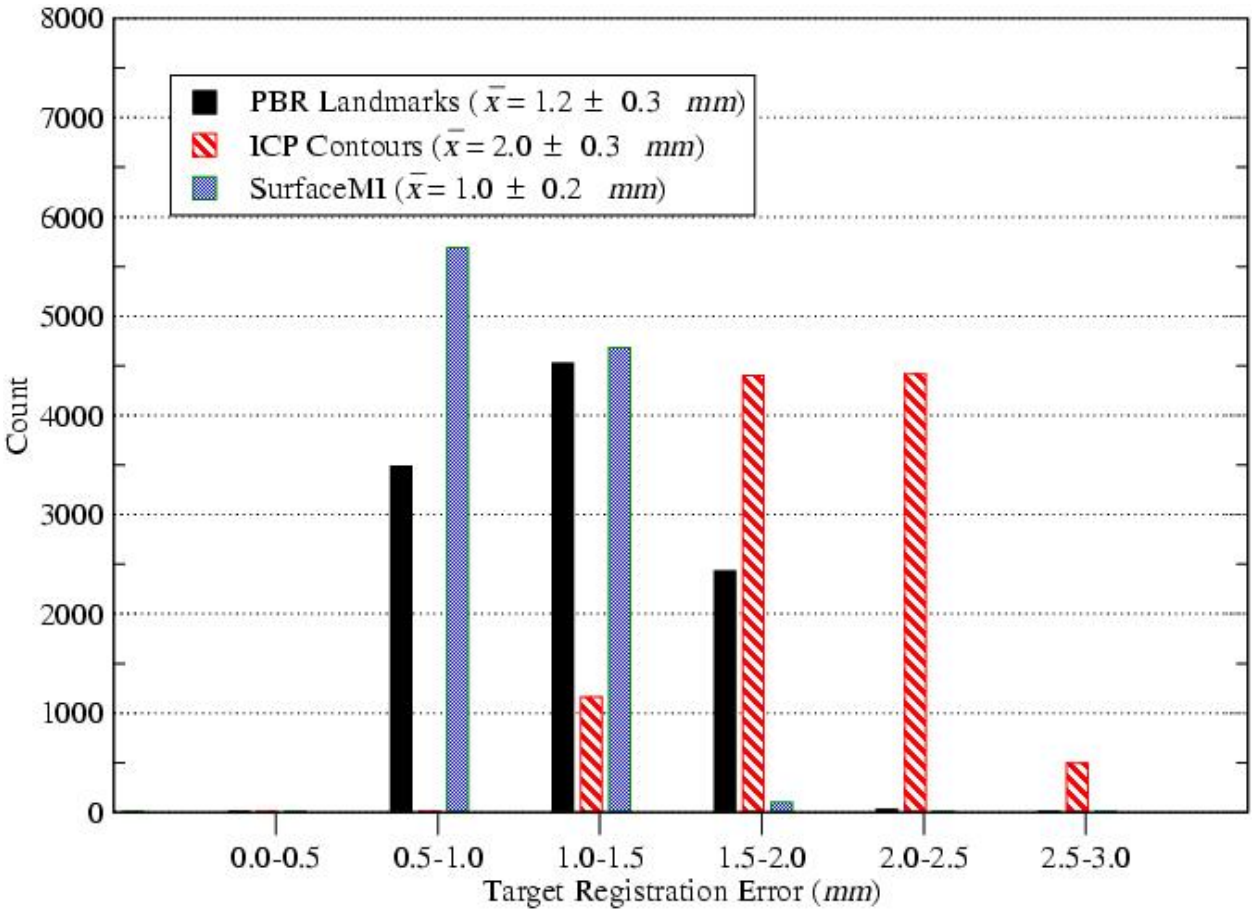

Figure 20: TRE histogram for deep tissue targets using PBR based registration on surface landmarks, ICP based registration on surface contours, and SurfaceMI on textured surfaces.

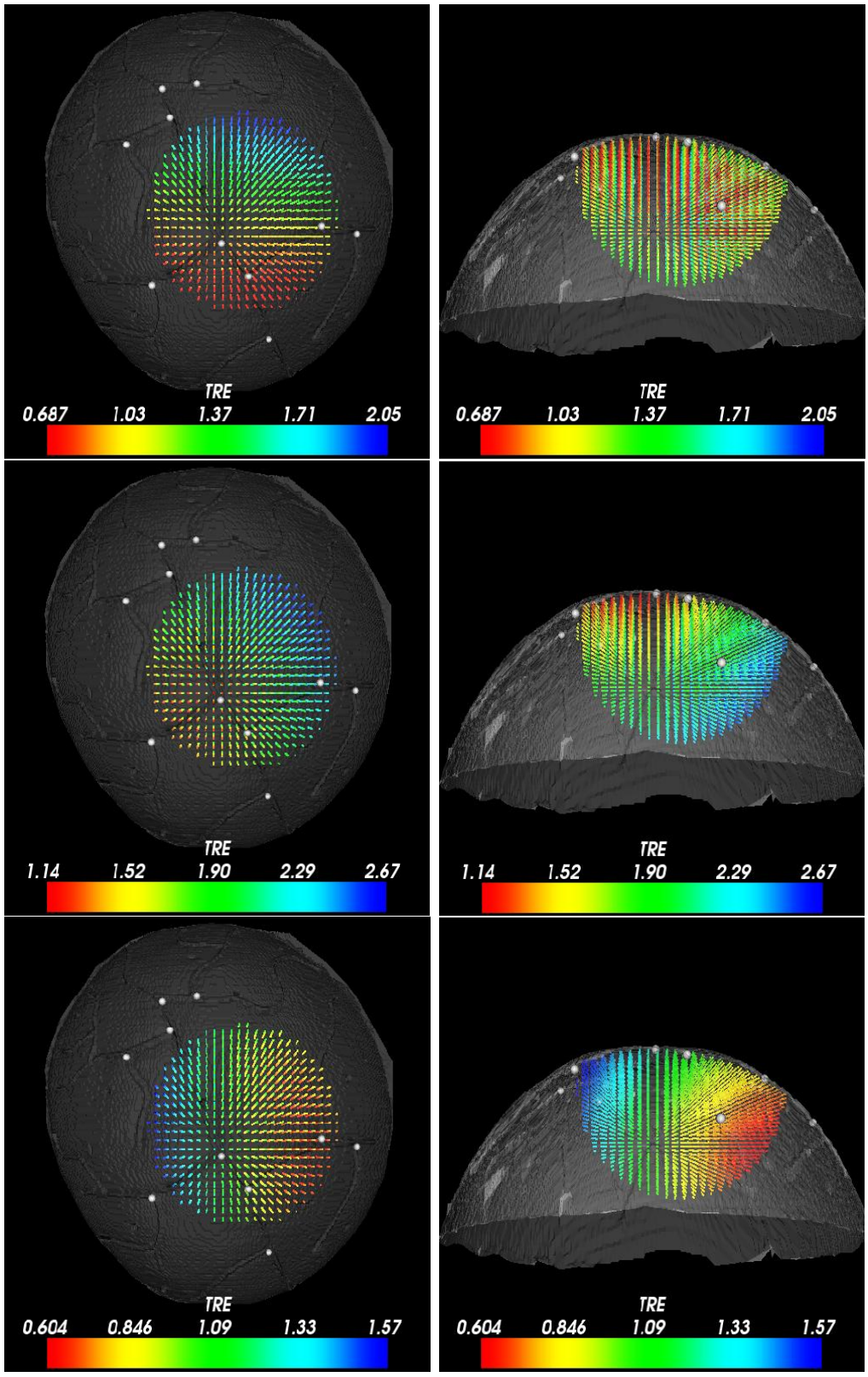

Figure 21: Three dimensional distribution of TRE for deep tissue targets. The left column shows a top-down view of the watermelon surface with a the TRE distribution shown for PBR (top), ICP (middle) and SurfaceMI(bottom). The right column shows the respective front view of the TRE distribution. Each deep tissue sample point is visualized with a scalar encoding of its corresponding TRE. The range of scalar values is shown in the colorbar associated with each figure.

ment framework, a series of robustness studies was performed to investigate the effects of varied initial guesses (i.e. approximate 1-6mm fiducial localization error with individual fiducial error as large as 9.3mm). Examples of the registration provided by ICP and SurfaceMI with a given initial landmark perturbation are show in Figure 22. FRE results from these perturbation studies for PBR, ICP, and SurfaceMI on the same cortical subregion used for the TRE studies of Table 1 are given in Figure 23 over 500 trials. The distribution of fiducial registration error ranged from 1.0 to 5.8 millimeters for the three landmarks used in initialization of the ICP and SurfaceMI registrations. ICP on the surface contours performed well and reduced FRE by approximately 43%. SurfaceMI also performed well, but produced some outliers. Using the Extreme Studentized Deviate (ESD)[195], 8 outliers were detected with >99.95% confidence. Removing these outliers from the SurfaceMI trials produced a mean FRE of $2.2 \pm 0.8mm$, reducing FRE by approximately 27%.

Central to using the LRS within the clinic is to demonstrate *in vivo* registration results. A clinical example is shown in Figure 24 with corresponding measures of registration error reported in Table 2. The first column in Table 2 represents the mean registration error associated with the cortical surface points used in PBR. The second column in Table 2 represents the mean closest point residual between contours. Although PBR performs better with respect to fiducial error, the results in Figure 24 suggest that the registration error reported for the contour points may be the better metric as to the quality of alignment.

Discussion

Several methods to register images to the exposed intraoperative cortical surface have been utilized within the context of phantom and clinical experiments. The methods include traditional approaches (point-based registration (PBR) and iterative closest point (ICP)) and highlight the development of a novel technique that takes advantage of unique data provided by a laser-range scanner (LRS). More specifically, the LRS captures the geometric complexity of the brain surface and maps the feature-rich texture as acquired by a color CCD to this geometric data. The new approach presented (called SurfaceMI) uses both forms of

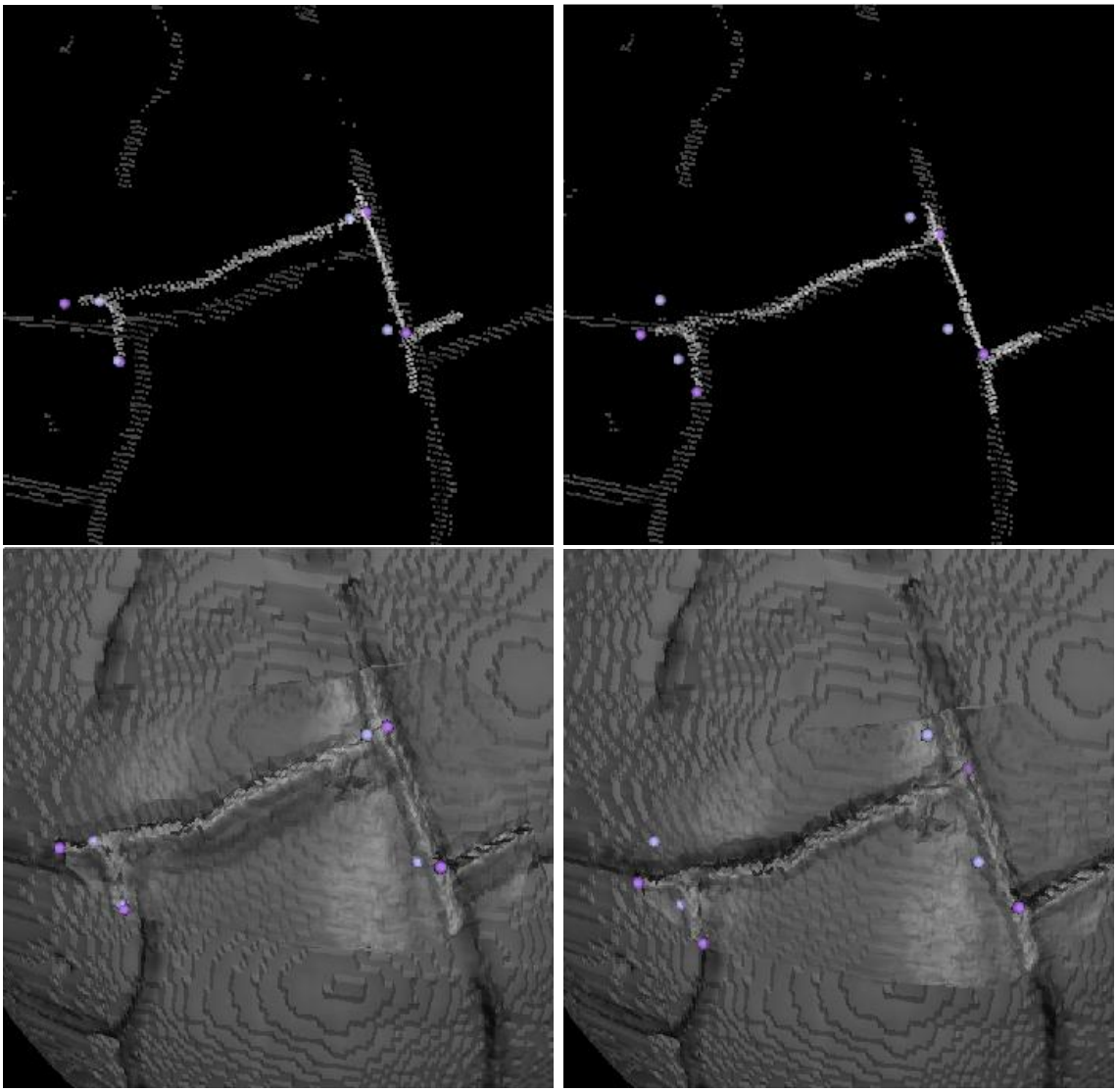

Figure 22: Results of ICP and SurfaceMI on inter-modality registration of two textured surfaces. ICP registration conditions are shown in the top row with perturbed initial condition shown left and ICP registered shown right. SurfaceMI registration conditions are shown in the bottom row with perturbed initial condition shown left and SurfaceMI registered shown right. It should be noted that there is a texture projected on the surface of the watermelon that is an artifact of the rendering process, i.e. this texture did not affect the registration process. A gross-scale representation of the texture, which is a result of the slice to slice spacing in the CT image, can be seen in Figure 17(a) for comparison.

Table 2: Registration errors for *in vivo* alignment using PBR, ICP and SurfaceMI frameworks.

Registration Type	Mean Error Measure (mm) Fiducial Points ($n = 3$)	Mean Error Measure (mm) Contour Points ($n = 468$)
PBR	2.4 ± 1.0	1.9 ± 1.0
ICP	3.4 ± 1.4	0.9 ± 0.6
SurfaceMI	3.5 ± 1.7	1.3 ± 0.5

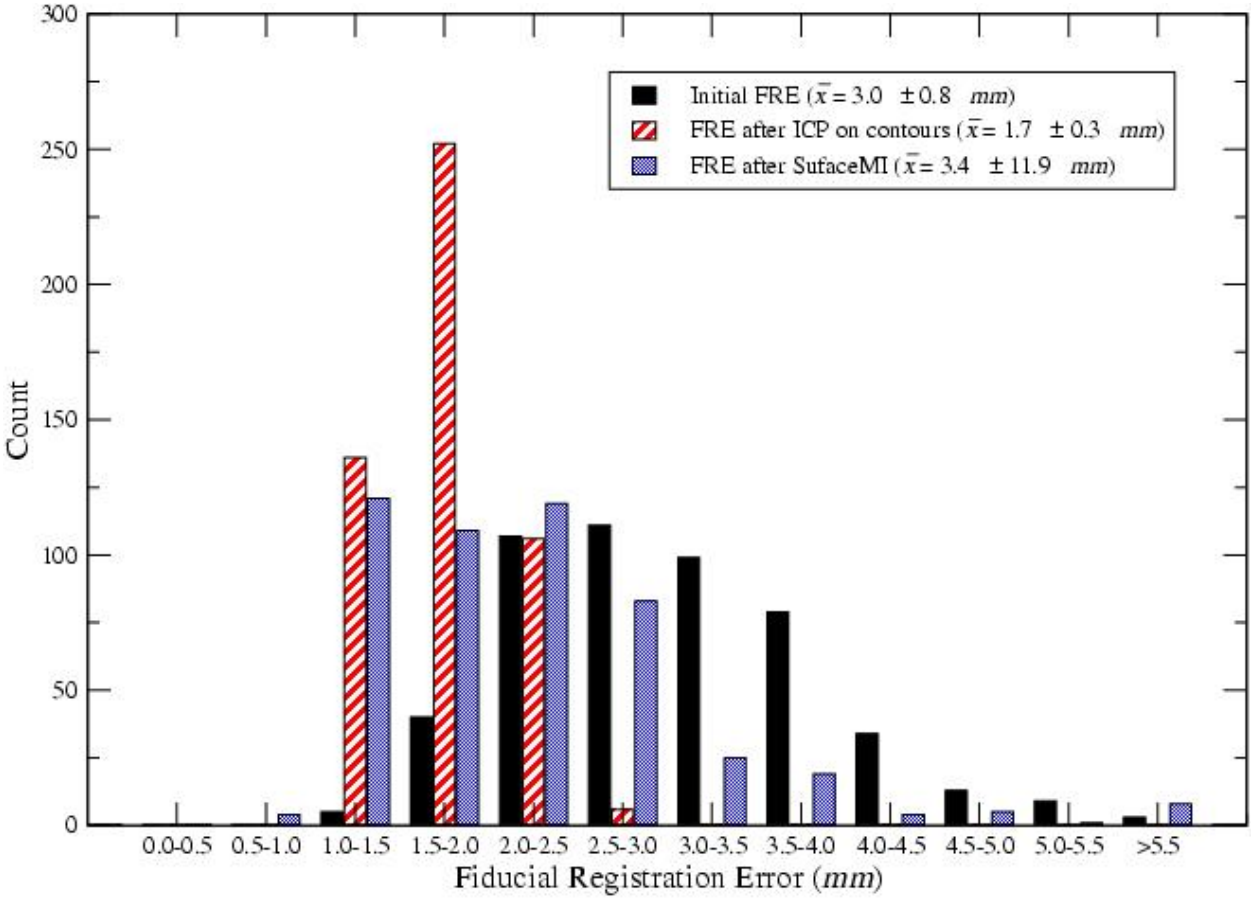

Figure 23: Fiducial registration error distribution given initial landmark perturbation. The landmarks in the field-of-view were perturbed up to ±2.5 degrees in each spherical coordinate (ϕ, ψ, θ) in img.

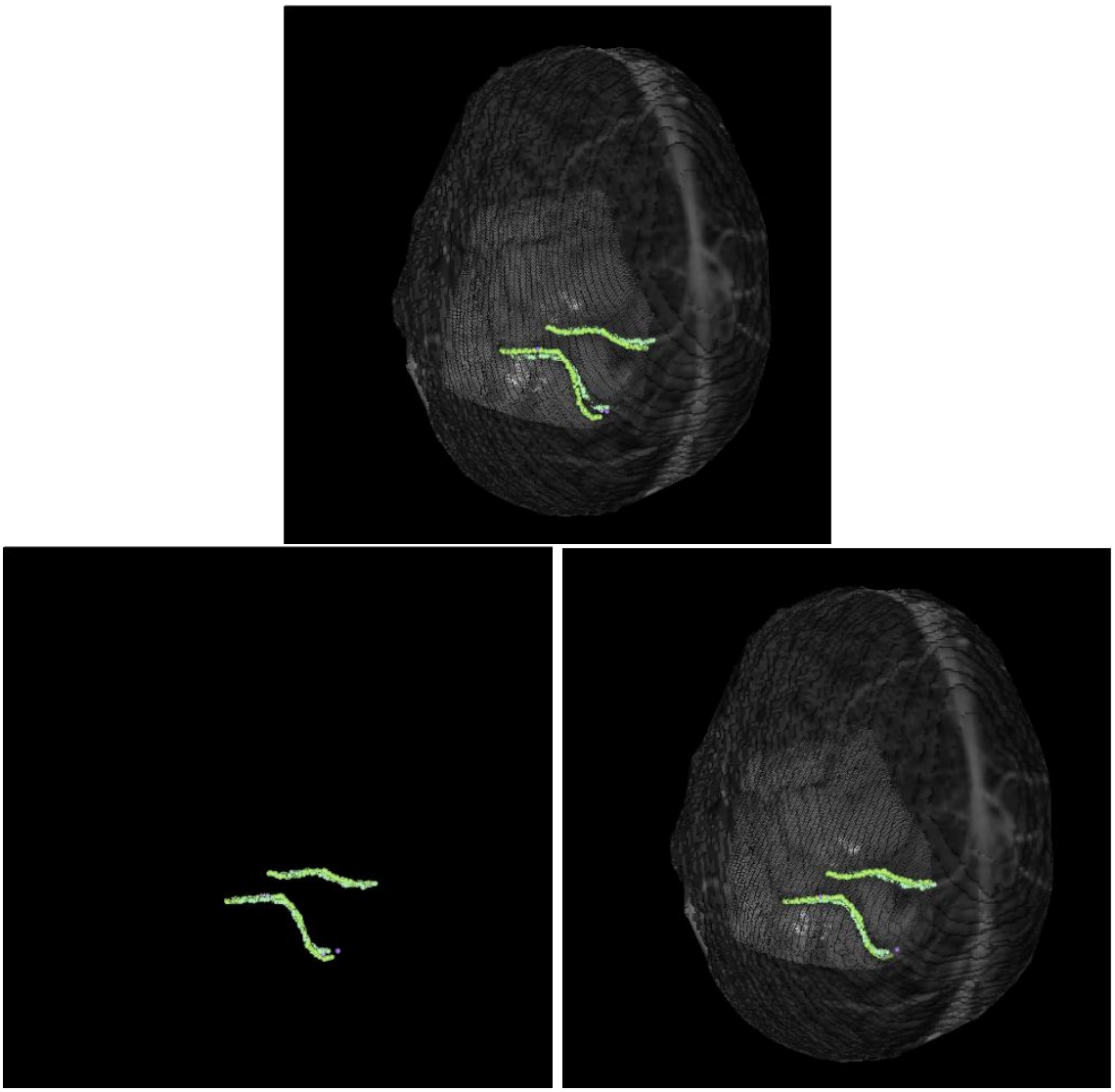

Figure 24: Registration results from intra-operative data. On top, the result of PBR based registration using manually localized landmarks in img and lrs. In the bottom row from left to right, ICP registration using highlighted contours in img and lrs, and SurfaceMI registration given the initial alignment provided by the PBR method. The highlighted contours are a prominent sulcal and vessel patterns visible in both spaces.

data to align the LRS-acquired surface to its image counterpart.

Initial studies using rigid markers were performed to provide a baseline registration accuracy with respect to unknown errors associated with the phantom and/or imaging method; results reflected comparable accuracies reported in the literature [36]. The next set of studies used vessel bifurcations localized in all modalities as the basis for registration. Reassuringly, the FRE between *img* and *opto* using the manually localized vessel bifurcations were comparable to values reported by Nakajima et al.. Similar values were also determined when registering vessel bifurcations using LRS data within the context of PBR, ICP and SurfaceMI. This would indicate that using techniques similar to Nakajima et al. should be achievable using LRS data. In addition to reporting error within the simulated craniotomy region, targets outside the focal region were also used to assess alignment quality. Overall, the difference between results among all three methods was negligible. The increased magnitude of TRE over FRE agrees with an accepted understanding regarding the effects of fiducial placement on target registration error; that is, even with a low FRE, a sparse number of fiducials localized within a concentrated area can precipitate a "lever-arm" effect in areas remote to the registration region. Interestingly, a different result is seen with respect to targets in close proximity to the subregion of interest on the melon surface. Figure 20 reports the distribution of TRE data compared among all three registration approaches. With respect to the mean TRE error for the entire region, SurfaceMI performed the best with an average TRE of $1.0mm$. When comparing deep tissue results between the PBR and SurfaceMI methods (see Figure 21), PBR has a greater range of TRE error than SurfaceMI which may be due to the difficulty in localizing bifurcations upon the LRS data for PBR methods. The ICP registration performed considerably worse and may be due to the contour thresholding process. More specifically, any spatial noise contained within the thresholded vessel structure is not averaged out as well within the ICP framework when compared to using a more dense point cloud. This possible source of error would not be present within the SurfaceMI approach since the dense geometric data are maintained and the fine adjustments to alignment are provided by an intensity-based registration. SurfaceMI and PBR

produced comparable results although the TRE spatial distribution for deep tissue targets was greater for the PBR method. This may suggest that the effects of a combined surface and intensity approach produce a lower error due to the averaging effects associated with the registration metrics used in SurfaceMI. When comparing SurfaceMI to ICP, the results suggest that vessel-contours alone may not be the best approach to cortical surface registration; but rather, the addition of the intensity data provides significant refinement to the alignment.

The results from the perturbation studies highlight that ICP is more robust with respect to poor initial alignment guesses (i.e. fiducial localization errors up to $9.3mm$). Figure 23 demonstrates that ICP maintains a better FRE on average with tighter standard deviation. SurfaceMI was not as robust and produced 8 outliers over 500 trials. In results not presented here, the function space has been characterized and has been shown to be populated with local extrema. More specifically the areas of local extrema are found near the global extrema and result in frustrating numerical optimization methods. It should be noted however that these outliers represent a less than 2% failure rate. Furthermore, if the outliers are eliminated from the trial set, the FRE is sharply reduced from mean error of $3.4mm$ to $2.2mm$. It is clear that investigation into a more sophisticated optimization strategy is needed and/or extending the registration to a multi-resolution approach might be helpful[196][197][198].

The results from the clinical experiment demonstrate the feasibility of cortical surface registration within the OR environment as well as provide a limited quantitative assessment to the approach's accuracy. Table 2 demonstrates that a PBR approach similar to Nakajima et al. (except using LRS data in lieu of optical digitization) produces a mean registration error for vessel fiducials that is $1mm$ less on average than that provided by ICP or SurfaceMI. However, in the region of the contours, the method did not fare as well. Figure 24 demonstrates a qualitatively better alignment in the area of the contours when using either ICP or SurfaceMI. Table 2 also quantifies this improved closest point residual for ICP and SurfaceMI over the PBR method. One likely reason for this discrepancy is that brain deformation may have occurred upon opening the cranium and may be distributed non-uniformly

over the brain surface. This would be consistent with the results in Table 2 since the PBR method relies on the selection of the vessel fiducials as the basis for registration while ICP and SurfaceMI only use these for initialization. Hence, if the brain surface is non-uniformly deformed, it would logically follow that methods which base their registration on the vessel fiducials (PBR) would be better within the fiducial region while methods that use contour information (SurfaceMI and ICP) would be better within the contour region.

The clinical results also demonstrate that the registration protocol used within this work may be a viable approach for surgeries where minimal brain shift is encountered. In addition, the visual results shown in Figure 24 may provide new anatomical cues to surgeons by correlating the FOV observed in the OR to the MR tomogram volume studied prior to surgery for preoperative planning. Furthermore, although not developed within this work, deformable registration coupled with serial range scans may allow for the detailed tracking of brain shift during surgery. We are currently exploring methods to allow deformable registration of inter-modal textured surfaces for the measurement and characterization of brain shift.

Another important aspect to the SurfaceMI results presented within this work is its ability to perform multi-modal registration. Within the phantom and clinical experiments, SurfaceMI represents a multi-modal registration between CT data and CCD color texture, and MR data and CCD color texture, respectively. This result is quite remarkable and adds impetus for the use of laser-range scanning within the neurosurgical OR environment.

Conclusion

In this paper, a unique intraoperative approach to registering patient images to the patient's cortical surface during brain surgery has been presented. The multi-registration platform under development is capable of aligning the brain surface to its intraoperative counterpart using traditional as well as novel alignment methods within the context of laser-range scanner data. To our knowledge, this paper represents the first quantitative evaluation of laser-range scanning used within the context of intraoperative cortical surface registra-

tion. Phantom experiments are presented that compare traditional point-based (Procrustes alignment) and surface-based (ICP) registration methods to a novel registration approach which uses a combined geometric and intensity-based metric (SurfaceMI). The registration approach is a 3D surface alignment technique that begins with an ICP-based initialization followed by a constrained Mutual Information-based refinement. The algorithm has demonstrated better accuracy with respect to deep tissue targets within the simulated craniotomy region. However, some limitations did appear within the robustness studies whereby a 2% failure rate occurred during phantom registration experiments. In results not presented here, the objective function space with the melon has been characterized and indicates that the multi-extrema exist and can confound the current method of optimization. Alternative optimization and multi-resolution methods need to be investigated further to decrease this failure rate. The SurfaceMI algorithm was capable of multi-modal registration in both phantom and clinical data. The data presented from the clinical case demonstrates the approach's feasibility within the OR as well as semi-quantitative estimates of registration accuracy.

The methods discussed in this paper in conjunction with the quantitative results provide substantial motivation for using LRS technology within the neurosurgical operating theater. More specifically, LRS methods provide rapid detailed characterization of the cortical surface during surgery and can be used as a tool for registration and the eventual measurement of deformation. This versatility will make LRS technology essential in pursuing model-updating strategies [115] for the compensation of brain shift during image-guided neurosurgery.

Acknowledgements

This work was supported in part by the **Vanderbilt University Discovery Grant Program**. Image segmentation techniques from Analyze AVW were used in this paper (Mayo Clinic, Rochester, MN). The Visualization Toolkit (Kitware Inc.) was used for all post-segmentation data processing and visualization. David Mount for The Approximate Nearest Neighbor library used for optimized kd-tree searches in this paper[1]. The Depart-

[1](www.cs.umd.edu/~mount/ANN)

ment of Neurosurgery at Vanderbilt University Medical Center for help in data collection, particularly Dr. Matthew Pearson for his assistance during surgery. Nita Collins for her help in acquiring the CT data used in this paper.

CHAPTER V

MANUSCRIPT 3 - NEUROSURGICAL PROCEDURES USING LASER-RANGE SCANNING FOR CORTICAL SURFACE CHARACTERIZATION

Abstract

OBJECTIVE: To demonstrate a novel intraoperative acquisition system based on a laser range scanner (LRS) that can generate textured (intensity-encoded) surface descriptions of the feature-rich intraoperative cortical surface.

METHODS: A LRS was used to acquire cortical surface descriptions of 8 patients undergoing neurosurgery for a variety of clinical presentations. Textured surface descriptions were generated from these intraoperative acquisitions for each patient. Corresponding textured surfaces were also generated from each patient's preoperative MR tomograms. Each textured surface pair (LRS and MR) was registered using cortical surface information only. Novel visualization of the combined surfaces allowed for a anatomical based assessment of alignment.

RESULTS: Successful textured LRS surface acquisition and generation was performed on all 8 patients. The data acquired by the LRS accurately presented the intraoperative surface of the cortex and the associated features within the surgical field-of-view. Registration results are presented as overlays of the intraoperative data with respect to the preoperative data. The overlays demonstrated that accurate registration can be provided between the preoperative and intraoperative data and emphasized a potential enhancement to cortical feature registration within the OR environment.

CONCLUSIONS: This paper demonstrates clinical deployment of a LRS capable of generating textured surfaces of the surgical field-of-view. Data from the LRS was registered accurately to the corresponding preoperative data. Visual inspection of the registration results was provided by overlays which put the intraoperative data within the perspective of the whole brain's surface. These visuals can be used as a navigational aid during surgery.

The results also hold implications for the use of LRS device as a method to monitor and report brain shift over the course of a neurosurgical procedure.

Introduction

Current image-guided neurosurgical procedures rely on the accurate alignment of the patient's anatomy in the operating room and their preoperative imaging data [36]. An implicit assumption in its application is that the brain is rigid[1] before and during surgery. However, many recent studies measuring the amount of brain motion during surgery (both surface and subsurface) have suggested this is inaccurate in many cases [38, 41, 44, 43]. These reports show that the brain is capable of deforming between millimeters and centimeters in a non-rigid manner depending on the type of surgery, distance from the craniotomy, the orientation of the patient, and the presence of pharmacological agents. Any such deformation of the brain during surgery compromises the accuracy associated with classic image-guided surgery (IGS) assumptions, and potentially hampers the ability to deliver therapy.

In light of these results there has been an effort to provide more accurate image-guidance for neurosurgery. One strategy to address this problem is to integrate traditionally pre-operative tomographic imaging modalities into the operating room. Starting in the late 1970's, efforts have been made to use computerized tomography within a surgical setting [48, 53, 57, 58, 59]. However, concerns over repeated exposure to ionizing radiation during surgery has limited the use of intraoperative CT (iCT). More recently, some institutions have deployed magnetic resonance imaging units into operating rooms (intraoperative MR, iMR) with some success [199, 180, 45, 46]. These systems have been applied as a method to increase the accuracy of image-guidance during neurosurgery[46, 81]. However, iMR systems are expensive, require MR-specific equipment, instrumentation, and operating rooms, factors which may prohibit their widespread adoption at most hospitals. Alternate intraoperative imaging modalities, such as intraoperative ultrasound (iUS) are also under investigation

[1]Rigidity, in this case, is defined mathematically such that relative distances and angles between corresponding points in the brain do not change spatially or temporally across different coordinate frames (modalities).

[40, 114, 109]. iUS is an attractive solution to intraoperative imaging due to its high clinical availability, low relative cost when compared to iMR, and ability to construct local 3D volumes rapidly. However, the lower image-quality in ultrasound and reduced clarity over the course of surgery are important considerations when adopting iUS as a solution for improving IGS accuracy. In general, one must consider the trade-off between cost and image-quality when evaluating intraoperative imaging modalities.

With these considerations in mind, another, more cost-effective strategy to provide accurate IGS is to use preoperative images within a computational framework that updates the images with intra-surgical events. Roberts et al. initially proposed this technique as an alternative to intraoperative imaging [115]. Since then, several researchers have proposed elegant mathematical models that predict brain deformation under realistic surgical loading conditions [119, 125, 131, 132]. Studies have shown that these models are capable of reconstituting up to 70-80% of the total imposed deformation in animal studies [125, 127]. The reports suggest that a model-updating approach to brain shift compensation is practical and relatively accurate. Furthermore, the inherent ability to update and register all preoperative image sets simultaneously to the intraoperative environment makes this method of image-updating even more attractive.

Central to using these models within an IGS framework is the acquisition of sparse intraoperative data[2]. Various devices have been listed in the model-driven shift-compensation literature as sparse-data acquisition systems, including tracked pen-probes, co-registered ultrasound, and stereo-pair camera systems [200, 114, 136, 130]. In this paper, a novel intraoperative acquisition system is introduced and demonstrated for intraoperative sparse-data acquisition.

The data acquisition system used in this paper is a laser-range scanner (LRS) capable of recording point clouds of the intraoperative scene that are textured by a digital image of the surgical field-of-view (FOV). The LRS, shown in Figure 25, provides a simple, non-contact, and cost-effective method to acquire intraoperative surface data rapidly. The calibration and

[2]Sparse intraoperative data is defined as data with limited extent or information.

Figure 25: RealScanUSB 200 LRS device used to acquire textured point clouds of the intra-operative brain surface mounted on a vibration damped monopod.

accuracy statistics of the LRS used in this paper have been described by Cash et al[172, 201]. Briefly, the resolution of the range-data produced by the scanner is on the order of 0.5 millimeters, with a reported depth accuracy of 30 microns at 300 centimeters. Furthermore, at 15 seconds per scan, the scanner is capable of producing datasets with 50,00-100,000 range points per scan. The LRS is an extremely efficient method of capturing cortical surface data when compared to existing methods, such as tracked pen-probes. Given these features, three-dimensional intraoperative range-data acquisition via LRS was originally proposed by Audette et al. in 1999 [164, 165]. However, clinical fidelity was not reported in that study. Since then Raabe et al. have demonstrated the use of a LRS to produce anatomic fiducials for intraoperative point-based registration of physical-space to image-space [163].

In this paper, we utilized range data in a similar manner to these papers but we have established a novel, more robust approach that uses range and texture information to register the cortical surface during neurosurgical procedures. Previously, Nakajima et al. demonstrated registration of intraoperative features to preoperative images using vessel bifurcations as landmarks [166]. In this work, we employed Nakajima's method of registration to align intraoperative LRS datasets to their preoperative patient-specific counterparts. In addition, due to the content of the LRS datasets (i.e. surface geometry and intensity patterns), other registration techniques were also explored. The results of these registrations provided the ability to generate enhanced views of the craniotomy with respect to preoperative images. Given the fact that the craniotomy is generally draped heavily for surgery, the visualizations provide new visual cues and context for intraoperative guidance.

Methods

The methods describe in detail how the two major objectives of this paper were accomplished: 1) to intraoperatively scan cortical surfaces of patients undergoing intra-cranial resection therapy using a LRS, and 2) to rigidly register the intraoperative scene provided by the LRS to the preoperative images and generate guidance visualizations.

8 patients (6 male; mean age 48.4±15.6) with primary or metastatic tumors were included

in this study (see Table 3). All patients were enrolled after obtaining written, informed consent for participation in this study, which was approved by the Institutional Review Board, Vanderbilt University School of Medicine.

All patients were imaged using a 1.5T MRI the day prior to surgery (GE Systems, Milwaukee, WI) with integration of $1.5mm$ thin axial, gadolinium-enhanced T1-weighted images into a Stealth Station (Medtronic, Minneapolis, MN). After anesthetic induction, patients were positioned on the operating room table, secured to the table using the Mayfield three-pin head holder (Ohio Medical, Cincinatti, OH) and the frameless stereotactic system was calibrated and confirmed. All patients received diuretics (Mannitol 0.5-1.0 $\frac{gm}{kg}$) and steroids (Dexanetharre) immediately prior to incision; no patient required additional diuretics. Surgery was then performed, and LRS surfaces were obtained after durotomoy but before tumor resection. Defined cortical landmarks, such as the veins of Trolard or the Sylvian fissure were identified for each case by visual inspection and recorded via digital camera.

Intraoperative range data acquisition

During surgery, the laser range scanner was brought into the surgical field-of-view (FOV), at the surgeon's discretion, to acquire range data of the cortical surface. The scanner was mounted on a monopod stand retro-fitted with a vibration damping base. In its most compact form, the monopod mount stands four feet in height, but may be extended to over 6 feet. The monopod mount provides the standard degrees of freedom (yaw, pitch, and roll) for accurate alignment of the surgical FOV and the LRS. During acquisition the monopod mount was placed near the surgical FOV. The stand was extended and yaw, pitch, and roll were adjusted to bring the scanner's acquisition camera to within 25-35 centimeters of the exposed cortical surface in a normal direction. The scanning extents (left and right scanning margins) were adjusted to encompass the craniotomy. At this point, minor calibration may have been required for the lighting conditions in the OR[3]. After set-up and calibration, a

[3]In general, ambient lighting provided ideal conditions for LRS acquisition. However, if the ambient conditions did not provide adequate lighting, then overhead focused lights were used to achieve acceptable

vertical laser stripe emitted from the LRS was passed over the exposed cortical surface and range data points were sampled as it passed from the left to right extent. Immediately after range data acquisition, a digital image of the surgical FOV was acquired by the LRS for the texturing process. After the scan the monopod was removed and the surgery proceeded. The entire scanning process (set-up, calibration, scan) takes approximately 1–2 minutes per scan.

At the conclusion of each acquisition, the scanner generates 5 dimensional data representing the geometry and intensity pattern of the cortical surface. An example dataset acquired by the LRS is demonstrated in Figure 26. The first three dimensions are the x, y, and z coordinates of the LRS sampled cortical surface. The remaining 2 dimensions, u and v, of the LRS data are dedicated to mapping intensity information in the digital image of the surgical FOV to the range data. Standard computer graphics techniques of texture mapping are used to encode each geometric point with a corresponding color from the digital image of the surgical FOV (see Figure 27)[202].

LRS dataset registration to preoperative images

After the intraoperative datasets were obtained, rigid-body registration was performed to align them with the preoperative image data. Registration provides an initial step towards incorporating the intraoperative data within an IGS framework. Future work with the LRS will use serial range datasets and the registration to the preoperative scene as constraints for the computational model. Nonetheless, the methods outlined in this paper demonstrate the LRS's ability to provide anatomical cues within the context of data provided by the preoperative images.

Registration of the intraoperative LRS data with preoperative image data necessitated the generation of textured surfaces from preoperative MR tomograms. Manually segmented MR tomograms were subjected to a marching cubes tessellation to generate an initial, faceted surface representation of the brain image volume. A radial-basis function representation [203]

scanning conditions.

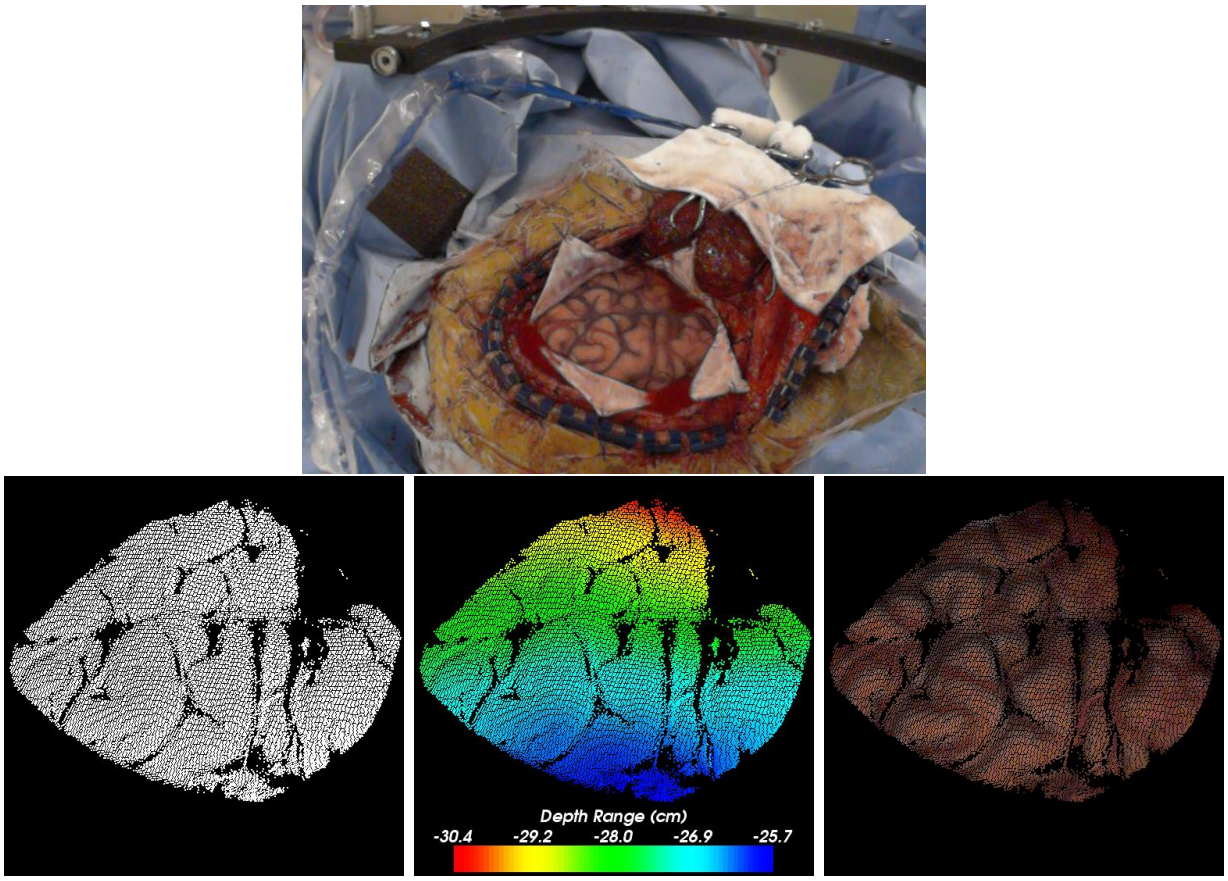

Figure 26: Example of an LRS acquisition. The top row shows a digital image of the scanning FOV. The bottom two row shows three representations of the data acquired by the LRS device (from left to right): raw point cloud, intensity encoded point cloud based on range distance, intensity encoded point cloud based on the digital texture image in the top row.

Table 3: Patient and intraoperative characteristics. *Definitions*: Pt, patient; #, number; *cm*, centimeters; M, male; F, female; OA-II, oligoastrocytoma, WHO classification grade II; Ca, cancer; GBM, gliobastoma multiforme (WHO classification, grade IV glioma); L, left; R, right; F, frontal; T, temporal; P, parietal; S, supine; A, awake craniotomy; G, craniotomy under general anethesia; M, mannitol; (dose, 1 gm/kg of body weight to maximum of 100 grams); Fl, furosemide, 0.25 mg/kg of body weight, to a maximum of 40 mg; GTR, gross total resection (based on post-operative gadolinium enhanced magnetic resonance (MR) image or, in the case od patients 2, 3, and 6 elimination of tumor as seen on T-2 weighted MR images); ATL, anterior temporal lobectomy (5.0*cm* of superior, middle, and inferior temporal gyrii); AHC, amygdalohippocampectomy, 3.0*cm* of hippocampus and lateral amygdalar nucleus, as confirmed on post-operative MR.

Pt. #	Age, Sex	Diagnosis	Craniotomy	Position	Orientation up (deg); turn (deg)	Anesthesia	Diuretic type	Resection	Lesion Size (*cm*)
1	37, M	OA-II	L posterior F-T	S	15; 25 to R	A	M	GTR	3.0 x 2.0 x 2.0
2	34, M	Ganglioglioma	L inferior F-T	S	15; 45 to R	A	M	GTR	2.6 x 2.0 x 1.8
3	50, F	Metatstatic Ca	R posterior F	S	15; 15 to R	A	M	GTR	2.5 x 2,5 x 2.0
4	23, M	Temporal lobe epilepsy	L F-T	S	15; 75 to R	G	M, Fl	ATL+ AHC	5.0 x 5.0 x 5.0
5	52, M	GBM	L F-P behind motor strip	S	30; 15 to R	A	M	GTR	3.5 x 3.0 x 3.0
6	26, M	Ganglioglioma	R temporal	S	15; 75 to L	A	M	ATL	5.0 x 5.0 x 5.0
7	64, M	GBM	R parietal	S	30; 25 to L	A	M	NTR	5.5 x 4.5 x 4.0
8	61, F	Meningioma	L posterior F-T	S	15; 25 to L	A	M	GTR	5.8 x 5.1 x 4.2

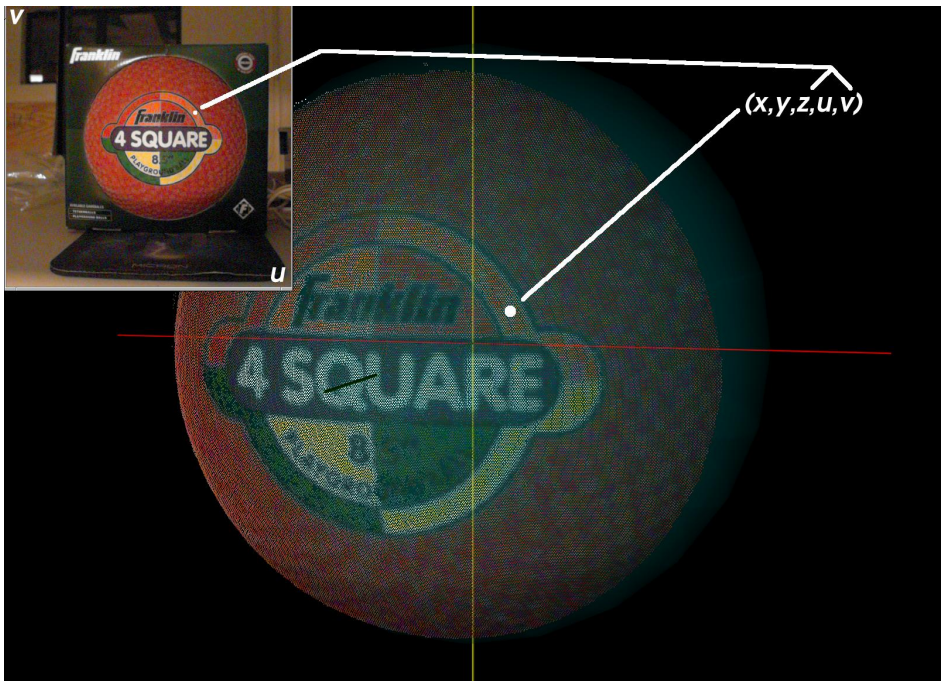

Figure 27: Texture Mapping. Each point acquired by the LRS has 5 dimensions of data. The first three represent the (x,y,z) position of the point, while the last two serve as lookup coordinates into a corresponding texture image. Intensities from the texture image can be mapped to positions on the point cloud using the (u,v) texture coordinates, resulting in textured point clouds.

of the surface was generated to provide a better representation of the surface normals (see Figures 28 and 29). Finally, a ray-casting process was used to encode a surface texture onto the smooth polygonal brain surface mesh (see Figure 30). The ray-casting proceeded by averaging the intensities of 5-10 voxels projected into the brain along the normal direction of a surface point on the polygonal mesh. The average intensity was placed at the surface point to represent the surface texture at that point.

After generating corresponding datasets, three registration algorithms were used to align the intraoperative scene to its preoperative counterpart and results from each registration algorithm were examined. The first registration method was alignment using manually localized surface landmarks in each textured surface through a Procrustes' least-squares fitting (point-based registration, or PBR) [28, 204]. This is similar to the method described by Nakajima et al. for organ based registration [166].

The second registration method is the iterative closes point (ICP) algorithm that uses geometry information to register surfaces [167]. The ICP algorithm works by determining correspondence between surfaces based on closest points and then registering via Procrustes' alignment using the determined correspondence. This process of determining correspondence and Procrustes' alignment is iterated upon until a termination criteria, such as minimal surface to surface distance, is met.

The final registration protocol is the SurfaceMI algorithm which uses both geometry and intensity information to align textured surfaces [205]. The SurfaceMI (SMI) algorithm uses closest point criteria to determine corresponding points in the two textured surfaces being registered. Once correspondence has been established, mutual information [190, 169] of the intensities in each point cloud is determined as a measure of registration accuracy. Mutual information is a measure of statistical dependence. The underlying premise to mutual information in registration is that two datasets (i.e. images or surfaces) are registered if they have maximized the mutual information (i.e. statistical dependence) of their data (i.e. intensity). Mutual information has been used extensively in the image registration community because of it's robustness in multi-modality image registration [190, 168, 169, 174]. The SurfaceMI

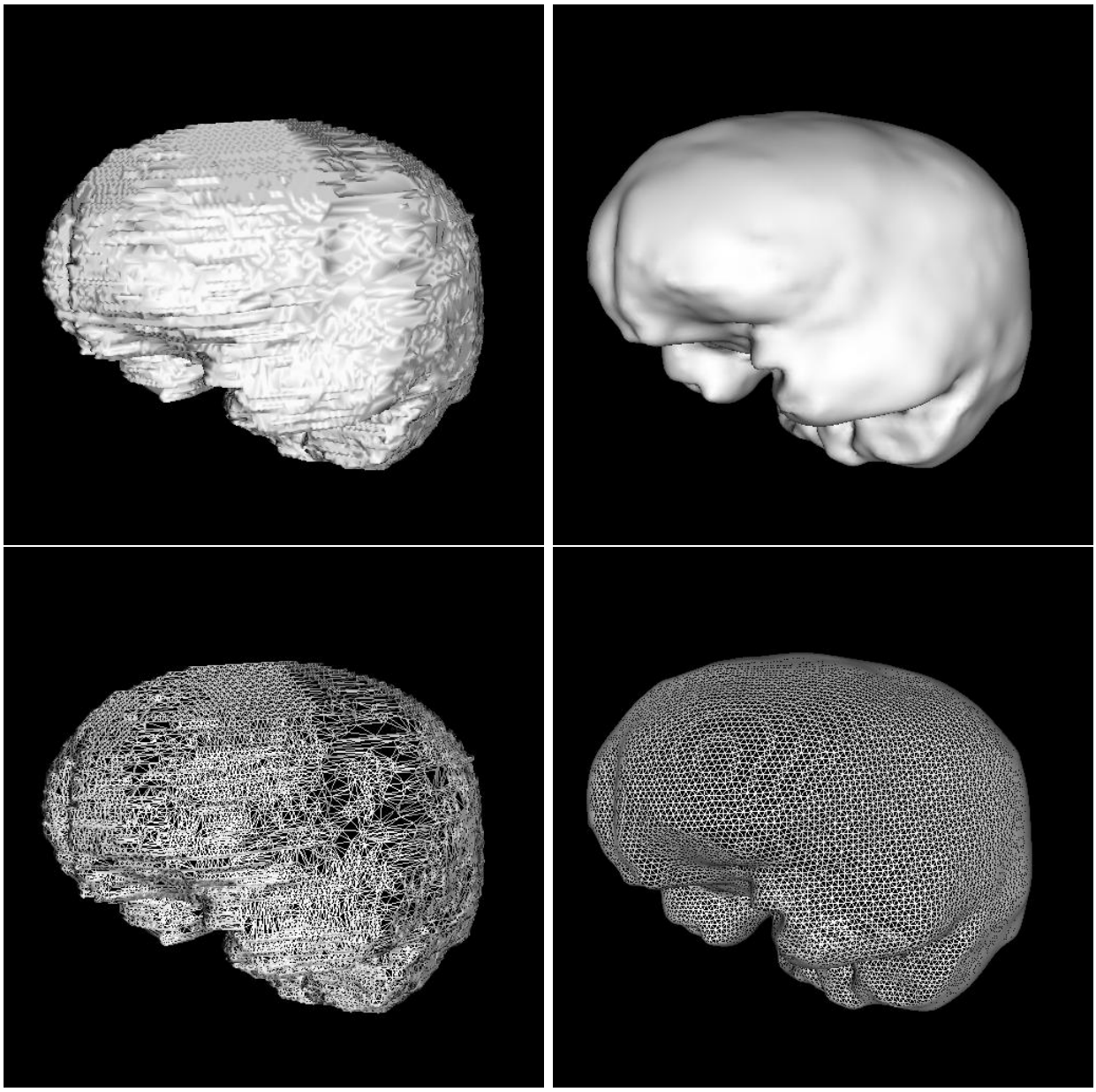

Figure 28: Textured surface generation from a segmented preoperative MR tomogram, step 1: polygonal surface tessellation. The left column shows a marching cubes tessellation of a segmented preoperative MR tomogram. The right column shows an radial-basis function fitting of the marching cubes surface, resulting in a smooth polygonal mesh. Wireframe views of the marching cubes and radial-basis function surfaces are shown in the bottom row for comparison purposes. Notice the even distribution of surface polygons in the radial-basis function wireframe surface.

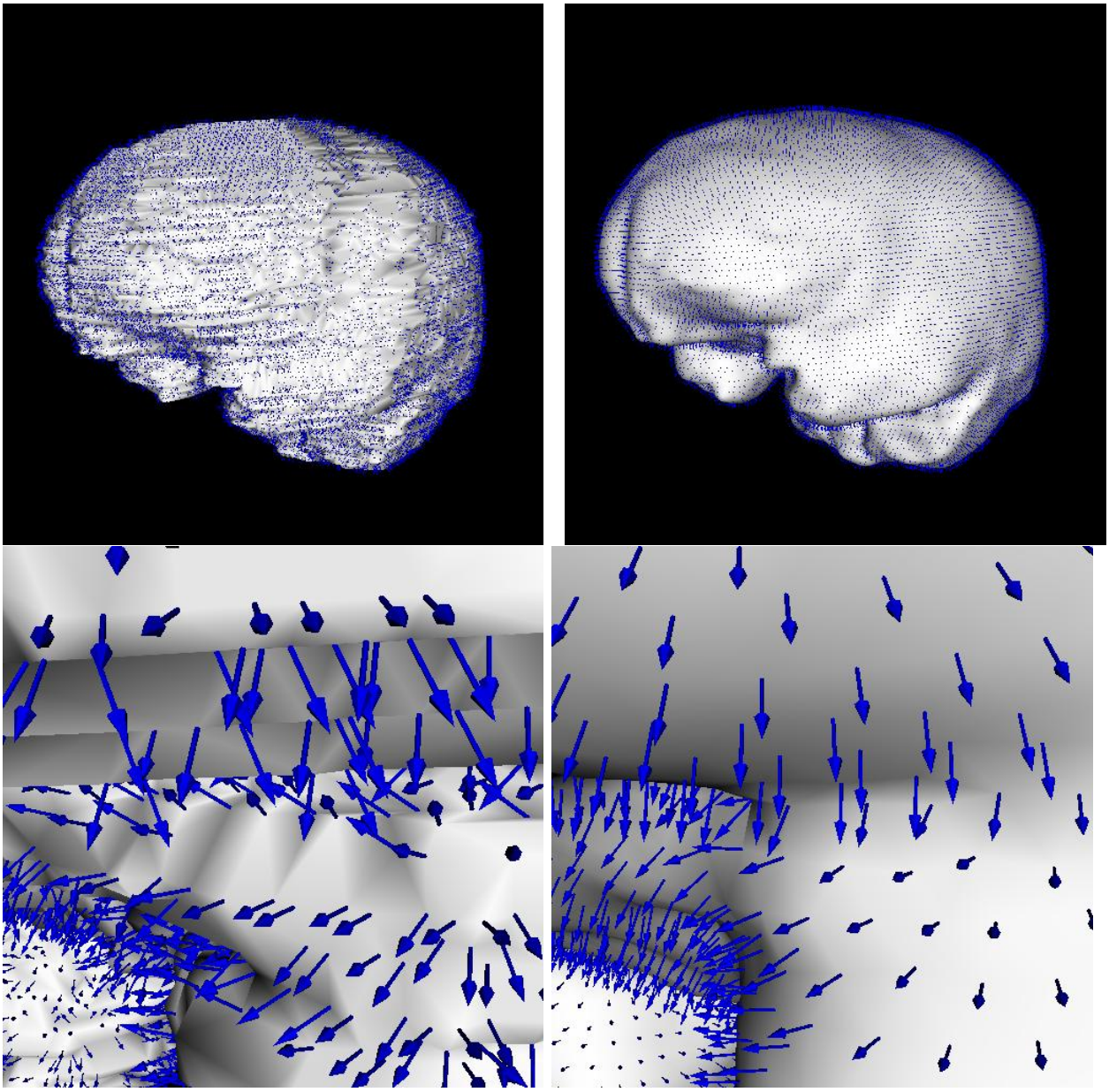

Figure 29: Textured surface generation from a segmented preoperative tomogram, step 2: normal generation. These figures illustrate the normals generated from both marching cubes and radial basis function surfaces. The top row of images shows a zoomed out view of both surfaces with normal glyphs assigned to each surface point shown in blue. The bottom row of images shows zoomed in views of corresponding locations from the zoomed out images. The normal glyphs are readily apparent as arrows pointed away from the surface. The smooth, uniform distribution of normals from the radial basis function surface (shown in the bottom right) are critical to generating well-resolved textured surfaces from preoperative tomograms.

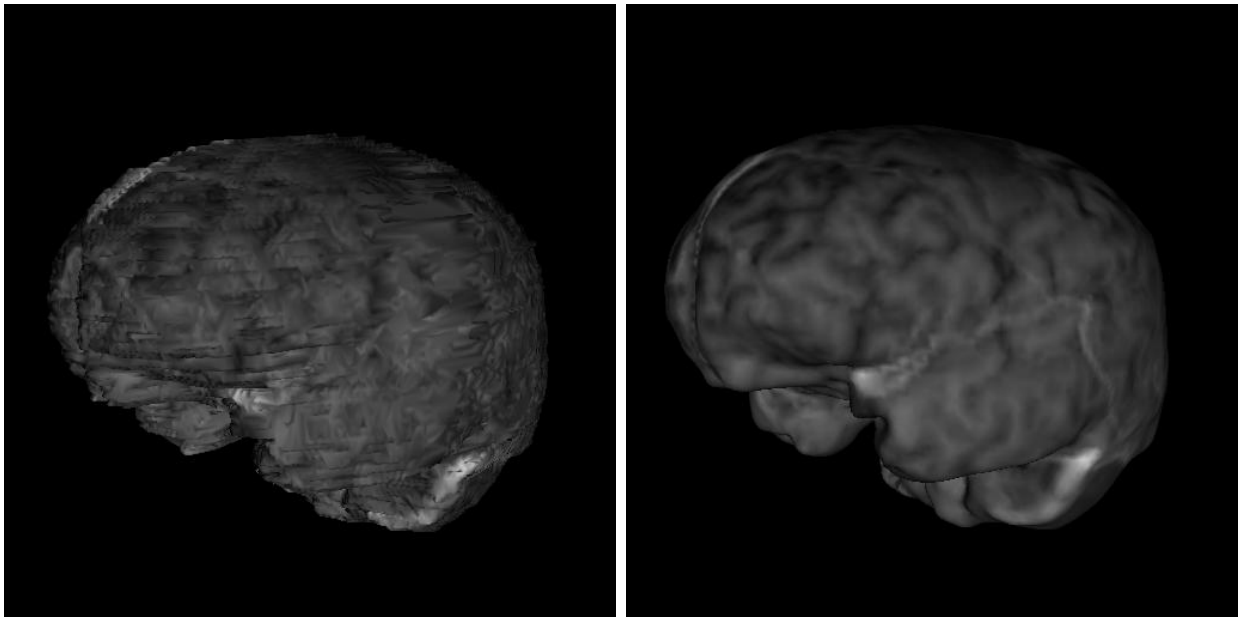

Figure 30: Textured surface generation from a segmented preoperative tomogram, step 3: ray-cast color encoding. These figures demonstrate the result of the ray-cast color encoding process on the marching cubes and radial basis function surfaces. The ray-cast algorithm starts at the voxel associated with a given surface point on the mesh and penetrates the preoperative tomogram along surface normal associated with that point. The algorithm uses the average intensity along the projection direction (normal) to represent the surface intensity for the polygonal mesh. From these images, one can see that smooth, uniform distributions of surface normals is critical to obtaining good textured surfaces of the brain from preoperative images.

registration is an optimization of the mutual information of each surface's texture information. Validation of the SurfaceMI algorithm on multi-modal phantom data is provided in [205].

For this paper the algorithm, originally described in [205], was enhanced to multi-scale/multi-resolution technique, in which the rigid registration was performed sequentially on coarse to fine versions of the input textured point clouds. Multi-scale implies varying degrees of geometry resolution (i.e. density of surface points). Multi-resolution implies varying degrees of texture information (i.e. the sharpness of the surface texture). Figure 31 shows an example of the progression from coarse to fine textured point clouds used in the multi-scale/multi-resolution version of SurfaceMI. Figure 31a shows a high scale, high resolution version of a textured surface generated from a preoperative tomogram. Notice the highly resolved texture pattern on the surface of the brain. The insert in Figure 31a shows the density of the surface points as being almost continuous. In contrast, Figure 31d shows a low scale, low resolution textured surface from the same preoperative MR. Notice the blurred texture pattern on the surface and low density of points in the insert image. The multi-scale/multi-resolution approach using these clouds allows for the mutual information registration to gradually align textured surfaces in a coarse to fine fashion.

Since a "ground-truth" measure of registration was not available at the time of acquisition for each of the patients, the results in this paper are assessed visually. For patients with striking features in both preoperative MR textured surfaces and intraoperative textured LRS surfaces, those features were highlighted manually and used to assist in visual assessment of registration accuracy. Currently, we are working towards validating the techniques used in this paper in quantitative manner using optical tracking during acquisition as a reference measurement system. The results presented here are an indication of the capabilities of the system developed and provide insight into the possible applications of LRS technology for intraoperative use.

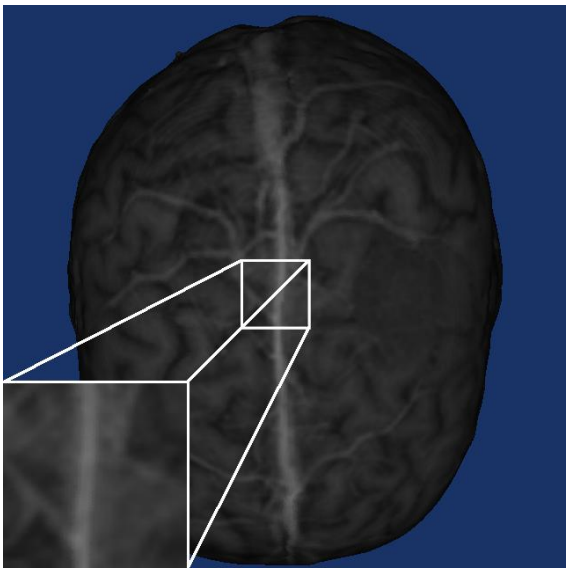

31(a) Resolution level 0

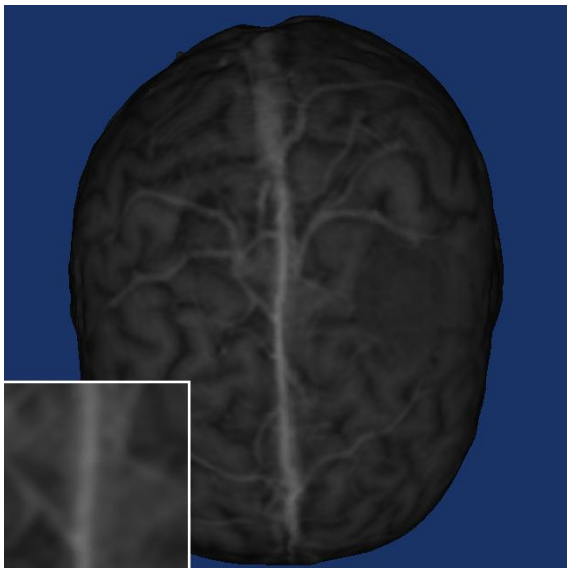

31(b) Resolution level 1

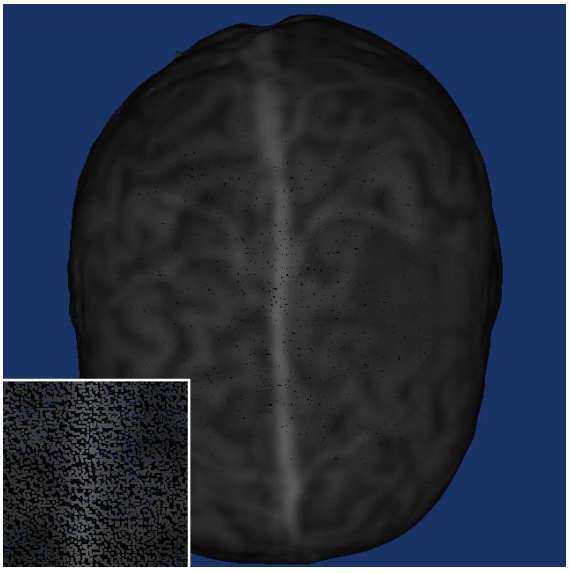

31(c) Resolution level 3

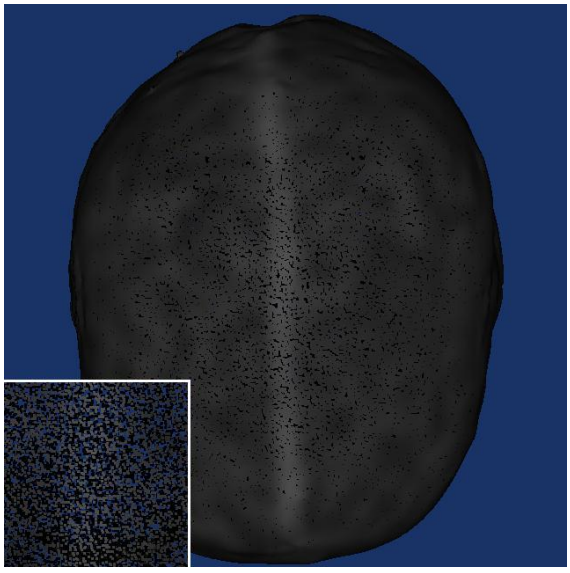

31(d) Resolution level 5

Figure 31: Multi-scale/multi-resolution textured LRS datasets. Each figure shows a different scale/resolution of a textured preoperative MR brain cloud. A region of interest is highlighted in (a) and zoomed into to show the effects of changing resolution levels on a finer scale. The same region of interest is shown, zoomed-in, as an inserting (b), (c), and (d).

Intraoperative acquisition

Figures 32 through 40 demonstrate: the intraoperative surgical FOV, the textured surface generated from the preoperative-MR tomogram, and segmented intraoperative textured LRS surface.

For Patient 1, the tumor can be seen in the preoperative textured surface as the shadowy area anterior to the vein of Trolard (see Figure 32b). The tumor does not show up as clearly in the intraoperative LRS textured surface. However, one can see the vein of Trolard and other significant sulcal landmarks are demonstrated clearly in the intraoperative dataset (Figure 32a).

The digital pictures for Patient 2 (Figures 33a and 33b) highlight the tumor and a significant vessel as viewed during surgery. The tumor can be seen in the preoperative MR surface near the front of the brain as an abnormal highlight in the surface texture (Figure 33c). The LRS dataset (Figure 33d) managed to capture a majority of the surgical FOV's exposed surface texture. The vessel highlighted in Figure 33b is clearly visible in the LRS textured dataset.

Patient 3's data is similar to that of Patient 2. The digital images (Figures 34a and 34b) demonstrate the tumor location and vessel of interest in the surgical FOV. The tumor can be seen clearly on the preoperative MR textured surface as the bright white disk in the middle of the cortical surface (see Figure 34c). The abutting vessel is also clearly shown in the preoperative surface just posterior to the tumor location. The vessel is also visible in the intraoperative data (Figure 34d). However, the tumor is not clearly evident in the LRS data.

The data for patient 4 are the first demonstration of data collected on a temporal lobe of the brain. In the digital image, the Sylvian fissure is located near the right margin of the exposed brain surface (Figure 35a). The preoperative MR textured surface is oriented to show the hemisphere associated with surgery (Figure 35b). Compared to the preoperative

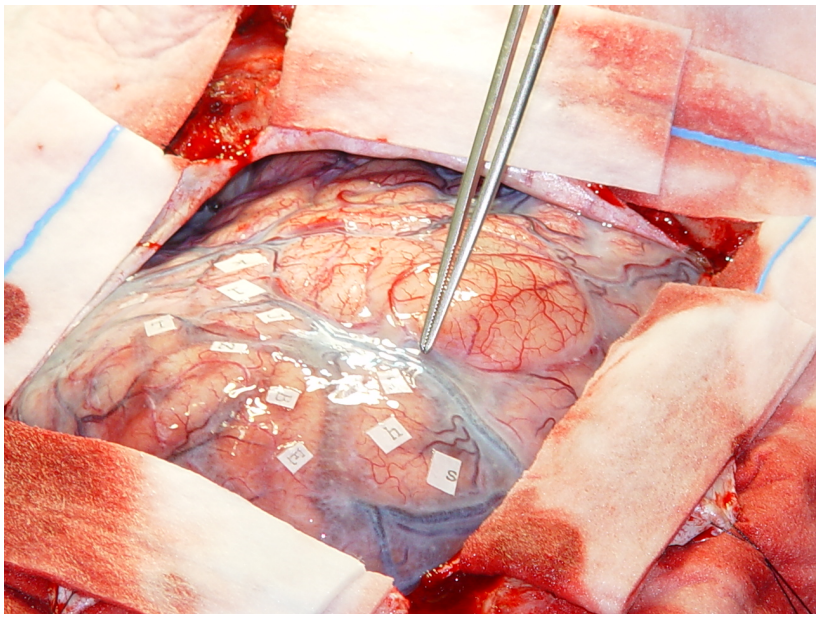

32(a) Digital Image

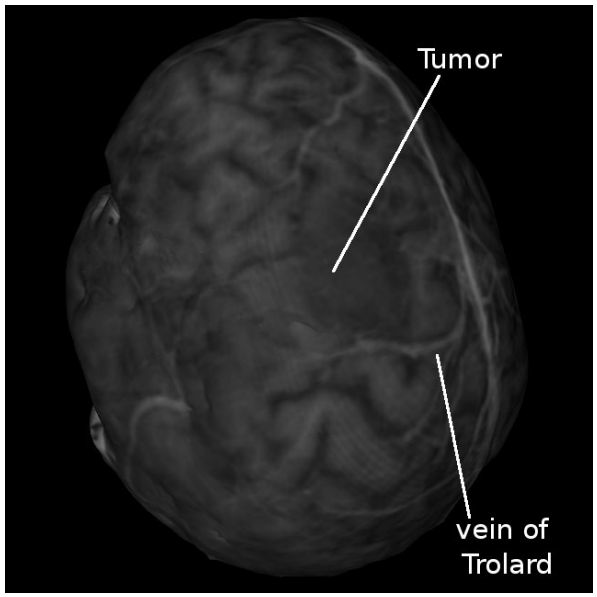

32(b) Preoperative Textured Surface

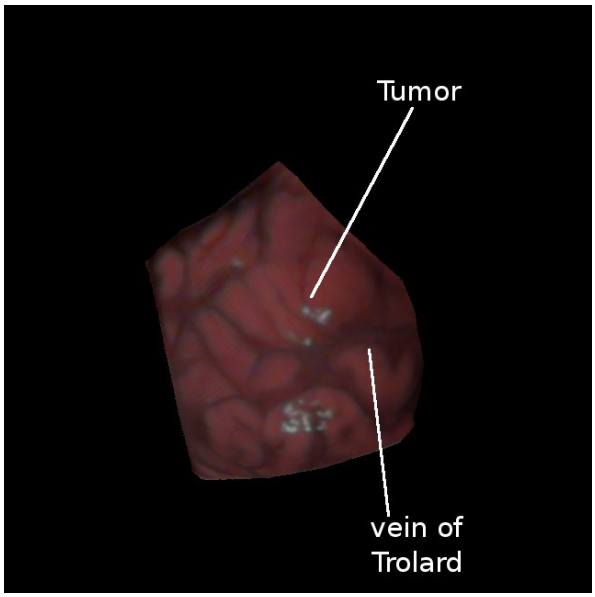

32(c) Intraoperative Textured Surface

Figure 32: Data for Patient 1. Top row: intraoperative high resolution of digital image of the surgical FOV. The vein of Trolard is highlighted with the forceps. The tumor of interest is just behind the forceps in the image, signified by the heightened vascularization. Bottom row, from left to right: preoperative MR textured surface and intraoperative textured LRS surface. The vein of Trolard and the tumor region has been indicated in both images.

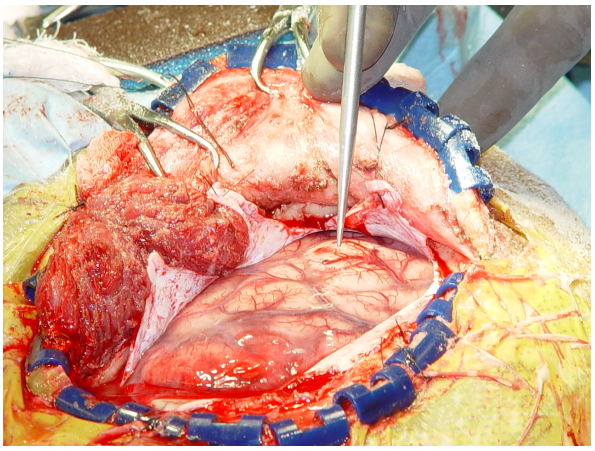

33(a) Digital Image: Tumor

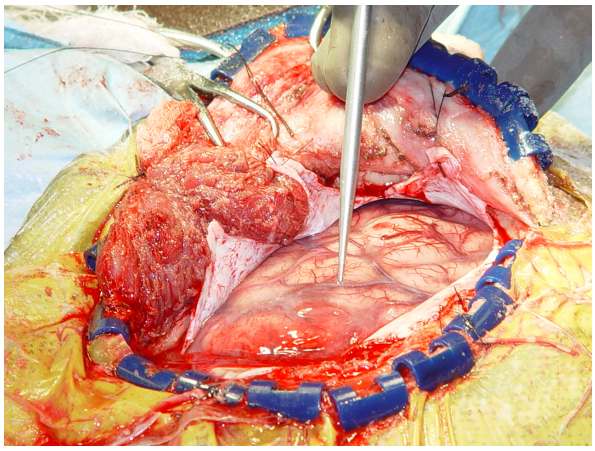

33(b) Digital Image: Vessel

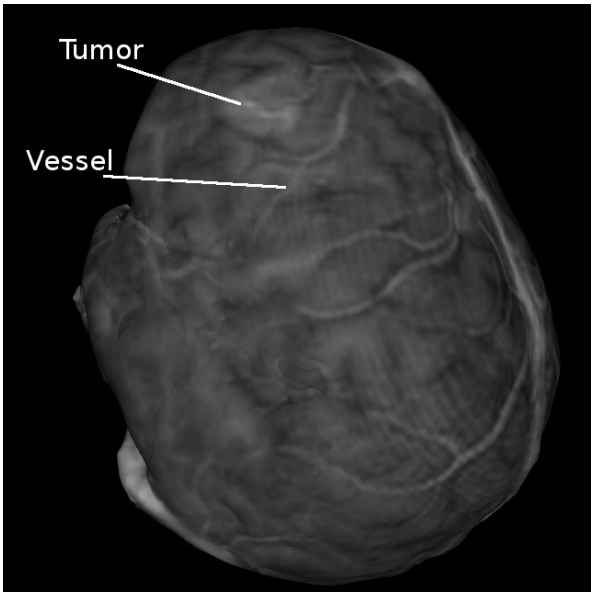

33(c) Preoperative Textured Surface

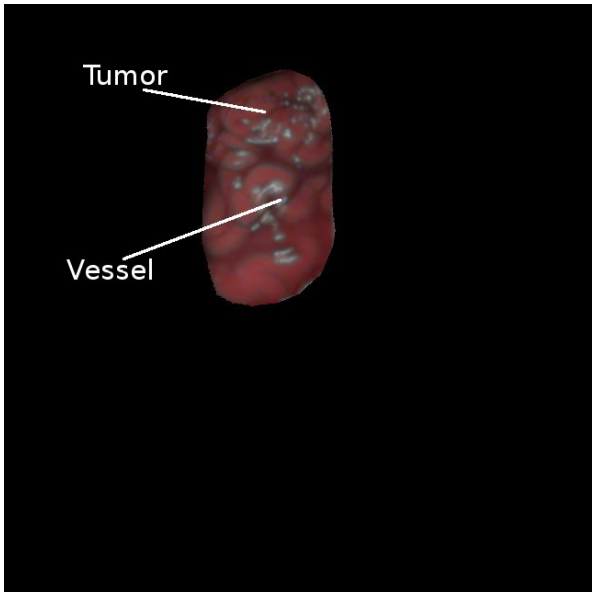

33(d) Intraoperative Textured Surface

Figure 33: Data for Patient 2. Top row: intraoperative high-resolution images of the surgical FOV with the tumor highlighted using forceps on the left and a significant vessel highlight on the right. Bottom row, from left to right: preoperative MR textured surface and intraoperative textured LRS surface. The tumor and vessel highlighted in the digital photos has been manually highlighted in each textured surface image.

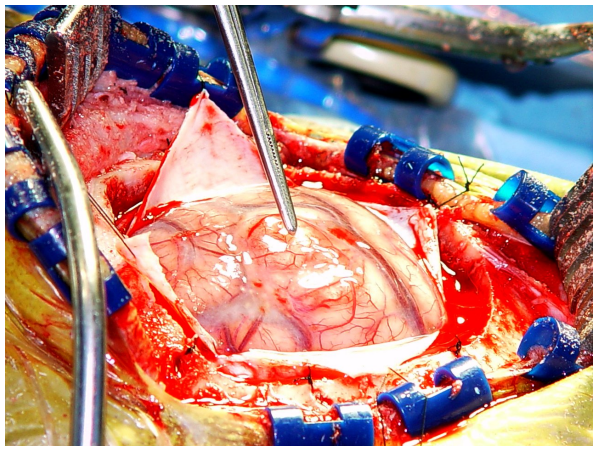

34(a) Digital Image: Tumor

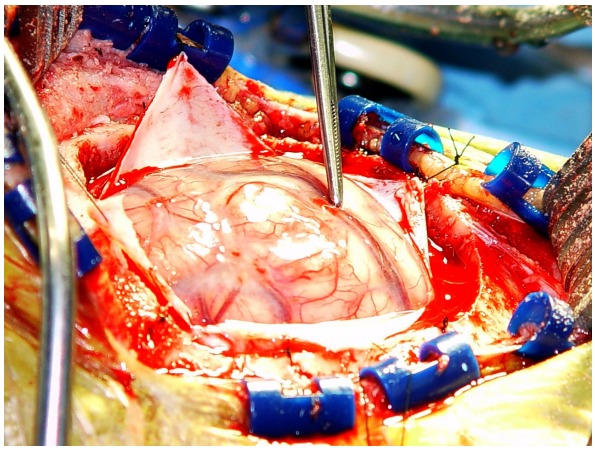

34(b) Digital Image: Vessel

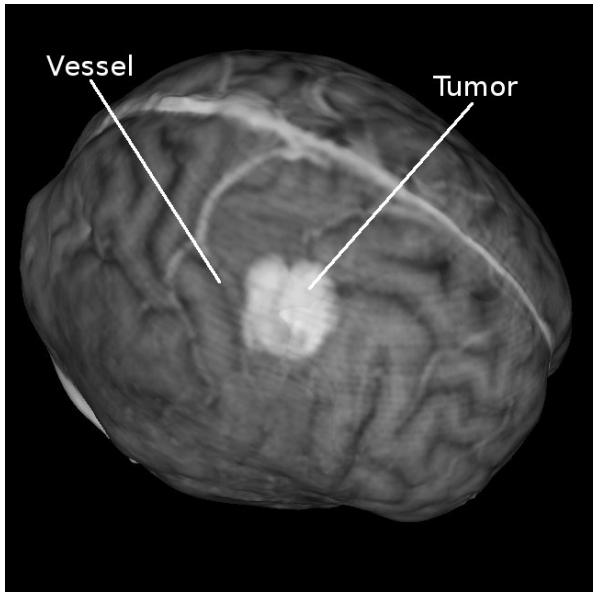

34(c) Preoperative Textured Surface

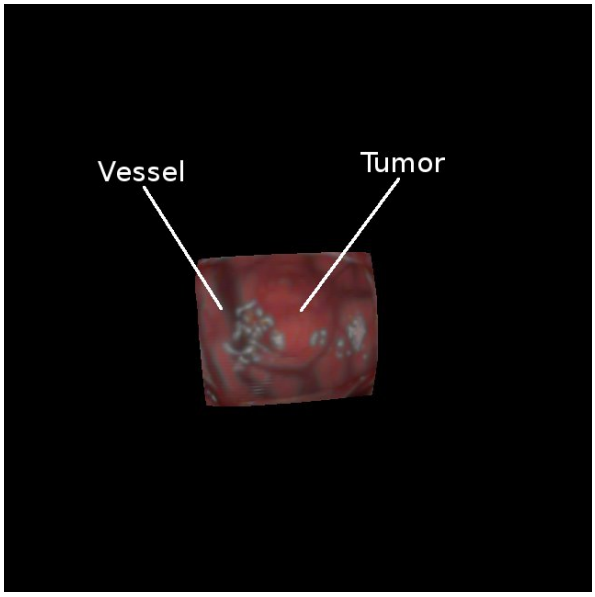

34(d) Intraoperative Textured Surface

Figure 34: Data for Patient 3. Top row: intraoperative high-resolution images of the surgical FOV with the tumor highlighted using forceps on the left and a significant vessel highlight on the right. Bottom row, from left to right: preoperative MR textured surface and intraoperative textured LRS surface. The tumor and vessel highlighted in the digital photos has been manually highlighted in each textured surface image.

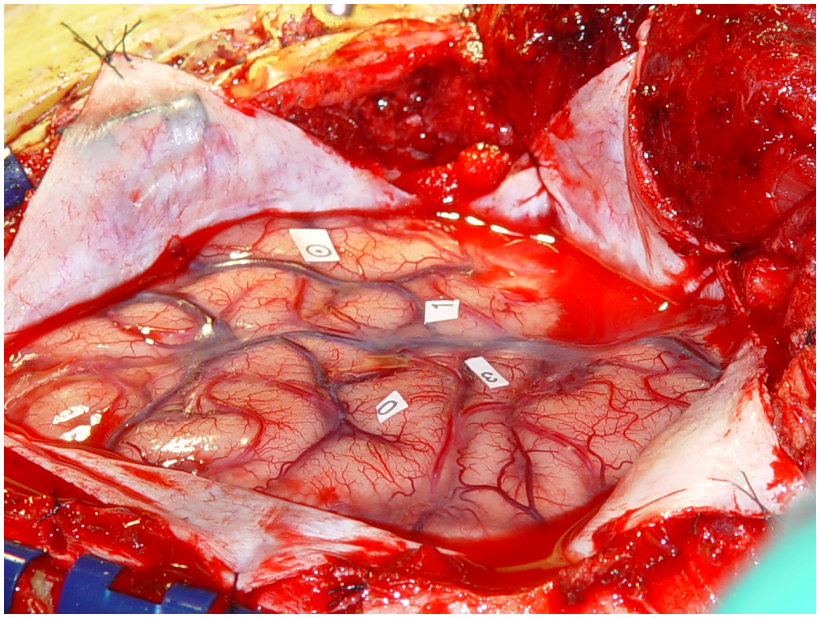

35(a) Digital Image

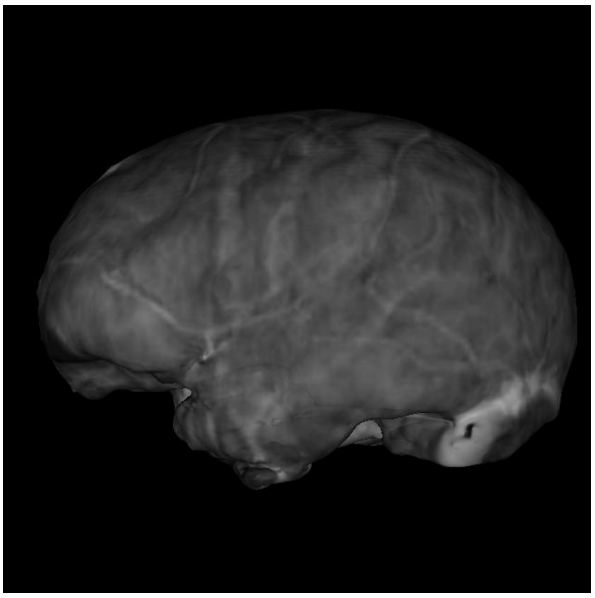

35(b) Preoperative Textured Surface

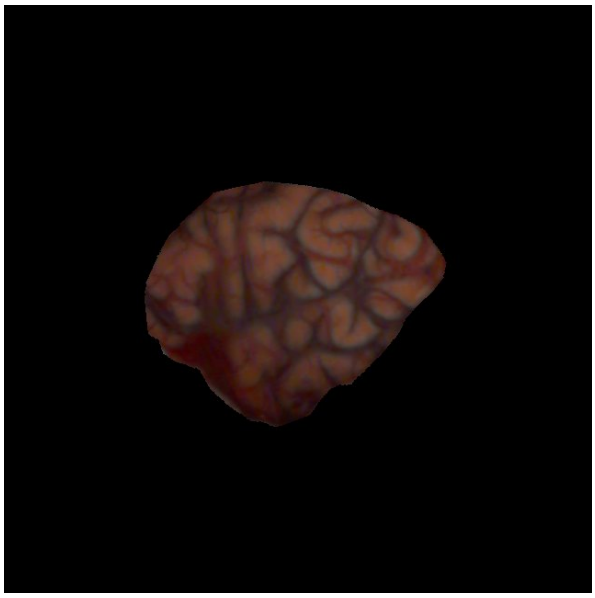

35(c) Intraoperative Textured Surface

Figure 35: Data for Patient 4. Top row: intraoperative high-resolution image of the surgical FOV. Bottom row, from left to right: preoperative MR textured surface and intraoperative textured LRS surface.

MR surface, the LRS textured surface nicely highlights the intricate vessel and sulcal patterns near region of the craniotomy (Figure 35c).

The preoperative MR textured surface for Patient 5 shows a significant vessel and tumor near the surgical FOV (Figure 36a). Patient 5's intraoperative data is limited to the textured LRS dataset acquired during surgery (Figure 36b); a digital image of the surgical FOV was not available for this patient. The LRS dataset shows vessel and sulcal features corresponding to those seen in the preoperative surface near (just posterior to) the region of the tumor.

Patient 6 presents another case where the surgical FOV is in one of the temporal lobes. The digital image of the surgical FOV shows the surgeon highlighting the Sylvian fissure (Figure 37a). The textured surface generated from the preoperative MR is shown in Figure 37b; the Sylvian fissure is highlighted manually. Figure 37c shows the surgical FOV as acquired by the LRS device. The Sylvian fissure from Figure 37a is highlighted artificially in Figure 37c for clarity. It is interesting to note that the intraoperative data generally has much more surface texture information as compared to the data generated from the preoperative MR tomogram.

Figure 38a shows the intraoperative FOV for a surgical case taking place in the parietal lobe. Figure 38b shows the textured surface generated from the preoperative MR image data. The preoperative textured surface presents limited information with respect to vessel and sulcal patterns when. The LRS dataset collected intraoperatively (Figure 38c), in contrast, shows a great deal more surface texture data.

Patient 8 represented an exceptional case for data collection and processing. Figures 39a and 39b show the digital images of this patient's intraoperative surgical FOV before and after resection, respectively. The textured surface from the preoperative MR (Figure 39c) clearly shows the location and area occupied by the tumor. The intraoperative data shows the surgical FOV as acquired by the LRS device (Figure 39d). For this case, it was necessary to embed cotton into the tumor to prevent bleeding. These cotton strips were captured by the LRS and are highlighted in Figure 39d. The size of the tumor extracted from this patient is shown in Figures 40a and 40b.

Registration Results

RMS fiducial registration error (FRE) [194] from the PBR registration results are presented in Table 4. RMS FRE measures the closeness-of-fit of the fiducial sets for the PBR. A low RMS FRE for the PBR registrations presented in this paper implies good localization of corresponding surface fiducials in each textured surface, as well as a good registration between the two surfaces based on the fiducials. A high RMS FRE implies poor or incorrect localization of surface fiducials in the two clouds. From Table 4, the lowest RMS FRE was seen in Patient 3, who had an RMS FRE of $1.8mm$. The highest RMS FRE was seen in Patient 4, who had an RMS FRE of $7.2mm$ with 5 fiducials. Removal of the fiducial with worst localization error reduced the RMS FRE for Patient 4's registration to $1.6mm$, which reduced the average RMS FRE over all patients to $3.3\pm1.5mm$.

The results for rigid-registration of the intraoperative data to preoperative data for Patient 1 are shown in Figure 41. The top row of images (Figures 41a–41c) shows the PBR, ICP and SMI registration, respectively. The bottom row (Figures 41d–41f) shows the PBR, ICP and SMI registration with artificially highlighted features in both surfaces. The registration shown in the bottom row provides an augmented indication of the performance of each registration method on the data. The PBR registration provided good correlation of surface features in both surfaces; this is seen by the good alignment of the vein of Trolard. The ICP registration, being a geometry based registration only, provided much poorer correspondence between surface features. The SMI registration provided good correspondence between both surfaces, similar to the results of the PBR. However, the SMI performs better in registering the sulcal groove just posterior to the vein of Trolard as compared to the registration provided by the PBR.

The rigid-registration results for Patient 2 are shown in Figure 42. Similar to the layout for Figure 41, the top row of Figure 42 demonstrate the results for PBR, ICP and SMI registration on the two textured surfaces, respectively. Figures 42d–42e show enhanced views of the registration results, where significant features in each surface have been manually painted to provide insight into the quality of the registrations. Among these results the ICP

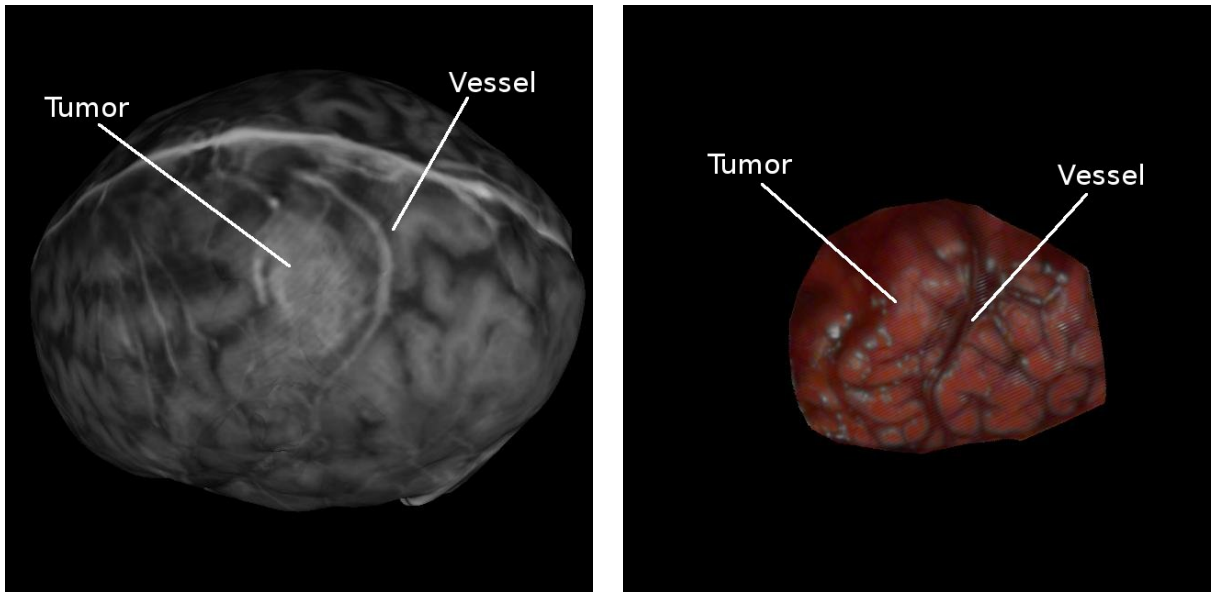

36(a) Preoperative Textured Surface

36(b) Intraoperative Textured Surface

Figure 36: Data for Patient 5. From left to right: preoperative MR textured surface and intraoperative textured LRS surface. The tumor and a significant vessel in both textured surfaces has been highlighted.

Table 4: Fiducial registration errors for PBR registration of the preoperative MR and LRS textured surfaces for each patient.

Patient #	RMS FRE in *mm* (# of fiducials)
1	5.4 (5)
2	4.9 (5)
3	1.8 (4)
4	7.2 (5)
5	2.4 (4)
6	4.7 (4)
7	2.8 (4)
8	3.3 (3)
Average	4.1±1.8 (4.25)

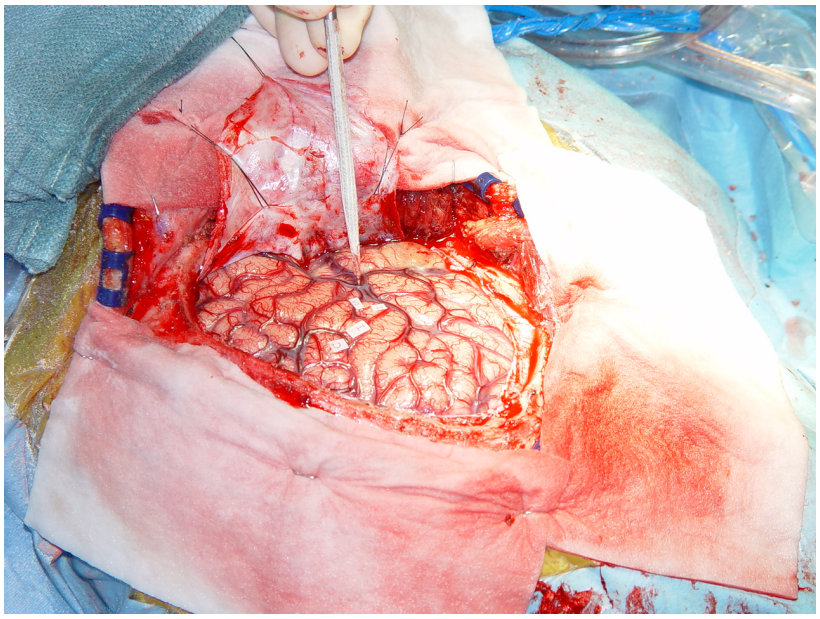

37(a) Digital Image

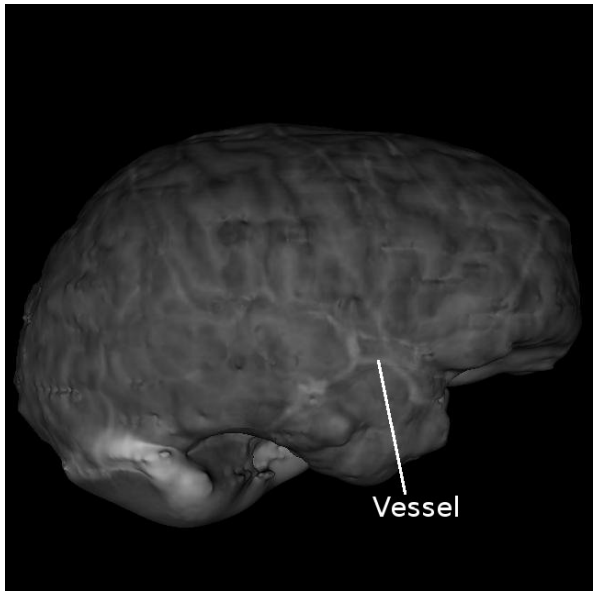

37(b) Preoperative Textured Surface

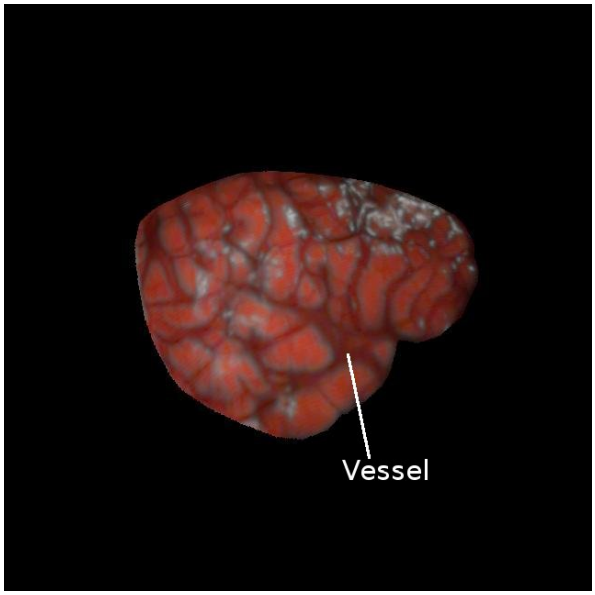

37(c) Intraoperative Textured Surface

Figure 37: Data for Patient 6. Top row: intraoperative high-resolution image of the surgical FOV with the Sylvian fissure highlighted by the forceps. Bottom row, from left to right: preoperative MR textured surface and intraoperative textured LRS surface. The Sylvian fissure has been highlighted artificially in each textured surface image.

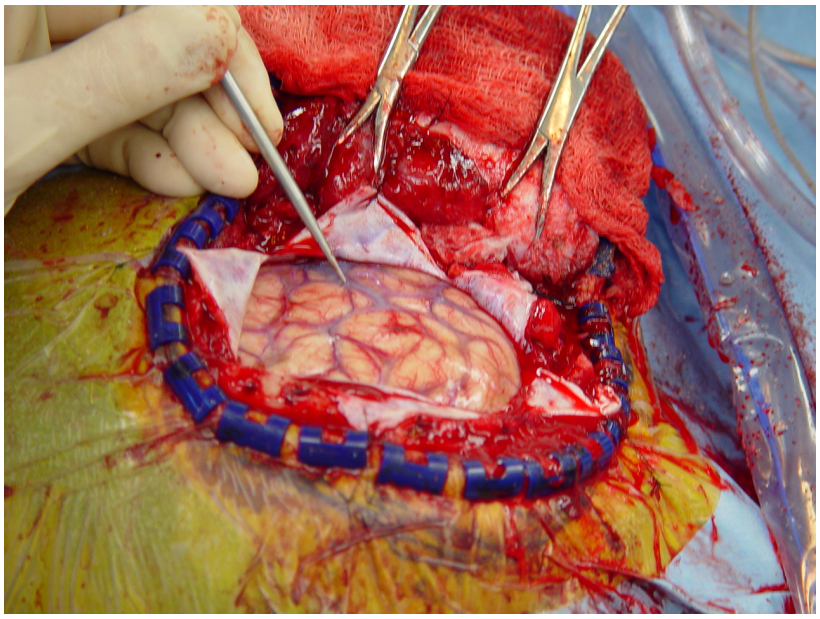

38(a) Digital Image

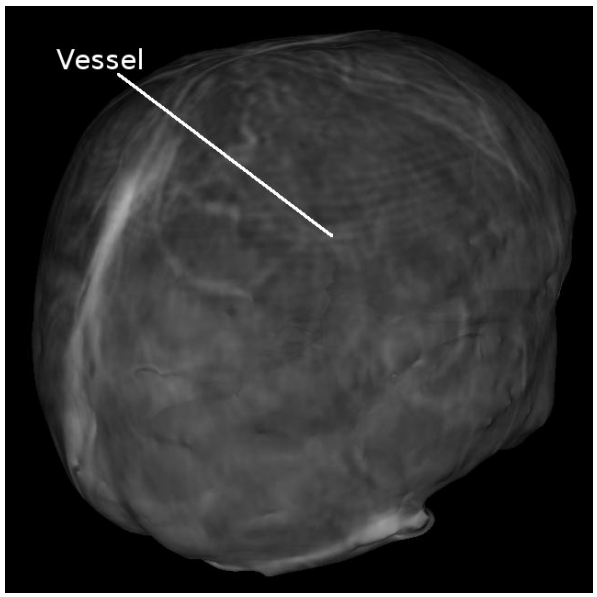

38(b) Preoperative Textured Surface

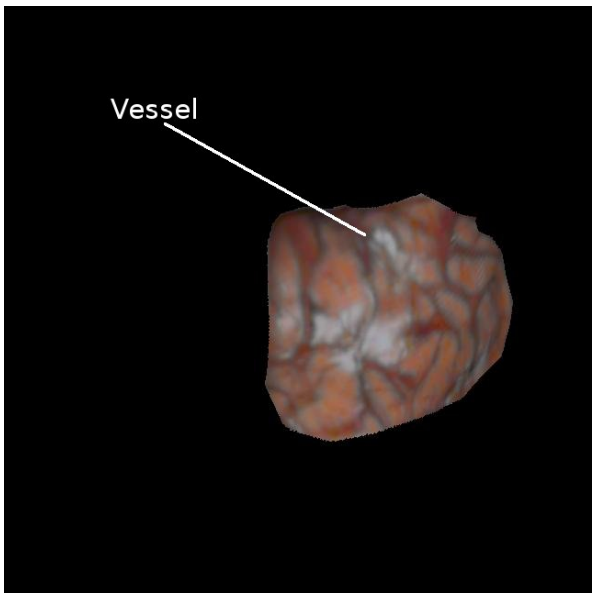

38(c) Intraoperative Textured Surface

Figure 38: Data for Patient 7. Top row: intraoperative high-resolution image of the surgical FOV with a significant vessel highlighted by the forceps. Bottom row, from left to right: preoperative MR textured surface and intraoperative textured LRS surface. The corresponding vessel has been highlighted manually in the two textured surface images.

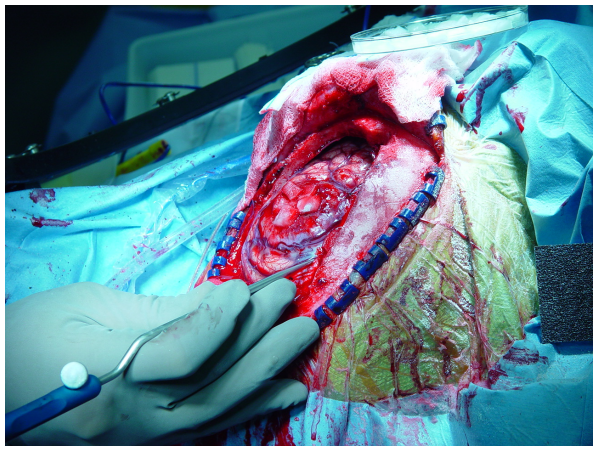

39(a) Digital image of the preresection surgical FOV

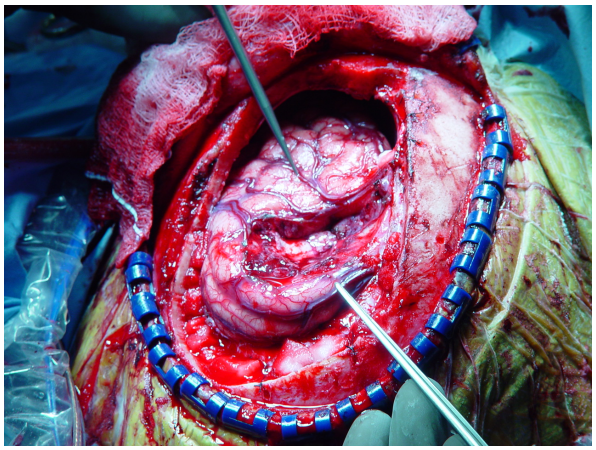

39(b) Digital image of the postresection surgical FOV

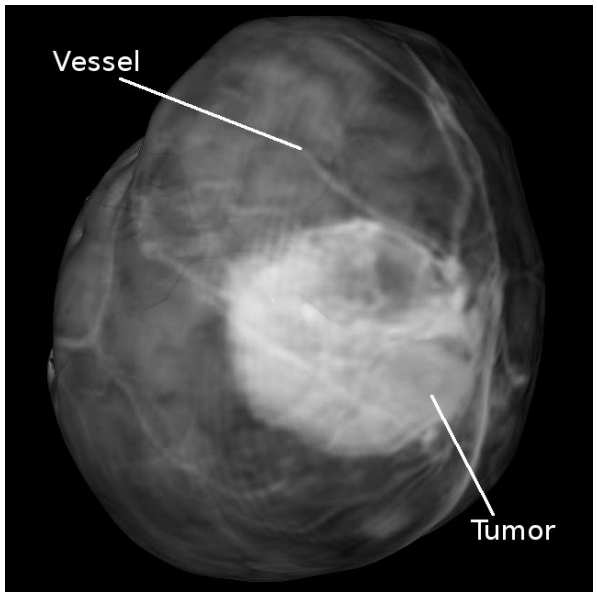

39(c) Preoperative Textured Surface

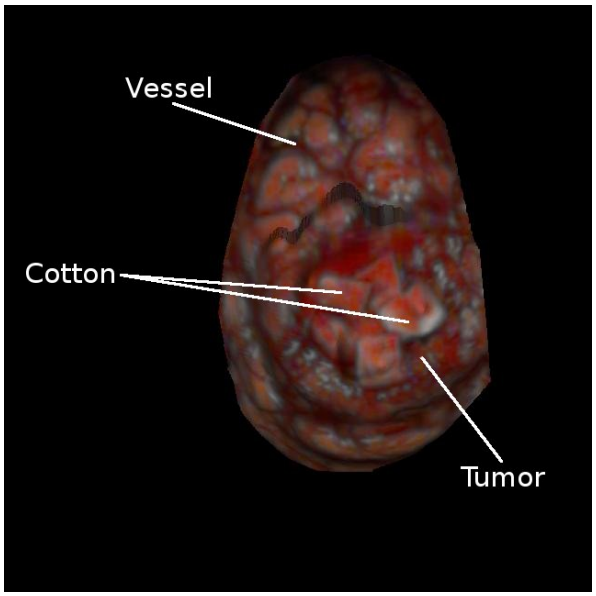

39(d) Intraoperative Textured Surface

Figure 39: Data for Patient 8. Top row: intraoperative high-resolution images of the surgical FOV; pre-resection on the left and post-resection on the left. A significant vessel near the top of the surgical FOV is highlighted in the post-resection digital image. Bottom row, from left to right: preoperative MR textured surface and intraoperative textured LRS surface. The intraoperative data for this patient demonstrate an extreme case due to the size of the lesion removed. This figure is complemented by Figure 40, which shows the size of the lesion removed. The tumor and vessel are highlighted in the two textured surface images. Cotton in the surgical FOV is also highlighted in the LRS textured surface as a disparate surface feature that does not exist in the preoperative surface texture.

registration provided the most accurate alignment of surface features. The worst registration was provided by the SMI registration. This result was provoked by the unconstrained nature of the SMI registration. Retrospective examination of the SMI registration result shows that the alignment gravitated towards surface features outside of the surgical FOV.

Patient 3's rigid-registration results (see Figure 43) show excellent results for all three registration protocols. PBR results demonstrate good alignment of corresponding structures. This result is likely due to the the abundance of easily identifiable features in both the preoperative and intraoperative textured surfaces. Due to the smoothness of the intraoperative surface acquired, the ICP registration did not deviate greatly from the PBR registration. Finally, SMI results demonstrate the robustness of the registration protocol by registering disparate surface textures accurately. That is, registering the bright region of the tumor in the preoperative surface against the homogeneous intensity pattern of the intraoperative data.

The registration results for Patient 4 (Figures 44a–44c) demonstrate a successful registration of LRS data acquired on the temporal region of the brain. Unfortunately, there were not enough significant features on the textured surface from the preoperative MR to allow for manually highlighting, and thus the augmented evaluation of the quality of the registrations previously reported was not possible. However, close inspection of the registration results from all three methods shows that the fine features of both surfaces are aligned well where the surfaces interface. That is, where the LRS surface ends in the overlay and the preoperative surface becomes visible. An example set of features available for close inspection from the PBR registration are shown in Figures 44d–44f. These figures examine a particular region of interest in both surfaces after PBR alignment and highlight registered features (i.e. vessels) near the interface of the two surfaces (Figure 44d). As the vessels on the preoperative textured surface come into the area of the LRS dataset, they segue directly into corresponding structures in the LRS dataset (Figures 44e and 44f).

Patient 5's registration results are shown in Figure 45. Figures 45d through 45f show the quality of each registration using manually highlighted features in each textured surface. In

this patient it seems as though ICP registration performed the best at aligning features in each surface. Both PBR and, to a larger extent, SMI misregistered the highlighted vessel by a significant margin.

The results from Patient 6 (Figure 46) show the second case done in the temporal region of the brain. As with the previous temporal region registration (Figure 44), all three registration protocols provided accurate alignment of the preoperative and intraoperative data. Figures 46d through 46f show the accurate SMI alignment of feature interfaces in the overlays of the two surfaces.

Patient 7's registration results are shown in Figure 47. All three registration processes performed similarly on this surface. Close inspection of corresponding features in both surfaces show that the three registration processes accurately registered the two surfaces (Figure 47d–47e).

Patient 8's results (Figure 48) demonstrate the ability to align the feature rich textured surfaces for a demanding dataset. The preoperative dataset was mostly devoid of relevant surface features (i.e. vessel and sulcal patterns) near the surgical FOV. For this patient, it seems as though only the PBR and ICP registration were able register the textured surfaces accurately as evidenced by the accurate alignment of vessel structures on the periphery of the surgical FOV (Figure 48d and 48e). The SMI registration seems to guide the LRS surface towards feature-rich areas on the preoperative surface that are remote to the surgical FOV (Figure 48f).

Discussion

The intraoperative acquisition results from the paper demonstrate the ability of laser-range scanning to be used in an operative environment. The LRS device used in this paper was amenable to various surgical approaches and provided relevant surface data in all cases tested. All intraoperative data acquired by the LRS device resembled, in shape and feature, the surgical FOV examined. Vessel and sulcal patterns evident on the surface of the brain during surgery were adequately captured using the LRS device with minimal impact to the

progress of surgery. In all cases the LRS was able to acquire significant features of the brain surface highlighted by the surgeon in the digital images (see Figures 32, 33, 34, 37, 38, and 39).

Incorporation of the textured LRS dataset to pre-existing imaging modalities such as MR tomograms has been achieved using three registration techniques: standard point-based, iterative closest point, and a novel surface/intensity registration method called SurfaceMI. All three registration methods provided visually compelling results across all patients. PBR generally provided the most consistent alignment of the two textured surfaces. The low mean RMS FRE (having removed the outlier fiducial in Patient 4) provided by PBR registration on all patients (i.e. $3.3 \pm 1.5mm$) demonstrates that corresponding fiducials could be localized and registered accurately in both textured surface sets. This mean RMS FRE is also in close agreement with FRE measurements provided by Nakajima et al. [166] for landmark based registration of the cortical surface. ICP and SMI registration each provided refined registrations relative to PBR for specific cases. ICP registration was very effective in aligning the data acquired for Patients 2 and 5. This result is not surprising given the high degree of corresponding heterogeneous surface geometry in the intraoperative and preoperative data. SMI provided a very accurate registration for Patient 1 as demonstrated by the vessel/sulcal feature agreement in the overlay images shown in Figure 41. An area of concern with the SMI registration is exhibited in the results from Patient 2 (Figure 42), where the alignment is clearly wrong. A local minima in the registration metric may have played a role in this mis-registration. Our previous reports, however, have shown that given an initial alignment via PBR, SMI is capable of refining the accuracy of the registrations consistently in a phantom setting [205] by correctly finding the global optimum for mutual information; in the phantom studies the global optimum occurred when the two clouds were correctly aligned. Given the results from [205] and the gross mis-registration provided by SMI in light of the close initial PBR alignment (Figure 42d) implies that the mutual information between the two clouds may not be globally optimal when the two clouds are correctly aligned. Instead the global optimum for mutual information is achieved when the two clouds are aligned as shown in

Figure 42f, which is incorrect. The reason for this may be related to limited spatial and color resolution of the texture image as compared to the preoperative MR tomogram. An enhancement to the current LRS device that may compensate for the limited resolution would be the incorporation of better camera optics similar to those used in the digital camera used to gather images of the surgical FOV's. Comparing the results of a digital photo of the operative scene compared to a corresponding texture image of the same FOV shows that the texture image does not resolve the FOV as well as the digital image in terms of fine features (Figure 49). Furthermore, the color contrast between the vessels and sulcal grooves has been reduced such that both surface features are approximated by the same color in the LRS texture. These limitations in the texture image may be the reason for the incorrect global optimum for mutual information and the lack of registration accuracy seen in SMI on some of the intraoperative data.

In addition to results presented by each method of registration, the results in Figures 32–48 are also important with respect to the enhancement of anatomical visualization provided by LRS technology. With current approaches to IGS, neurosurgeons often develop a surgical treatment plan by studying the patient's MR tomogram as a segmented reconstructed gray-scale encoded volume rendering. By visualizing the segmented brain in its three-dimensional state with the MR gray-scale providing anatomical landmarks, the surgeon can identify sensitive regions which may be important in the delivery of therapy. For example, gyri that are associated with primary motor, somesthetic, auditory and visual functions can be identified usually on these renderings or with the assistance of cortical stimulation and/or functional magnetic resonance (fMR) imaging. Unfortunately, these regions can often be difficult to recognize intraoperatively due to the lack of landmark recognition within the surgeon's field of view, i.e. the intraoperative presentation of the cortical surface. While overlays of virtual anatomy have been performed on patients using special displays [181, 177], the work presented here is unique in the degree of correspondence provided between the intraoperative three-dimensional cortical surface and the patient2̆019s MR tomogram. One fundamental observation taken Figures 32–39 is that textured LRS data provide an excellent

method to quantitatively record the visual and geometric characteristics of the surgeon's field of view. The functionality of this data is shown in Figures 41–48 in two critical aspects: (1) by quantitatively correlating preoperative cortical surface imaging data (MR, fMR, etc.) to the surgeon's field of view through the process of registration, and (2) by providing new anatomical cues to the surgeon during surgery that can assist in navigation. Although research is still needed to make the technology completely compatible with today's ORs, the visual assistance provided by textured LRS technology is evident and warrants continued consideration as essential equipment for neuro-navigation.

An extension to the current scanning protocol and visualization system currently being explored is the determination of brain surface shift during surgery. Serial acquisitions of the brain surface during surgery, if registered, can be used to determine the motion of the surface over the course of surgery. When used as a feedback system for current image-guided surgery systems, the calculated shift can be used to update position of navigational aids with respect to brain shift. We are currently developing and validating a shift-tracking protocol using the LRS in the OR. At the same time we are taking steps towards a quantitative validation of the registration methods described in this paper on intraoperative LRS acquisitions.

Conclusion

This paper describes the use of a laser range scanning device in the OR during surgery within an exploratory framework. The data acquired by the scanner is shown within a custom-built visualization platform specifically designed for this new mode of intraoperative surface imaging. The methods required to deploy and use the scanner in the OR are described and used to collect patient data from 8 cases that involved varying surgical presentations. In all cases, the scanner successfully recorded three-dimensional textured point cloud data of the patient's intraoperative cortical surface. A series of registration methods were utilized to provide correspondence between preoperative MR tomograms and the patient's scanned cortical surface. The registration results were then assessed visually by observing the continuance of feature (e.g. vessels, sulcal patterns, etc.) within the overlays. The reported

displays illustrate compelling quantitative relationships between the exposed intraoperative brain surface and the preoperative grayscale-encoded tomogram volume. More importantly, this preliminary study suggests that LRS is an excellent candidate technology to merge the extensive preoperative planning capabilities available to surgeons with the practical aspects of applying surgical therapy in their ORs.

Acknowledgments

The authors would like to thank Dr. Matthew Pearson, Dr. Daniel Oberer, Ms. Terri Harrel and the operating room support staff for their help in data collection.

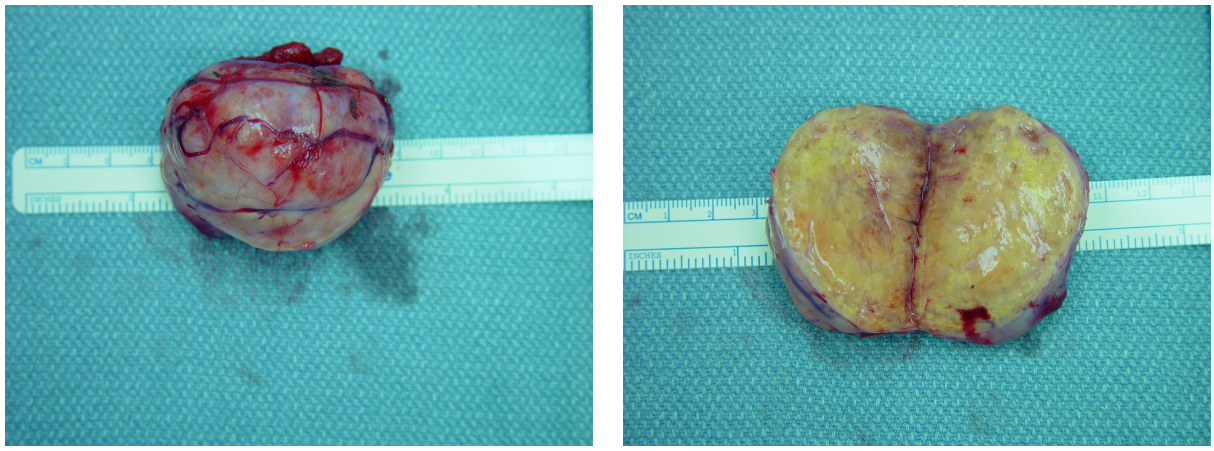

40(a) 40(b)

Figure 40: Tumor data for Patient 8. From left to right, the tumor from Patient 8 displayed as-is after removal; the tumor sliced open to display the internal structure of the excised lesion. The whole tumor measured approximately $6cm$ in diameter.

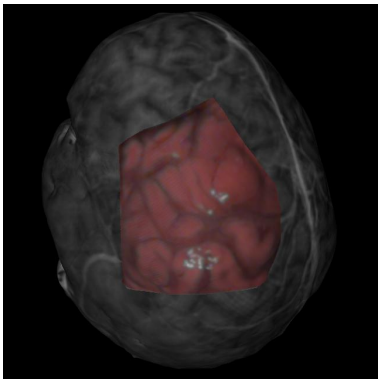

41(a) PBR Registration

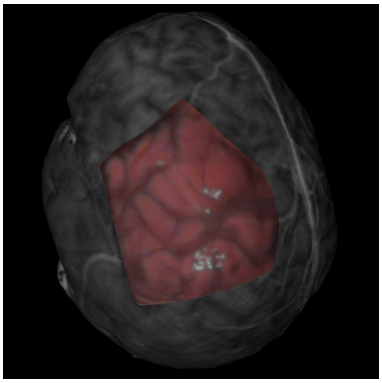

41(b) ICP Registration

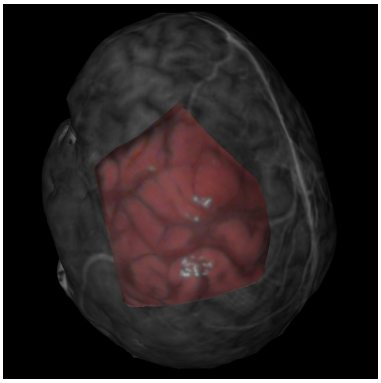

41(c) SMI Registration

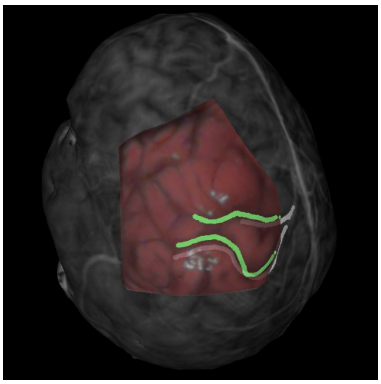

41(d) Augmented Visualization for PBR Registration

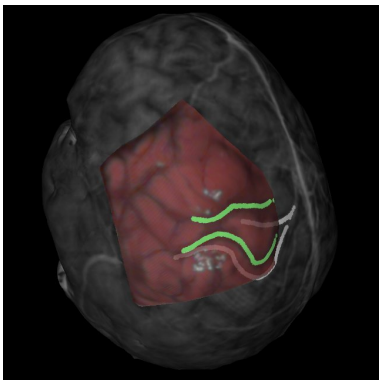

41(e) Augmented Visualization for ICP Registration

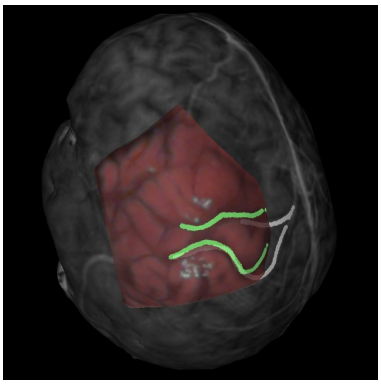

41(f) Augmented Visualization for SMI Registration

Figure 41: Registration results for Patient 1. The top row, from left to right, shows registration results for: PBR, ICP and SMI registrations. The bottom row shows corresponding registrations with manually highlighted vessel and sulcal features for comparison.

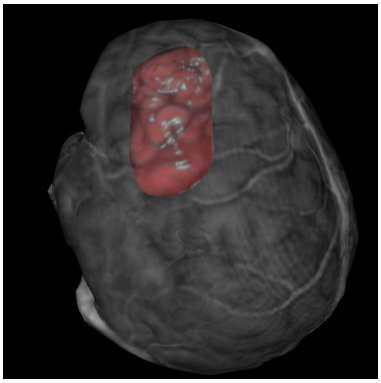

42(a) PBR Registration

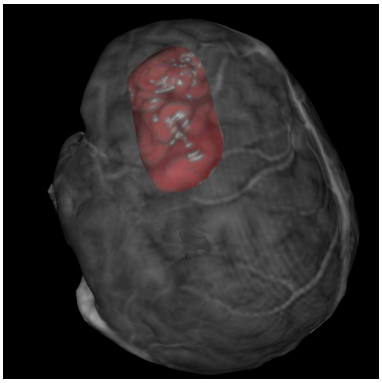

42(b) ICP Registration

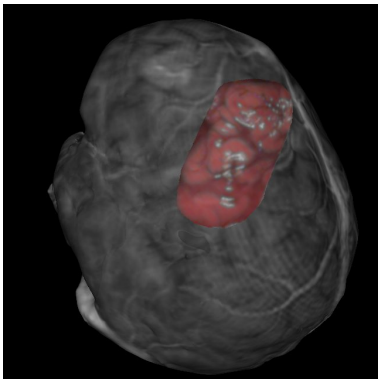

42(c) SMI Registration

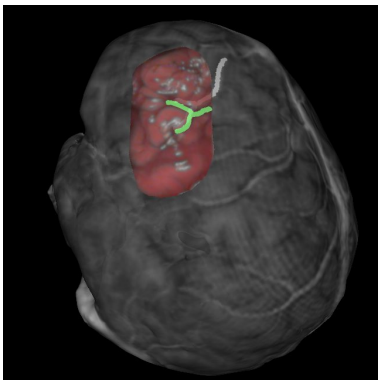

42(d) Augmented Visualization for PBR Registration

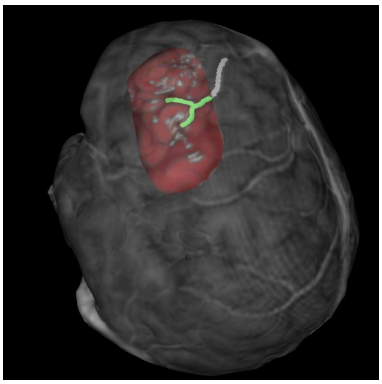

42(e) Augmented Visualization for ICP Registration

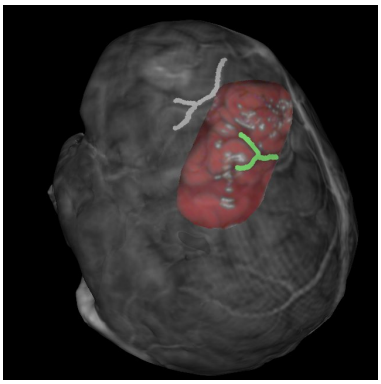

42(f) Augmented Visualization for SMI Registration

Figure 42: Registration results for Patient 2. The top row, from left to right, shows registration results for: PBR, ICP and SMI registrations. The bottom row shows corresponding registration results with a significant vessel in the FOV highlighted in both textured surfaces.

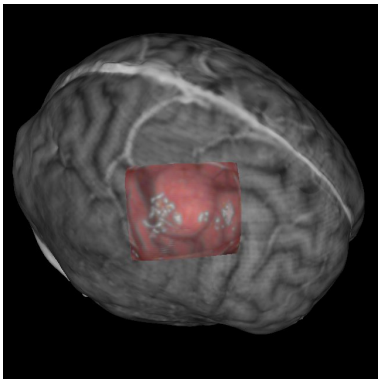

43(a) PBR Registration

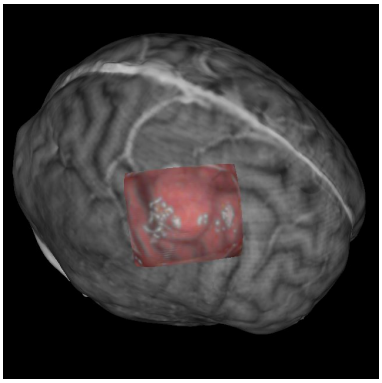

43(b) ICP Registration

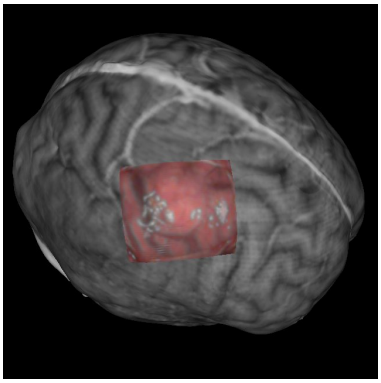

43(c) SMI Registration

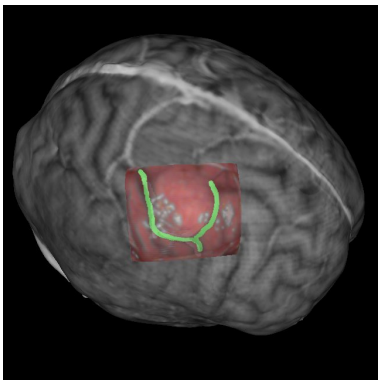

43(d) Augmented Visualization for PBR Registration

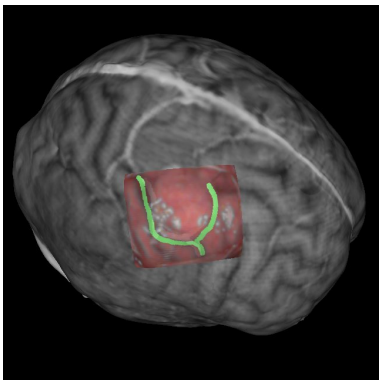

43(e) Augmented Visualization for ICP Registration

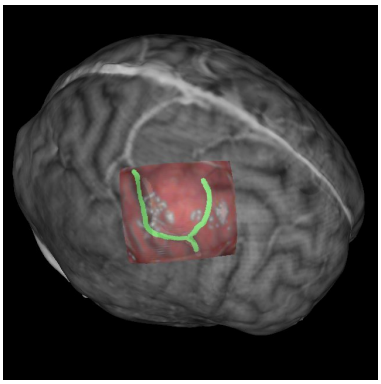

43(f) Augmented Visualization for SMI Registration

Figure 43: Registration results for Patient 3. The top row, from left to right, shows registration results for: PBR, ICP and SMI registrations. The bottom row shows corresponding registration results with a significant vessel in the FOV highlighted in both textured surfaces.

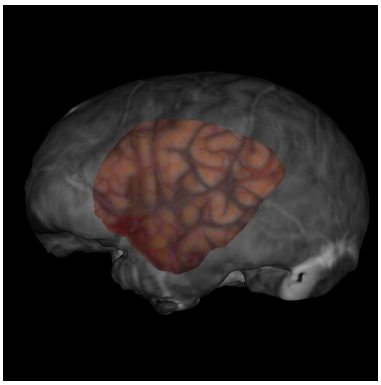

44(a) PBR Registration

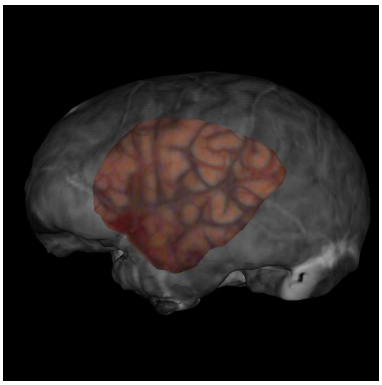

44(b) ICP Registration

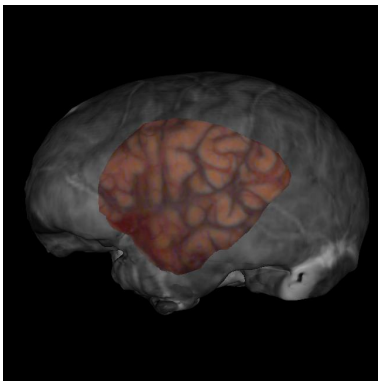

44(c) SMI Registration

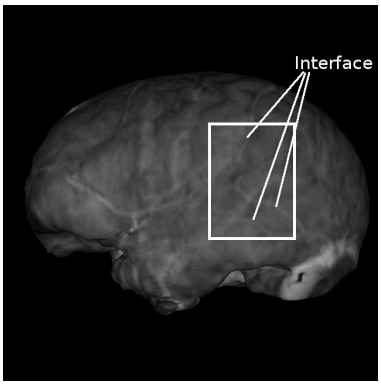

44(d) Region of Interest with Features Highlighted

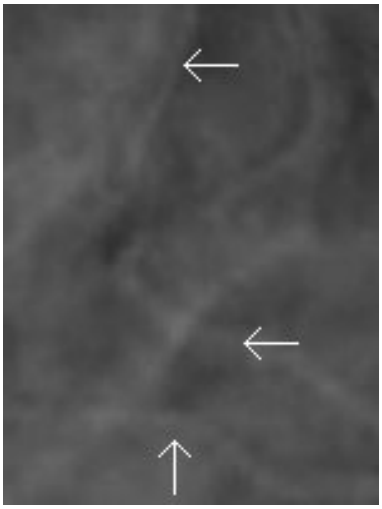

44(e) Zoomed Region of Interest without LRS Textured Surface

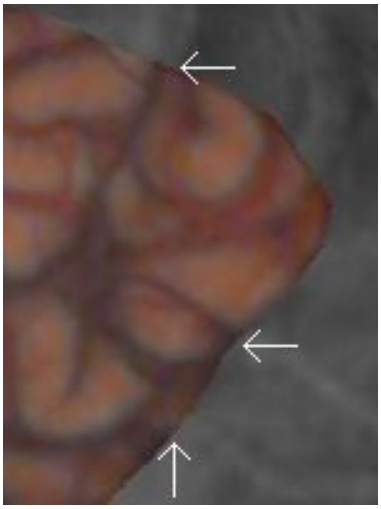

44(f) Zoomed Region of Interest with LRS Textured Surface

Figure 44: Registration results for Patient 4. The top row, from left to right, shows registration results for: PBR, ICP and SMI registrations. The bottom row shows feature interfaces between the two textured surfaces which show the accuracy of the PBR registration, from left to right: region of interest with interface points highlighted, preoperative textured surface with interface points highlighted, overlay of the textured LRS surface and preoperative surface with interface points highlighted.

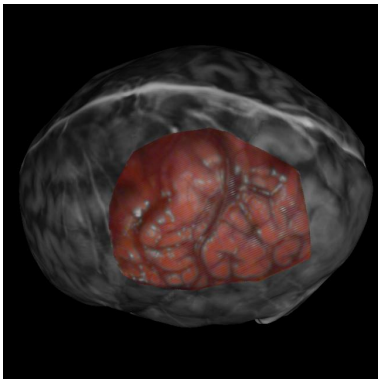

45(a) PBR Registration

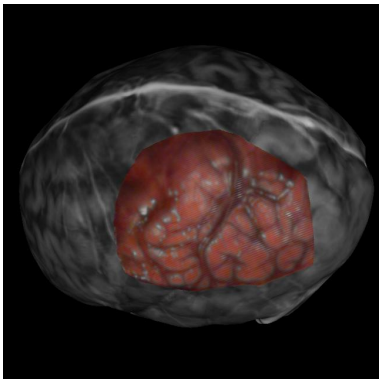

45(b) ICP Registration

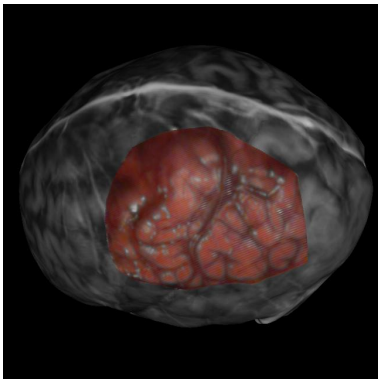

45(c) SMI Registration

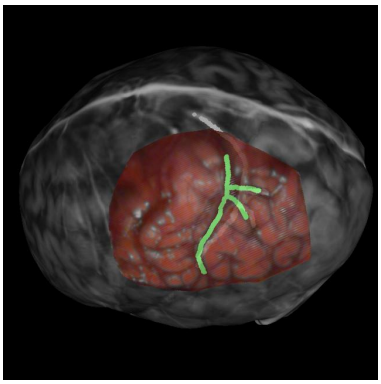

45(d) Augmented Visualization for PBR Registration

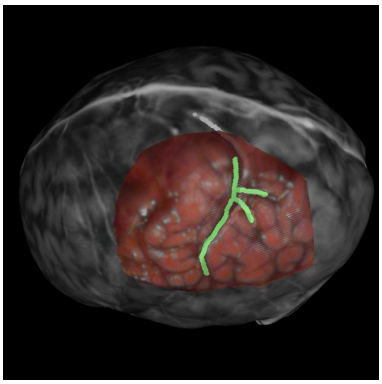

45(e) Augmented Visualization for ICP Registration

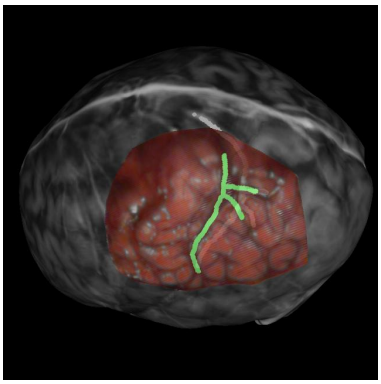

45(f) Augmented Visualization for SMI Registration

Figure 45: Registration results for Patient 5. The top row, from left to right, shows registration results for: PBR, ICP and SMI registrations. The bottom row shows corresponding registration results with a significant vessel in the FOV highlighted in both textured surfaces.

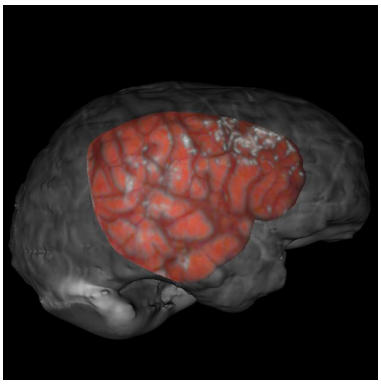

46(a) PBR Registration

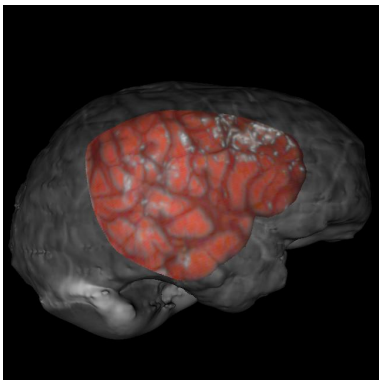

46(b) ICP Registration

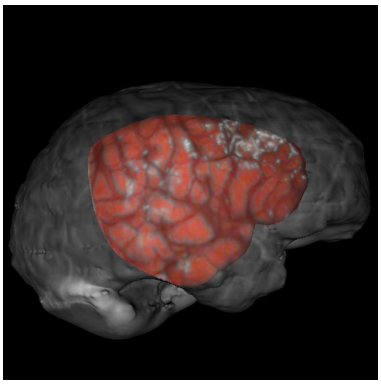

46(c) SMI Registration

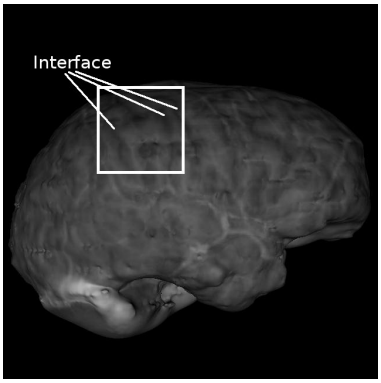

46(d) Region of Interest with Features Highlighted

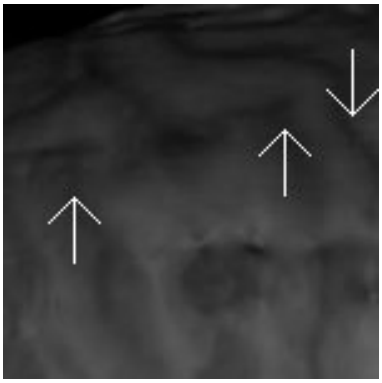

46(e) Zoomed Region of Interest without LRS Textured Surface

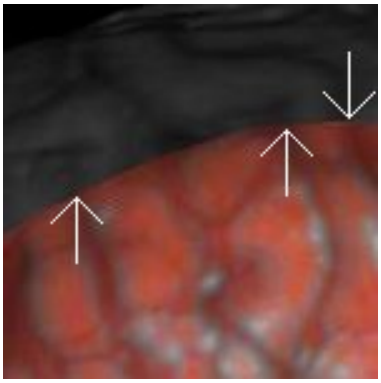

46(f) Zoomed Region of Interest with LRS Textured Surface

Figure 46: Registration results for Patient 6. The top row, from left to right, shows registration results for: PBR, ICP and SMI registrations. The bottom row shows feature interfaces between the two textured surfaces which show the accuracy of the SMI registration, from left to right: region of interest with interface points highlighted, preoperative textured surface with interface points highlighted, overlay of the textured LRS and preoperative surface with interface points highlighted.

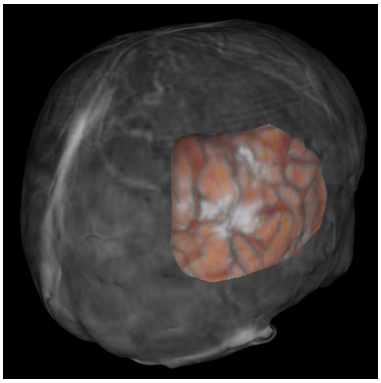

47(a) PBR Registration

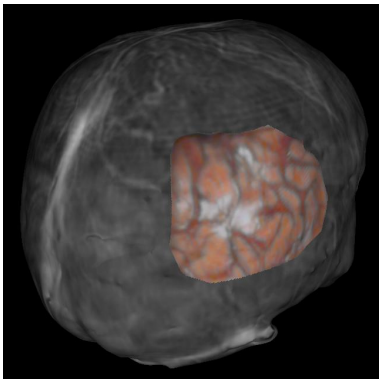

47(b) ICP Registration

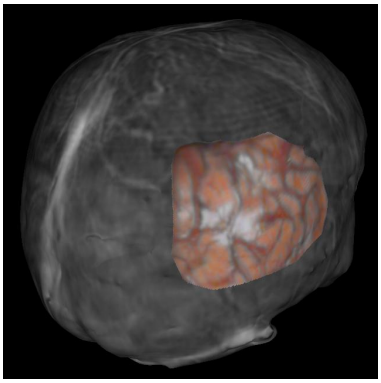

47(c) SMI Registration

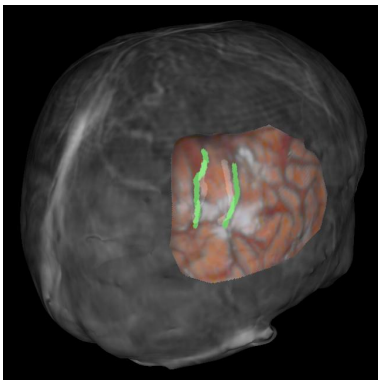

47(d) Augmented Visualization for PBR Registration

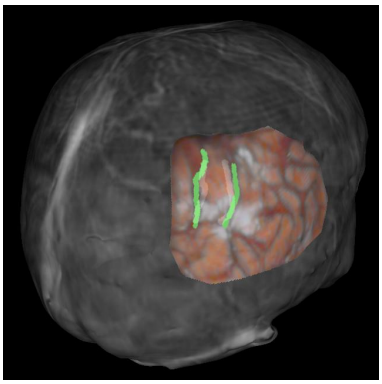

47(e) Augmented Visualization for ICP Registration

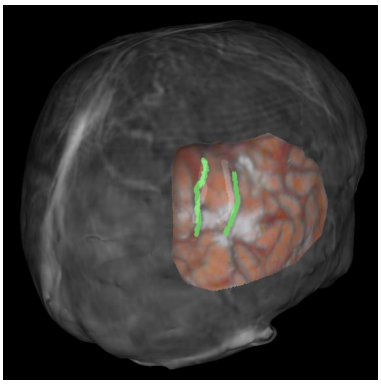

47(f) Augmented Visualization for SMI Registration

Figure 47: Registration results for Patient 7. The top row, from left to right, shows registration results for: PBR, ICP and SMI registrations. The bottom row shows corresponding registration results with significant vessels in the FOV highlighted in both textured surfaces.

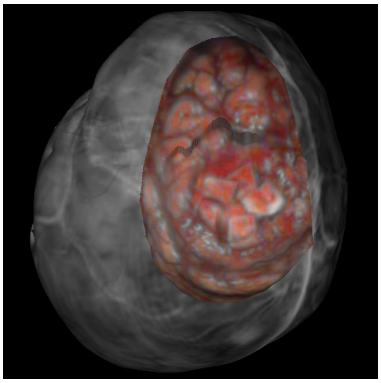

48(a) PBR Registration

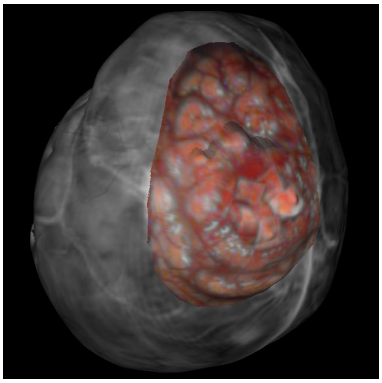

48(b) ICP Registration

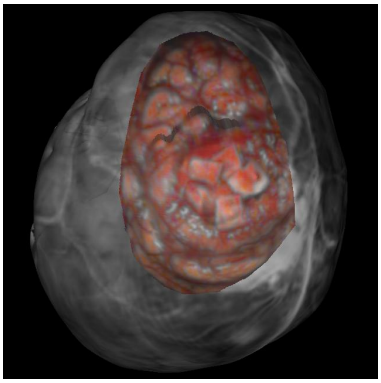

48(c) SMI Registration

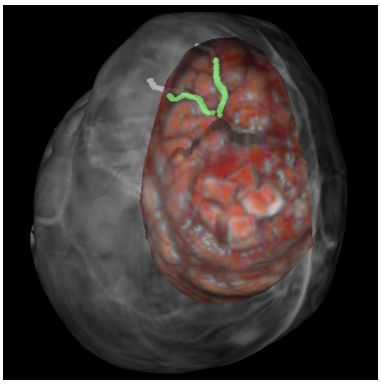

48(d) Augmented Visualization for PBR Registration

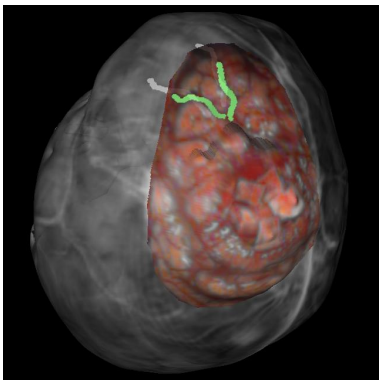

48(e) Augmented Visualization for ICP Registration

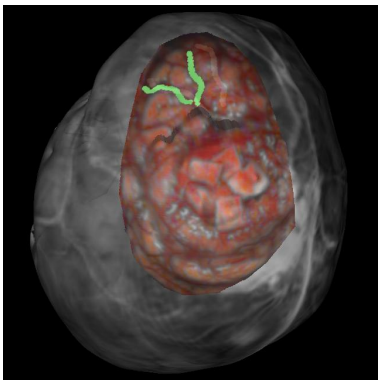

48(f) Augmented Visualization for SMI Registration

Figure 48: Registration results for Patient 8. The top row, from left to right, shows registration results for: PBR, ICP and SMI registrations. The bottom row shows corresponding registration results with significant vessels in the FOV highlighted in both textured surfaces.

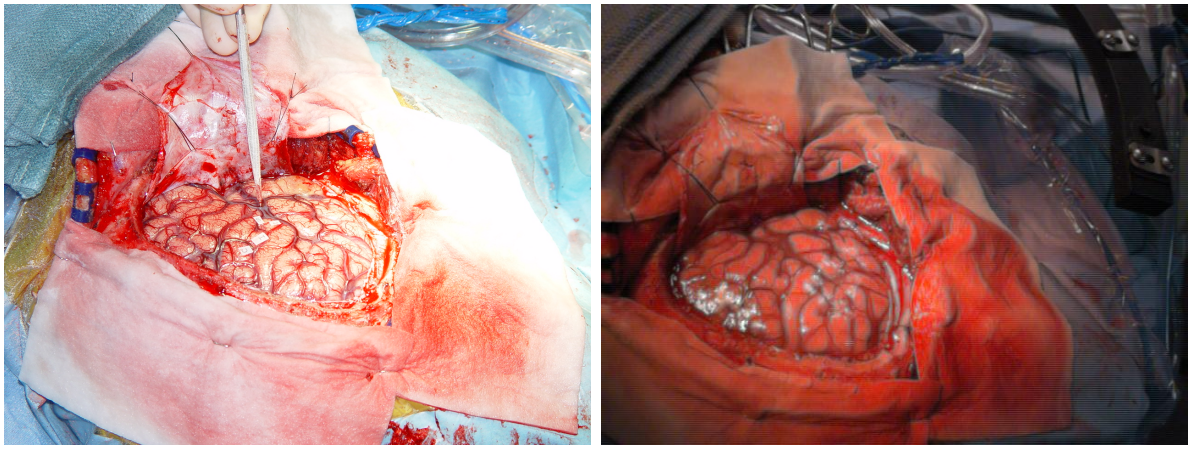

Figure 49: Comparison of the digital image quality versus texture image quality provided by the LRS device. On the left is a high-resolution digital image of the surgical FOV, on the left is a texture image of the same FOV. Notice the lack of resolution in the texture image of the surgical FOV. Specifically, fine vessels present in the digital image are masked in the texture image.

CHAPTER VI

MANUSCRIPT 4 - CORTICAL SHIFT TRACKING USING A LASER-RANGE SCANNER AND DEFORMABLE REGISTRATION METHODS

Original form of manuscript appears in LNCS: Medical Image Computing and Computer Assisted Intervention: 2003, 2879: 166-174, 2003.

Abstract

A novel brain shift tracking protocol is introduced in this paper which utilizes laser range scan (LRS) data and 2D deformable image registration. This protocol builds on previous efforts to incorporate intra-operative LRS data into a model-updated image guided surgery paradigm for brain shift compensation. The shift tracking method employs the use of a LRS system capable of capturing textures of the intra-operative scene during range data acquisition. Textures from serial range images are then registered using a 2D deformable registration approach that uses local support radial basis functions and mutual information. Given the deformation field provided by the registration, 3D points in serial LRS datasets can then be tracked. Results from this paper indicate that the error associated with tracking brain movement is $1.1mm$ on average given brain shifts of approximately $20.5mm$. Equally important, a strategy is presented to rapidly acquire intra-operative measurements of shift which are compatible with model-based strategies for brain deformation compensation.

Introduction

Current image guided procedures (IGP) proceed with a rigid registration of the patient to their patient-specific pre-operative image sets using fiducials. Recent literature has shown that this protocol for IGP may lead to inaccuracies related to the shifting of the brain during surgery [38]. As a result, there is substantial rationale in current IGP research to measure, track, and compensate for brain shift.

There are two emergent compensation strategies for the brain shift problem in IGP. The first strategy is to use intra-operative imaging during surgery to capture and account for brain shift. Modalities such as intra-operative CT, intra-operative MR and intra-operative US have been, or are being, investigated as image-based compensation strategies [52, 71, 113]. However, unique challenges in each of these modalities have limited their widespread adoption as the *de facto* brain shift compensation strategy.

An alternative strategy to compensate for brain shift is to use computational models and sparse intra-operative data to correct for deformation during surgery [115]. In this paradigm, a physical or statistical model of brain shift is driven with sparse data (i.e. data with limited intra-operative extent or information) to accurately deform pre-operative images to their intra-operative position. By definition, this method has the advantage of incorporating all forms of spatially-encoded pre-operative data (positron emission tomography, functional MR, etc.). This is not the case with intra-operative imaging methods which only provide data associated with the particular imaging modality (MR, CT or US,). Furthermore, computational methods for shift compensation are effective [125] and have minimal logistical constraints for intra-operative use. For successful deployment of a model-based shift compensation strategy, some quantitative information regarding brain deformation is necessary to constrain model calculations. Many intra-operative data acquisition devices exist for this purpose [200][40][206], however, in this paper laser-range scanning is used as the data acquisition system. Laser range scanning provides a relatively inexpensive, time-efficient, non-contact method of surface data acquisition.

Once the intra-operative data has been acquired, an effective method of incorporating this data into the computational model must be developed. In previous reports [192], a rigid registration approach was developed to align the intra-operative range scan data to pre-operative image-sets. In this paper, a deformable registration extension is explored to allow for shift tracking based on serial laser-range scan data. The deformable registration is provided by local support radial basis functions [207] and mutual information optimization [168]. Once calculated, the deformation field allows for easy calculation of surface shift in

serial range scans. The result of this shift tracking can then be used as driving conditions within a computational framework for model-updated image guided neurosurgery.

Methods

For range data acquisition, a laser-range scanning device is used (RealScan3D USB, 3D Digital Corp, Bethel, CT, USA). The scanner (Figure 50) is mounted on a vibration-damped monopod that is brought into and out of the surgical field-of-view (SFOV) manually. A thorough discussion of the range scanner can be found in [205]. After dural opening, the monopod and scanner are brought into the SFOV and the laser scanning extents (left and right margins) are calibrated to cover the width of the craniotomy. A laser stripe is then passed over the brain's surface and range data is collected using the principle of optical triangulation. After acquisition, the scanner and monopod are moved out of the SFOV. The entire data acquisition process adds approximately 1.5 minutes per scan to the operating time and has been approved for clinical use by the Vanderbilt University IRB (VUIRB).

A unique feature of the scanner is that it reports texture map coordinates that allow for intensity values to be assigned to the range points. For this process, an RGB bitmap is captured at the time of scanning. Texture map coordinates are generated given a manufacturer calibration of range space to texture space. The coordinates can then be used to generate textured point clouds of the SFOV. An example SFOV with its corresponding textured LRS data is shown in Figure 51.

For the shift tracking algorithm, serial LRS datasets are registered to each other via deformable 2D image registration. The registration process occurs entirely in texture space. Textures from serial range scans are, first, rigidly registered using mutual information methods that optimize a rigid 2D transformation. Local support radial basis functions are then used to register the images in a deformable fashion that optimizes the mutual information between the two textures. Furthermore, each LRS acquisition acquires a unique depth map associated with each texture; hence, the non-rigid registration of the texture images provides correspondence between these two unique depth maps and ultimately results in a distinct

Figure 50: Laser range scanner mounted on vibration damping monopod in OR.

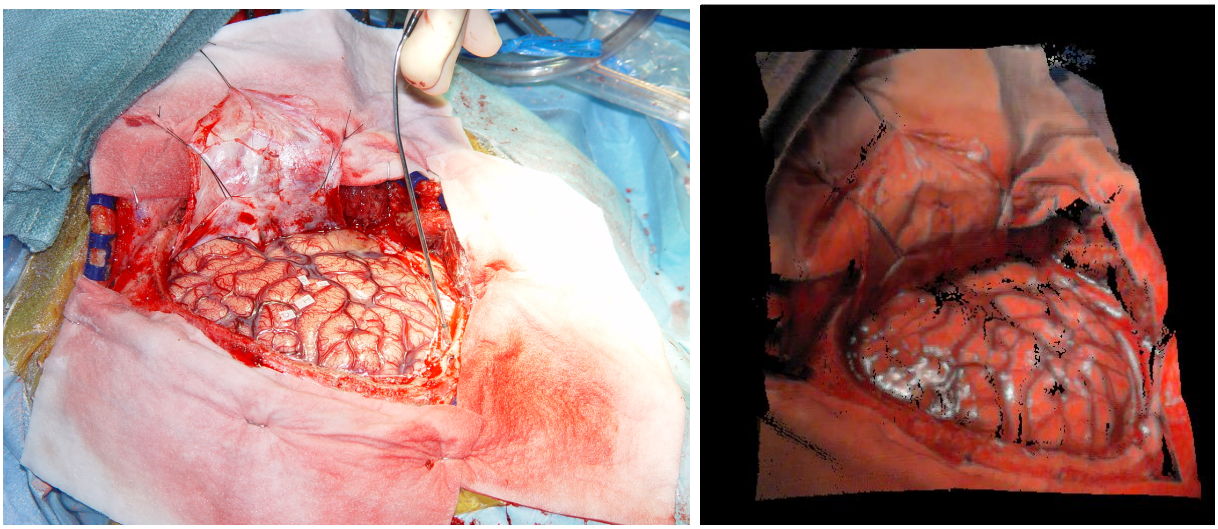

Figure 51: A digital photograph is shown on the left with the corresponding textured range scan data on the right.

three-dimensional trajectory for each point.

Once the deformation field between the two textures is known, shift between serial LRS datasets can be calculated. For this process, a target point is selected in one of the two serial datasets, and is transformed into texture space using its texture coordinates (Figure 52(a)). The transformed point is then deformed into the second texture space (Figure 52(b & c)) and projected back into the 3D space of the second LRS dataset, 52(d). Using this method, the motion of a point, in a single LRS dataset can be tracked in three dimensions through serial LRS datasets.

In this paper, we demonstrate the shift tracking protocol in a phantom experiment and on a single *in vivo* case. A silicon impression of a cortical surface mold, with the sulcal grooves artificially highlighted (see Figure 53), was used as the scanning phantom. The phantom was scanned three times (in three different poses) while in a deformation apparatus: undeformed, compression applied to one side, and compression applied to both sides. For each pose, physical-space locations for surface landmarks were acquired using an OPTOTRAK 3020 (Northern Digital Inc, www.ndigital.com) localization system. Deformation magnitudes were calculated for corresponding landmarks between the undeformed pose and each deformed pose. Similar magnitudes for the same points were calculated in LRS-space by the automated shift tracking protocol. Absolute magnitude differences between physical-space and LRS-space were calculated as a measure of shift-tracking accuracy relative to the "ground-truth" shift observed in physical-space.

The *in vivo* case was provided by a consenting patient undergoing cortical resection therapy and acquired according to the guidelines of the VUIRB approved acquisition procedure. To test the accuracy of the shift tracking protocol in the *in vivo* case, corresponding points in the source and target LRS data were selected manually.[1] The source landmarks (see Figure 54) were then registered to the target cloud as per the shift tracking protocol. Shift tracking error (STE) was calculated as the residual distance between the manually selected position

[1]The tracked points were localized three times for each LRS dataset and averaged to minimize uniform noise in the localization.

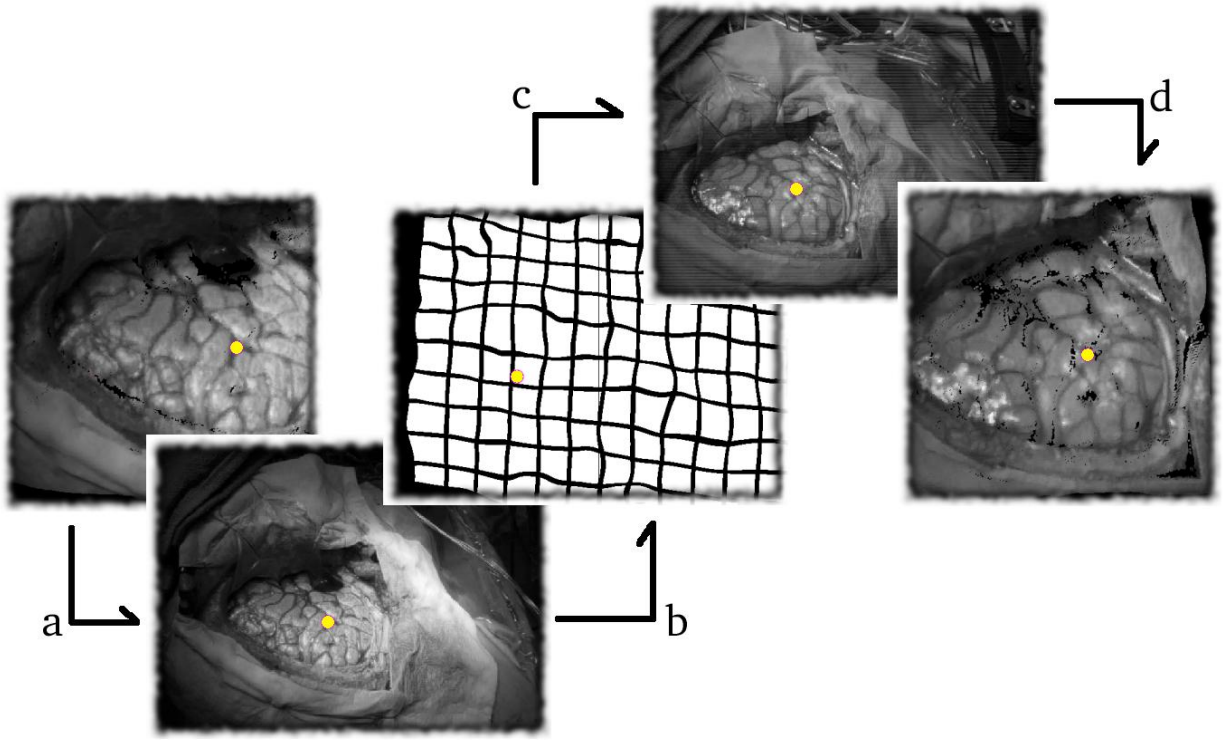

Figure 52: A schematic outlining the deformable registration process. The point of interest is shown transformed into its texture space in (a). The same point shown deformable transformed into a serial texture space in (b) and (c). Finally, the point is projected back into the three dimensional space of the second LRS dataset in (d).

of the landmarks in target cloud space and the registered position, i.e. Equation 4.

$$STE = ||x_j - T(y_j)||_2 \tag{4}$$

where, STE is the shift tracking error, x_j is a manually localized point in the target LRS data, and $T(y_j)$ is the corresponding point in source LRS data *deformably* transformed into target cloud space. STEs for the targets are reported in this paper along with the mean STE for all points.

Results

Figure 55 shows an example result of the deformable registration on the phantom. The numerical data associated with the correlation study between shift in LRS-space and physical-space are listed in Table 5. In registering both deformed poses to the undeformed pose, the calculated shift was not statistically different when compared to the shift observed in physical-space (unpaired t-test, equal variances: $p(T \leq t) = 0.55$ and $p(T \leq t) = 0.68$ for the one- and two-sided compressions, respectively). The tracking efficiencies, as defined by Equation 5, were 92.52 % and 92.22 % for the one- and two-sided compressions, respectively.

$$TE = \frac{\overline{d_{exp}} - \overline{\epsilon}}{\overline{d_{exp}}} \tag{5}$$

where TE is the tracking efficiency, $\overline{d_{exp}}$ is the mean value of the initial deformation, and $\overline{\epsilon}$ is the mean error between experimental displacement and the displacement provided by the shift-tracking protocol (values can be found in the last row of Table 5).

The numerical data corresponding to the landmark tracking experiment for the *in vivo* case are given in Table 6. The STE and initial deformation for this case are significantly different ($p(T \leq t) < 0.05$).

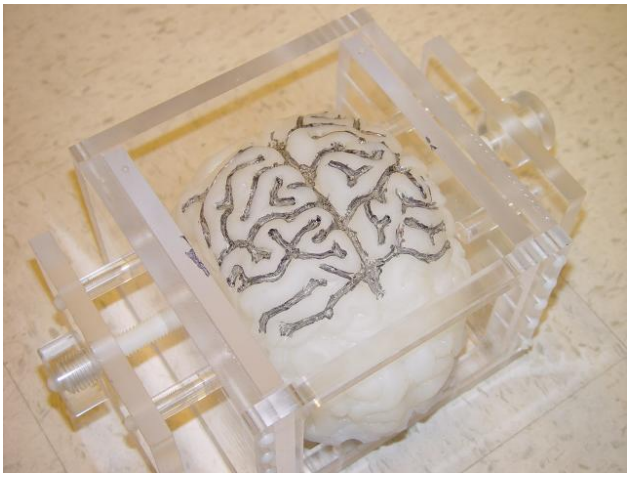

Figure 53: Silicon phantom and deformation chamber used for validation studies.

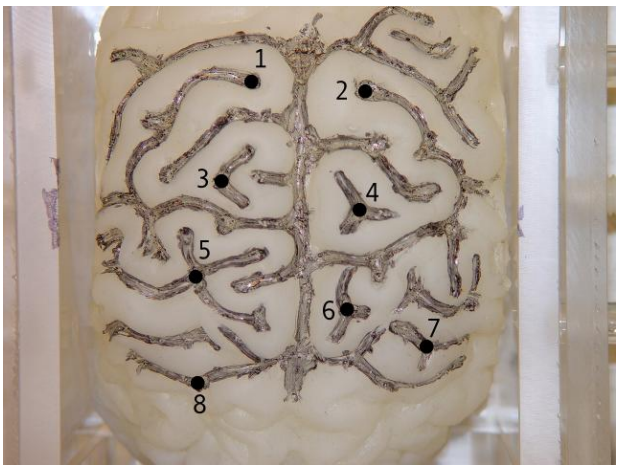

54(a) Source cloud target landmarks

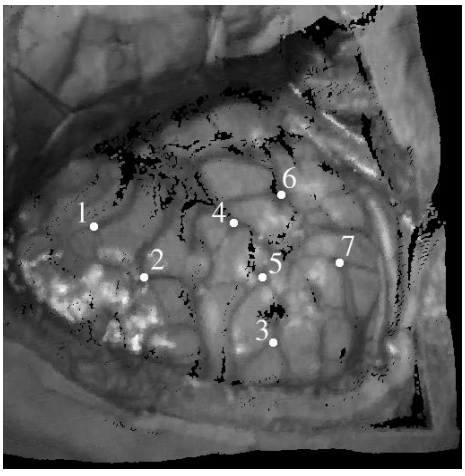

54(b) Target cloud target landmarks

Figure 54: Landmarks used in the phantom and *in vivo* cloud for shift tracking error assessment.

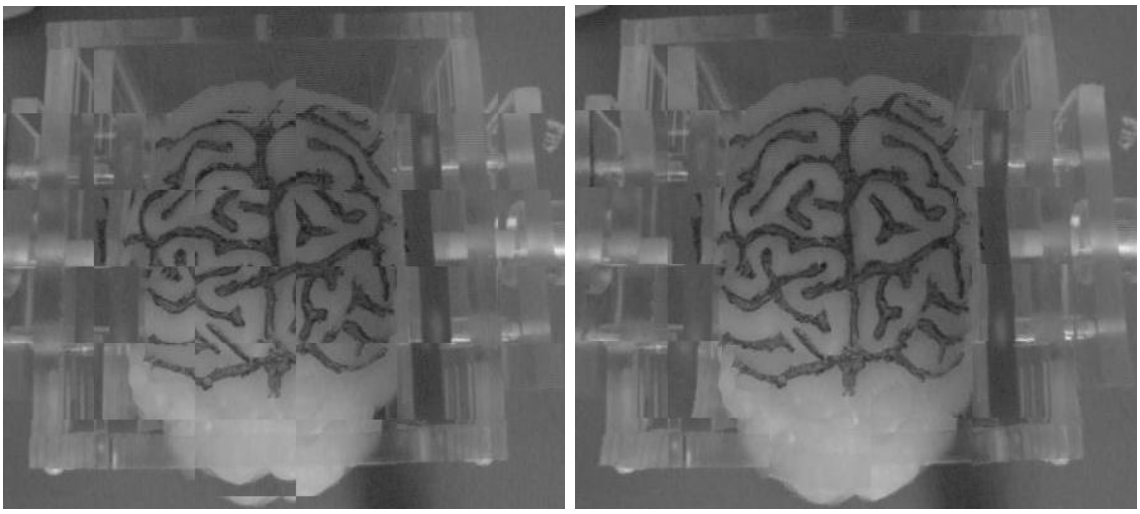

Figure 55: Example deformable registration results using the phantom textures. The results are presented using checkerboard images of the pre-registered (left) and post-registered (right) views.

Table 5: Phantom shift tracking experiment results. ϵ represents the difference in magnitudes of shift observed in physical-space and shift calculated via the shift-tracking protocol. Initial deformation magnitudes (d_{exp}) are reported from the physical-space measurements provided by the OPTOTRAK system.

	One-sided compression		Two-sided compression	
Landmark #	d_{exp} (mm)	ϵ (mm)	d_{exp} (mm)	ϵ (mm)
1	9.11	1.61	7.64	0.91
2	6.87	0.11	5.81	1.06
3	8.35	0.08	7.65	0.65
4	6.43	0.08	6.06	0.83
5	9.63	1.10	7.91	0.07
6	6.96	0.56	6.87	0.51
7	8.44	0.97	6.02	0.10
8	10.43	0.31	7.48	0.27
Mean±SD	8.03±1.58	0.60±0.57	7.07±1.27	0.55±0.38

Discussion

For both phantom and *in vivo* experiments, the results show that the shift tracking protocol outlined in this paper can effectively characterize landmark motion through serial LRS datasets. In the phantom experiments, the controlled data acquisition and comparison to independent measurements provided by the OPTOTRAK system provides insight into the method's ability to account for pure deformation (i.e. scanner was stationary during all acquisitions). Furthermore, the statistical analysis (t-test) results, imply that the shifts calculated algorithmically obey shift characteristics observed physically.

In the *in vivo* case, the results demonstrate that the shift-tracking protocol can measure large scale shifts on clinical data. Additionally, a distinct strength to the approach was the ability to register large scale rigid-body motion. Specifically, the results reflected in Table 6 demonstrate effective shift tracking in the midst of large positional changes in the camera (since the magnitudes of shift in Table 6 reflect rigid body motions of the camera as well as deformations of the brain surface). Although, the delineation of deformation from rigid body motion cannot be made in this clinical case (i.e. the scanner was not tracked in physical-space), the results do indicate feasibility of this approach on clinical data. This claim is supported by the low mean and standard deviations seen in the STE's of the *in vivo* case.

Conclusions

The methods and results of this paper outline a novel and efficient method for cortical shift tracking that is amenable to a model-based approach to shift compensation. The deformable registration approach allows for the tracking of manually localized points on the brain surface using 2D deformable registration techniques and intra-operative SFOV textures. The viability of the LRS as an intra-operative data acquisition device is enhanced given the preliminary shift tracking results presented in this paper. Future work regarding the methods outlined in this paper include more validation studies on phantoms and *in vivo* datasets. Nonetheless, the results presented within this paper provide a critical step in the

development of model-based methods for correcting brain deformations within IGS.

Acknowledgements

Financial support provided by the Vanderbilt Discovery Grant program.

Table 6: Shift tracking errors for the *in vivo* case. d_{exp} represents the shift calculated by manually localizing corresponding points in each the serial LRS datasets. The shift tracking error (as defined by Eq. 4) represents the difference in localized position to registered position.

Landmarks #	d_{exp} (mm)	STE (mm)
1	21.94	0.53
2	20.28	1.69
3	18.14	1.03
4	22.76	1.41
5	18.85	1.06
6	22.33	1.27
7	19.35	0.51
Mean±SD	20.524±1.84	1.07±0.44

CHAPTER VII

MANUSCRIPT 5 - A METHOD TO TRACK CORTICAL SURFACE DEFORMATIONS USING A LASER RANGE SCANNER

Abstract

This paper reports a novel method to track brain shift using a laser-range scanner (LRS) and non-rigid registration methods. The laser-range scanner used in this paper is capable of generating textured point-clouds describing the surface geometry/intensity pattern of the brain as presented during cranial surgery. Using serial LRS acquisitions of the brain's surface and 2D non-rigid image registration techniques, we developed a method to track surface motion during neurosurgical procedures. A series of experiments devised to evaluate the performance of the shift-tracking protocol are reported. The results demonstrate that the surface shift tracking protocol is capable of resolving shift to an accuracy of approximately $1.6mm$ given initial shifts on the order of $15mm$ in a phantom setting. For *in vivo* data, the protocol was able to reconstruct brain shift with an accuracy of $1.6mm$. The results suggest that a LRS is an effective tool for tracking brain surface shift during neurosurgery.

Introduction

An active area of research in image-guided neurosurgery is the determination and compensation of brain shift during surgery. Reports have indicated that the brain is capable of deforming during surgery for a variety of reasons, including pharmacologic responses, gravity, edema, and pathology[44, 81, 46]. Studies examining the extent of deformation during surgery indicate that the brain can shift a centimeter or more and in a non-uniform fashion throughout the brain [43].

The non-rigid motion of the brain during surgery compromises the rigid-body assumptions of existing image-guided surgery systems and may reduce navigational accuracy. In an effort to provide consistent intra-operative tracking information, researchers have explored

computational methods of shift compensation for surgery, also called model-updated image guided surgery (MUIGS)[126, 117, 131, 133, 134, 186, 208]. Typical MUIGS systems use a patient-specific pre-operative model of the brain. During surgery, this model is used to deform the patient's pre-operative image to provide a consistent mapping between the phyiscal-space of the OR and image-space. Invariably, a critical component of any MUIGS system is the accurate characterization of sparse[1] intra-operative data that drives and constrains the patient-specific model. Possible sources of such data include intra-operative imaging (such as intra-operative ultrasound and intra-operative MR), tracked surgical probes, and surface acquisition methods (such as photogrammetry and laser-range scanning). Regardless of the method of acquisition, incorrect measurement of intra-operative sparse-data will generate inaccurate boundary conditions for the patient-specific computer model. As a result, the MUIGS approach to brain shift compensation could be compromised and lead to surgical navigation error. Therefore, it is critical to any MUIGS system that the method for intra-operative sparse-data acquisition be efficient and accurate.

Previous efforts have been made to characterize intra-operative brain position for shift measurement. An early method of shift assesment and correction was described by Kelly et al in 1986 [16]. In that report, $5mm$ stainless steel balls were used in conjuction with projection radiographs to determine brain shift during surgery. All measurements and corrections in that paper were based on the qualitative assesment of the surgeon. Subsequent reports have demonstrated quantitative measurements of brain tissue location using framed and frameless stereotaxy. Nauta et al. used a framed stereotaxy system to track the motion of the brain and concluded that the brain tissue near the surgical area can move approximately $5mm$ [38]. Dorward et al. used frameless stereotaxy to track both surface and deep tissue deformation of the brain and observed movements on the order of a centimeter near tumor margins in resection surgeries [41]. More recently, researchers have made whole-brain measurements of shift using intraoperative-MR systems [81, 46, 43] and have confirmed earlier findings regarding the degree of brain deformations during surgery. While these reports quantify the

[1]Sparse data is defined as data with limited information or extent within the surgical environment.

amount of shift, strategies to measure brain shift in real-time for surgical feedback have not been as forthcoming.

In previous work [205], textured laser range scanning (LRS), or a LRS system that generates three-dimensional intensity-encoded point cloud data, was shown to be an effective way to characterize the geometry and intensity properties of the intra-operative brain surface. A series of phantom and *in vivo* experiments investigated a novel, multi-modal, image-to-patient rigid registration framework that used both brain surface geometry and intensity derived from LRS and magnetic resonance (MR) data. When compared to point-based and iterative closest point registration methods, textured LRS registration results demonstrated an improved accuracy with phantom and *in vivo* experiments. Similar to the work of Audette et al. [165], this work asserts that the brain surface during surgery can be used as a reference for registration. However, unlike others, the framework being developed here takes advantage of both geometric and visual/intensity information available on the brain surface during surgery.

In the work presented here, the use of LRS within neurosurgery is extended to include a novel method to accurately measure intra-operative brain surface shift in an automatic and rapid fashion. Specifically, the paper builds on previous work by employing a non-rigid registration method to provide correspondence between deformed serial textured-LRS data. Although the data acquired by the LRS system is a two-step process (i.e. scanning and texture mapping of a 2D image of the field of view), the data can generate intensity-encoded point clouds that may be integrated with recent work investigating non-rigid point registration methods. Reports have demonstrated effective registration algorithms that provide non-rigid correspondence in featured point clouds using shape and other geometric attributes [209, 210, 130, 211, 152]. Although these approaches may be a viable avenue for accomplishing brain-shift tracking, an alternative strategy has been explored within this work that is particularly appropriate for the unique texture-mapping capability provided by the LRS system.

Detailed phantom studies and preliminary *in vivo* work has been performed using data

generated by LRS. An optical tracking system was used in the phantom studies to provide an independent reference measurement system, to which results from the shift-tracking protocol were compared. In the *in vivo* case, the intra-operative brain shift of a single patient was approximated using the shift-tracking protocol and compared to manually determined reference measurements.

Methods

Laser Range Scanning

The LRS device used in this paper is a commercially available system (RealScanUSB 200, 3DDigital Inc., Bethel, CT), as shown in Figure 56. The LRS device is capable of generating point clouds with an accuracy of $0.3mm$ at a distance of $30cm$ from the scanned object, with a resolution of approximately $0.5mm$. For intra-operative scanning, the LRS device is capable of acquiring surface clouds with 40,000 to 50,000 points in the area of the craniotomy within approximately 10 seconds, while requiring an intra-operative footprint of approximately $0.1m^2$. A detailed look at the LRS device and its scanning characteristics can be found in [201], [172] and [205].

To obtain absolute measurements of shift and shift-tracking error, the scanner was modified by the attachment of 12 infra-red light emitting diode (IRED) markers, as shown in Figure 56. This arrangement of IRED markers represents an enhancement over previous IRED tracking strategies for the LRS device [201]. Standard software tools from Northern Digital Inc., in conjunction with a calibration phantom, were utilized to develop a transformation that relates textured-point clouds acquired in LRS-space to the physical-space as provided by an optical tracking system - OPTOTRAK 3020 (Northern Digital Inc.). Appendix A describes the registration process for relating the LRS- and physical-spaces. Having established a method to register the LRS-space to physical-space, the shift measurements for all phantom experiments provided by the shift-tracking protocol were correlated and verified using corresponding physical-space measurements provided by the OPTOTRAK system.

The scanner is also capable of generating textured (intensity-encoded) point clouds of

56(a)

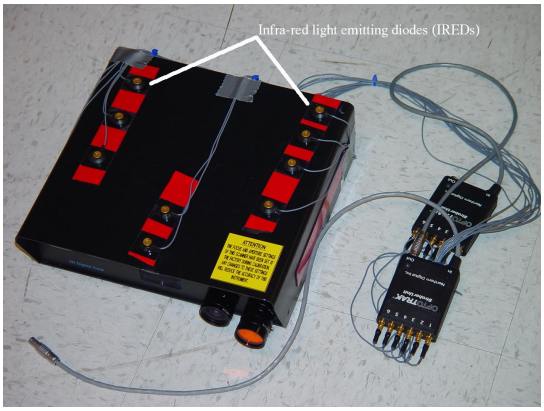

56(b)

56(c)

Figure 56: RealScanUSB 200. (a): A close-up view of the scanner's acquisition lenses. (b): The scanner out-fitted with infrared light emmitting diodes for physical-space tracking using the OPTOTRAK 3020 system. (c): The scanner mounted on a collapsable monopod mount for operating room use. The monopod can be extended to an elevation of approximately 5 ft and has standard yaw, pitch, and roll controls for LRS positioning.

objects in its scanning field-of-view (FOV) using a digital image acquired at the time of scanning. Using a calibration[2] between scanner's range and digital image spaces, each range point in the LRS device's FOV is assigned texture-map coordinates [202] corresponding to locations in the digital image acquired at the time of scanning. Thus, the scanner reports 5 dimensions of data corresponding to (x,y,z) cartesian coordinates of locations in LRS-space and (u,v) texture-map coordinates of locations in texture-space (i.e. the digital image). Texture-mapping, mapping of the texture image intensities to the corresponding locations in the point cloud, generates a textured point cloud of the scanner's FOV. The data acquired by the scanner and texture-mapping process are shown in Figure 57. The work in this paper builds on this unique data by taking full advantage of the geometry and intensity information to develop correspondence between serial LRS datasets. The protocol developed is fast, accurate, non-contact, and efficient for intra-operative use.

Shift-tracking protocol

The context of the shift-tracking protocol can be defined as follows: consider an idealized system in which LRS is used to scan an object, the object then undergoes deformation, and LRS is used to acquire a serial range scan dataset of the object after deformation. The shift tracking protocol, in this case, must determine homologous points and provide correspondence between them in the initial and serial range datasets using only the information in each LRS dataset. We hypothesize that providing correspondence between serial LRS textures is sufficient for determining correspondence of their respective range data. If true, non-rigid alignment of two-dimensional serial texture images allows for the measurement of three-dimensional shifts of the brain surface.

This approach to measuring brain shift marks a distinct departure from other non-rigid point matching methods. As opposed to a fully unconstrained three-dimensional non-rigid point matching method, the shift-tracking protocol is a multi-step process whereby correspondence is ultimately provided via a two-dimensional non-rigid image registration method

[2]The calibration is generated and provided by the manufacturer; it is intrinsic to the scanner.

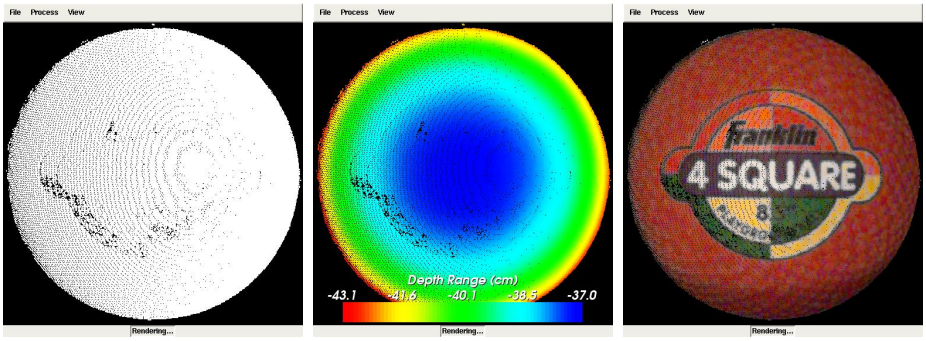

57(a)

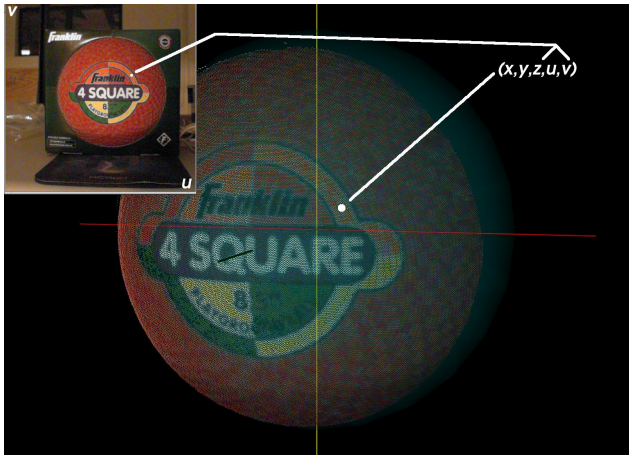

57(b)

Figure 57: Different representations of data acquired by the LRS device and the texture mapping process. (a): From left to right, raw range points, range points colored according to their distance (in Z) from the origin of the scanning space, and the textured point cloud generated after texture-mapping. (b): A visualization of the texture mapping process.

applied to the serial texture images acquired with each LRS scan (see Figure 58). This approach has two distinct advantages: it simplifies the correspondence process greatly and minimizes the loss of information acquired by the LRS.

The former advantage is readily realized since this framework reduces three-dimensional point correspondence to that of a two-dimensional image registration problem that is arguably not as demanding. The latter advantage is more subtle and only with careful analysis of the textured LRS process does it become apparent. The textured LRS process begins with the acquisition of a point-cloud by standard principles of laser/camera triangulation (labeled 1 in Figure 58). At the conclusion of scanning, a digital image of the field of view (FOV) is acquired and texture coordinates are assigned to the point-cloud data (labeled 2 in Figure 58). It should be noted that the resolution of the point cloud is routinely coarser than the resolution of the digital image at the typical operating ranges for surgery. As a result, there are pixels within the digital image that do not have a corresponding range coordinate. Consequently, in the process of creating an intensity-encoded point cloud, some of the image data from the acquired digital image must be discarded. Although it may be possible to interpolate these points, they are not specifically acquired during the LRS process and the interpolation process becomes more difficult when considering the quality and consistency of data collected (i.e. specularity, edge-effects, and absorption variablities can leave considerable regions that are devoid of data). Hence, providing correspondence by non-rigidly registering the 2D LRS texture images (labeled 3a in Figure 58) prevents the loss of image information and simplifies the correspondence problem. The alternative is to process a 3D textured point-cloud with a 3D non-rigid point matching algorithm (labeled 3b in Figure 58).

An important and central component of the shift-tracking protocol is the method of 2D non-rigid image registration used to register serial texture images. While a variety of methods could be employed, we have utilized the adaptive bases algorithm (ABA) of Rohde et al [207] to provide this registration. Briefly, the ABA registers two disparate images by maximizing the statistical dependence of corresponding pixels in each image using mutual information

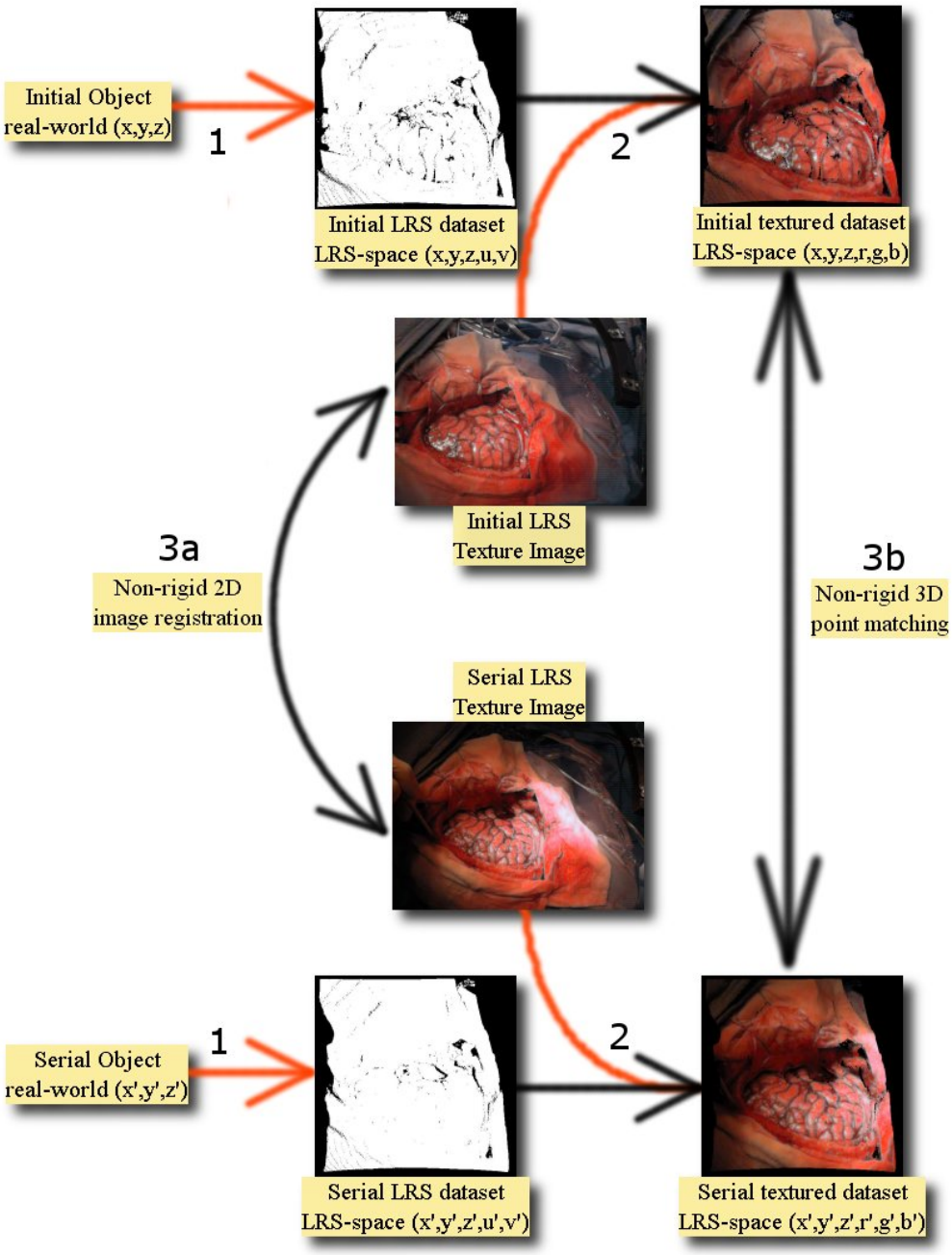

Figure 58: Conceptual representation of non-rigid point correspondence methods for the registration of textured LRS data. The three points of interest in this figure are highlighted with numbers. 1: Real world objects with continuous surface descriptions are discretized into the LRS datasets with information loss related to the resolution of the LRS system (represeted with the orange arrow). 2: Incorporation of intensity information via texture mapping resulting in textured LRS dataset, this step incurs information loss related to the limited resolution of the spatial coordinates with respect to the texture image. 3: two methods to register textured LRS dataset, a) Non-rigid 2D image registration; b) non-rigid 3D point matching.

as a measure of dependence [190, 169]. Initial rigid alignment is provided between images using a multi-scale, multi-resolution mutual information registration. The ABA then locally refines the rigid registration to account for non-rigid mis-alignment between the texture images. Image deformation in the ABA is provided by radial-basis functions (RBFs), whose coefficients are optimized for registration. The robustness and accuracy of the ABA on *in vivo* texture images from the LRS device has been explored and verified in Duay et al. [212] and an example registration of *in vivo* LRS texture images is shown in Figure 59.

The remaining steps in the shift-tracking protocol prescribe a method by which one can transform an independent point-of-interest (POI) from the initial LRS-space, through the initial texture-space, into the serial texture-space, and finally back into the serial LRS-space. These steps are critical for the protocol as they provide a method to track the shift of novel POIs from one LRS-space to a serial LRS-space. In this paper, the novel POIs are usually provided by the optical tracking system. Transforming these POIs from physical-space to LRS-space does not, in general, align the POIs with pre-existing LRS acquired points. Thus, the POI's generally do not have the full five dimensions of data for points provided by LRS, and a system to provide continuous transformations between LRS-space and texture-spaces is needed. A schematic of these steps and the transformations used between steps is shown in Figure 60.

Suppose a POI has been acquired with the optical tracking system and transformed into the initial LRS-space. For shift tracking, the POI is then projected from its geometric location, (x, y, z), to its texture location, (u, v), using a projection transformation, T_a in Figure 60. The transformation used for this projection is derived using the direct linear transformation (DLT) method [213]. The DLT uses at least eight geometric fiducials, $\overline{X}_i = (x_i, y_i, z_i)$, and their corresponding texture coordinates, $\overline{u}_i = (u_i, v_i)$, to calculate 11

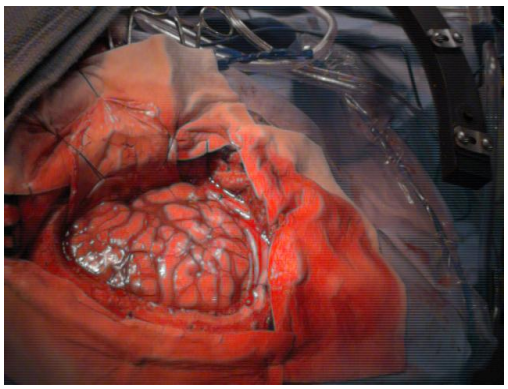

59(a) Initial *in vivo* texture image

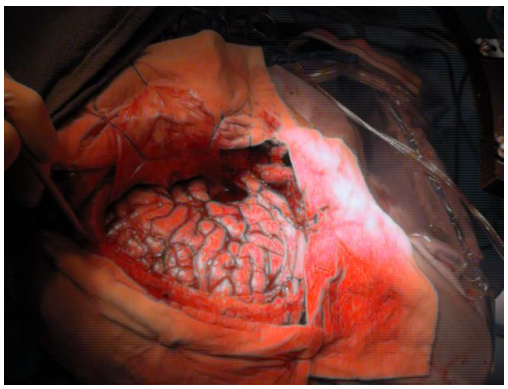

59(b) Serial *in vivo* texture image

59(c) Vessels from initial texture image overlayed onto serial texture

59(d) Vessels from initial texture registered to serial texture using ABA deformation field

Figure 59: Results of the adaptive bases algorithm (ABA) on *in vivo* texture images. The top row shows initial and serial texture images taken intra-operatively. The second row shows registration results of vessels segmented from the initial texture to the serial image.

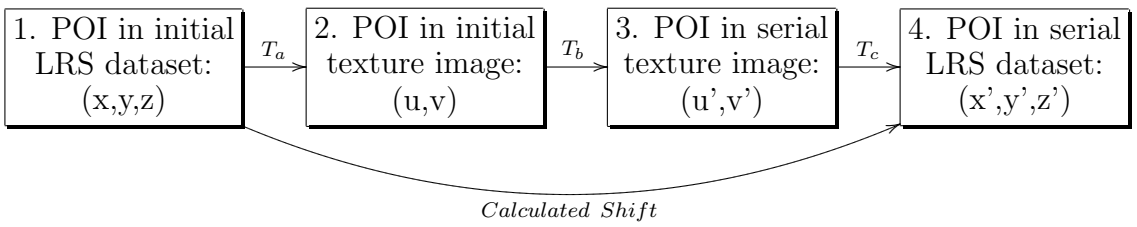

Figure 60: Schematic describing the shift tracking protocol used in this paper. Protocol transformations are indicated and referred to in the text with letters. POI is a point of interest that exists in both initial and serial LRS datasets. The overall goal of the shift tracking protocol in this paper is to resolve the "calculated shift" of points-of-interest (POIs) from one LRS dataset to a serial LRS dataset.

projection parameters [214], which can be used to map $\overline{X}$ to $\overline{u}$ as follows:

$$u_i - \Delta u_i = \frac{l_1 x_i + l_2 y_i + l_3 z_i + l_4}{l_9 x_i + l_{10} y_i + l_{11} z_i + 1} \tag{6}$$

$$v_i - \Delta v_i = \frac{l_5 x_i + l_6 y_i + l_7 z_i + l_8}{l_9 x_i + l_{10} y_i + l_{11} z_i + 1}, \tag{7}$$

where Δu_i and Δv_i are the point specific correction parameters for radial lens and decentering distortions and the l's are the DLT projection parameters.

From the initial texture space, the POI is transformed into serial texture images using the deformation field provided via the ABA on the two texture images (denoted T_b in Figure 60). This transformation takes the initial texture coordinates, (u, v), and results in serial texture coordinates, (u', v'). Figure 61 demonstrates the transformation of fiducials from an initial texture image to a serial texture image using the deformation field provided by the ABA registration.

Finally, T_c, in Figure 60, provides a method to transform serial texture coordinates, (u', v'), back into serial LRS-space, (x', y', z'). This mapping is the inverse to T_a, however, since reconstruction of 3D points from the DLT parameters requires at least two independent texture images of the same FOV, the DLT cannot be used for the reprojection. Instead, a series of B-spline interpolants are used to approximate the transformation from texture-space to LRS-space. The FITPACK package by Paul Dierckx (www.netlib.org/dierckx) uses a B-spline formulation and a non-linear optimization system to generate knot vectors and control point coefficients automatically for a spline surface of a given degree. The Dierckx algorithm also balances the smoothness of the fitted surface against the closeness of fit [215]. The FITPACK library is used to fit three spline interpolants, one for x, y, and z, which provides a continuous transformation of texture space coordinates projected to LRS space:

$$T_c(u, v) = \big(s_x(u, v), s_y(u, v), s_z(u, v)\big), \tag{8}$$

where, $s_x(u, v)$, $s_y(u, v)$, and $s_z(u, v)$ are spline interpolants for x, y, and z, respectively.

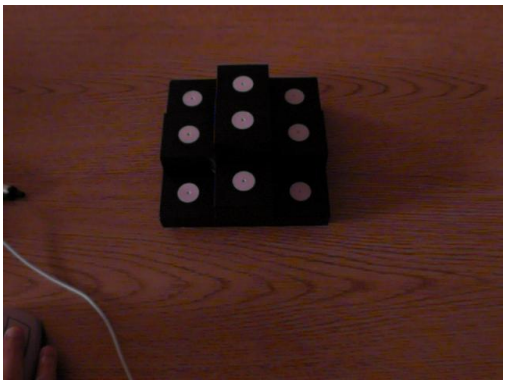

61(a) Fixed image

61(b) Moving image

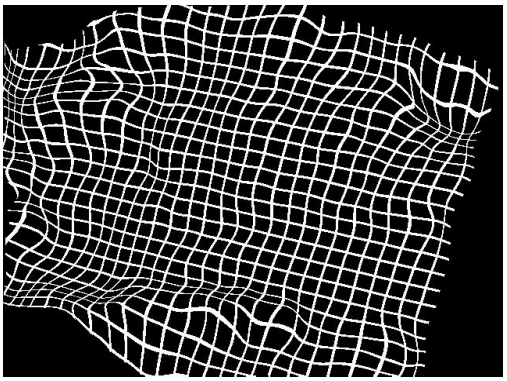

61(c) Deformation field

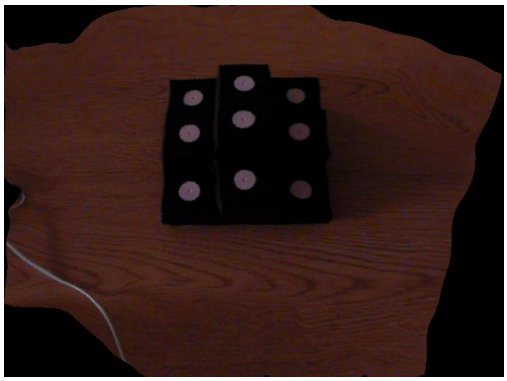

61(d) Moving image registered to fixed

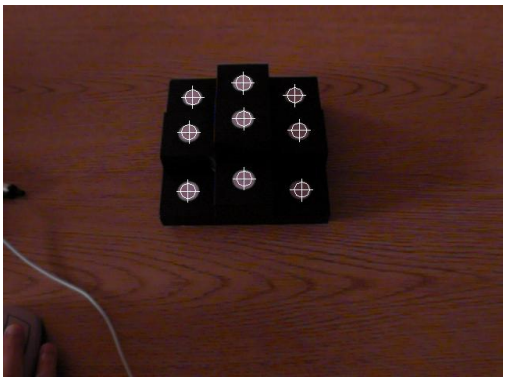

61(e) Fiducials in initial texture

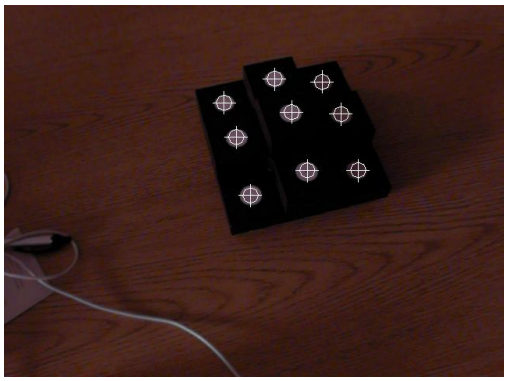

61(f) Fiducials in serial texture

Figure 61: This figure demonstrates the transformation of targets from an initial texture image to a serial image. The top row, left to right, shows the initial (fixed) and final (moving) textures. The middle row, left to right, shows the deformation field calculated via ABA registration on a reference grid and the result of registering the serial texture using the deformation field. The bottom row, left to right, demonstrates the locations of the targets in the initial texture image and the corresponding locations in the serial image found using the ABA deformation field.

Experiments not reported here indicated that biquadratic splines provided low interpolation errors while providing generally smooth surfaces. For *in vivo* datasets acquired by the LRS, the mean RMS fitting error (i.e. the Euclidean distance between fitted point and actual point) is $0.05mm$ over 15 datasets. In general, the spline interpolants $s_x(u,v)$ and $s_y(u,v)$ used 6-9 knots in u and v; $s_z(u,v)$ provided adequate interpolation using approximately 25 knots in u and v.

The product of these three transformation steps provides a global transformation, T_{ST} (see Equation 9), for the shift of a POI from initial to serial range datasets.

$$\tilde{X}' = (\tilde{x}', \tilde{y}', \tilde{z}') = T_{ST}X = T_c T_b T_a X, \tag{9}$$

where $\tilde{X}'$ is the calculated location of a point X that has undergone some shift. Results from T_{ST} operating on POI's in the initial LRS dataset were compared against optical localizations of POI's in serial LRS datasets for shift-tracking accuracy validation. The OPTOTRAK 3020 system (Northern Digital Inc.) and stylus used for point digitization has an accuracy of $0.3mm$ and served as a reference measurement system.

Experiments

A series of phantom experiments were conducted to quantify the fidelity of the framework with respect to rigid, projective, and non-rigid target movement. Figure 62 is a visual representation of the experiments performed to ascertain the effects of rigid movement on the tracking framework developed. These experiments specifically tested the effects of: (a) LRS scanning extents - which affect the LRS dataset resolution, (b) target position changes within a full scanning extent, (c) target position changes with focused scanning extents, (d) LRS pose changes with stationary target, (e) target pose changes with a moving LRS, and (f) changing the incidence angle of the laser with respect to the texture mapping process. For each scenario in Figure 62, the centroid of the white disks could act as a point target since it could be accurately digitized by both an independent optically tracked pen-probe and tracked LRS. In each experiment, an initial scan was acquired and used for calibration

(see Appendix A). Subsequent scans used the calibration transform from the initial scan to transform LRS-space points into physical-space. Tracking accuracy was estimated using the target registration error (TRE, see Equation 10) of novel[3] targets acquired by the optical tracking system and novel targets acquired by the LRS (transformed into physical-space) [216, 217, 194, 193].

$$TRE = \sqrt{\big(X' - T(X)\big)\big(X' - T(X)\big)^T}, \tag{10}$$

where X' and X are corresponding points in different reference frames, and $T()$ is a transformation from X's to X''s reference frame.

For the experiment outlined in Figure 62(a) the laser scanning extents ranged between $17cm$ and $35cm$. In experiments (b) and (c) the phantom was positioned in a rectangle area of approximately 35x15cm corresponding to the full scanning extent of the LRS. In experiment (d) the centroid of the LRS system was translated a minimum of $4.1cm$ and a maximum of $12.1cm$, which is estimated to be the intra-operative range of motion for the LRS device. Figure 62(f) illustrates a special tracking experiment aimed at ascertaining the fidelity of the texture mapping process of the scanner. For each scan in experiment (f), the physical-space localizations were transformed into LRS-space and then into texture-space using the DLT projection. In texture space, the disk centroids were localized via simple image processing and region growing[4]. Corresponding transformed physical-space fiducial locations were compared against the texture space localizations to measure the accuracy of the texture mapping and projection processes for objects scanned at increasingly oblique angles to the plane normal to the scanner's FOV.

After determining the accuracy of the rigid tracking problem, we then determined the shift-tracking accuracy of the protocol for situations in which the shift was induced using

[3]Unique and reproducibly identified points across all modalities that were not used in the registration process.

[4]The image processing done in the texture space included thresholding of the intensities such that only the white discs were apparent; all other pixels were set to a termination value (i.e. -1). A region growing technique was then used to collect all image pixels belonging to a single disc. The region growing was terminated based on the intensity value of the 8-neighbor pixels from the current pixel in the region growing.

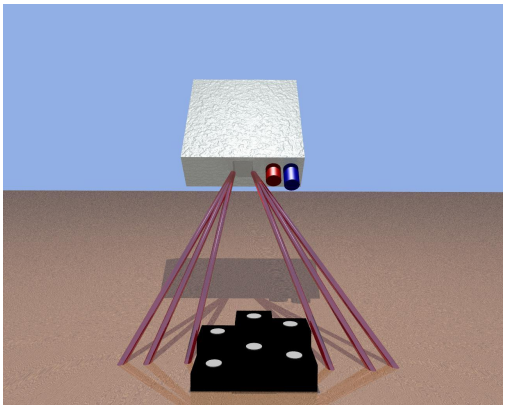

62(a) Tracking accuracy given varying scanning extents

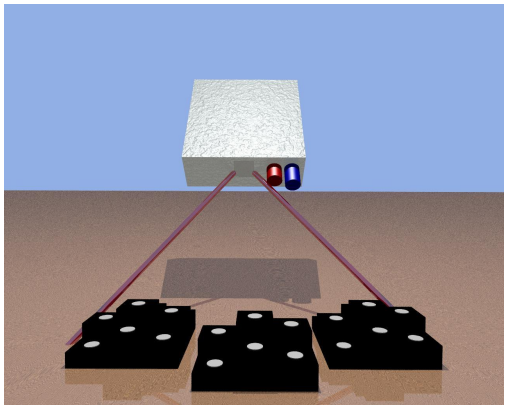

62(b) Tracking accuracy given a moving phantom in full extents

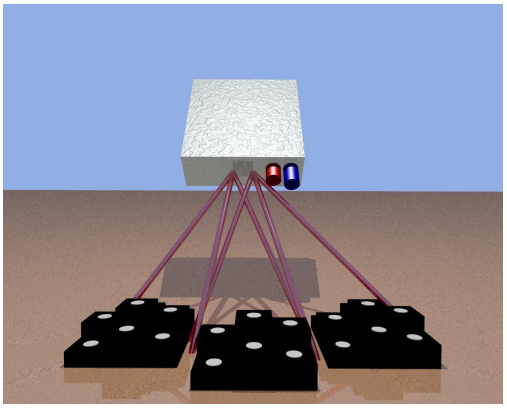

62(c) Tracking accuracy given a moving phantom and focused extents

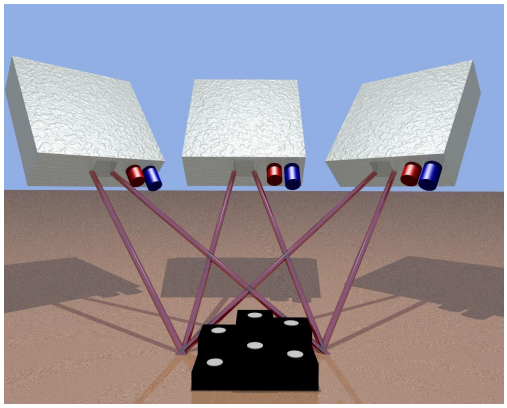

62(d) Tracking accuracy given camera pose changes and a stationary phantom

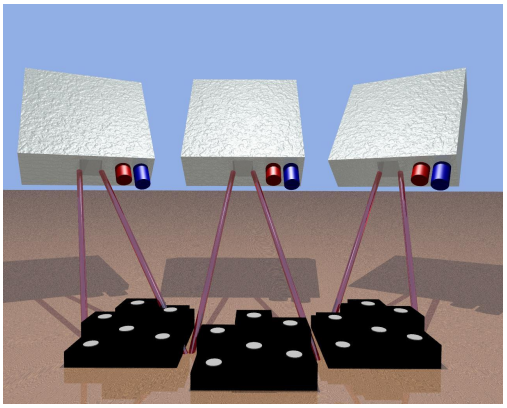

62(e) Tracking accuracy given camera and phantom pose changes

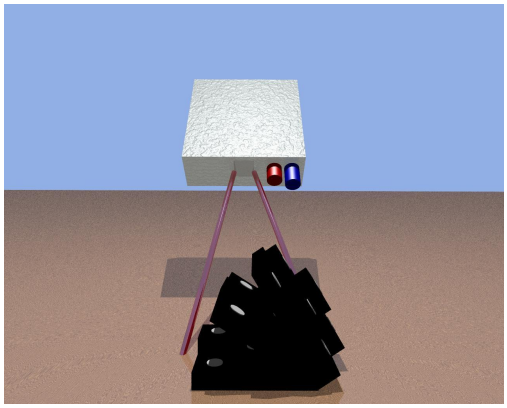

62(f) Tracking accuracy given various scanning incidence angles

Figure 62: Figures demonstrating the different rigid-body tracking experiments performed to evaluate tracking capabilities of the experimental setup.

projective transformations (i.e. the culmination of 3D translation and rotation, and perspective changes related to projecting the 3D scene on to the 2D texture image). The first series of experiments examined the results of the shift tracking protocol on the experiments shown in Figure 62. Although the experimental setup of the LRS acquisitions mimicked the previous rigid-body tracking experiments, it is important to note that the shift-tracking protocol, i.e. T_{ST} from Equation 9, is used to determine the target's transformation from the initial to the serial LRS dataset for these experiments. Since these experiments used a rigid tracking phantom and rigid-body motions of the LRS device and phantom, they provided a method to quantitatively examine the shift-tracking protocol in resolving projective changes between the initial and serial LRS textures. Target shifts were calculated using the shift tracking protocol and compared against shift measurements provided by the optical tracking system. RMS shift tracking error (STE), as defined in Equation 11, was used to quantify the accuracy of the shift-tracking protocol.

$$RMS\ STE = \sqrt{\frac{1}{N}\sum_{i=0}^{N}\Big((X_i' - T_{ST}(X_i))(X_i' - T_{ST}(X_i))^T\Big)}, \tag{11}$$

where, X_i' is the shifted location of a point X_i as reported by the optical localization system and T_{ST} is defined in Equation 9.

In a subsequent set of experiments, a non-rigid phantom was used to ascertain the performance of the shift tracking protocol in an aggregate projective/non-rigid deformation system. A compression device and pliant phantom (see Figure 63) were used in this series of experiments. The phantom was made of a rubber-like polymer (Evergreen 10, Smooth-On, Inc., Easton, PA). The surface of the phantom was designed to simulate the vascular pattern of the brain during surgery (a permanent marker was used to generate vessels). The compression device permits controlled compression of the phantom. For the tracking experiments, the phantom was scanned under minimal (or no) compression, then with compression from one side of approximately $5cm$ and, finally, with compression of $5cm$ from both sides. Target vessel bifurcations and features on the phantom were marked optically at each com-

pression stage. Reproducibility of the markings was found to have a standard deviation of approximately $0.5mm$. The accuracy of the shift-tracking protocol was determined by the STE of the target points. The last experiment examined the accuracy of the shift tracking protocol in situations with both projective and non-rigid changes in the surface. For this, the deformable phantom was scanned using a novel camera pose while under two-sided compression. Figure 64 demonstrates the four poses used to determine the accuracy of the shift-tracking protocol.

In addition to phantom experiments, a preliminary experience with the shift tracking protocol is reported for a human patient. For this case, the LRS system was deployable in the OR, but, rigid body tracking capabilities during LRS acquisition were not yet incorporated within the OR environment. All results regarding the fidelity of tracking are relative to the coordinate reference established in the initial scan provided by a rigid-body iterative closest point (ICP) registration [167] of the serial LRS dataset based on non-deforming features in the FOV, i.e. the skull walls of the craniotomy region. Target points were highlighted manually in both the pre-resection and post-resection LRS datasets. Inter-user reproducibility for target point localizations in the LRS datasets was found to be $1.0\pm0.29mm$[5]. The shift magnitudes and vectors for these points, after ICP registration was assumed to be the intra-operative shift of the brain. Using the shift-tracking protocol and the points from the pre-resection scan, the STEs, shift magnitudes, and shift vectors were calculated and compared against results from the manual localization. It is important to note that the shift-tracking protocol is used to measure all forms of shift in the experiment, i.e. shift due to camera position changes and deformation. A view of the surgical area, texture images of the scanning FOV, and the manually localized landmarks for this experiment are shown in Figure 65.

[5]Reproducibility for these markings was measured by determining the accuracy with which one could reselect target landmarks from a textured LRS dataset. Reproducibility trials were performed with 10 individuals marking 7 target landmarks from an intra-operative LRS dataset. The reported number was the average targeting error across all individuals and all trials.

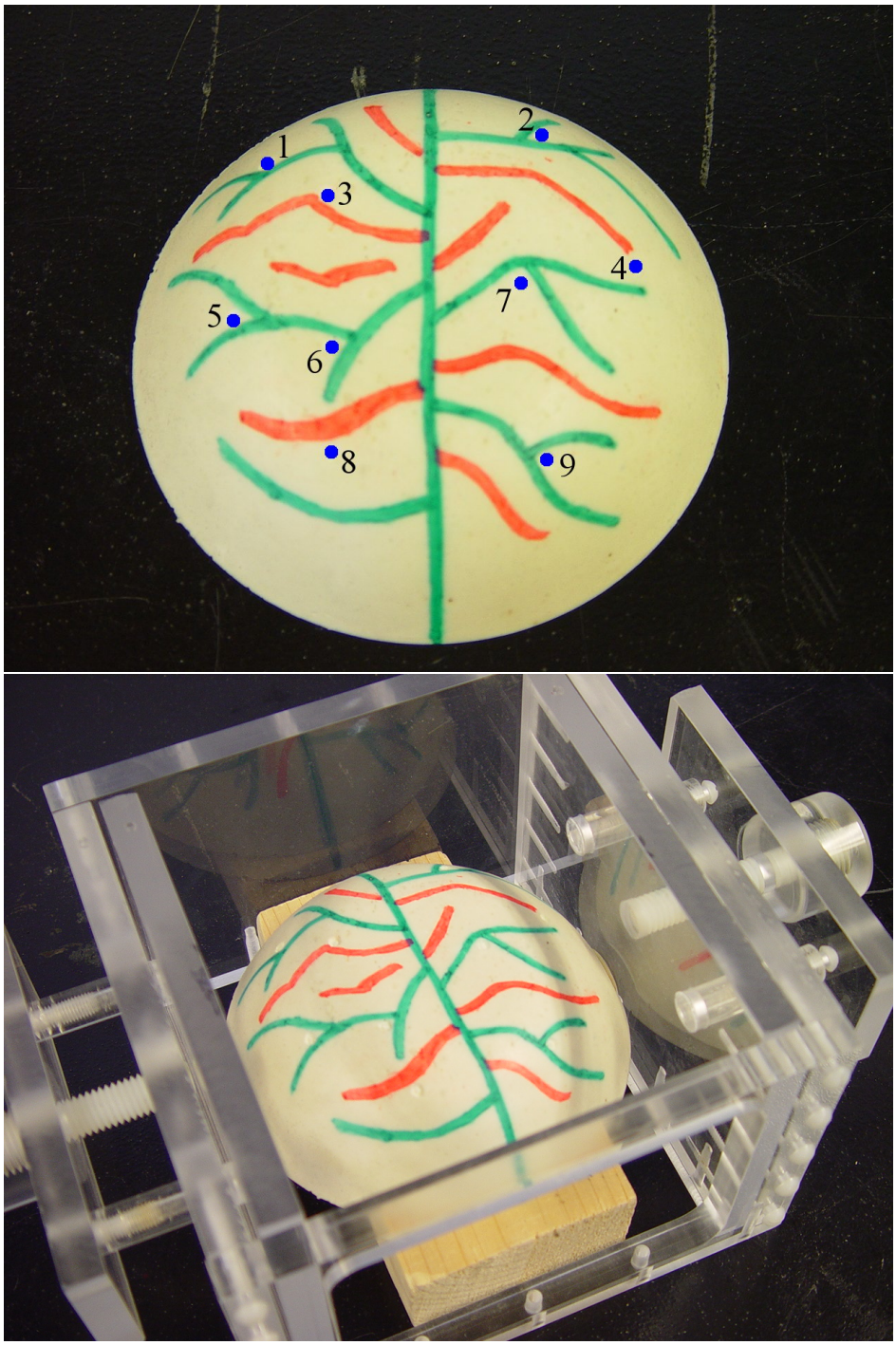

Figure 63: Shift tracking phantom used to determine shift tracking accuracy. On top is the pliant phantom with target locations highlighted. On the bottom is the phantom in the Plexiglass compression chamber used to apply deformations to the phantom.

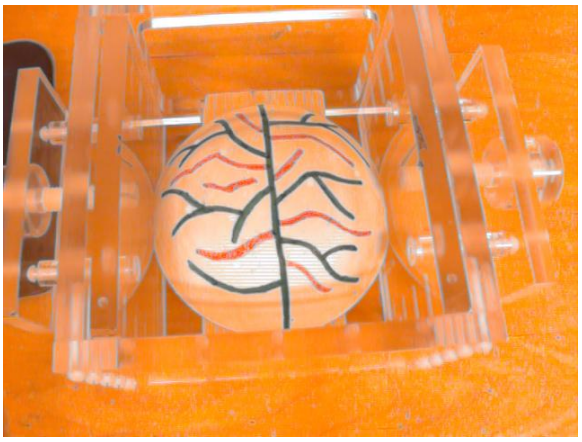

64(a) Uncompressed

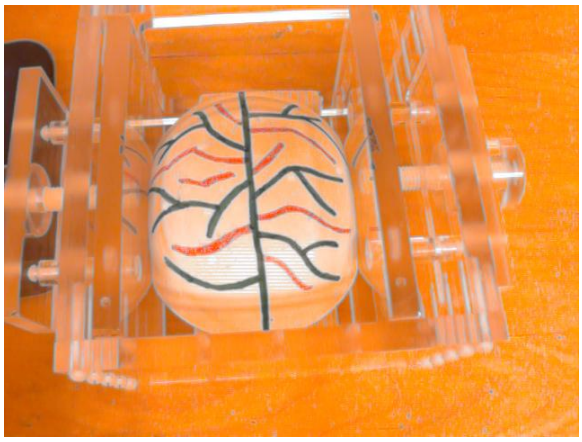

64(b) One-sided compression, from the right

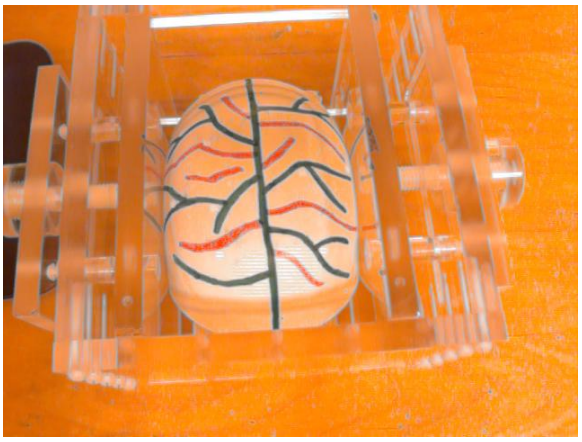

64(c) Two-sided compression

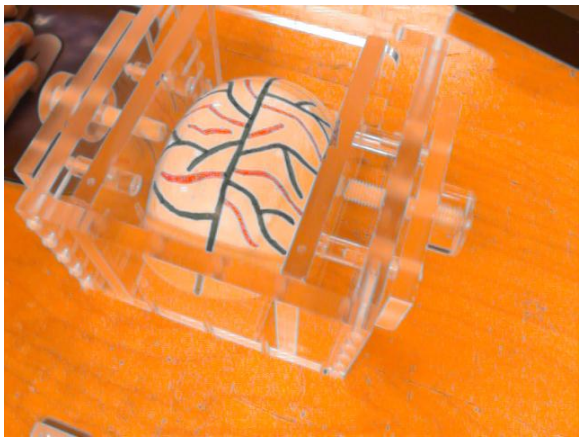

64(d) Two-sided compression w/ projective change in the texture image (related to change in the LRS position during scanning)

Figure 64: Shift tracking phantom under various compression levels and positions for LRS acquisition.

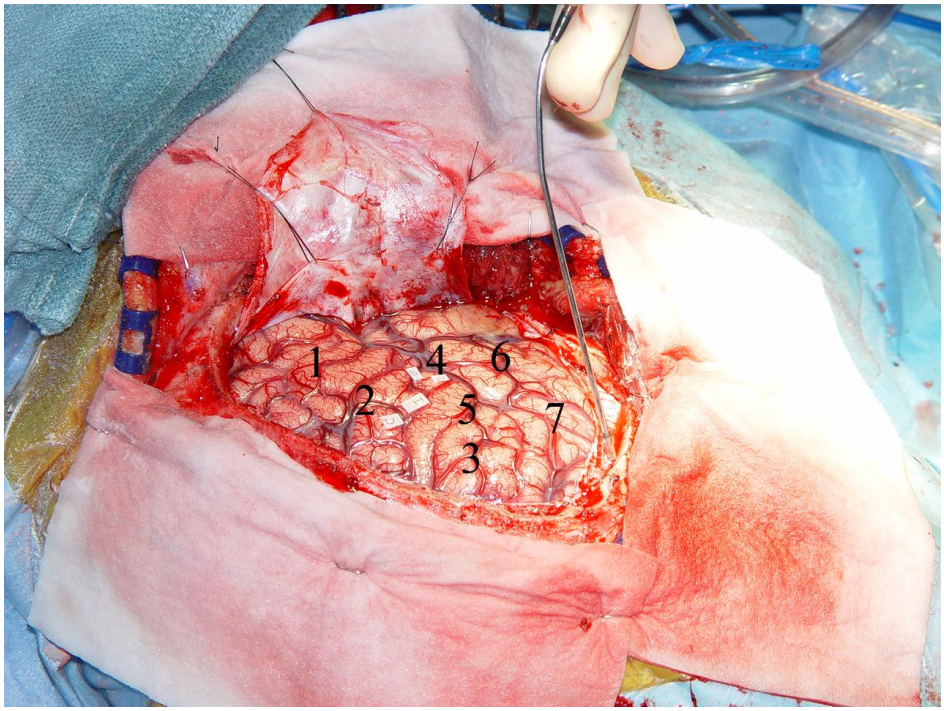

65(a) High resolution intra-operative digital image showing the surgical FOV

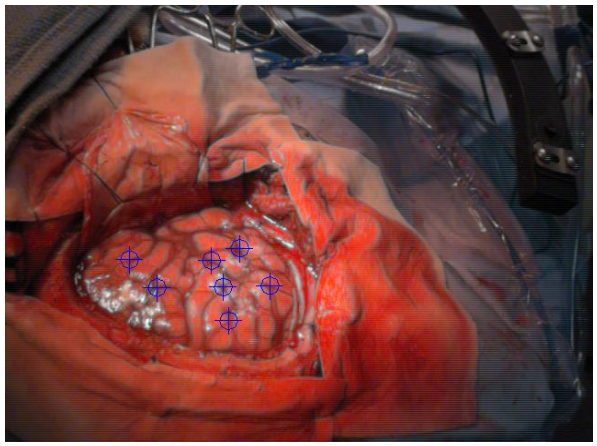

65(b) Initial intra-operative LRS Texture with manually localized landmarks highlighted

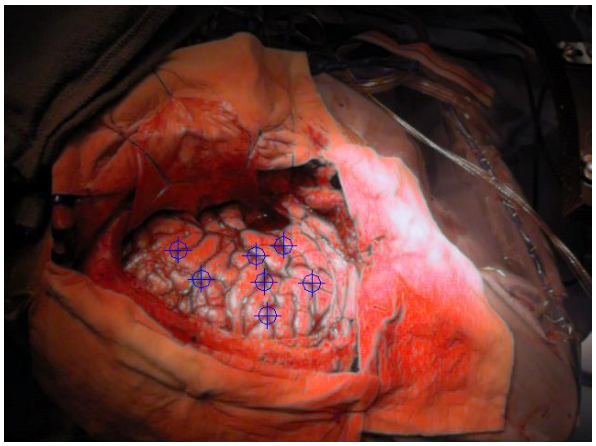

65(c) Serial intra-operative LRS Texture with manually localized landmarks highlighted

Figure 65: *In vivo* texture images and landmarks used to calculate shift and STE.

Results

The calculated rigid-body description of the IRED pattern on the LRS device demonstrated an accuracy of $0.5mm$ RMS fitting error using seven static views of the IRED orientations. The fitting error was on the order of the accuracy of the OPTOTRAK 3020 optical tracking system[6], which suggests that the scanner's rigid-body was created accurately.

Thirty-three calibration registrations of the phantom in Figure 70 generated an average RMS fiducial registration error (FRE) of $0.70\pm0.14mm$. These results indicated that the LRS device and optical tracking system can be registered to each other with an accuracy that allows for meaningful assessment of the accuracy of the shift tracking protocol.

The results of the rigid tracking experiments are categorized and reported in Table 7 according to the experiment types shown in Figure 62.

The low mean RMS TRE's verified that the LRS tracking system is capable of resolving and tracking physical points accurately and precisely. An interesting observation from these results is the increased tracking accuracy when using focused scanning extents as compared to the full scanning extents (see results from Experiments (b) and (c)). In light of this fact, only focused extents were used for each range scan acquisition in the shift tracking experiments.

Shift tracking results of the rigid-body calibration phantom in the projective registration experiments produced an average RMS STE of $1.72\pm0.39mm$ in nine trials. A sample of the results from the pose shift-tracking experiments is shown in Figure 66.

Shift tracking results for the non-rigid phantom provided encouraging results. Table 8 highlights the RMS STE for target landmarks at each compression stage of the non-rigid shift tracking experiment while Figure 67 demonstrates the shift vectors and results from the one-sided compression experiment.

From Table 8 one can see that the protocol is capable of RMS STEs of $2.7mm$, $2.5mm$, and $7.8mm$ for the 1-sided, 2-sided and 2-sided with projective change experiments, respec-

[6]The accuracy of the OPTOTRAK system in tracking individual infrared emitting diodes is reported to be (0.1, 0.1, 0.15)mm in x, y and z at $2.25m$, respectively (www.ndigital.com/optotrak-techspecs.php)

Table 7: Target registration errors according for rigid-body tracking experiments outlined in Figure 62. n indicates the number of LRS and OPTOTRAK acquisitions used to generate the mean value reported. The mean RMS FRE describes the accuracy with which the calibration between physical-space and LRS was generated. The mean RMS TRE represents the tracking accuracy of targets acquired by the LRS and OPTOTRAK independently of the calibration scans.

Experiment Type	Mean RMS FRE n=number of poses examined	Mean RMS TRE
a: varying extents	0.62±0.10 (n=4)	0.95±0.22 (n=12)
b: varying phantom position	0.74±0.23 (n=4)	1.63±0.49 (n=12)
c: focused extents, varying phantom position	0.57±0.05 (n=4)	1.20±0.32 (n=12)
d: varying camera position	0.54±0.04 (n=3)	1.29±0.44 (n=6)
e: varying camera and phantom position	0.79±0.08 (n=4)	0.94±0.14 (n=12)

Table 8: Induced shift magnitudes and shift tracking errors (STEs) for the target points on the non-rigid phantom. All measurements and results are reported in millimeters. The *Shift* column describes the total shift of the target point. The *STE* column describes the shift tracking error of protocol on this point. The *cos(Θ)* column describes the deviation of the calculated shift vector from the measured shift vector. A perfect tracking would produce low STE's and a cos(Θ) of 1.

Target Point Number	Compression Type								
	One-sided			Two-sided			Two-sided w/ pose change		
	Shift	STE	cos(Θ)	Shift	STE	cos(Θ)	Shift	STE	cos(Θ)
1	13.31	2.17	0.991	13.84	1.99	0.993	13.42	10.41	0.914
2	14.50	1.99	0.992	17.38	2.28	0.997	16.47	4.90	0.993
3	14.11	1.93	0.996	15.87	1.21	0.999	15.45	1.67	0.998
4	11.98	6.11	0.974	10.26	6.04	1.000	9.57	18.14	0.944
5	12.26	0.66	0.998	10.65	1.76	0.991	11.21	8.99	0.824
6	14.07	1.87	0.994	15.47	1.80	0.997	15.82	1.20	1.000
7	13.25	2.27	0.991	14.39	1.08	1.000	14.20	1.55	0.997
8	14.81	1.70	0.996	17.82	1.00	0.999	17.89	1.60	0.997
9	14.08	1.46	0.996	15.77	1.37	0.997	15.34	1.46	0.996

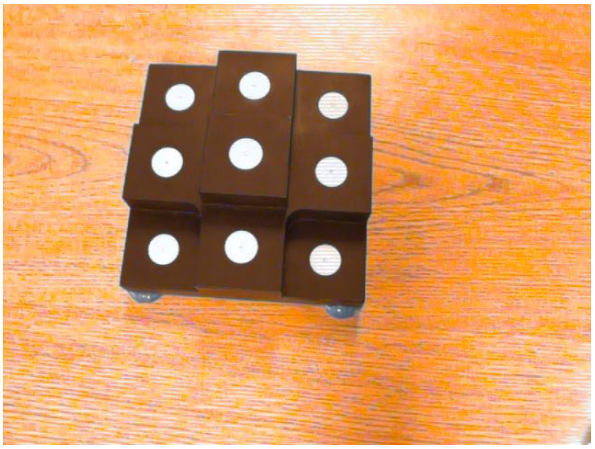

66(a) Initial position

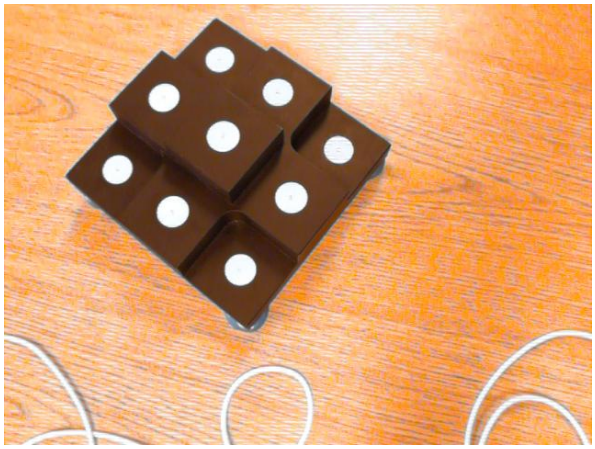

66(b) Camera pose and phantom position change

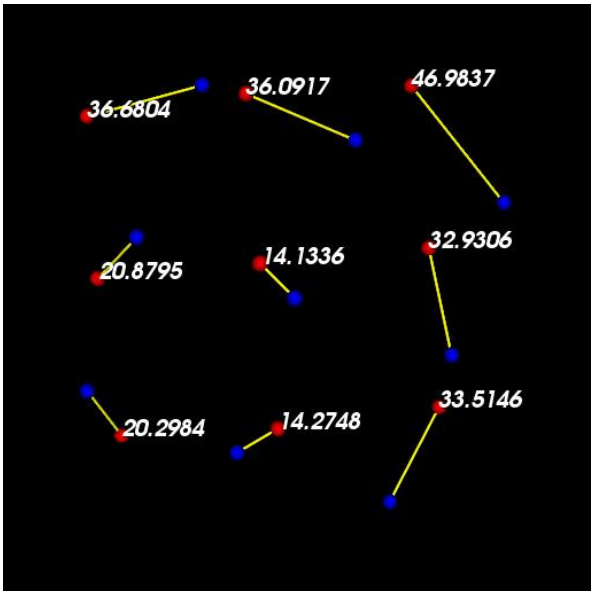

66(c) Induced shift vectors observed via optical tracking system

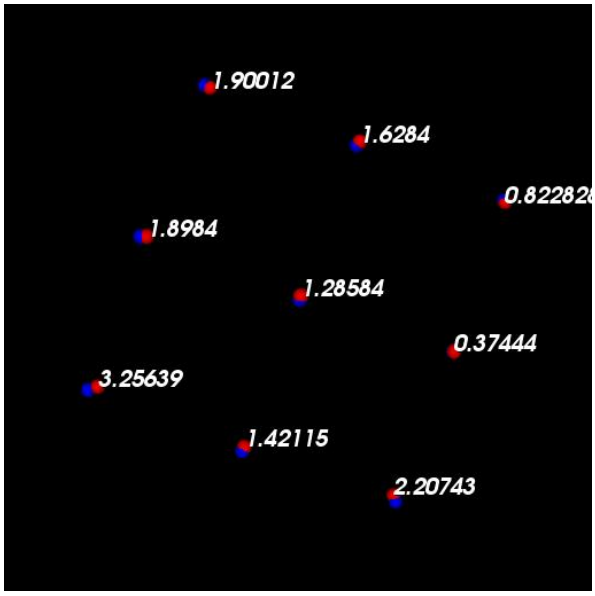

66(d) Shift tracking error vectors produced from shift tracking protocol

Figure 66: Example projective shift-tracking experiment and results. The top row shows the initial and serial positions of the phantom and scanning FOV. The bottom row shows the initial shift vectors and the error vectors for the shift calculated via shift-tracking protocol.

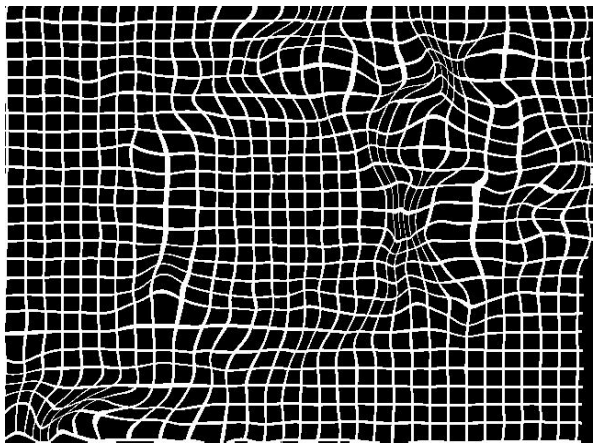

67(a) One-sided compression deformation field

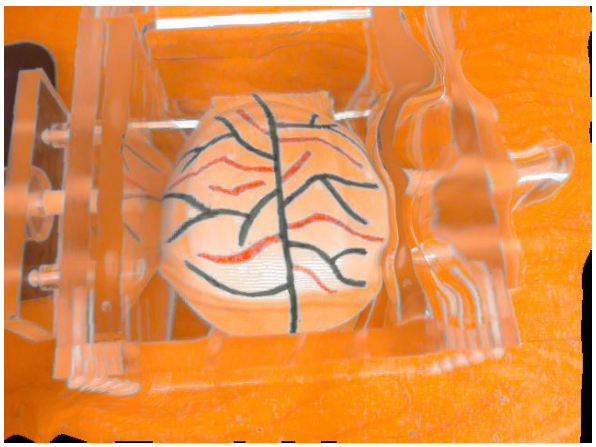

67(b) One-sided compression registered image

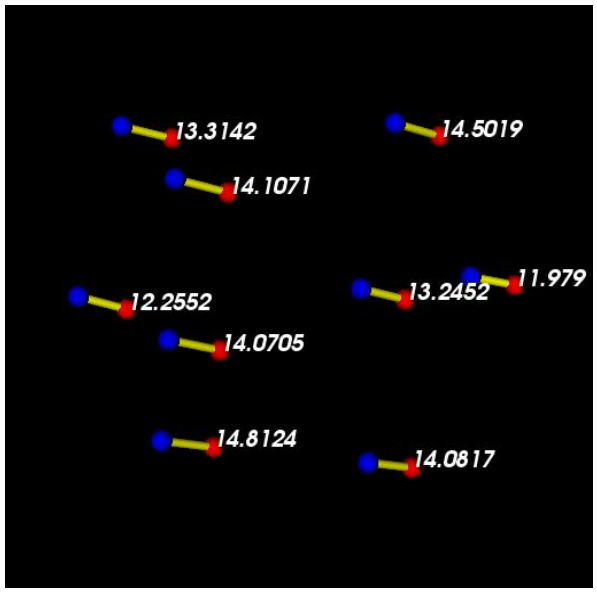

67(c) One-sided compression induced shift vectors

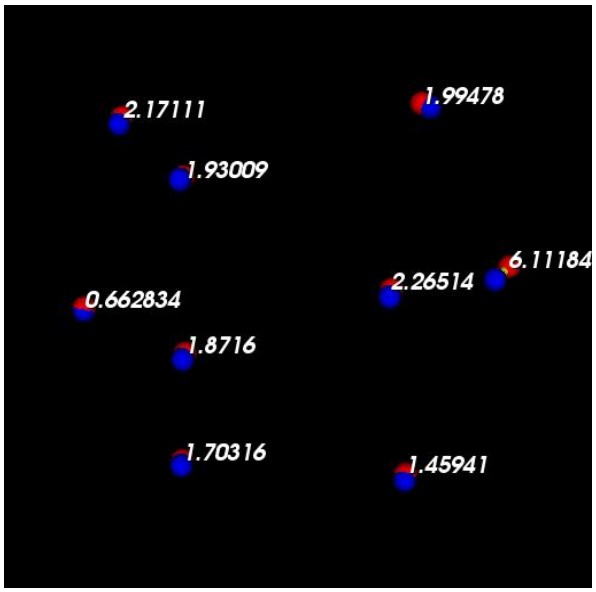

67(d) One-sided compression shift tracking error vectors

Figure 67: Results from the non-rigid, one-sided compression shift-tracking experiment.

tively; while preserving the directionality of the the shift vectors. There are, however, some outliers in each experiment which require closer examination. In the one-sided and two-sided compression experiments (with minimal projective changes in the textures) target point 4 experienced increased STE and according to the Grubb's test [195] was identified as a statistical outlier in the results. The aberrant result is most likely due to point 4's location near the periphery of the scanning FOV. During compression this point was obscured from scanning and therefore was not accurately registered. Removing point 4 and calculating the RMS STE for the remaining 8 points yielded a result of $1.8mm$ and $1.6mm$ for the one-sided and two-sided compression experiments, respectively. Similar results can be seen in the two-sided compression with projective change. Points 1, 4, and 5 all displayed atypical results for this experiment. Examination of the LRS datasets showed that those points were occluded during the scanning process and therefore were not registered correctly. Removing these points from the RMS STE calculation resulted in a accuracy of $2.4mm$. Factoring in the overall rigid-body and projective tracking accuracies into the STE's seen in the non-rigid shift-tracking experiments imply that the shift-tracking protocol may in fact be determining shift to approximately 1.5-2mm error. The increased errors seen in the non-rigid experiments were likely due to larger localization errors in the target points on the surface of the phantom. This observation is supported by the tracking results reported from the previous series of projective shift-tracking experiments using the rigid tracking object.

The *in vivo* dataset results demonstrate the potential of the protocol for automatic intra-operative shift-tracking (see Figure 68 and Table 9). The RMS STE of the *in vivo* landmarks was $1.62mm$ with a minimum and maximum error of $0.88mm$ and $2.58mm$, respectively (see Figure 68(a-b)). The recovered intra-operative brain shift vectors are similar in magnitude and direction to the manually localized brain shift (see Figure 68(c-d)). Furthermore, these results are in close agreement with previously observed intra-operative brain shift.

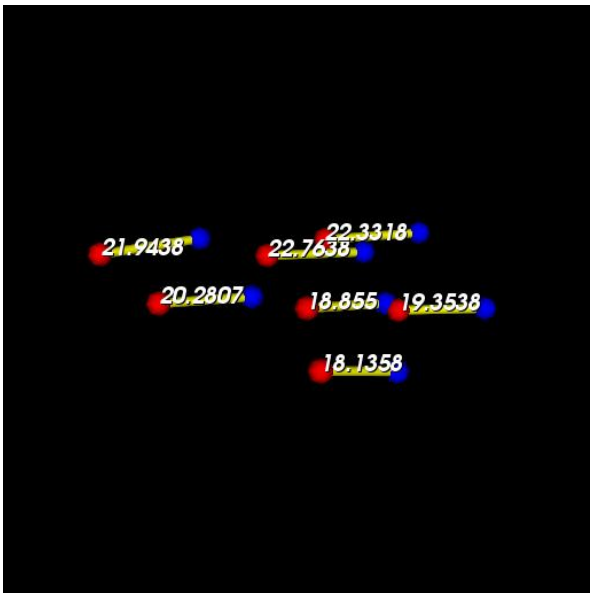

68(a) Total shift between manually localized landmarks in each dataset (w/o ICP registration)

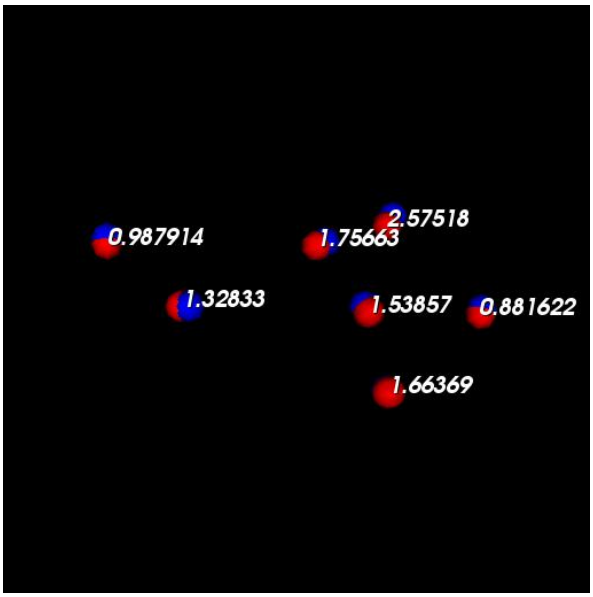

68(b) Shift tracking error between calculated landmarks and manually localized landmarks

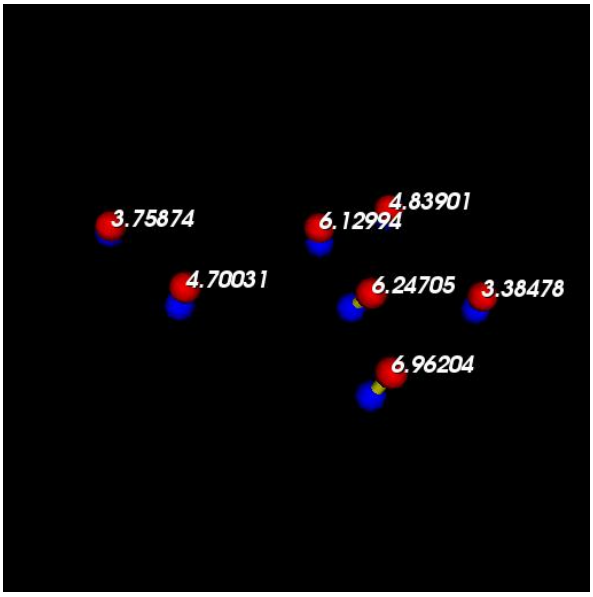

68(c) Manually localized intra-operative brain shift (using ICP rigid-body correction)

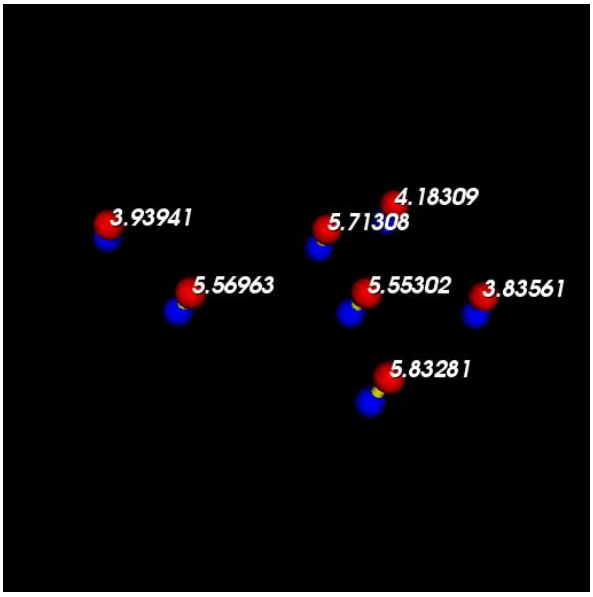

68(d) Calculated intra-operative brain shift (using ICP rigid-body correction)

Figure 68: Shift tracking results on an intra-operative dataset. Manual shift calculations between corresponding points was calculated after a rigid-registration of non-deforming structures in the two FOVs.

Discussion

Figures 56 and 57 illustrate the experimental setup and unique data provided by the laser-range scanner. Figure 56 illustrates the minimal impact that the LRS system has to the OR environment while Figure 57 shows the multi-dimensional data provided by the unit (x, y, z, u, and v). In some sense, the data generated represents four distinct dimensions: Cartesian coordinates and texture (as characterize by an RGB image of the field of view). Compared to other LRS work for intra-operative data acquisition [164], the inclusion of texture is particularly important. More specifically, capturing spatially correlated brain texture information allows the development of novel alignment and measurement strategies that can take advantage of the feature-rich brain surface routinely presented during surgery. In previous work [205], these feature-rich LRS data sets were used in a novel patient-to-image registration framework. The work presented here dramatically extends that effort by establishing a novel measurement system for non-rigid brain motion. As a result, a fundamental advancement in establishing quantitative relationships between high-resolution pre-operative MRI and/or CT data and the exposed brain during surgery has been provided by this LRS-brain imaging platform. The methods described in this paper can also be used with data provided by other intra-operative brain surface acquisition methods that can generate texture-mapped point-clouds (i.e. binocular photogrammetry) [152, 131, 211].

Figures 58 – 61 and Equation 9 represent this novel approach to measuring cortical surface shifts within the OR environment. The method greatly simplifies the measurement of three-dimensional brain shifts by using advanced methods in deformable 2-D image registration (e.g. Figure 59) and standard principles of computer vision (i.e. the DLT). In addition, the shift-tracking framework maximizes the information acquired from this particular LRS system by directly determining correspondence using the acquired texture images of the FOV rather than establishing correspondence using coarser textured point clouds. This approach is illustrated, within the context of rigid-body motion, in Figure 61. In this image series, the only shift is associated with a pose change of the phantom (i.e. rigid body movement).

The resulting rigid-body change is captured by the stationary LRS as a projective change in the digital images of the field of view. The ABA accounts for these changes non-rigidly and yields excellent results with respect to specific targets, i.e. the centroids of the white disks.

To quantify the effects of projective changes on the ability to track shift (e.g. Figure 61), a series of experiments were proposed and shown in Figure 62. Figure 66 is an example of a typical result from one of these experiments and demonstrates the marked ability to recover rigid movement of the targets of $28.4 \pm 11.4mm$ to $1.6 \pm 0.8mm$, on average. Table 7 reports the full details of these experiments that investigated changes in LRS device pose and target positions. Interestingly, a target localized central to the LRS extents produces the best results (Figure 62(a) and 62(e) with corresponding TREs from Table 7). This is in contrast to the results observed from the experiment described by Figure 62(b). In experiments presented elsewhere [201], there has been some indication than an increased radial distortion occurs in the periphery of the LRS scanning extents. This would suggest that placing the target central to the extents is an important operational procedure for shift tracking. However, in our experience, the ability to place the brain surface central to the extents has been relatively easy within the OR environment and is not a limiting factor. In Figure 62(f), the fidelity of the texture mapping process is tested by scanning at increasingly oblique angles to the scanner's FOV normal. Figure 69 demonstrates that at angles routinely used within the OR (i.e. $\pm$ 5–10 degrees), the DLT error associated with mapping the texture is on the order of $1mm$. Considering that the localization error of the OPTOTRAK is on the order of $0.15mm$ and a low-resolution camera is being used to capture the FOV, this is an acceptable result for this initial work.

The non-rigid phantom experiments relayed in Figures 63 and 64 demonstrate the full extent of the shift-tracking protocol within the context of a controlled phantom experiment. The results in Figure 67 and Table 8 demonstrate the fidelity with which simulated cortical targets are tracked. As shown in Figure 67, all points experienced similar shifts ($13.6mm$) with points on the periphery having increased STEs as compared to those located internally. Specifically, point 4 ($6.1mm$ error) is very close to the edge of the phantom in the com-

Table 9: Shift tracking results from the *in vivo* experiment. All measurements and results are reported in millimeter units. The first column describes the total shift calculated from the manual localized targets. The remaining four columns describe the intra-operative brain shift observed. The *Manual* column describes the intra-operative brain shift as calculated using manual localizations in both (initial and serial) LRS datasets after ICP registration of rigid features outside of the craniotomy. The *Calculated* column shows the shifts predicted using the ICP-corrected landmarks from the serial LRS dataset. The *STE* column is the vector difference of the shift vectors found manually and calculated using the shift-tracking protocol (see Equation 11). Finally, the *cos(Θ)* column describes the directional deviation in the vectors from the *Manual* and *Calculated* shift calculations.

		Brain shift calculated using ICP correction			
Target Point	Total shift between LRS datasets	Manual	Calculated	STE	cos(Θ)
1	21.94	3.76	3.94	0.99	0.968
2	20.28	4.70	5.57	1.33	0.981
3	18.14	6.96	5.83	1.66	0.982
4	22.76	6.12	5.71	1.76	0.958
5	18.86	6.25	5.55	1.54	0.973
6	22.33	4.84	4.18	2.58	0.847
7	19.35	3.38	3.84	0.88	0.978
RMS	20.59	5.29	5.02	1.63	0.96

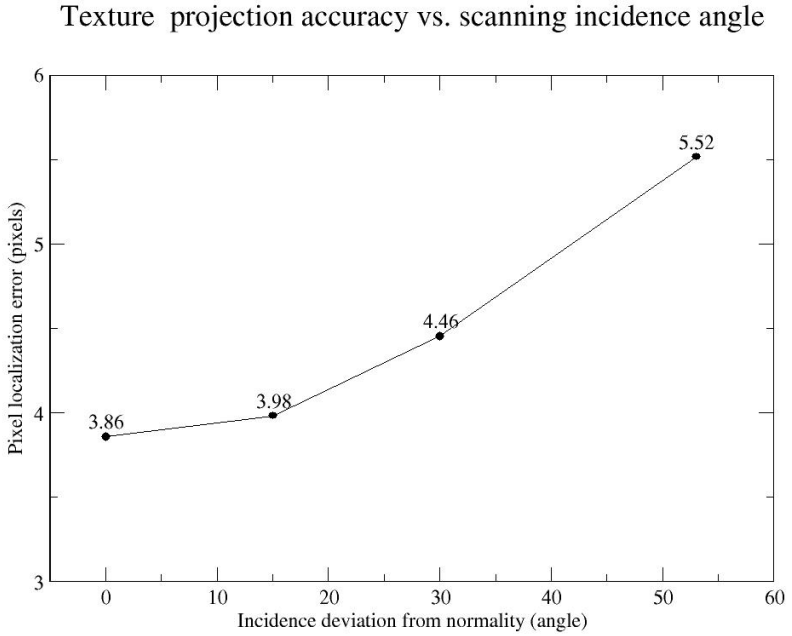

Figure 69: Texture mapping and projection accuracy as a function of scanning angle, where scanning angle is the angle deviation from normal to the scanning plane. Three pixels equals approximately $1mm$ in physical-space.

pressed state and in the subsequent dual-compression becomes somewhat obscured. In some sense, there is a necessity for the ABA registration to have similar structures within the two images being registered. Otherwise the statistical dependence sought by mutual information registration is confounded. The implications to this requirement are more salient when considering the nature of the brain surface during surgery. In cases of substantial tissue removal, measurements of deformation immediately around voids in the surface may be less accurate. Further studies need to be conducted to understand the influence of missing regions on shift measurement but the fidelity of measurement within close proximity is promising (e.g. point 7 is in close proximity to 4 and experienced STE's between $1mm$-$2mm$). Interestingly, Table 8 does indicate some variability with respect to measuring shift especially in the combined projective and non-rigid experiment (Table 8, last 3 columns). The primary cause of this behavior appears to be from the compression device. Figures 64 and 67(b) show that the compression plate displays a reflected image of the phantom which may affect the ABA registration. In addition, some points become somewhat obscured by the device itself during the combined non-rigid and projective shift experiment (i.e. points 1, 4 and 5). While the ABA registration produces a result in these regions, the disappearance of feature between serial scans is still something that needs further study. This emphasizes that special care may be needed when measuring shifting structures in close proximity to the craniotomy margin or around resected regions in the *in vivo* environment. However, it should be noted that with respect to directionality as measured by the directional cosines, all results have excellent agreement with their comparison measurements.

Figure 65 illustrates a preliminary *in vivo* case used for assessing the shift tracking protocol. For this case, the LRS unit was not tracked by the OPTOTRAK system, so shift measurements could only be made manually and relative to the initial LRS acquisition. The craniotomy margin from the initial LRS scan was used as the rigid reference and all measurements were be placed within it's frame of reference. Figure 68 and Table 9 quantify the shift tracking capabilities for this *in vivo* case. On average the combined non-rigid and projective changes in the LRS textures entailed approximately $20.5mm$ of shift in the cortical surface

targets between initial and serial acquisitions. Using the shift-tracking protocol, this error was reduced to 1.5mm while preserving the directionality. It should be noted that while a majority of the shift between these two LRS datasets was rigid, there is still some non-rigid motion of the brain between datasets, and both of types of shift were handled in a uniform manner with the shift tracking protocol. Interestingly, these results report shift-tracking with the presence of an excised region. Comparing the image in Figure 65(b) to 65(c), a resected region is shown in the upper right quadrant of the brain surface. Points 4 and 6 are the points closest to the craniotomy and despite their location and a combined shift (i.e. projective+non-rigid) of 22.76mm and 22.33mm, the shift tracking error was reduced to 1.8mm and 2.6mm, respectively. Calculating brain shift vectors for these points using ICP correction shows close agreement with manually calculated brain shift vectors, e.g. STEs of 1.76mm and 2.58mm, and cosine deviations of 0.96 and 0.85 for points 4 and 6, respectively.

The results presented here are encouraging given the early stages of development in this work. Many factors need to be studied further such as: the performance of the ABA registration on multiple sets of brain surface images, the impact of missing structures, the influence of line-of-sight requirements, the effects of craniotomy size on algorithm fidelity, and the speed of measurement. However, the methods and results described here do present a fundamental advance in identifying and measuring three-dimensional brain shift during surgery.

Conclusions

This paper represents a critical step in addressing the brain-shift problem within IGS systems. Unlike other methods [152, 164] to quantify shift, the added dimensionality of surface texture allows full three-dimensional correspondence to be determined which is not usually possible using other geometry based methods. The work presented here represents a complete solution, i.e. a method to track three-dimensional representations of the brain surface and provide correspondence between serial range scans.

When considering the advancements embodied in this work coupled with our previous

study in aligning textured LRS data to the MR volume rendered image tomogram [205], a novel visualization and measurement platform has been developed. This platform offers surgeons an unprecedented ability to correlate the intra-operative brain surfaces with their preoperatively acquired image volume counterparts. It also offers surgeons the ability to render cortical targets identified on MR image volumes into the surgical FOV in a quantitative rather than qualitative manner. Lastly, the quantitative measurement of brain shift afforded by textured LRS technology presents exciting opportunities in developing shift compensation strategies for IGS systems using computer modeling approaches.

Acknowledgments

The authors would like to thank Colin Caughran and Tanoy Sinha for their assistance in data collection and processing.

Appendix A: Registering LRS-space to physical-space

The registration of the LRS scanning space to physical-space is achieved using a registration phantom with the registration schematic in Figure 70. The phantom is $15cm$ x $15cm$ x $6cm$, with white disc fiducials $9.5mm$ in radius. Three-millimeter diameter hemispherical divots were machined into the center of each of the nine discs to compensate for the $3mm$ diameter ball tip used to capture physical-space points. The phantom is painted with non-reflective paint to minimize the acquisition of non-disc range points.

During registration, physical space locations of each disc's center was acquired three times. The average location of the three acquisitions was used as the physical-space location of the fiducial (P_p). Corresponding fiducials[7] were localized in LRS-space by segmenting each disc from the native LRS dataset. A region growing technique was used to identify all points corresponding to an individual disc. Calculating the centroid of each group of points resulted in fiducial locations in LRS-space (P_r). A point-based rigid-body registration of the two point

[7]Correspondence was established *a priori* by numbering the fiducials discs and localizing each fiducial in order.

sets provides the transformation ($T_{r\rightarrow r'}$) from LRS-space (X_r) to a pose-dependent physical-space (X'_r) [204]. The reason for the pose-dependence is that the physical-space points are acquired relative to a reference rigid-body affixed to the scanning object. If the scanner is moved relative to the reference rigid-body, $T_{r\rightarrow r'}$ will not provide consistent physical-space coordinates. As a result, the final step in the registration process is to incorporate the pose of the LRS relative to the reference rigid-body ($T_{r\rightarrow p}$) at the time of scanning, leading to the formulation of the registration transform in Equation 12.

$$T_{r\rightarrow p} = T_{r'\rightarrow p} T_{r\rightarrow r'}, \tag{12}$$

where $T_{r'\rightarrow p}$, the scanner pose relative to the reference rigid-body, is provided by the OPTOTRAK. Subsequent LRS datasets can now be transformed into physical-space by using $T_{r\rightarrow p}$ and the new pose of the scanner $T^{new}_{p\rightarrow r'}$ according to Equation 13.

$$P_p = T^{new}_{p\rightarrow r'} T_{r\rightarrow p} P_r. \tag{13}$$

Appendix B: Clinical Impact of the Technology and Intraoperative Design Concerns

Principle concerns with using any device during a surgical procedure include the device's impact on the progress of surgery, the device's intrusiveness with respect to data acquisition and the quality of the data acquired. In this work, we have used the LRS system in a proof-of-concept framework. Three important, distinct clinical issues with respect to the full realization of this framework are: (1) disruption of the procedure, (2) the effects of retraction on the measuring methodology, and (3) issues concerned with lighting in the OR that could confound the approach.

The current OR design of the LRS unit allows for accurate and effective clinical data acquisition at the cost of some surgical intrusiveness, i.e. the surgeons must move away from the patient and allow for the LRS to come into the surgical FOV. The surgeons we have worked with have indicated that this has been minimally obstructive to their progress

in surgery due to the fast nature of our approach (2-4 minutes to get an acquisition which includes: movement into the FOV, setup, scan, and withdrawal). Nonetheless, future generations of the scanning device can be greatly improved with respect to this intrusive design. Although some surgeons rely on the surgical microscope to different degrees, in principle, one could mount this technology to an existing surgical microscope. Based on work with our industrial collaborators, the size of the scanner can be significantly reduced. In fact, there is very little inherent OR constraints that prevent the adoption of this technology.

While retraction is used to different degrees also (with some neurosurgeons seldom using the tool), the obstruction to the brain surface would undoubtedly result in a loss of data. However, the LRS unit can readily capture the location and application point of a retractor within the surgical field. Arguably, in these cases, capturing the retractor contact position relative to the brain surface would be of great importance for estimating brain shift with computer models. We assert that the LRS unit can capture this type of information and that it could be used as a source of data for MUIGS frameworks [126].

With respect to the quality of the data acquired, our current experience leads us to believe that lighting conditions can be an issue. However, we have found that ambient lighting conditions are sufficient for clean, accurate and highly resolved texture LRS datasets with the current scanner. In our current intra-operative data acquisition protocol, the surgeons usually turn overhead focused lights and head-lamps away from the surgical FOV. Again, future designs could greatly improve on these constraints by calibrating the LRS capture CCD's to the lighting characteristics of the surgical microscope to which they are mounted. Another enhancement to the current design would most likely be the resolution and capture characteristics of the texture image CCD. Currently, the CCD used to acquire the texture image is not ideal for capturing high resolution, high contrast digital images. This is mainly due to the intended purpose of the LRS device in scanning larger objects with limited texture information. A higher resolution digital image of the surgical FOV would allow for highly resolved deformation fields between serial texture images and would in turn increase the overall accuracy of the shift tracking protocol. These enhancements, being very feasible,

could help alleviate many of the acquisition concerns that currently face us. Furthermore, they will help increase the clinical impact of the shift-tracking protocol.

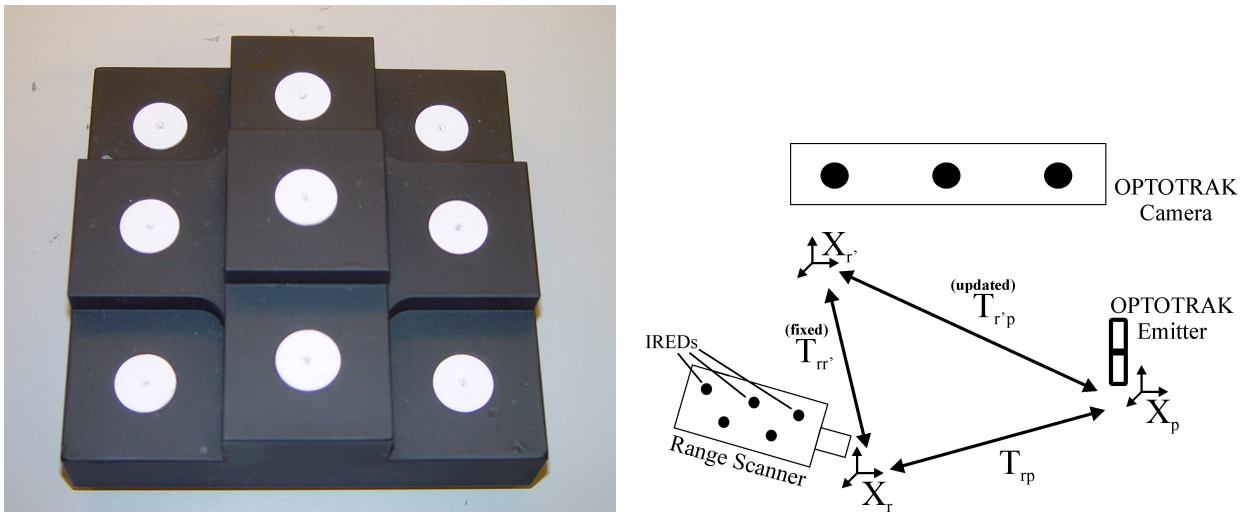

Figure 70: Registration phantom and process used to align LRS-space to physical-space. On the left is the registration phantom used to register LRS-space to physical-space. On the right is a figure outlining the registration process used to register LRS-space to physical-space.

CHAPTER VIII

MANUSCRIPT 6 - EXTENSIONS TO SURFACEMI AND THE SHIFT-TRACKING PROTOCOL DEVELOPED FOR CORTICAL SURFACE TRACKING WITH PRELIMINARY *IN VIVO* VALIDATION

Abstract

A comprehensive method to automatically track cortical surface shifts intraoperatively using a laser range scanner is presented in this paper. Tracking cortical surface shifts intraoperatively is a critical component to acheiving a model-updated image-guided surgery system that can compensate for whole brain deformation during surgery. A laser range scanner, capable of generating textured surfaces, is used in this paper to characterize the intraopertaive brain's surface. The methods in the paper describe a way to align the intraoperative brain's surface to preoperative MR tomograms, as well as a procotol to track cortical shifts using serial laser range scan data. These methods build on unique textured surfaces provided by the preoperative and intraoperative datasets. Clinical validation of the registration protocols is performed on two patients. The results indicate the ability to track shift to an accuracy of $3mm$ when measured against an idependent measurement system. Furthermore, the results demonstrate the capability to render intraoperative shift characteristics to preoperative images, a significant step in the realization of a model-updated image guided surgery system.

Introduction

Shift tracking for neurosurgery is an important step for model-updated image-guided surgery (IGS) [44]. Current systems for image-guided surgery rely on a rigid-body registration of the intraoperative patient to the preoperative image sets to provide coherent tracking of physical-space locations in the OR during surgery. This method of intraoperative navigation requires that structures in the preoperative images and corresponding structures in the OR remain rigid during surgery. During surgery, however, the brain shifts in a non-rigid

manner which compromises the assumptions in current image-guidance systems. Studies examining the extent of brain shift have observed movements on the order of a centimeter and have demonstrated non-uniform movements throughout the brain [38, 39, 44, 43, 81, 46]. The movement of the brain during surgery compromises the rigid-body assumptions of the current image guided surgery systems and results in inaccurate physical-space tracking.

In light of these results, researchers are now exploring methods to calculate and compensate for brain shift intraoperatively. One of the earliest methods for brain shift tracking was a qualitative method described by Kelly et al. in 1986 [16]. During surgery, Dr. Kelly used $5mm$ stainless steel balls and projection radiograms to determine the brain's motion relative to preoperative images. More recent methods of quantitative measurement include framed and frameless stereotactic measurement [38, 41], and intraoperative measurements using magnetic resonance imaging [81, 46, 43] or ultrasound [113, 114]. However, these methods do not present a complete solution for cortical surface shift compensation (in the case of stereotactic systems) or do not present wholly effective methods for shift measurement due to cost and data quality issues (in the case of intraoperative imaging). An alternative method for brain shift correction is to use preoperative images that have been deformed to match intraoperative conditions using a computation model, then applying the deformed images to an existing IGS system. Called model-updated IGS by some [121, 131], this computational method for shift correction requires intraoperative sparse data which acts as constraints for the mathematical model driving the deformation of the brain. Sparse data implies intraoperative information about the brain with limited extent. This paper explores an automatic method to collect intraoperative measurements of the cortical surface shift to act as sparse data in a model-updated IGS system.

We employ a laser-range scanning (LRS) device capable of generating textured (intensity-encoded) point clouds as an intraoperative data acquisition system. Work by Audette et al. prescribe a method for brain shift quantification using laser range scanning [165, 164]. However, those reports do not explore validation of cortical shift-tracking *in vivo* as we demonstrate in this paper. In our previous reports we have indicated a method for intra-

operative shift measurement built on the textured point cloud data acquired by the LRS device [212, 205, 192]. In [192] we introduce the LRS device and demonstrate a method to rigidly register the uniqe textured data from LRS. Quantitative validation of the registration algorithm for multi-modal textured point clouds was provided in [205]. This registration method demonstrates a way to align intraoperative undeformed surface to the preoperative tomograms, which acts as a baseline for subsequent shift measurement using the LRS [218]. A distinct method to deformably register serial LRS datasets was introduced and examined in [212] and [219]. Using the two registration protocols in concert allows for the automatic measurement of the exposed cortical surface intraoperatively and the alignment of that shift within a preoperative context (i.e. the preopertive image datasets).

This paper examines enhancements to the overall LRS-based shift tracking strategy developed thus far. While the earlier reports indicate that the strategy developed for tracking shift is capable of resolving surface motion with millimetric accuracy [219], extensions to the algorithms are necessary for more robust performance. We will examine some of the extensions developed to enhance the rigid and non-rigid registration protocols in a systematic manner. Topics of interest include: the development of highly resolved textured mesh surfaces from the LRS unit and preoperative images as opposed to simple point surfaces, multi-scale/multi-resolution rigid-registration strategies, and 2D registration of textured surfaces using homotopic spherical transforms.

Methods

Textured surface generation from intraoperative LRS and preoperative MR data

In previous studies [205], the native data acquired from the scanner was used (with minor processing including segmentation and linear supersampling) in the registration studies. In this paper, radial-basis functions are used to parameterize the points collected by the LRS, and then determine smooth surface interpolations of the native LRS data. Radial basis

function parameterizations of scalar-valued functions can be described as follows:

$$\tilde{f(x)} = W(x) + \sum_{i}^{N} \lambda_i \phi(r_i), \tag{14}$$

where $W(x)$ is a monomial function, N is the number of control points, λ_i's are the control point coefficients, $\phi(r_i)$ is a radial-basis function, and r is the distance from x to the i^{th} control point. The estimation is controlled by the control points' distribution and coefficients. Automatic parameterization using radial basis functions is provided by solving the following system of equations:

$$\begin{bmatrix} \Phi_C & C \\ \Phi_O & O \\ C^T & 0 \end{bmatrix} \begin{bmatrix} \lambda \\ w \end{bmatrix} = \begin{bmatrix} f \\ 0 \end{bmatrix}, \tag{15}$$

where Φ_X are design matrices of the form:

$$\begin{bmatrix} \phi(c_1 x_1) & \phi(c_1 x_2) & \dots & \phi(c_1 x_N) \\ \phi(c_2 x_1) & \phi(c_2 n_2) & \dots & \phi(c_2 x_N) \\ & & \ddots & \\ \phi(c_N x_1) & \phi(c_N x_2) & \dots & \phi(c_N x_N) \end{bmatrix}, \tag{16}$$

and C are the control points of the parameterization, O are the off-surface points, and w are the monomial coefficients. In Equation 16, $c_i x_j$ is the distance from a point x_j to the control point c_i. radial-basis function weight given the distance from the i^{th} control point to the j^{th} input point. For Φ_C, x are the control points which have radial-basis function parameterizations of $f(x) = 0$; for Φ_O, x are off-surface points with $f(x) \neq 0$. Example radial-basis function parameterizations of $y = x^2$ are shown in Figure 71. Figure 71a demonstrates the control points and off-surface points used to generate the linear system in Equation 15. While Figures 71b and 71c demonstrate RBF fittings using two different radial-basis functions.

An optimized, fast implementation of this formulation of radial-basis fitting is provided

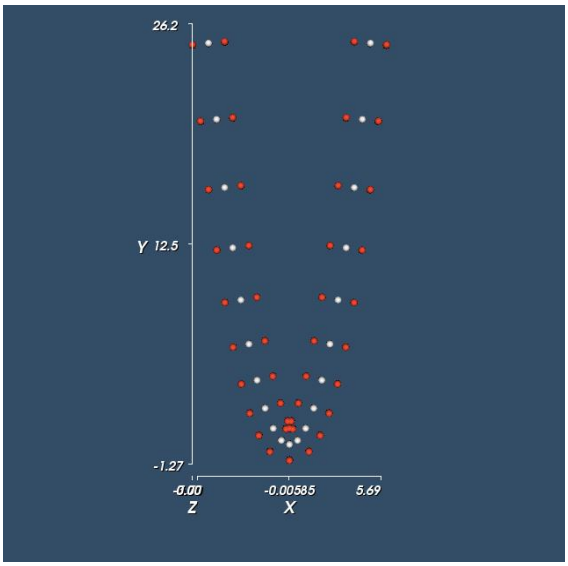

71(a) Control points and off-surface points used to fit RBF.

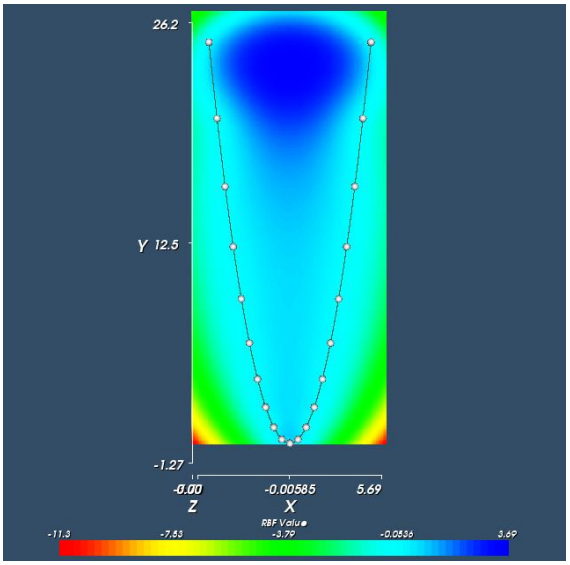

71(b) Biharmonic radial-basis function fit of a parabola. The biharmonic radial basis function is: $\phi(r) = -r^2 \log r^2$.

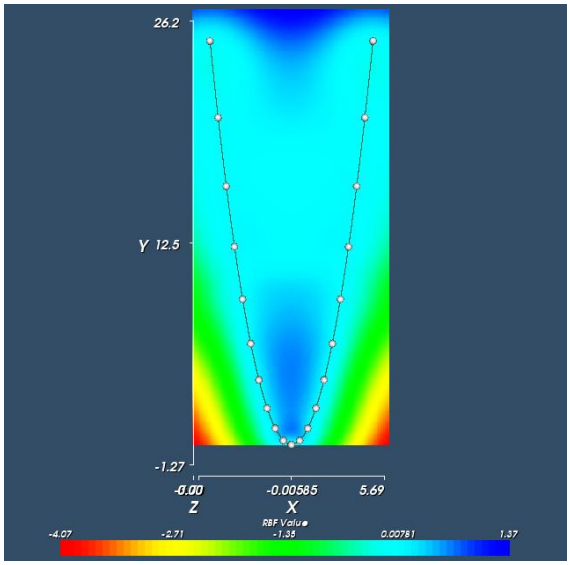

71(c) Wu radial-basis function fit of a parabola. The Wu radial-basis function is: $\phi(r) = (1-r)^4(3r^3 + 12r^2 + 16r + 4)$ when $|r| < 1$ and $\phi(r) = 0$

Figure 71: Radial-basis function fitting of a parabola. The zero isocontour in each of the fitted images represents the desired parabola. In these images, the zero isocontour is located in the cyan region.

by the FastRBF Toolbox (Farfield Technologies, www.farfieldtechnology.com). We used the FastRBF Toolbox to implement RBF fitting of all textured datasets in this paper. For LRS acquisitions, the FastRBF Toolbox was used to fit three RBF's parameterizations to the range/texture data: (u, v, x), (u, v, y), and (u, v, z). Each of these RBF's interpolates the two-dimensional texture coordinates to corresponding three-dimensional coordinates in the LRS dataset. The zero isosurface, found using a secant optimization, of each fitted RBF function space provided the correct interpolation for an (x, y, z) coordinate given any (u, v) coordinate in the LRS texture. An example of the RBF fitting on an LRS dataset is shown in Figure 72. The highly refined nature of these surfaces directly impacts the textured based rigid registration protocol, by providing more unique data during registration.

In [192] a method to generate textured surfaces from preoperative MR tomograms was demonstrated to produce corresponding data for textured point clouds generated by the scanner. The described method used a parallel ray-casting algorithm (PRCA) to produce sparse, super-sampled point clouds. Sparse, in this case, refers to the fact that the generated point clouds did not represent the entire brain, only the portion that faced the ray projection source (see Figure 73). While the PRCA method of textured point cloud generation produced acceptable results for the registration process, it did not allow for textured surface generation of the whole brain. A new method, called the normal ray-casting algorithm (NRCA) for textured surface generation was used in this paper to generate textured surfaces of the whole brain from preoperative MR images.

The preliminary steps to the NRCA are similar to those of the PRCA. The first step was to generate a segmented volume from a preoperative MR. For the clouds used in the previous reports the segmentation was provided manually. In the current PRCA, an automatic atlas segmentation algorithm was used. The atlas was derived from manually segmenting the MR tomogram from a single patient and saving the segmentation as a binary image stencil. Subsequent patient tomograms were then non-rigidly registered to the atlas MR using the adaptive-bases algorithm (ABA) for non-rigid 3D image registration [207]. Using the non-rigid transformation from the ABA, the atlas stencil was warped and applied to the target

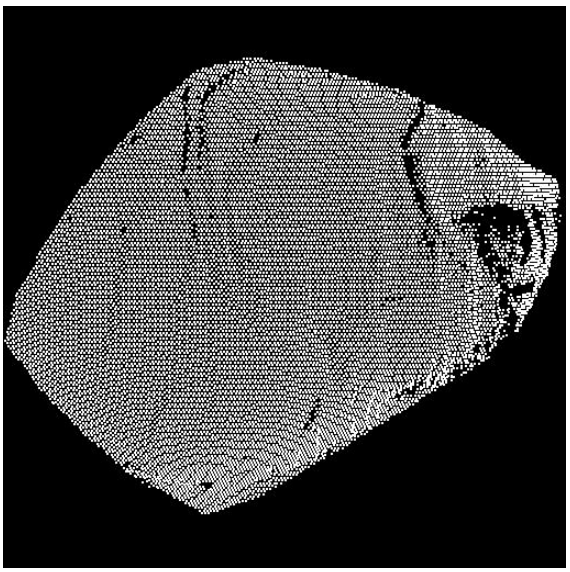

72(a) Segmented points acquired by the LRS device.

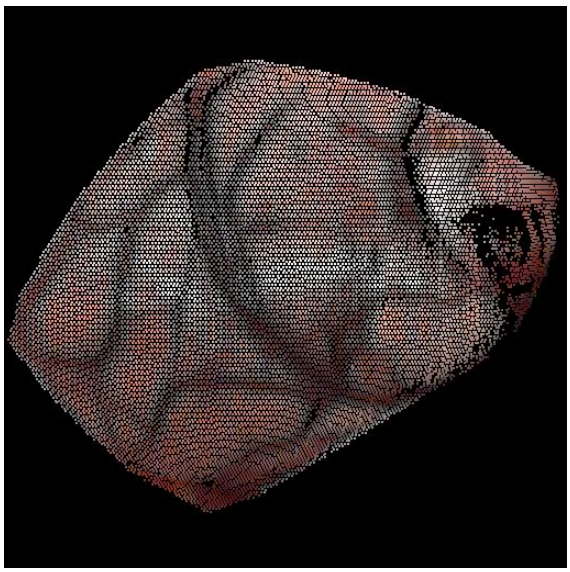

72(b) Textured points acquired by the LRS device.

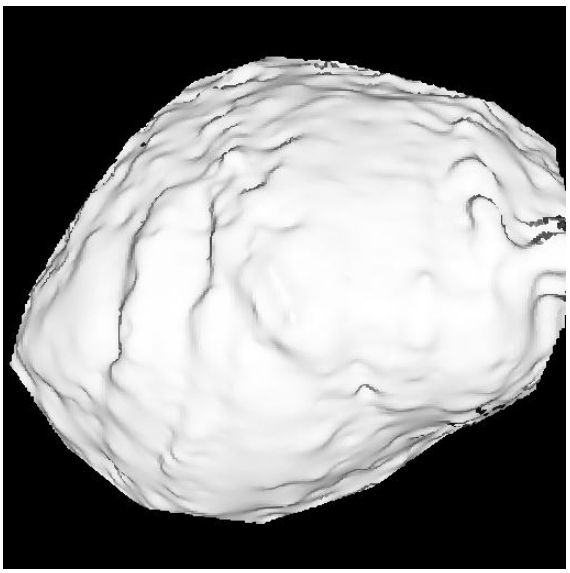

72(c) FasRBF fitting of the segmented points acquired by the LRS device.

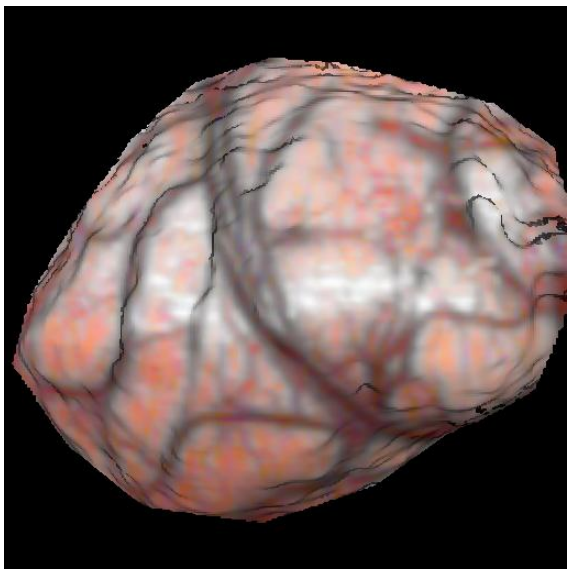

72(d) Textured FasRBF fitted surface.

Figure 72: Radial-basis function fitting of a segmented LRS points.

MR volume resulting in an automatic segmentation of the target MR tomogram.

The following steps, which used the segmented MR tomogram, distinguished the NRCA from the PRCA and allowed the NRCA to generate highly resolved textured surfaces. A marching cubes algorithm [220] was used on the segmented MR data to generate an initial approximation of the surface of the brain. Radial-basis functions, provided by the FastRBF Toolbox, were then used to define a parametric version of the marching cubes surface. The parametric estimation provided for a smoother, more regular representation of the brain's surface. An important effect of the smoother representation was the accurate and uniform distribution of surface normals. The FastRBF Toolbox also provided auxiliary methods to convert parametric representations of surfaces into discretized, polygon meshes with surface normal information. These methods were used to create dense surface meshes of the whole brain's surface. The surface normals from each point in the RBF fitted mesh were used as direction vectors for ray-casting into the preoperative MR tomogram. Between 5 and 10 voxels along normal direction were averaged and placed as the texture at the corresponding surface mesh point. The process of generating textured RBF fitted surfaces from preoperative images is shown in Figures 74 through 76.

Multi-scale/multi-resolution rigid texture surface registration

The RBF fitted surfaces, because of their highly resolved nature, were used within a multi-scale/multi-resolution rigid registration framework that aligned intraoperative LRS data to preoperative MR data. Multi-scale, in terms of textured surfaces, refers to the inter-point resolution of the point cloud. Multi-resolution refers to the resolution of the texture on the surface. There is evidence that multi-scale/multi-resolution registration of images using mutual information helps the registration process avoid local minima, which results in a more robust registration[221]. We adopt this philosophy for texture based mutual information registration of the intraoperative and preoperative surfaces in this paper. Multi-scale point clouds are generated by masking (or sampling) points from the full (or high) resolution textured surface according to some reduction factor. A reduction factor of 3 implies a

masking of the input textured surface such that, on average, the number of points in the sampled output is one-third of the initial point set. Multi-resolution clouds are generated in this paper by averaging texture information of all points in the high resolution textured surface within a given radius of a sampled point in the low resolution point cloud. An example of the multi-scale/multi-resolution point clouds generated using these methods is shown in Figure 77.

2D Textured surface registration using spherical homotopic transforms

The multi-scale/multi-resolution clouds are used within a mutual information surface registration protocol that simplifies the optimization space from six degrees-of-freedom (DOF) to three (DOF). An initial version of this method was described in [192]. In that paper, point-based registration [204] and iterative closest point (ICP) [167] methods were used to initially align the intraoperative textured surface to its preoperative counterpart. Subsequent texture based registration was constrained such that the LRS dataset was only allowed to move along the surface of a sphere fitted to the preoperative textured brain cloud. While this method simplified the registration, it required the incorporation of distance thresholds when determining inter-cloud correspondence. The reason for this was that the brain's surface, while similar to a sphere, is not completely spherical and optimizing along the fitted sphere allowed the textured LRS dataset to tilt into and out of the preoperative surface. This ultimately would allow multiple points on the textured surface to share a single corresponding closest point on the preoperative surface. In some instances this would allow mutual information to be maximized with erroneous statistical dependencies between the two textured clouds, resulting in a inaccurate registration.

In this paper the spherical transform is extended using the idea of homotopic transforms as proposed by Henri Poincaré. Poincaré conjectured that any simply-connected manifold in $n+1$ dimensional space could be reduced to a $n-sphere$. For three-dimensional space, this implies that a surface without holes (i.e. is simply connected) can be effectively reduced to the surface of a sphere. Observing that the brain is simply connected, we chose to reduce

the preoperative MR brain's surface to a fitted sphere. The intraoperative LRS data was also reduced to the same sphere. This resulted in a 2D registration problem of two textured surfaces about the surface of a sphere without the inconvenience of the LRS surface tilting into and out of the preoperative surface.

There are some considerations that have to be made to justify the use of this homotopic transform. The first is that we assume the texture based registration is a refinement of two already closely registered surfaces. This assumptions limits the effect of disparate warping in the two textured surfaces when projected onto the surface of the fitted sphere. Thus, a good approximation to the correct registered pose must be provided before texture registration. In this paper a portion of the initial alignment is provided using a point-based registration of corresponding points in each surface. However, point-based registration alone may not provide minimal surface-to-surface distance between the two clouds (which directly affects the amount of warping each surface receives relative to the other) and thus an extra step was taken to ensure good initial alignment.

In our previous work [192, 205], we employed ICP transforms to minimize surface to surface distance between the two could being registered. While, the ICP registration did provide transforms that minimized surface-to-surface distance it also introduced extraneous refinement of the registration that ultimately misaligned the feature in the two clouds. This mis-registration limited the effectiveness of the mutual information based alignment. In this paper, a surface normal based registration is used instead of the ICP registration to minimize surface to surface distance while maintaining the existing feature alignment provided by PBR registration. Registering via surface normals is essentially a point based registration whereby the correspondence between point clouds is generated using the intersection on the target surface of the surface normal from the source cloud. This process of generating correspondence is shown in Figure 78.

Once the surfaces are reasonably aligned via PBR and surface-normal registration, spherical descriptions were generated for each surface based on a sphere fitted to the target surface. Each point on a given surface is projected from the center of the fitted sphere outward along

the normal defined the surface point and the center of the sphere. The projected distance is equal to the radius of the fitted sphere. Any residual distance in the projection is recorded and used to reconstruct the original, un-warped surface after registration. An example of the spherical homotopic transform applied to a preoperative MR textured surface is shown in Figure 79.

Experiments

Two patients undergoing tumor resection therapies were examined using the methods described above and validated for intraoperative accuracy.

The first patient was a 65 year old male with a history of esophageal cancer (adenocarcinoma). He presented with progressive speech and language difficulty. An MRI revealed a $3cm$ area of abnormal enhancement in the left frontal lobe with significant edema. The imaging results were most consistent with a metastatic tumor. As a result, he underwent a stereotactic left frontal craniotomy for microsurgical resection of the tumor with image-guidance provided by the StealthStation system (Medtronic, Inc., Minneapolis, MN). The surgery resulted in an image complete resection of the tumor and he had no neurological deficits post-operatively.

The second patient was a 36 year old right handed male who had been complaining of headaches for several weeks. Similarly, he was noted by friends and coworkers to have undergone subacute changes in his personality. This symptomatology progressed and he was evaluated in the emergency room where an MRI of the brain was obtained. This demonstrated a 6x8cm mass originating in the left frontal lobe and crossing across the midline in the corpus callosum to the contralateral frontal lobe. The patient was taken to the operating room where a left frontal craniotomy was performed for tumor debulking using the StealthStation for intraoperative guidance. At operation, a large grayish, friable infiltrating mass was encountered. The frozen pathologic diagnosis was consistent with anaplastic astrocytoma.

Intraoperative characterizations of each patient's cortical surfaces were acquired by LRS

after removal of the dura (but before tumor resection), and then again after tumor resection. These two time points were used to determine brain shift over the course of the entire surgery. During these cases the LRS device was optically tracked in physical-space using the OPTOTRAK 3020 (Northern Digital, Inc., www.ndigital.com) localization system. This provided a method to register LRS-space datasets to physical-space, and thus allowed for the OPTOTRAK to act as a independent measure of accuracy. During each acquisition, the LRS was brought to within 20-30cm and a LRS dataset was acquired and registered to physical-space[1]. After LRS acquisition, 4-7 easily identifiable landmarks on the brain surface (e.g. vessel bifurcations) were localized in physical-space using the OPTOTRAK and a tracked pen-probe. The physical-space points from the pen-probe acted as independent targets for the shift-tracking protocol. The data acquired from each patient were subjected to the rigid registration and shift-tracking protocol methods described earlier and the results were examined.

Rigid registration results in this paper are demonstrated visually. Quantitive validation of the rigid-registration methods proposed here are still under development. In the future, target points acquired by the OPTOTRAK will be expertly identified in the preoperative tomograms and registration errors between the two localizations will be given as a measure of registration accuracy. However, for this paper, expert localizations were not available, thus the results of the rigid-registration protocol are demonstrated in overlay visualizations.

Shift tracking accuracies are quantified using a variety of measures. Points acquired just after dural opening were transformed from physical-space to corresponding locations in the initial LRS dataset and subjected to the shift-tracking protocol. The calculated shifted positions of the targets were then transformed from the serial LRS dataset's (after resection) space to physical space and compared against corresponding physical space localizations for shift tracking accuracy. Measured and calculated shift magnitudes are reported as a measure of the shift tracking protocol's ability to determine the extent of motion. Directional accuracy of the resolved shift vectors is also reported as a cosine measure of the angle formed

[1]The registration process for aligning LRS-space to physical-space is provided in [219]

by the calculated and measured shift vectors. A $\cos(\Theta)$ of 1 between the calculated and measured shift vectors indicates a perfect tracking, in terms of direction only; values less than 1 indicate there is some directional error in the calculated shift. Finally, discrepancies between calculated physical-space target locations (via the shift-tracking protocol) and measured physical-space target locations (via OPTOTRAK) are quantified as shift-tracking error (STE), defined as follows:

$$STE = X_i^{final} - T_{ST}(X_i^{initial}), \tag{17}$$

where $X_i^{initial}$ is the initial position (after dural opening) of target X_i, T_{ST} is the shift tracking protocol represented as a transform, and X_i^{final} is the final physical-space location of the target point (after resection).

Results

Figures 80 and 81 display the pre-resection data acquired from each patient during surgery. For Patient 1 the area of resection is located between targets 5 and 6 (see Figure 80(b) and 80(c)). The tumor for this patient was located sub-surface and therefore presented little evidence of its existence on either the preoperative or intraoperative surfaces. The tumor/resection region for Patient 2 is located anterior to target point 2 (see Figure 81(b)). This tumor was close to the surface and manifested itself as the darker region in the preoperative textured cloud.

The reader should note that, in both cases, intraoperative tracking of physical space locations and transforms was not complete and therefore some post-processing was required. For Patient 1, the LRS data were acquired within the focal length of the device lens. This lead to systematic distortions in the LRS-space localization of the acquired point cloud. Figure 82 shows the discrepancy in the location of the tracked LRS dataset reported by OPTOTRAK and the location of the corresponding fiducials for this dataset. The effect of this error was inaccurate initial alignment of the image-space with LRS-space for the SurfaceMI

and inaccurate validation results for the shift-tracking protocol. This systematic error was overcome retrospectively by manually relocalizing the target points on the pre- and post-resection LRS clouds in LRS-space. These points were then registered to their physical-space counterparts and this transformation was used to align pre- and post-resection LRS-spaces to physical-space[2]. After re-alignment, data from the OPTOTRAK were used for validation of the shift-tracking protocol. In Patient 2, we believe that the reference coordinate system was disturbed at the time of draping. This resulted in physical space localizations before sterilization to be inconsistent with localizations during surgery. However, localizations during the surgery (i.e. after dural opening and post-resection) were consistent. The result of this inconsistency manifested itself as an inaccurate initial registration, provided by the patient fiducials, for the SurfaceMI protocol (see Figure 83). To correct for this, fiducials were manually localized on the preoperative LRS-cloud and transformed into physical-space. Corresponding localizations were made in image-space and used to register the image-space to physical-space. The alignment provided by the manual localizations was used only as the initial estimate of alignment for the SurfaceMI algorithm and did not affect the OPTOTRAK validation of the shift tracking protocol.

Figure 84 demonstrates the results of the SurfaceMI rigid registration protocol on the preoperative and intraoperative surfaces for Patients 1 and 2. Visual inspection of the overlays shows that the area of resection is accurately aligned with the corresponding region on the preoperative surface. For Patient 1, the target points 5 and 6 in Figure 80(b) show the region of resection. The corresponding region in Figure 80c is accurately oriented in Figure 84(a). Similar results are shown for Patient 2. The large vessel near the tumor, highlighted in Figure 81(b) and 81(c), is correctly registered in Figure 84(b).

Figures 85 and 86 indicate the localized and calculated shift vectors for the target points acquired by the OPTOTRAK for Patients 1 and 2, respectively. Tables 10 and 11 provide corresponding quantitative results of the shift-tracking protocol on each patient's intraop-

[2]The RMS fiducial registration error (FRE) [216] for the pre- and post-resection alignment transforms were: $1.4mm$ and $1.2mm$, respectively.

erative data. The figures show the serial tracked LRS dataset along with the initial and serial positions of the target points as determined by the OPTOTRAK and shift-tracking protocol. For patient one, the average shift measured by OPTOTRAK was $5.56mm$ with the largest shift observed at target point 1 ($9.33mm$) and the smallest shift observed at point 4 ($1.24mm$). Calculated shifts averaged $6.49mm$, with the largest shift observed at point 1 ($9.69mm$) and the smallest shift at point 3 ($4.48mm$). The average cosine deviation for Patient 1 was $cos(\Theta) = 0.77$, or approximately 40 degrees. For Patient 2, the average shift observed by OPTOTRAK was $8.33mm$, with the largest shift at point 0 ($12.29mm$) and the smallest at point 3 ($4.64mm$). The average calculated shift was $9.85mm$ with the largest shift at point 0 ($13.83mm$) and the smallest at point 3 ($5.92mm$). The average cosine deviation for Patient 2 was $cos(\Theta) = 0.93$, or 21.6 degrees.

Figures 87 and 88 show shift tracking visualizations with respect to preoperative textured surfaces. These figures use the results of the SurfaceMI registration, the tracked position of the serial LRS textured surface and the shift-tracking protocol to juxtapose the intraoperative shift-tracking data with the preoperative images sets.

Discussion

The results from the SurfaceMI rigid registration and shift tracking protocol exhibit the ability to automatically determine shift relative to the patient-specific preoperative image sets using a LRS system. The rigid registration results show that the algorithm is capable of providing relevant alignment of preoperative and intraoperative data, e.g. see Figure 84. Considering the corresponding results shown in Figures 87 and 88 that demonstrate the location of brain shift relative to the preoperative images sets, the SurfaceMI registration results allow for the accurate placement of intraoperative shift within a preoperative framework.

With respect to the calculated shifts for each patient, the results closely resemble the OPTOTRAK observed shifts. Paired two-tail t-tests for the observed and calculated shifts from Patients 1 and 2 yielded no significant difference in the means of either sample set. For Patient 1 an apparent outlier was point number 4, whose observed shift was relatively low

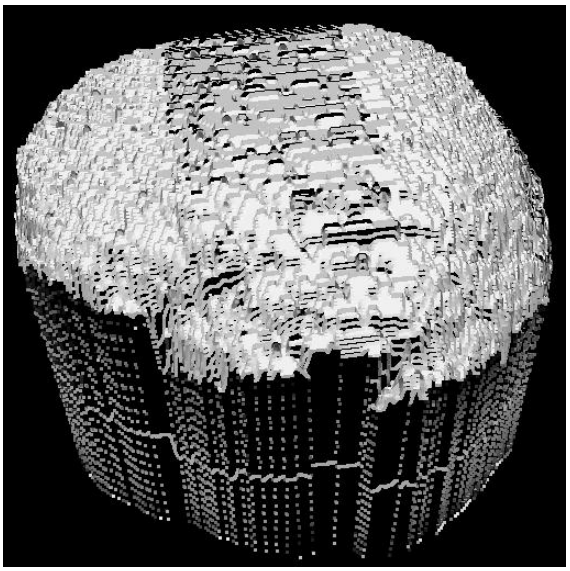

73(a) PRCA results demonstrating the supersampled point distribution from the ray-casting algorithm.

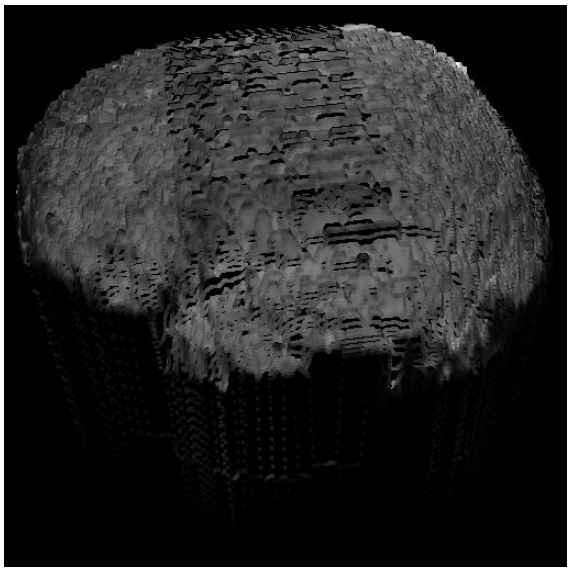

73(b) PRCA results demonstrating a textured supersampled point cloud from preoperative MR images.

Figure 73: Results from the parallel ray-cast algorithm for textured point cloud generation from preoperative MR images.

Table 10: Results of *in vivo* shift-tracking for Patient 1.

Target Point Number	Shift Magnitude		STE	$\cos(\Theta)$
	Observed	Calculated		
0	7.89	7.72	4.14	0.86
1	9.33	9.69	3.39	0.94
2	4.41	4.64	2.93	0.79
3	3.32	4.48	3.98	0.50
4	1.24	6.07	5.11	0.82
5	3.99	5.15	2.99	0.82
6	8.83	7.64	3.38	0.93
AVERAGE	5.56±3.12	6.49±1.93	3.70±0.77	0.81±0.14

Table 11: Results of *in vivo* shift-tracking for Patient 2.

Target Point Number	Shift Magnitude		STE	$\cos(\Theta)$
	Observed	Calculated		
0	12.29	13.83	3.78	0.96
1	8.65	8.91	1.61	0.98
2	7.77	10.75	3.80	0.97
3	4.64	5.92	3.44	0.81
AVERAGE	8.33±3.15	9.85±3.31	3.16±1.04	0.93±0.08

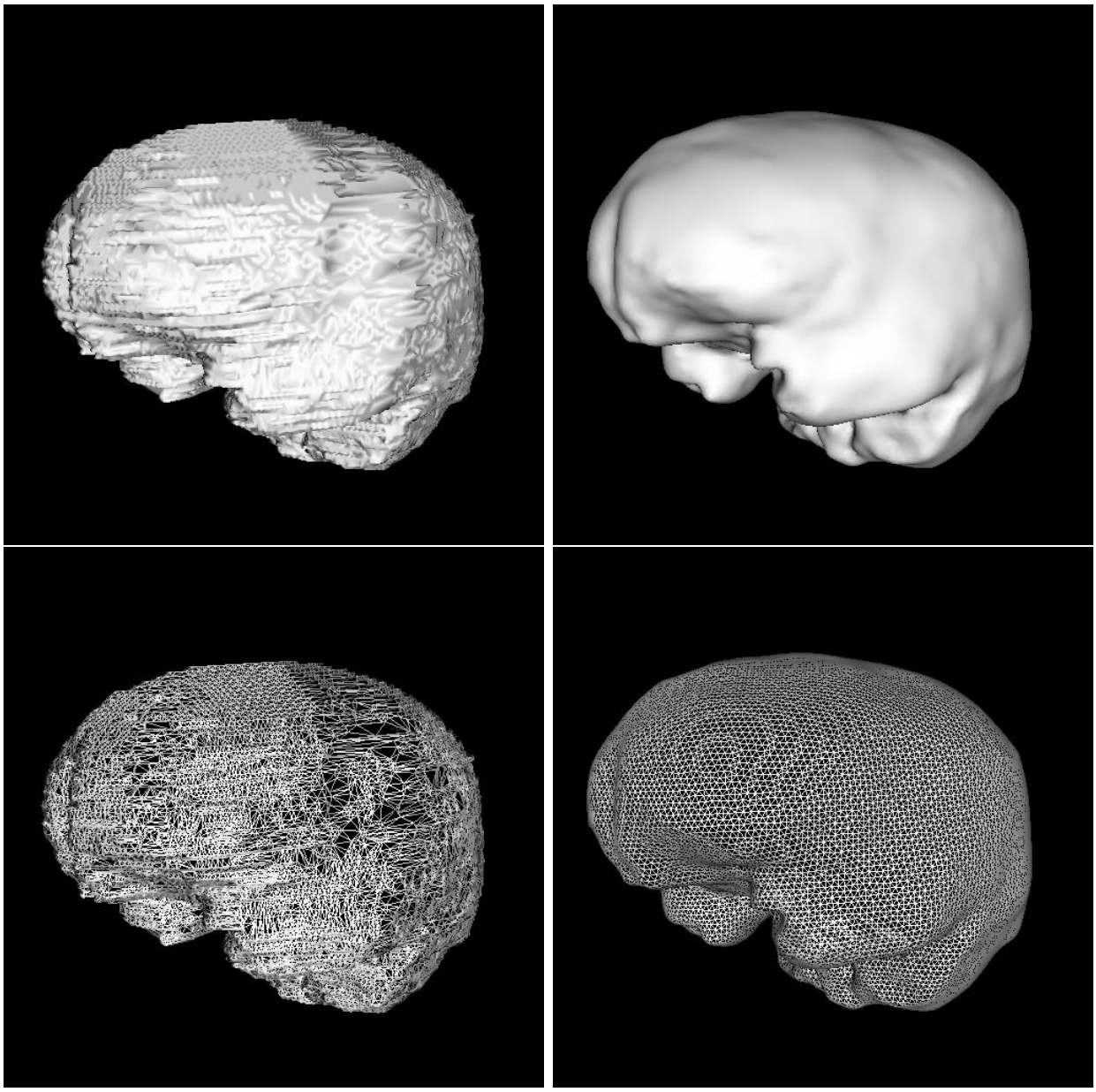

Figure 74: Textured surface generation from a segmented preoperative MR tomogram, step 1: polygonal surface tessellation. The left column shows a marching cubes tessellation of a segmented preoperative MR tomogram. The right column shows an radial-basis function fitting of the marching cubes surface, resulting in a smooth polygonal mesh. Wireframe views of the marching cubes and radial-basis function surfaces are shown in the bottom row for comparison purposes. Notice the even distribution of surface polygons in the radial-basis function wireframe surface.

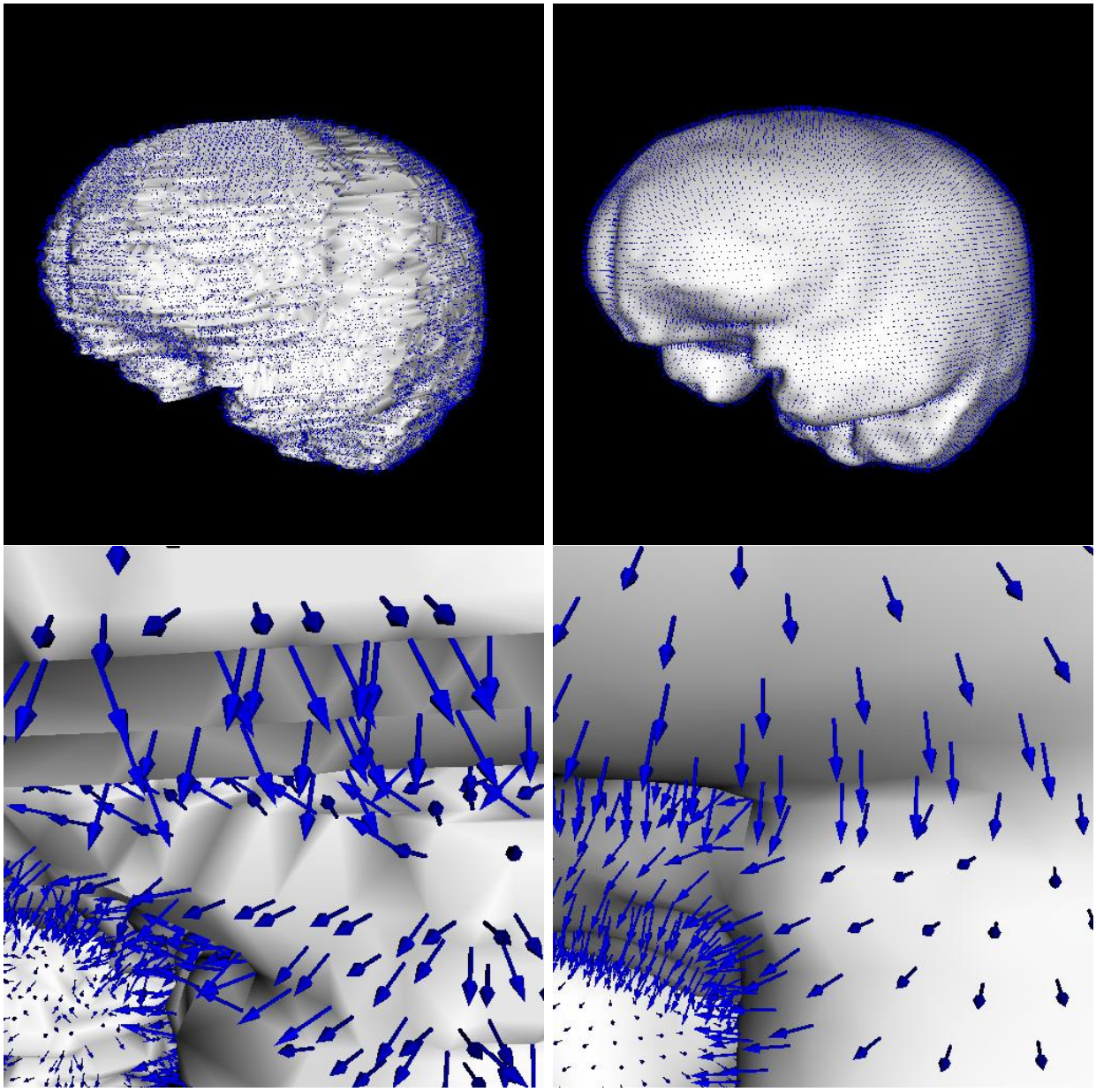

Figure 75: Textured surface generation from a segmented preoperative tomogram, step 2: normal generation. These figures illustrate the normals generated from both marching cubes and radial basis function surfaces. The top row of images shows a zoomed out view of both surfaces with normal glyphs assigned to each surface point shown in blue. The bottom row of images shows zoomed in views of corresponding locations from the zoomed out images. The normal glyphs are readily apparent as arrows pointed away from the surface. The smooth, uniform distribution of normals from the radial basis function surface (shown in the bottom right) are critical to generating well-resolved textured surfaces from preoperative tomograms.

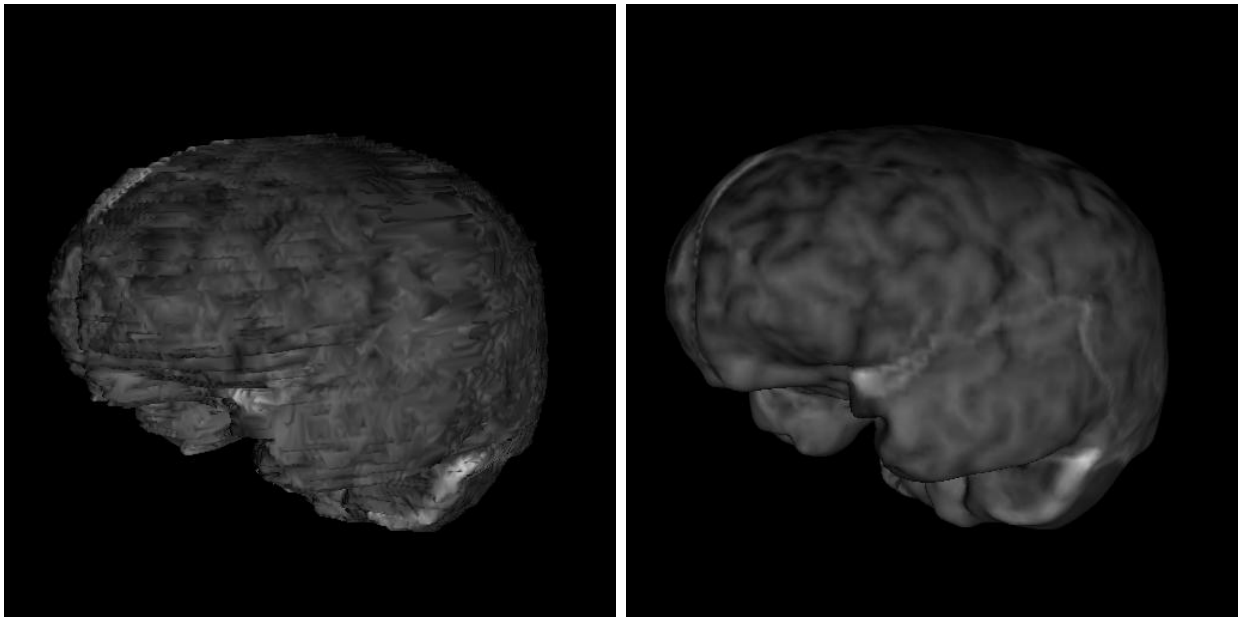

Figure 76: Textured surface generation from a segmented preoperative tomogram, step 3: ray-cast color encoding. These figures demonstrate the result of the ray-cast color encoding process on the marching cubes and radial basis function surfaces. The ray-cast algorithm starts at the voxel associated with a given surface point on the mesh and penetrates the preoperative tomogram along surface normal associated with that point. The algorithm uses the average intensity along the projection direction (normal) to represent the surface intensity for the polygonal mesh. From these images, one can see that smooth, uniform distributions of surface normals is critical to obtaining good textured surfaces of the brain from preoperative images.

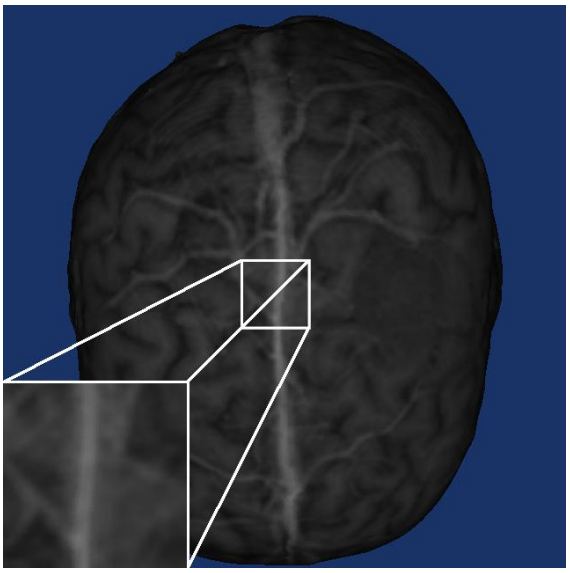

77(a) Resolution level 0

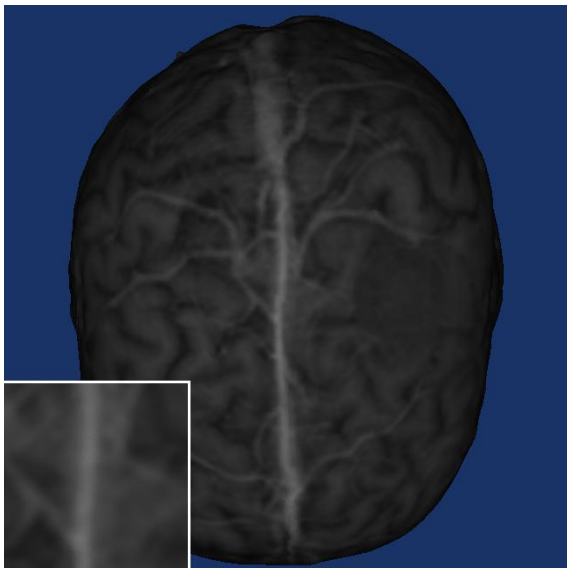

77(b) Resolution level 1

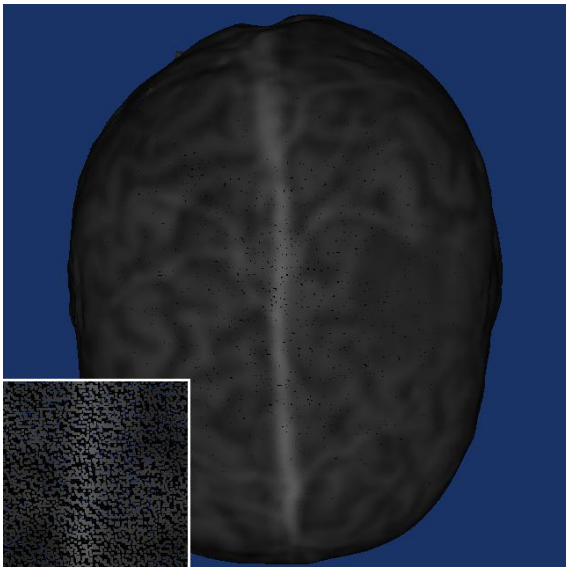

77(c) Resolution level 3

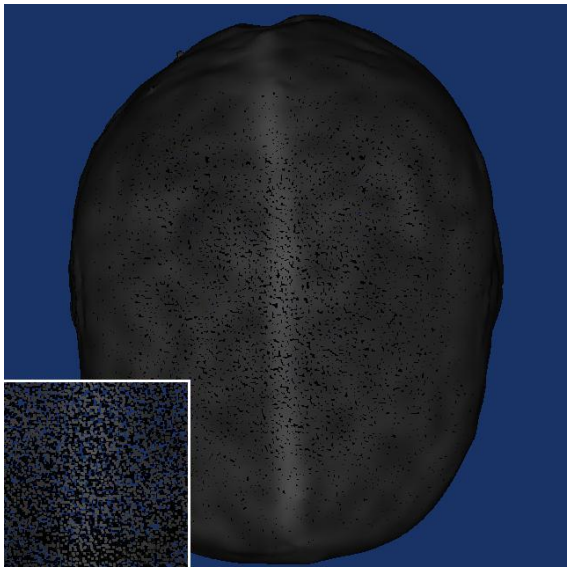

77(d) Resolution level 5

Figure 77: Multi-scale/multi-resolution textured LRS datasets. Each figure shows a different scale/resolution of a textured preoperative MR brain cloud. A region of interest is highlighted in (a) and zoomed into to show the effects of changing resolution levels on a finer scale. The same region of interest is shown, zoomed-in, as an insert in (b), (c), and (d).

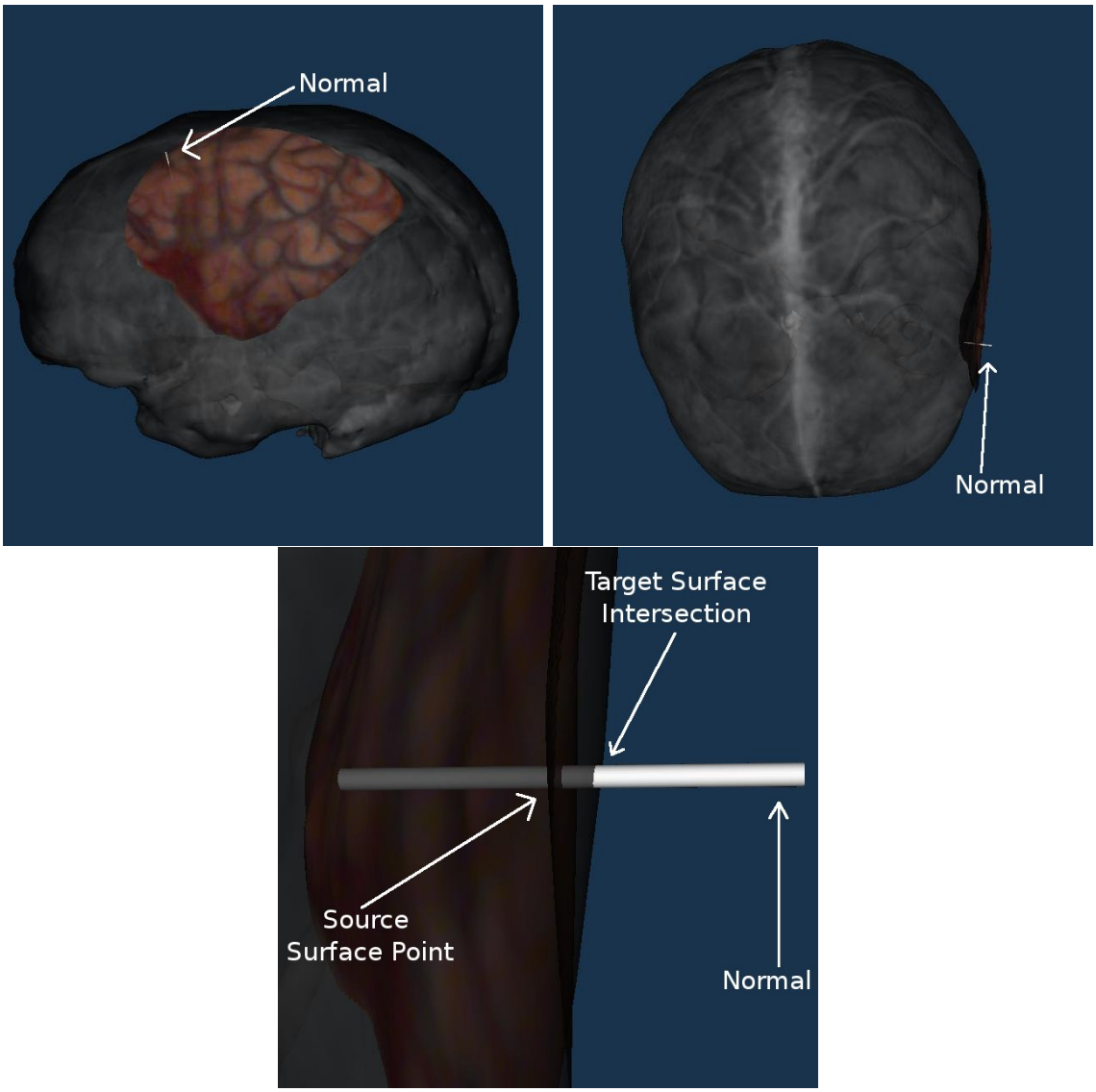

Figure 78: Inter-surface correspondence based on surface normals. The top row shows sagittal and axial views, respectively, of a point on the source cloud and its associated normal. The bottom figure shows the determination of correspondence based on the intersection of the surface normal and the target surface.

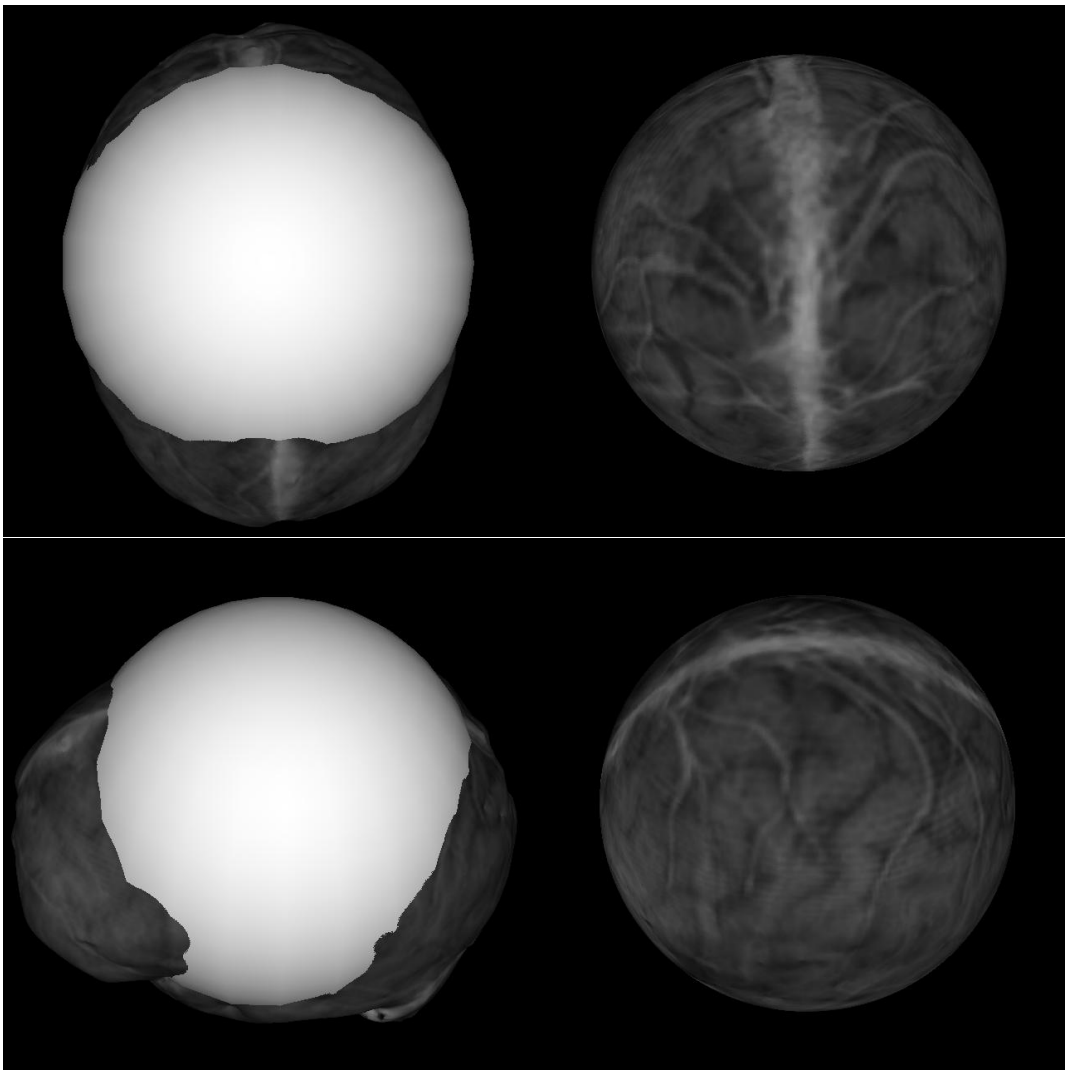

Figure 79: Spherical homotopic transform for textured surfaces of the brain. In the top row, on the left is a axial view of the brain surface and the fitted sphere. In the top row, on the right is the transformed cloud. The bottom row shows corresponding images in from a sagittal point of view.

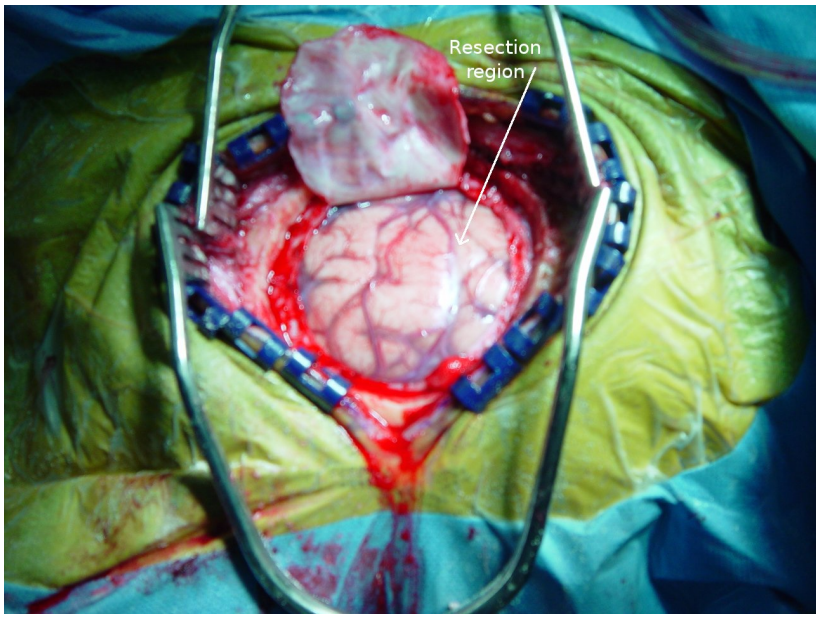

80(a) Digital Image

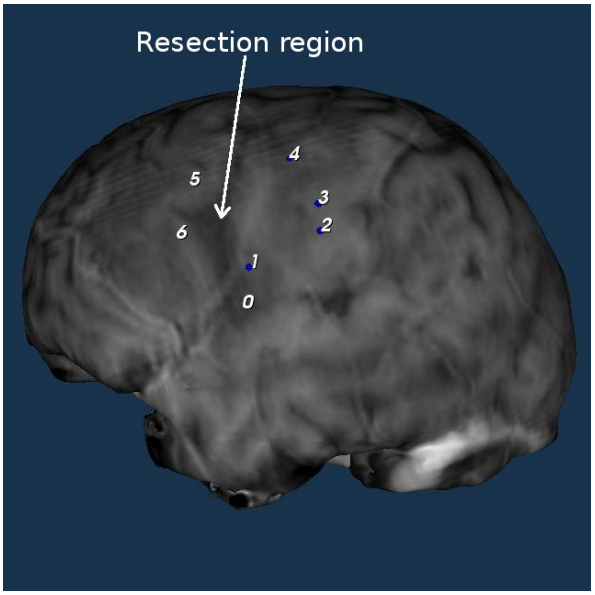

80(b) Preoperative Textured Surface

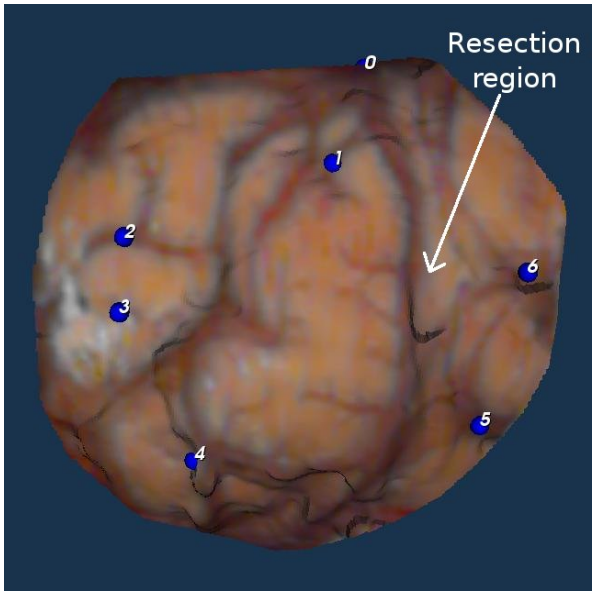

80(c) Intraoperative Textured Surface

Figure 80: Data for Patient 1. Top row: intraoperative high resolution of digital image of the surgical FOV. Bottom row, from left to right: preoperative MR textured surface and intraoperative textured LRS surface. The resection region in each image is highlighted for clarity.

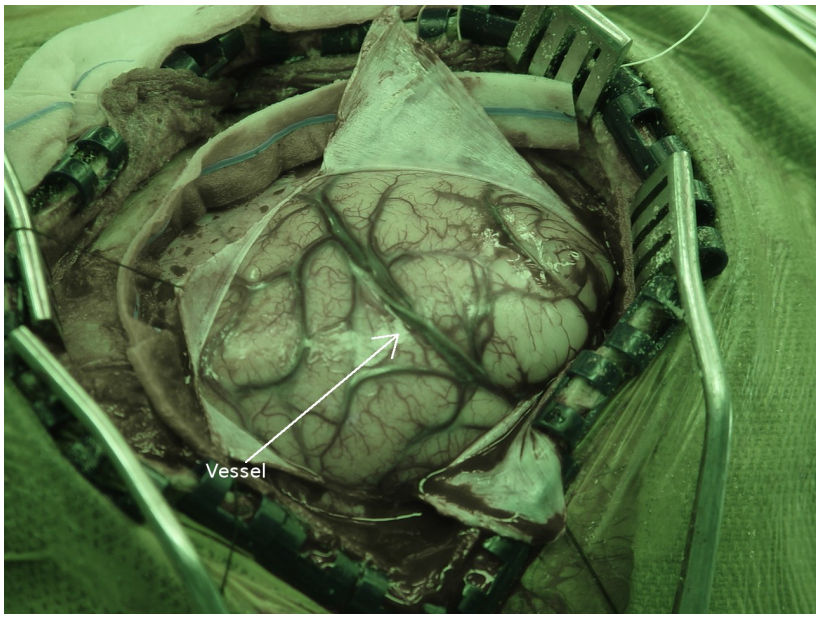

81(a) Digital Image

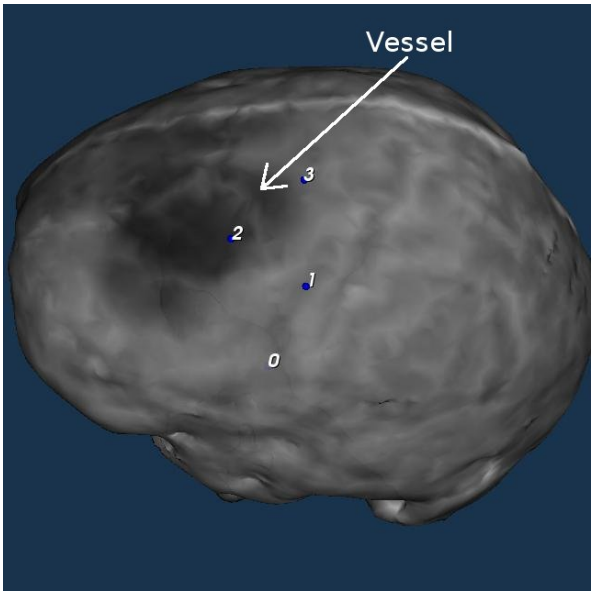

81(b) Preoperative Textured Surface

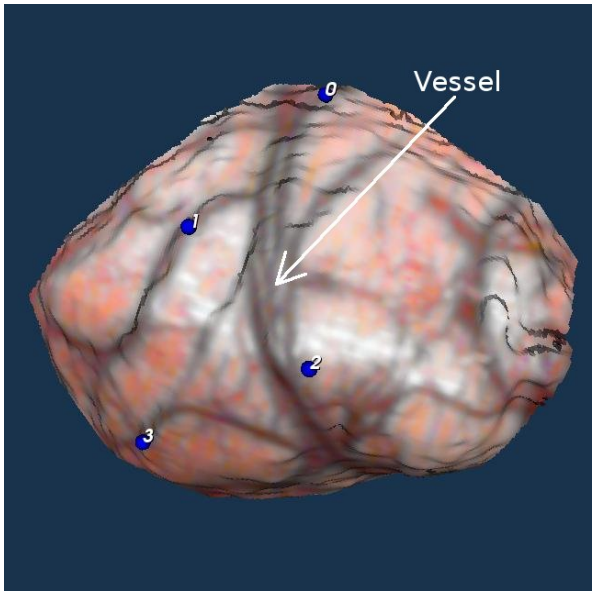

81(c) Intraoperative Textured Surface

Figure 81: Data for Patient 2. Top row: intraoperative high resolution of digital image of the surgical FOV. Bottom row, from left to right: preoperative MR textured surface and intraoperative textured LRS surface. A corresponding vessel in the three images is highlighted for clarity.

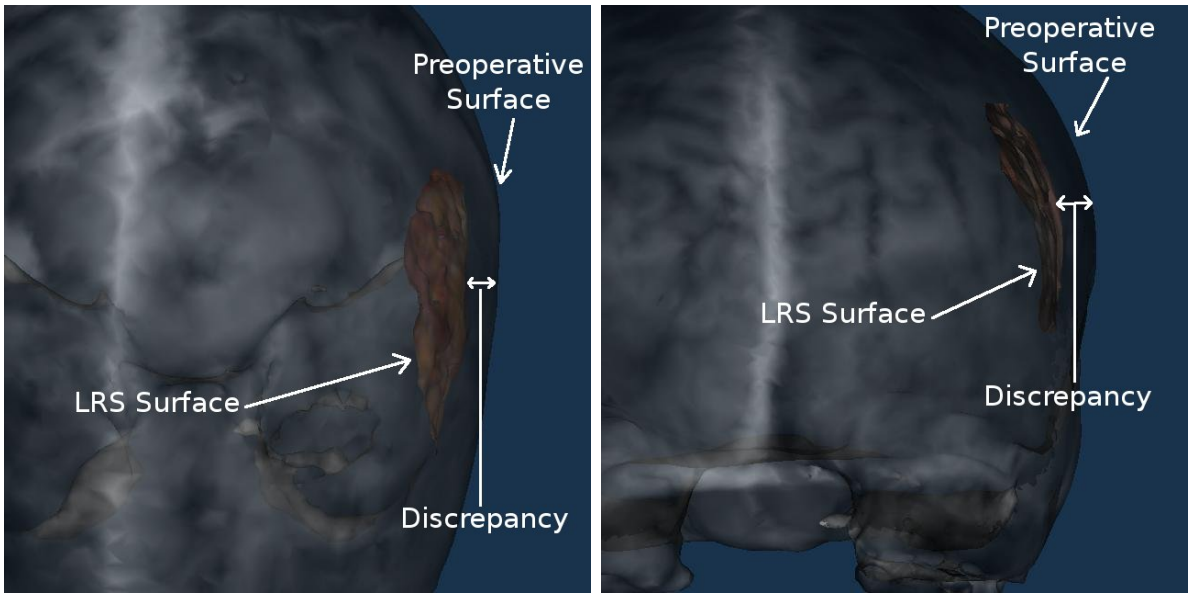

Figure 82: Discrepancies in physical space tracking experienced for Patient 1. The image on the left shows an axial view of the overlay of preoperative and intraoperative data using tracking data provided by the OPTOTRAK. The image on the right shows the corresponding scene from a coronal view.

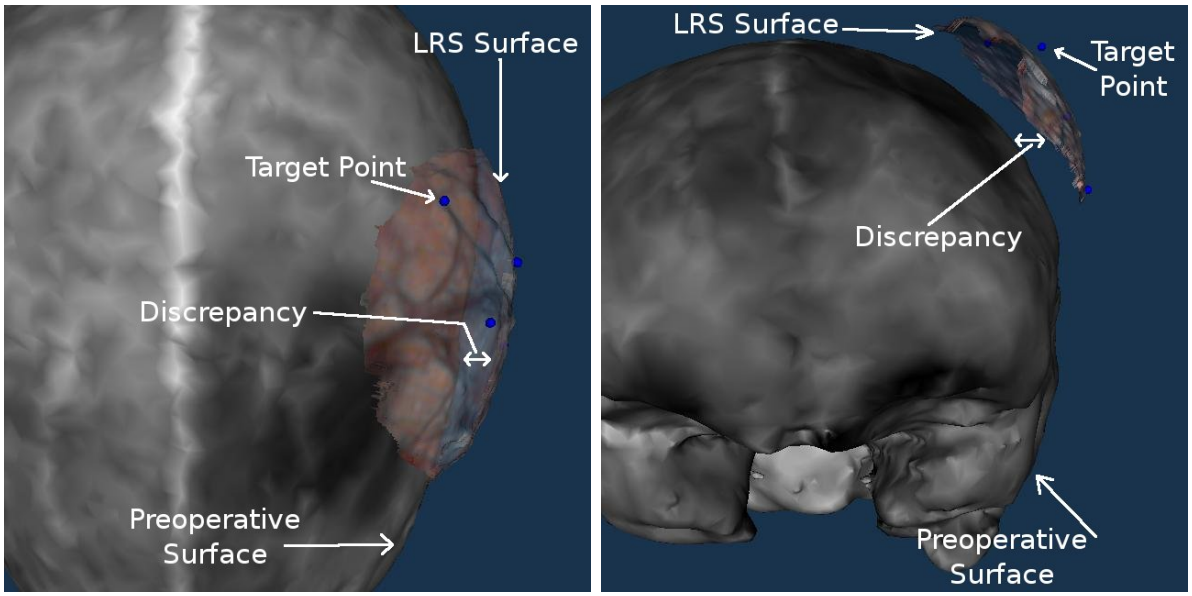

Figure 83: Discrepancies in physical space tracking experienced for Patient 2. The image on the left shows an axial view of the overlay of preoperative and intraoperative data using tracking data provided by the OPTOTRAK. The image on the right shows the corresponding scene from a coronal view.

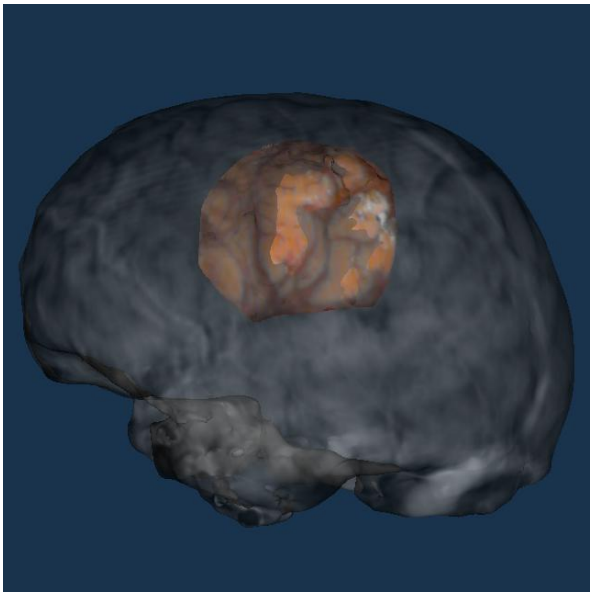

84(a) SurfaceMI registration results for Patient 1.

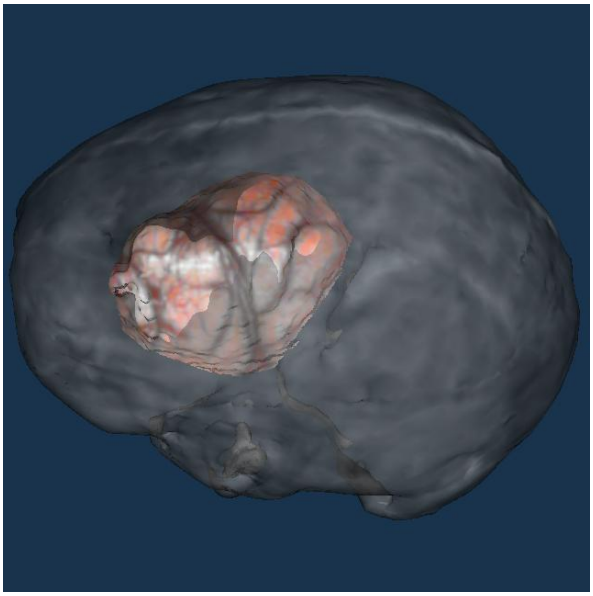

84(b) SurfaceMI registration results for Patient 2.

Figure 84: Textured surface registration results for Patients 1 and 2. On the left are the rigid-registration results for Patient 1, and on the right are the Results for Patient 2. These results were generated using each of the methods outlined in this paper, i.e.: textured RBF fitted surface generation, multi-scale/multi-resolution registration, and homotopic transforms.

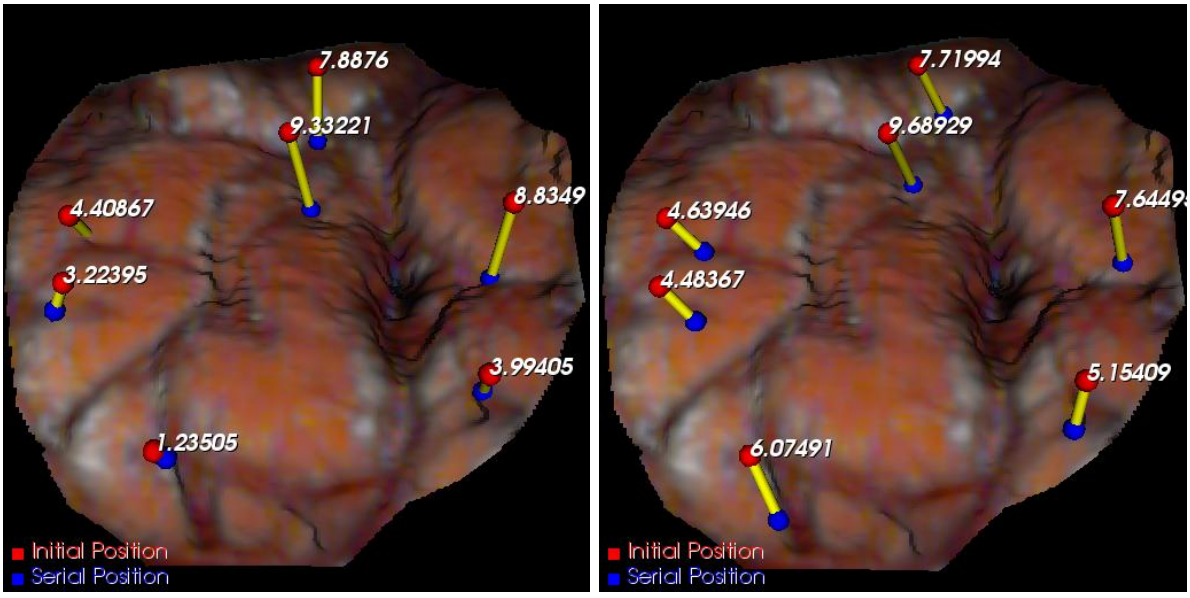

Figure 85: Observed and calculated shift-vectors for Patient 1. On the left is the observed shift vectors (using OPTOTRAK) from the initial (after dural opening) to serial (after resection) acquisition. On the right are the calculated shift vectors provided by the shift-tracking protocol for initial and serial acquisitions.

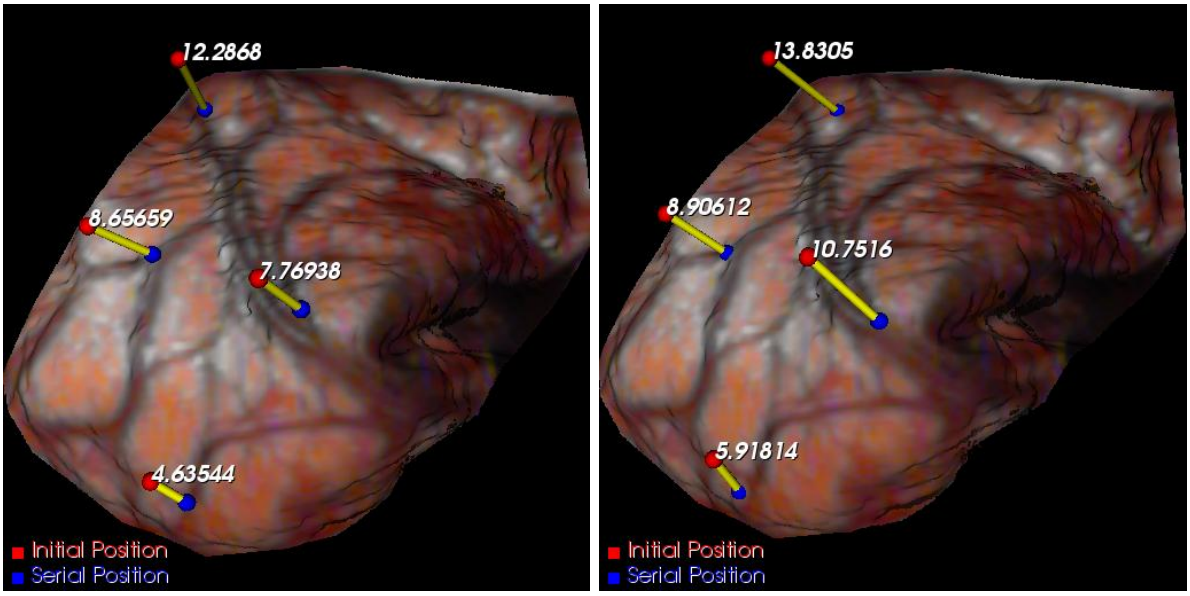

Figure 86: Observed and calculated shift-vectors for Patient 2. On the left is the observed shift vectors (using OPTOTRAK) from the initial (after dural opening) to serial (after resection) acquisition. On the right are the calculated shift vectors provided by the shift-tracking protocol for initial and serial acquisitions.

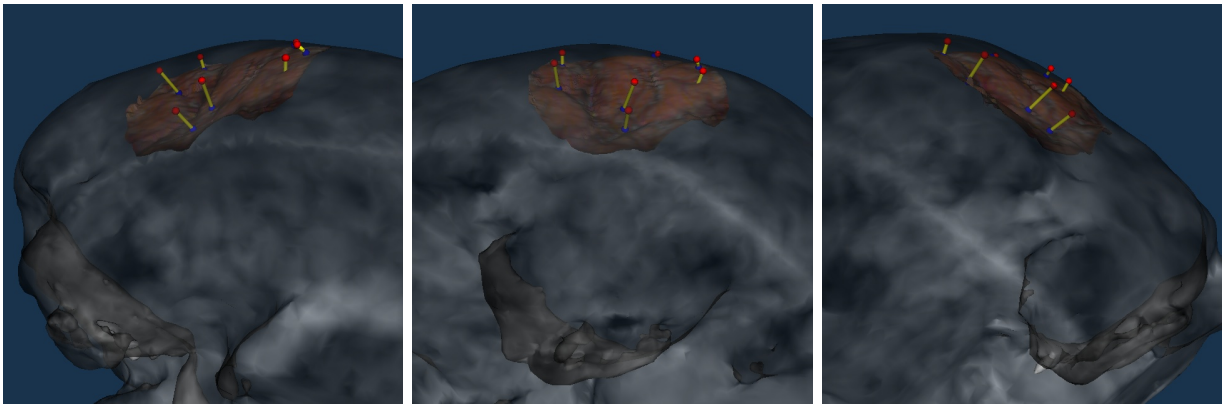

Figure 87: Shift measurement for Patient 1 overlaid onto preoperative textured MR surface. Each figure, from left to right, demonstrates the overlay from a different camera angle to assist with depth perception.

(1.24mm) but the calculated shift was markedly higher (6.11mm), resulting in a 5.11mm STE between the two points. This results is most likely due to the location of point 4 being near the craniotomy margin. These regions are generally subject to large feature discrepancies as portions of the brain surface disappear under and appear from the skull margins. Disparate feature structures like these confound mutual information based registration methods [222]. In the case of this dataset, the deformable registration of the texture images did not register this area of the brain as well as the interior area (away from the craniotomy margin). As a result the calculated shift location of the target point is significantly different from that observed by the OPTOTRAK system. Removing point 4 from the mean and standard deviation calculation, based on its outlier status, reduces the mean STE for Patient 1 to 3.47$\pm$0.50mm. Patient 2 exhibited similar outliers in point 0 and point 3. Again, these target points were near the craniotomy margin and were most misregistered by the non-rigid textured image registration. Incidentally, the STE results for point 0 are compensated by a faulty physical space localization as well. That is, given a more accurate OPTOTRAK localization of the serial target for point 0, the STE would have been larger. An exceptional shift tracking result is demonstrated by point 1 in Figure 86. The magnitude and alignment for this vector are in excellent agreement with what was observed by OPTOTRAK.

Concatenating the results of the two registration protocols provides the novel shift visualizations see in Figures 87 and 88. These are the first images demonstrating the capability of an LRS device accurately depicting intraoperative brain shift relative to preoperative tomograms. The shift overlay images for Patient 1 clearly show the area of the resection dipping into the preoperative brain tissue (see Figure 87). Regions near the craniotomy margin do exhibit as much shift for this patient. This result is in stark contrast to the brain shift observed from Patient 2 (see Figure 88). Patient 2's brain also sagged in the direction of gravity near the resection margin, but other areas near the craniotomy margin also collapsed as the surgery progressed. These two figures demonstrate the complex response of the brain's surface to resection therapy.

The discrepancy seen between the OPTOTRAK and shift-tracking protocol in localiz-

ing brain surface shift (i.e. STE's of approximately $3mm$ across both patients) owes itself to many factors. Some of the most significant causes of error while validating the shift-tracking protocol include the non-rigid registration method, physical-space localization, and respiratory motion of the brain surface during acquisition.

The non-rigid registration method used in this paper does not account for feature discrepancies over the course of surgery. Future work related to the texture image registration will require the adequate identification of disparate features in the serial texture images. This may require more texture images over the course of surgery (as compared to the initial and final textures acquired in this paper) to slowly track the feature movements over the course of surgery. The ultimate solution may require user intervention to assist in the identification of non-interesting regions in the two texture images.

Another source of error in the validation process is the accurate and reproducible identification of surface targets that: 1) are easily localizable, 2) will remain in the FOV over the course of surgery, and 3) are reasonably distal to the craniotomy margin. The localization of the targets in the cases presented in this paper were assisted with image-guidance, but were mostly a function of the surgeons memory as to the exact location marked. We are currently working on strategies to employ high resolution images of the brain surface as a method to precisely preserve target point locations between pre- and post-resection acquisitions. The other sources of target localization error are subject to case-by-case refinement based on what features are available after craniotomy and the planned resection margins. However, the results and experiences from the intraoperative data collected in this paper suggest that well thought out target point identification during surgery is critical to *in vivo* validation.

Respiratory motion and motion related to the cardiac cycle is another area of consideration in the current validation strategy. In Patient 1, motion artifacts due to respiration and the cardiac cycle were not observed to a large extent. That is not to say that the motion was not there and did not confound some of the results for that patient, just that at the time of acquisition the motion of the brain was not immediately noticeable. In Patient 2, however, respiratory motion was clearly evident. In fact, for Patient 2, all LRS acquisitions were done

under breath hold at end expiration and all physical space localizations were timed with end expiration. While this may be an acceptable solution for the current design, clinical validation and deployment of the LRS device will require a more spontaneous measurement of the brain's surface. A static laser range scanner system is now under investigation as a method to instantaneously acquire range data of the brain's surface, as compared to the moving laser stripe method of the current scanning system.

Conclusions

Placed within the perspective of an initial clinical validation of brain shift tracking using a LRS device, the results of this paper demonstrate feasibility and viability of the methods described *in vivo*. The rigid-registration results demonstrate the ability to accurately register intraoperative data to preoperative image sets. The quantitative validation of the shift-tracking protocol and low STEs (approximately $3mm$) for the preliminary cases provide support for the use of an LRS device as a cortical surface shift measurement tool. These results are augmented by the visualizations shown in Figures 87 and 88, which provide 3-dimensional insight into the non-rigid motion of the brain during surgery along with the therapeutic context found in the preoperative images. These figures also present an initial step in the incorporation of intraoperative shift measurement within a computational method of updating whole-brain deformation during surgery for IGS applications. The results provide encouragement for future work related to comprehensive clinical validation of the methods described in this paper.

Acknowledgments

The authors would like to thank Logan W. Clements, Prashanth Dumpuri, Dr. Todd Sun and the neurosurgical OR staff for their assistance in data collection.

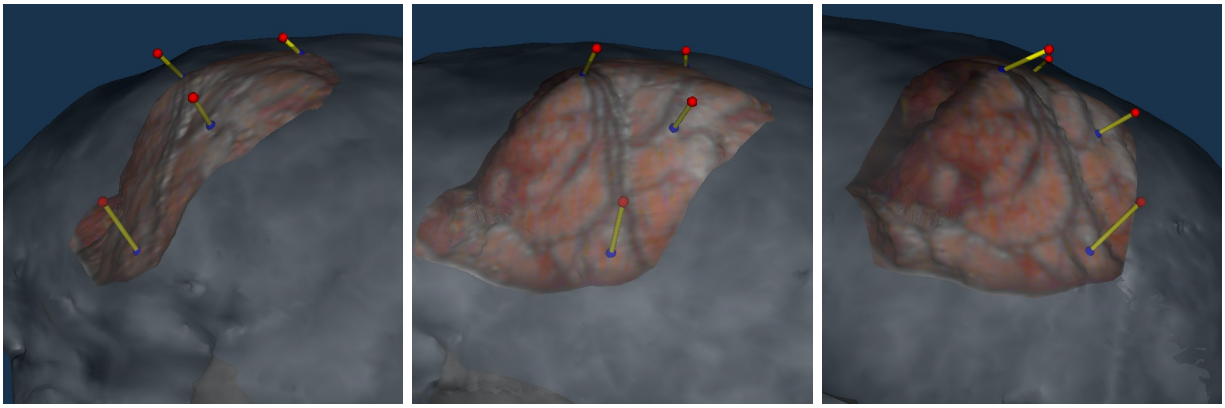

Figure 88: Shift measurement for Patient 2 overlaid onto preoperative textured MR surface. Each figure, from left to right, demonstrates the overlay from a different camera angle to assist with depth perception.

CHAPTER IX

SUMMARY

This dissertation documents the process and development of a cortical shift tracking procedure using a laser range scanner during neurosurgery. The impetus for this research was provided by the need for sparse-data within an model-updated image-guided surgery (IGS) system. Current IGS systems require rigidity during surgery, which is not possible due to soft-tissue deformation of the brain. Model-updated IGS provides correction for these soft-tissue deformations, allowing for more accurate neuro-navigation during surgery.

Laser range scanning (LRS) provides a simple and effective method for sparse-data acquisition of the cortical surface during neurosurgery. It is non-contact and efficient at providing relevant geometry data of the exposed brain. The LRS device used throughout this dissertation is also capable of providing a mapping of surface intensity along with the geometry data. The resulting data is feature-rich and enables shift tracking based using both geometry and intensity information from the exposed cortical surface.

In developing a method to incorporate the unique data acquired by the LRS into a model-updated IGS framework, two main goals were achieved: (1) rigid alignment of the LRS data to preoperative MR tomograms, and (2) non-rigid registration of serial LRS acquisitions for brain shift tracking. Chapters III through V describe the method developed for rigid registration of the intraoperative data to preopertive MR tomograms via texture surface registration. Chapter III introduces the registration algorithm and demonstrates it's ability to register phantom textured surfaces. Chapter IV demonstrates the validation of the algorithm on true multi-modal surfaces and introduces use of the algorithm on intraoperative data. Chapter V expands on the initial clinical experiment and presents results for intraoperative to preoperative registration based on 8 clinical cases. Chapter V also presents a novel visualization system which provides context sensitive cues of the surgical field-of-view (FOV) using intraoperative and preoperative data.

Given the baseline alignment of the intraoperative surface to preoperative data, a shift-tracking protocol that uses serial LRS datasets was developed and explored in Chapters VI and VII. Chapter VI introduces the shift-tracking algorithm which utilizes texture image registration to provide correspondence between serial LRS datasets. Chapter VII validates the algorithm on phantom data and presents a clinical example of cortical shift tracking. The results of the phantom trials indicate highly accurate shift tracking is possible under phantom conditions. The *in vivo* example demonstrates proof-of-concept of the algorithm on intraoperative data.

Chapter VIII describes extensions to the methods described in Chapters III to VII. These extensions are specific enhancements to shift tracking using LRS which make the algorithms and visualization systems more robust. Furthermore, Chapter VIII presents preliminary clinical validation of the shift tracking method developed in this dissertation.

Future work with respect to the research presented in this dissertation will include clinical validation of the methods and algorithms devised. There are many questions which will require investigation, including: respiratory motion effects on the accuracy of shift tracking, the appearance and disappearance of cortical surface features on the registration methods developed, and the application and validation of the the shift tracking results into a computational model. The current model for LRS data acquisition intraoperatively is to suspend respiration during acquisition. Another, more instantaneous, method for range acquisition may be required for regular use in the OR. A modification to the current LRS unit using a static laser pattern instead of a sweeping laser stripe may be used to accomplish instantaneous range acquisition. Feature discrepancy over time the LRS datasets will require novel feature identification algorithms that can intelligently and automatically identify areas that exist in serial LRS datasets. Furthermore, new registration methods may be required to accommodate the identified feature discrepancies. Finally, validation of the resolved shift measurements within a computational model will be required for effective use of LRS within a model-update IGS system.

REFERENCES

[1] W. C. Rontgen. Ueber eine neue Art von Strahlen (On a new kind of rays). *Nature*, 53:274, 1896. English translation by Arthur Stranton for Nature.

[2] W. C. Rontgen. The Classis - On a new kind of rays. *Clinical orthopaedics and related reserach*, 65:3–8, 1969. Reprint with historical perspective.

[3] S. Webb. *The Physics of Medical Imaging*, chapter In the beginning, pages 7–16. Hilger, 1988.

[4] R. L. Galloway. The process and development of image-guided procedures. *Annual Review of Biomedical Engineering*, 3:83–108, 2001.

[5] J. A. Simpson and E. S. C. Weiner, editors. *Oxford English Dictionary*. Oxford University Press, 2nd edition, 1989. http://dictionary.oed.com.

[6] V. Horsley and R. H. Clarke. The structure and functions of the cerebellum examined by a new method. *Brain*, 31:45, 1908.

[7] E. A. Spiegel, H. T. Wycis, M. Marks, and A. Lee. Stereotactic apparatus for operations on the human brain. *Science*, (106):349, 1947.

[8] L. Leksell. Stereotaxic aparatus for intracerebral surgery. *Acta Chirurgica Scandinavica*, 99:229, 1949.

[9] T. Reichert and M. Wolff. Ueber ein neues Zielgeraet zur intrakraniellen elektrischen Abteilung und Ausschaltung. *Arch. Psychiatr. Z. Neurol.*, 186:225, 1951.

[10] J. Talairach, M. Hecaen, M. David, M. Monnier, and J. Ajuriaguerra. Recherches sur la coagulation therapeutique des structures sous-corticales chez l'homme. *Rev. Neuro.*, 81:4, 1949.

[11] R. L. Galloway, R. J. Maciunas, and C. A. Edwards. Interactive, image-guided neurosurgery. *IEEE Transactions on Biomedical Engineering*, 39(12):1226–1231, December 1992.

[12] L. Leksell and B. Jernberg. Stereotaxis and tomography. *Acta Neurochirurgica*, 52:1–7, 1980.

[13] W. Birg and F. Mundinger. Direct target point determination for stereotactic brain operations from CT data and the calculation of setting parameters for polar-coordinate stereotactic devices. *Applied Neurophysiology*, 45(4/5):387–395, 1982.

[14] J. Talairach and G. Szikla. Application of stereotactic concepts to the surgery of epilepsy. *Acta neurochirurgica: Supplementum*, 30:35–54, 1980.

[15] S. Goerss, P. J. Kelly, B. Kall, and G. J. Alker. A computed tomographic stereotactic adaptation system. *Neurosurgery*, 10:375–379, 1982.

[16] P. J. Kelly, B. Kall, S. Goerss, and F. I. Earnest. Computer-assisted stereotaxic laser resection of intra-axial brain neoplasms. *Journal of Neurosurgery*, 64:427–439, 1986.

[17] D. W. Roberts, J. W. Strohbehn, J. F. Hatch, W. Murray, and H. Kettenberger. A frameless stereotaxic integration of computerized tomographic imaging and the operating microscope. *Journal of Neurosurgery*, 65(4):545–549, 1986.

[18] Y. Kosugi, E. Watanabe, J. Goto, T. Watanabe, S. Yoshimoto, K. Takakura, and J. Ikebe. An articulated neurosurgical navigation system using mri and ct images. *IEEE Transactions on Biomedical Engineering*, 35(2):147–52, 1988. English.

[19] E. Watanabe, Y. Mayanagi, Y. Kosugi, S. Manaka, and K. Takakura. Open surgery assisted by the neuronavigator, a stereotactic, articulated, sensitive arm. *Neurosurgery*, 28(6):792–9; discussion 799–800, 1991. English.

[20] G. Strassman, C. Kolotas, R. Heyd, S. Walter, D. Baltas, and et al. Navigation system for interstitial brachytherapy. *Radiotherapy and Oncology*, 56:49–57, 2000.

[21] K. H. Manwaring, M. L. Manwaring, and S. D. Moss. Magnetic field guided endoscopic dissection through a burr hole may avoid more invasive craniotomies. A preliminary report. *Acta neurochirurgica: Supplementum*, 61:34–39, 1994.

[22] L. J. Zamorano, L. Nolte, A. M. Kadi, and Z. Jiang. Interactive intraoperative localization using an infrared-based system. *Neurological Research*, 15(5):290–8., 1993.

[23] M. J. Ryan, R. K. Erickson, D. N. Levin, C. A. Pelizarri, R. L. MacDonald, and G. J. Dohrman. Frameless stereotaxy with real-time tracking of patient head movement and retrospective patient-image registration. *Journal of Neurosurgery*, 85:287–292, 1996.

[24] A. C. Colchester, J. Zhao, K. S. Holton-Tainter, C. J. Henri, N. Maitland, and et al. Development and preliminary evaluation of VISLAN, a surgical planning and guidance sytem using intraoperative video imaging. *Medical Image Analysis*, 1:73–90, 1996.

[25] R. Khadem, C. C. Yeh, M. Sadeghi-Tehrani, M. R. Bax, J. A. Johnson, and et al. Comparative tracking error analysis of five different optical trakcing systems. *Computer Aided Surgery*, 5:98–107, 2000.

[26] Faul I. A theoretical comparison of 2-camera and 3-camera optical localizers with active or passive instrumentation. *Stud. Health Technol. Inf.*, 50:284–290, 1998.

[27] R. L. Galloway and R. J. Maciunas. Stereotactic Neurosurgery. *Critical Reviews in Biomedical Engineering*, 18(3):207–233, 1990.

[28] Peter H. Schonemann. A generalized solution of the orthogonal procrustes problem. *Psychometrika*, 31:1–10, 1966.

[29] E. Watanabe, T. Watanabe, S. Manaka, Y. Mayanagi, and K. Takakura. Three-dimensional digitizer (neuronavigator): new equipment for computed tomography-guided stereotaxic surgery. *Surgical Neurology*, 27(6):543–7, 1987. English.

[30] E. P. Sipos, S. A. Tebo, S. J. Zinreich, D. M. Long, and H. Brem. In vivo accuracy testing and clinical experience with the ISG viewing wand. *Neurosurgery*, 39:194–202, 1996.

[31] J. G. Golfinos, B. C. Fitzpatrick, L. R. Smith, and R. F. Spetzler. Clinical use of a frameless stereotactic arm: results of 325 cases. *Journal of Neurosurgery*, 83:197–205, 1995.

[32] O. Ganslandt, R. Steinmeier, H. Kober, J. Vieth, J. Kassubek, and et al. Magnetic source imaging combined with image-guided, frameless stereotaxy: a new method in surgery around the motor strip. *Neurosurgery*, 41:621–627, 1997.

[33] G. H. Barnett, D. W. Miller, and J. Weisenberger. Frameless stereotaxy with scalp-applied fiducial markers for brain biopsy procedures: experience in 218 cases. *Journal of Neurosurgery*, 91(4):569–76., 1999.

[34] M. Y. Wang, J. M. Fitzpatrick, and C. R. Maurer. Design of fiducials for accurate registration of CT and MR volume images. In *Proceedings of SPIE Medical Imaging*, volume 95, pages 96–108, 1995.

[35] F. C. Vinas, L. Zamorano, R. Buciuc, Li Q. H., F. Shamsa, and et al. Application on accuracy study of a semipermanent fiducial system for frameless stereotaxy. *Computer Aided Surgery*, 2:257–263, 1997.

[36] C. R. Maurer, J. M. Fitzpatrick, M. Y. Wang, R. L. Galloway, R. J. Maciunas, and G. S. Allen. Registration of head volume images using implantable fiducial markers. *IEEE Transactions on Medical Imaging*, 16(4):447–462, 1997.

[37] J. D. Stefansic, W. A. Bass, S. L. Hartmann, R. A. Beasley, T. K. Sinha, D. M. Cash, A. J. Herline, and R. L. Galloway. Design and implementation of a PC-based image-guided surgical system. *Computer Methods and Programs in Biomedicine*, 69:211–224, 2002.

[38] H. J. Nauta. Error assessment during "image guided" and "imaging interactive" stereotactic surgery. *Computerized Medical Imaging and Graphics*, 18(4):279–87., 1994.

[39] D. L. G. Hill, C. R. Maurer, R. J. Maciunas, J. A. Barwise, J. M. Fitzpatrick, and M. Y. Wang. Measurement of intraoperative brain surface deformation under a craniotomy. *Neurosurgery*, 43(3):514–526, 1998.

[40] R. D. Bucholz, D. D. Yeh, J. Trobaugh, L. L. McDurmont, C. D. Sturm, C. Baumann, J. M. Henderson, A. Levy, and P. Kessman. The correction of stereotactic inaccuracy caused by brain shift using an intraoperative ultrasound device. In *LNCS: CVRMED-MRCAS '97*, volume 1205, pages 459–466. Springer-Verlag, 1997.

[41] N. L. Dorward, O. Alberti, B. Velani, F. A. Gerritsen, W. F. J. Harkness, N. D. Kitchen, and D. G. T. Thomas. Postimaging brain distortion: magnitude, correlates, and impact on neuronavigation. *Journal of Neurosurgery*, 88(4):656–662, 1998.

[42] C. R. Maurer, D. L. G. Hill, A. J. Martin, H. Y. Liu, M. McCue, D. Rueckert, D. Lloret, W. A. Hall, R. E. Maxwell, D. J. Hawkes, and C. L. Truwit. Investigation of intraoperative brain deformation using a 1.5-t interventional mr system: Preliminary results. *IEEE Transactions on Medical Imaging*, 17(5):817–825, 1998.

[43] T. Hartkens, D. L. G. Hill, A. D. Castellano-Smith, D. J. Hawkes, C. R. Maurer, A. J. Martin, W. A. Hall, H. Liu, and C. L. Truwit. Measurement and analysis of brain deformation during neurosurgery. *IEEE Transactions on Medical Imaging*, 22(1):82–92, January 2003.

[44] D. W. Roberts, A. Hartov, F. E. Kennedy, M. I. Miga, and K. D. Paulsen. Intraoperative brain shift and deformation: A quantitative analysis of cortical displacement in 28 cases. *Neurosurgery*, 43(4):749–758, 1998.

[45] C. Nimsky, O. Ganslandt, S. Cerny, P. Hastreiter, G. Greiner, and R. Fahlbusch. Quantification of, visualization of, and compensation for brain shift using intraoperative magnetic resonance imaging. *Neurosurgery*, 47(5):1070–1079, 2000.

[46] A. Nabavi, P. M. Black, D. T. Gering, C. F. Westin, V. Mehta, R. S. Pergolizzi, M. Ferrant, S. K. Warfield, N. Hata, R. B. Schwartz, W. M. Wells, R. Kikinis, and F. A. Jolesz. Serial intraoperative magnetic resonance imaging of brain shift. *Neurosurgery*, 48(4):787–797, 2001.

[47] S. J. Hassenbusch, J. S. Anderson, and P. K. Pillay. Brain tumor resection aided with markers placed using stereotaxis guided by magnetic resonance imaging and computed tomography. *Neurosurgery*, 28(6):801–805, 1991.

[48] M. N. Shalit, Y. Israeli, S. Matz, and M. L. Cohen. Intra-operative Computerized Axial Tomography. *Surgical Neurology*, 11:382–384, May 1979.

[49] Shalit M. N., Israeli Y., Matz S., and Cohen M. L. Experience with intra-operative CT scanning in brain-tumors. *Surgical Neurology*, 17(5):376–382, 1982.

[50] L. D. Lunsford. A dedicated CT system for the stereotactic operating room. *Applied Neurophysiology*, 45:374–378, 1982.

[51] L. D. Lunsford, L. Leksell, and B. Jernberg. Probe holder for stereotactic surgery in the CT scanner. a technical note. *Acta Neurochirurgica*, 69(3-4):297–304, 1983.

[52] L. D. Lunsford and A. J. Martinez. Stereotactic exploration of the brain in the era of computed tomography. *Surgical Neurology*, 22(3):222–30., 1984.

[53] L. D. Lunsford, R. Parrish, and L. Albright. Intraoperative imaging with a therapeutic computed tomographic scanner. *Neurosurgery*, 15(4):559–61., 1984.

[54] L. D. Lunsford, A. J. Martinez, and R. E. Latchaw. Stereotaxic surgery with a magnetic resonance- and computerized tomography-compatible system. *Journal of Neurosurgery*, 64(6):872–878, 1986.

[55] D. J. Engle, L. D. Lunsford, and T. Panichelli. Rigid head fixation for intraoperative computed tomography. *Neurosurgery*, 19(2):258–62., 1986.

[56] D. J. Engle and L. D. Lunsford. Brain tumor resection guided by intraoperative computed tomography. *Journal of Neuro-Oncology*, 4(4):361–70, 1987.

[57] H. Okudera, K. Kobayashi, H. Gibo, T. Takemae, and K. Sugita. Development of the operating computerized tomographic scanner system for neurosurgery. *Acta Neurochirurgica (Wein)*, 111:61–63, 1991.

[58] H. Okudera, T. Takemae, and S. Kobayashi. Intraoperative computed tomography scanning during transsphenoidal surgery: technical note. *Neurosurgery*, 32(6):1041–1043, June 1993.

[59] W. E. Butler, C. M. Piaggio, C. Constantinou, L. Niklason, R. G. Gonzalez, G. R. Cosgrove, and N. T. Zervas. A mobile computed tomographic scanner with intraoperative and intensive care unit applications. *Neurosurgery*, 42(6):1304–1310, June 1998.

[60] L. D. Lunsford. A mobile computed tomographic scanner with intraoperative and intensive care unit applications. *Neurosurgery*, 42(6):1310, June 1998. Comment.

[61] P. McL. Black. Intraoperative computed tomographic scanning during transsphenoidal surgery: technical note. *Neurosurgery*, 32(6):1043, June 1993. Comment.

[62] J. F. Schenck, F. A. Jolesz, P. B. Roemer, H. E. Cline, W. E. Lorensen, R. Kikinis, S. G. Silverman, C. J. Hardy, W. D. Barber, E. T. Laskaris, and et al. Superconducting open-configuration MR imaging system for image-guided therapy. *Radiology*, 195:805–814, 1995.

[63] V. M. Tronnier, C. R. Wirtz, M. Knauth, G. Lenz, O. Pastyr, M. M. Bonsanto, F. K. Albert, R. Kuth, A. Staubert, W. Schlegel, K. Sartor, and S. Kunze. Intraoperative diagnostic and interventional magnetic resonance imaging in neurosurgery. *Neurosurgery*, 40(5):891–900, 1997.

[64] C. R. Wirtz, V. M. Tronnier, M. M. Bonsanto, M. Knauth, A. Staubert, F. K. Albert, and S. Kunze. Image-guided neurosurgery with intraoperative mri: Update of frameless stereotaxy and radicality control. *Stereotactic and Functional Neurosurgery*, 68(1-4):39–43, 1997.

[65] C. R. Wirtz, V. M. Tronnier, F. K. Albert, M. Knauth, M. M. Bonsanto, A. Staubert, O. Pastyr, and S. Kunze. Modified headholder and operating table for intra-operative mri in neurosurgery. *Neurol Res*, 20(7):658–61., 1998.

[66] M. Knauth, C. R. Wirtz, V. M. Tronnier, A. Staubert, S. Kunze, and K. Sartor. [intraoperative magnetic resonance tomography for control of extent of neurosurgical operations]. *Radiologe*, 38(3):218–24., 1998.

[67] V. Tronnier, A. Staubert, R. Wirtz, M. Knauth, M. Bonsanto, and S. Kunze. Mri-guided brain biopsies using a 0.2 tesla open magnet. *Minimally Invasive Neurosurgery*, 42(3):118–22., 1999.

[68] C. R. Wirtz, M. Knauth, A. Staubert, M. M. Bonsanto, K. Sartor, S. Kunze, and V. M. Tronnier. Clinical evaluation and follow-up results for intraoperative magnetic resonance imaging in neurosurgery. *Neurosurgery*, 46(5):1112–1120, 2000.

[69] M. Knauth, C. R. Wirtz, N. Aras, and K. Sartor. Low-field interventional mri in neurosurgery: finding the right dose of contrast medium. *Neuroradiology*, 43(3):254–258, 2001.

[70] P. M. Black, E. Alexander, C. Martin, T. Moriarty, A. Nabavi, T. Z. Wong, R. B. Schwartz, and F. Jolesz. Craniotomy for tumor treatment in an intraoperative magnetic resonance imaging unit. *Neurosurgery*, 45(3):423–431, 1999.

[71] A. Nabavi, C. T. Mamisch, D. T. Gering, D. F. Kacher, R. S. Pergolizzi, W. M. Wells, R. Kikinis, P. M. Black, and F. A. Jolesz. Image-guided therapy and intraoperative mri in neurosurgery. *Minimally Invasive Therapy and Allied Technologies*, 9(3-4):277–286, 2000.

[72] Jr. Pergolizzi, R. S., A. Nabavi, R. B. Schwartz, L. Hsu, T. Z. Wong, C. Martin, P. M. Black, and F. A. Jolesz. Intra-operative mr guidance during trans-sphenoidal pituitary resection: preliminary results. *Journal of Magnetic Resonance Imaging*, 13(1):136–141, 2001.

[73] F. A. Jolesz, A. Nabavi, and R. Kikinis. Integration of interventional mri with computer-assisted surgery. *Journal of Magnetic Resonance Imaging*, 13(1):69–77., 2001.

[74] M. Hadani, R. Spiegelman, Z. Feldman, H. Berkenstadt, and Z. Ram. Novel, compact, intraoperative magnetic resonance imaging- guided system for conventional neurosurgical operating rooms. *Neurosurgery*, 48(4):799–807, 2001.

[75] R. Steinmeier, R. Fahlbusch, O. Ganslandt, C. Nimsky, M. Buchfelder, M. Kaus, T. Heigl, G. Lenz, R. Kuth, and W. Huk. Intraoperative magnetic resonance imaging with the magnetom open scanner: concepts, neurosurgical indications, and procedures: a preliminary report. *Neurosurgery*, 43(4):739–747, 1998.

[76] C. Nimsky, O. Ganslandt, H. Kober, M. Moller, S. Ulmer, B. Tomandl, and R. Fahlbusch. Integration of functional magnetic resonance imaging supported by magnetoencephalography in functional neuronavigation. *Neurosurgery*, 44(6):1249–1255, 1999.

[77] C. Nimsky, O. Ganslandt, M. Buchfelder, and R. Fahlbusch. Intraoperative magnetic resonance tomography - experiences in neurosurgery. *Nervenarzt*, 71(12):987–994, 2000.

[78] R. Fahlbusch, O. Ganslandt, and C. Nimsky. Intraoperative imaging with open magnetic resonance imaging and neuronavigation. *Childs Nervous System*, 16(10-11):829–831, 2000.

[79] M. Buchfelder, O. Ganslandt, R. Fahlbusch, and C. Nimsky. Intraoperative magnetic resonance imaging in epilepsy surgery. *Journal of Magnetic Resonance Imaging*, 12(4):547–555., 2000.

[80] C. Nimsky, O. Ganslandt, H. Kober, M. Buchfelder, and R. Fahlbusch. Intraoperative magnetic resonance imaging combined with neuronavigation: a new concept. *Neurosurgery*, 48(5):1082–1089, 2001.

[81] C. Nimsky, O. Ganslandt, P. Hastreiter, and R. Fahlbusch. Intraoperative compensation for brain shift. *Surgical Neurology*, 56(6):357–364, 2001.

[82] C. Nimsky and R. Fahlbusch. Serial intraoperative magnetic resonance imaging of brain shift. *Neurosurgery*, 48(4):797, 2001. Comment.

[83] R. J. Bohinski, A. K. Kokkino, R. E. Warnick, M. F. Gaskill-Shipley, D. W. Kormos, R. R. Lukin, and J. M. Tew. Glioma resection in a shared-resource magnetic resonance operating room after optimal image-guided frameless stereotactic resection. *Neurosurgery*, 48(4):731–742, 2001.

[84] G. R. Sutherland, T. Kaibara, D. Louw, D. I. Hoult, B. Tomanek, and J. Saunders. A mobile high-field magnetic resonance system for neurosurgery. *J Neurosurg*, 91(5):804–13., 1999.

[85] T. Kaibara, J. K. Saunders, and G. R. Sutherland. Advances in mobile intraoperative magnetic resonance imaging. *Neurosurgery*, 47(1):131–7; discussion 137–8., 2000.

[86] G. R. Sutherland, T. Kaibara, C. Wallace, B. Tomanek, and M. Richter. Intraoperative assessment of aneurysm clipping using magnetic resonance angiography and diffusion-weighted imaging: Technical case report. *Neurosurgery*, 50(4):893–897, 2002.

[87] T. Kaibara, S. T. Myles, M. A. Lee, and G. R. Sutherland. Optimizing epilepsy surgery with intraoperative mr imaging. *Epilepsia*, 43(4):425–429, 2002.

[88] J. S. Lewin, A. Metzger, and W. R. Selman. Intraoperative magnetic resonance image guidance in neurosurgery. *J Magn Reson Imaging*, 12(4):512–24., 2000.

[89] M. S. Berger. Ultrasound-guided stereotaxic biopsy using a new apparatus. *Journal of Neurosurgery*, 65:550–554, 1986.

[90] W. R. Chandler, J. E. Knake, J. E. McGillicuddy, K. O. Lillehei, and T. M. Silver. Intraoperative use of real-time ultrasonography in neurosurgery. *Journal of Neurosurgery*, 57(2):157–163, 1982.

[91] G. A. W. Gooding, J. E. Boggan, S. K. Powers, N. A. Martin, and P. R. Weinstein. Neurosurgical sonography - intraoperative and postoperative imaging of the brain. *American Journal of Neuroradiology*, 5(5):521–525, 1984.

[92] G. A. W. Gooding, J. E. Boggan, and P. R. Weinstein. Characterization of intracranial neoplasms by CT and intraoperative sonography. *American Journal of Neuroradiology*, 5(5):517–520, 1984.

[93] G. A. W. Gooding, M. S. B. Edwards, A. E. Rabkin, and S. K. Powers. Intraoperative real-time ultrasound in the localization of intracranial neoplasms. *Radiology*, 146(2):459–462, 1983.

[94] J. E. Knake, R. A. Bowerman, T. M. Silver, and S. McCracken. Neurosurgical applications of intraoperative ultrasound. *Radiologic Clinics of North America*, 23(1):73–90, 1985.

[95] J. E. Knake, W. F. Chandler, T. O. Gabrielsen, J. T. Latack, and S. S. Gebarski. Intraoperative sonographic dilneation of low-grade brain neoplasms defined poorly by computed-tomography. *Radiology*, 151(3):735–739, 1984.

[96] J. Koivukangas and P. J. Kelly. Application of ultrasound imaging to stereotaxic brain-tumor surgery. *Annals of Clinical Research*, 18:25–32, 1986.

[97] S. C. Lange, J.F. Howe, W. P. Shuman, and J. V. Rogers. Intra-operative ultrasound detection of metastatic tumors in the central cortex. *Neurosurgery*, 11(2):219–222, 1982.

[98] J. Machi, B. Sigel, J. J. Jafar, R. Menoni, J. C. Beitler, R. A. Bernstein, R. M. Crowell, J. R. Ramos, and D. G. Spigos. Criteria for using imaging in ultrasound during brain and spinal-cord surgery. *Journal of Ultrasound in Medicine*, 3(4):155–161, 1984.

[99] R. M. Quencer and B. M. Montalvo. Intraoperative cranial sonography. *Neuroradiology*, 28(5-6):528–550, 1986.

[100] J. M. Rubin and G. J. Dohrmann. Efficacy of intraoperative US for evaluating intracranial masses. *Radiology*, 157(2):509–511, 1985.

[101] U. Sjolander, P. G. Lindgren, and R. Hugosson. Ultrasound sector scanning for the localization and biopsy of intracerebral lesions. *Journal of Neurosurgery*, 58(1):7–10, 1983.

[102] Y. Tsutsumi, Y. Andoh, and N. Inoue. Ultrasound-guided biopsy for deep-seated brain-tumors. *Journal of Neurosurgery*, 57(2):164–167, 1982.

[103] C. R. B. Merritt, R. M. Voorhies, E. Connolly, and R. Coulon. Intraoperative neurosurgical ultrasound. *Seminars in Ultrasound, CT, and MRI*, 6(1):31–47, 1985.

[104] R. M. Voorhies, I. Engel, F. W. Gamache, R. H. Patterson, R. A. R. Fraser, M. H. Lavyne, and M. Schneider. Intraoperative localization of subcortical brain-tumors - further experience with B-mode real-time sector scanning. *Neurosurgery*, 12(2):189–194, 1983.

[105] P. D. LeRoux, M. S. Berger, G. A. Ojemann, K. Wang, and L. A. Mack. Correlation of intraoperative ultrasound tumor volumes and margins with preoperative computerized tomography scans. *Journal of Neurosurgery*, 71:691–698, November 1989.

[106] P. D. Leroux, T. C. Winter, M. S. Berger, L. A. Mack, K. Wang, and J. P. Elliott. A comparison between preoperative magnetic-resonance and intraoperative ultrasound tumor volumes and margins. *Journal of Clinical Ultrasound*, 22(1):29–36, 1994.

[107] A. Gronningsaeter, G. Unsgard, S. Ommedal, and B. A. J. Angelsen. Ultrasound-guided neurosurgery: A feasibility study in the 3-30 mhz frequency range. *British Journal of Neurosurgery*, 10(2):161–168, 1996.

[108] A. Gronningsaeter, T. Lie, A. Kleven, T. Morland, T. Lango, G. Unsgard, H. O. Myhre, and R. Marvik. Initial experience with stereoscopic visualization of three- dimensional ultrasound data in surgery. *Surgical Endoscopy-Ultrasound and Interventional Techniques*, 14(11):1074–1078, 2000.

[109] A. Gronningsaeter, A. Kleven, S. Ommedal, T. E. Aarseth, T. Lie, F. Lindseth, T. Lango, and G. Unsgard. Sonowand, an ultrasound-based neuronavigation system. *Neurosurgery*, 47(6):1373–1379, 2000.

[110] F. Lindseth, T. Lango, J. Bang, and T. A. N. Hernes. Accuracy Evaluation of a 3D Ultrasound-based Neuronavigation System. *Computer Assisted Surgery*, 7:197–222, 2002.

[111] G. Unsgaard, S. Ommedal, T. Muller, A. Gronningsaeter, and T. A. N. Hernes. Neuronavigation by intraoperative three-dimensional ultrasound: Initial experience during brain tumor resection. *Neurosurgery*, 50(4):804–812, 2002.

[112] R. M. Comeau, A. Fenster, and T. M. Peters. Intraoperative us in interactive image-guided neurosurgery. *Radiographics*, 18(4):1019–1027, 1998.

[113] D. G. Gobbi, R. M. Comeau, and T. M. Peters. Ultrasound/mri overlay with image warping for neurosurgery. In *LNCS: Medical Image Computing and Computer-Assisted Intervention: MICCAI '00*, volume 1935, pages 106–114. Springer-Verlag, 2000.

[114] R. M. Comeau, A. F. Sadikot, A. Fenster, and T. M. Peters. Intraoperative ultrasound for guidance and tissue shift correction in image-guided neurosurgery. *Medical Physics*, 27(4):787–800., 2000.

[115] D. W. Roberts, M. I. Miga, A. Hartov, S. Eisner, J. M. Lemery, F. E. Kennedy, and K. D. Paulsen. Intraoperatively updated neuroimaging using brain modeling and sparse data. *Neurosurgery*, 45(5):1199–1206, 1999.

[116] K. Miller and K. Chinzei. Constitutive modelling of brain tissue: Experiment and theory. *Journal of Biomechanics*, 30(11-12):1115–1121, 1997.

[117] K. Miller. Constitutive model of brain tissue suitable for finite element analysis of surgical procedures. *Journal of Biomechanics*, 32(5):531–537, 1999.

[118] M. Miga, K. Paulsen, F. Kennedy, J. Hoopes, A. Hartov, and D. Roberts. Initial in-vivo analysis of 3d heterogeneous brain computations for model-updated image-guided neurosurgery. In *Medical Image Computing and Computer-Assisted Intervention - Miccai'98*, volume 1496 of *LECTURE NOTES IN COMPUTER SCIENCE*, pages 743–752. 1998.

[119] K. D. Paulsen, M. I. Miga, F. E. Kennedy, P. J. Hoopes, A. Hartov, and D. W. Roberts. A computational model for tracking subsurface tissue deformation during stereotactic neurosurgery. *IEEE Transactions on Biomedical Engineering*, 46(2):213–225, 1999.

[120] M. I. Miga, D. W. Roberts, A. Hartov, S. Eisner, J. Lemery, F. E. Kennedy, and K. D. Paulsen. Updated neuroimaging using intraoperative brain modeling and sparse data. *Stereotactic and Functional Neurosurgery*, 72(2-4):103–106, 1999.

[121] M. I. Miga, K. D. Paulsen, J. M. Lemery, S. D. Eisner, A. Hartov, F. E. Kennedy, and D. W. Roberts. Model-updated image guidance: Initial clinical experiences with gravity-induced brain deformation. *IEEE Transactions on Medical Imaging*, 18(10):866–874, 1999.

[122] M. Miga, K. Paulsen, F. Kennedy, A. Hartov, and D. Roberts. Model-updated image-guided neurosurgery using the finite element method: Incorporation of the falx cerebri. In Taylor and Colchester, editor, *Lecture Notes in Computer Science for 2nd International Conference on Medical Image Computing and Computer-Assisted Intervention*, volume 1679, pages 900–909. Springer Verlag, New York, 1999.

[123] M. I. Miga, K. D. Paulsen, F. E. Kennedy, P. J. Hoopes, A. Hartov, and D. W. Roberts. In vivo analysis of heterogeneous brain deformation computations for model-updated image guidance. *Computational Methods in Biomechanics and Biomedical Engineering*, 3(2):129–146, 2000.

[124] M. I. Miga, K. D. Paulsen, P. J. Hoopes, F. E. Kennedy, A. Hartov, and D. W. Roberts. In vivo modeling of interstitial pressure in the brain under surgical load using finite elements. *Journal of Biomechanical Engineering-Transactions of the Asme*, 122(4):354–363, 2000.

[125] M. I. Miga, K. D. Paulsen, P. J. Hoopes, F. E. Kennedy, A. Hartov, and D. W. Roberts. In vivo quantification of a homogeneous brain deformation model for updating preoperative images during surgery. *IEEE Transactions on Biomedical Engineering*, 47(2):266–273, 2000.

[126] M. I. Miga, D. W. Roberts, F. E. Kennedy, L. A. Platenik, A. Hartov, K. E. Lunn, and K. D. Paulsen. Modeling of retraction and resection for intraoperative updating of images. *Neurosurgery*, 49(1):75–84, 2001.

[127] L. A. Platenik, M. I. Miga, D.W. Roberts, K. E. Lunn, F. E. Kennedy, A. Hartov, and K. D. Paulsen. In vivo quantification of retraction deformation modeling for updated image-guidance during neurosurgery. *IEEE Transactions on Biomedical Engineering*, 49(8):823–835, August 2002.

[128] O. Skrinjar, D. Spencer, and J. Duncan. Brain shift modeling for use in neurosurgery. In *LNCS: Medical Image Computing and Computer-assisted Intervention: MICCAI '98*, volume 1496, pages 641–649. Springer-Verlag, 1998.

[129] O. Skrinjar, C. Studholme, A. Nabavi, and J. Duncan. Steps Toward a Stereo-Camera-Guided Biomechanical Model for Brain Shift Compensation. pages 183–189. Information Processing in Medical Imaging (IPMI 2001), Davis, CA, USA, June 2001.

[130] O. Skrinjar, A. Nabavi, and J. Duncan. A stereo-guided biomechanical model for volumetric deformation analysis. In *IEEE Workshop on Mathematical Methods in Biomedical Image Analysis, 2001*, pages 95–102, December 2001.

[131] O. Skrinjar, A. Nabavi, and J. Duncan. Model-driven brain shift compensation. *Medical Image Analysis*, 6(4):361–373, December 2002.

[132] M. Ferrant, S. K. Warfield, A. Nabavi, F. A. Jolesz, and R. Kikinis. Registration of 3d intraoperative mr images of the brain using a finite element biomechanical model. In *LNCS: Medical image computing and computer-assisted intervention: MICCAI '00*, volume 1935, pages 19–28. Springer Verlag, 2000.

[133] P. J. Edwards, D. L. Hill, J. A. Little, and D. J. Hawkes. A three-component deformation model for image-guided surgery. *Medical Image Analysis*, 2(4):355–67., 1998.

[134] E. Fontenla, C. A. Pelizzari, J. C. Roeske, and G. T. Y. Chen. Using serial imaging data to model variabilities in organ position and shape during radiotherapy. *Physics in Medicine and Biology*, 46(9):2317–2336, September 2001.

[135] N. Hata, A. Nabavi, W. M. Wells, S. K. Warfield, R. Kikinis, P. M. Black, and F. A. Jolesz. Three-dimensional optical flow method for measurement of volumetric brain deformation from intraoperative mr images. *Journal of Computer Assisted Tomography*, 24(4):531–538, 2000.

[136] D. G. Gobbi and T. M. Peters. Interactive Intra-operative 3D Ultrasound Reconstruction and Visualization. In *LNCS: Medical Image Computing and Computer-Assisted Intervention: MICCAI 2002*, volume 2489, pages 156–163. Springer-Verlag, 2002.

[137] R. Burtch. History of Photogrammetry. World Wide Web. http://www.ferris.edu/htmls/academics/course.offerings/burtchr/sure340/notes/History.pdf.

[138] P. E. Debevec. *Modeling and rendering architecture from photographs*. PhD thesis, University of California at Berkeley, 1996. http://www.debevec.org.

[139] G. Borshukov. New algorithms for modeling and rendering architecture from photographs. Master's thesis, University of California at Berkeley, May 1997. http://www.virtualcinematography.org.

[140] H. S. Flora, N. Woodhouse, S. Robson, and M. Adiseshiah. Micromovements at the aortic aneurysm nexk measured during open surgery with close-range photogrammetry: Implications for aortic endografts. *Journal of Endovascular Therapy*, 8(5):511–520, 2001.

[141] F. A. van den Heuvel. Editorial: Theme issue on medical imaging and photogrammetry. *ISPRS Journal of Photogrammetry & Remote Sensing*, 56:283–285, 2002.

[142] N. Börlin. Comparison of resection-intersection algorithms and projection geometries in radiostereometry. *ISPRS Journal of Photogrammetry & Remote Sensing*, 56:390–400, 2002.

[143] N. D'Apuzzo. Surface measurement and tracking of human body parts from multi-image video sequences. *ISPRS Journal of Photogrammetry & Range Sensing*, 56:360–375, 2002.

[144] E. R. Valstar, C. P. Botha, M. van der Glas, P. M. Rozing, F. C. T. van der Helm, F. H. Post, and A. M. Vossepoel. Towards computer-assisted surgery in shoulder joint replacement. *ISPRS Journal of Photogrammetry and Remot Sensing*, 56:326–337, 2002.

[145] E. R. Valstar, R. G. H. H. Nelissen, J. H. C. Reiber, and P. M. Rozing. The use of Roentgen stereophotogrammetry to study micromotion of orthopaedic implants. *ISPRS Journal of Photogrammetry and Range Sensing*, 56:376–389, 2002.

[146] P. Patias. Medical imaging challenges photogrammetry. *ISPRS Journal of Photogrammetry & Range Sensing*, 56:295–310, 2002.

[147] H. L. Mitchell and I. Newton. Medical photogrammetric measurement: overview and prospects. *ISPRS Journal of Photogrammetry and Range Sensing*, 56:286–394, 2002.

[148] H. Broers, H. Hemken, T. Luhmann, and P. Ritschl. Photogrammetric calibration of a C-arm X-ray system as a verification tool for orthopaedic navigation systems. *ISPRS Journal of Photogrammetry and Range Sensing*, 56:338–346, 2002.

[149] E. Corona, S. Mitra, M. Wilson, T. Krile, Y. H. Kwon, and P. Soliz. Digital stereo image analyzer for generating automated 3-D measures of optic disc deformation in glaucoma. *IEEE Transactions on Medical Imaging*, 21(10):1244–1253, October 2002.

[150] H. Liu, Y. Yu, M. C. Schell, W. G. O'Dell, R. Ruo, and P. Okunieff. Optimal marker placement in photogrammetry patient positioning system. *Medical Physics*, 30(2):103–110, February 2003.

[151] H. Sun, H. Farid, and K. D. Paulsen. Cortical vessels for patient registration during image-guided neurosurgery, H. Sun, H. Farid, K. D. Paulsen. In *Proceedings of SPIE: Medical Imaging 2003*, February 2003.

[152] H. Sun, H. Farid, K. Rick, A. Hartov, D. W. Roberts, and K. D. Paulsen. Estimating cortical surface motion using steropsis for brain deformation models. In *LNCS: Medical Image Computing and Computer Assisted Intervention: MICCAI '03*, volume 2878, pages 794–801. Springer-Verlag, 2003.

[153] M. Amann, R. Bosch, M. Lescure, R. Myllyla, and M. Rioux. Laser ranging: a critical review of usual techniques for distance measurement. *Optical Engineering*, 40(1):10–19, January 2001.

[154] F. Lu and E. Milios. Robot pose estimation in unknown environments by matching 2D range scans. *Journal of intelligent and robotic systems*, 18:249–275, 1997.

[155] C. Doria, G. Wang, A. K. Jain, and C. Mercer. Registration and intergration fo multiple object views for 3D model construction. *IEEE Transactions on Pattern Analysis and Machine Intelligence*, 20(1):83–89, January 1998.

[156] J. Gregor and R. T. Whitaker. Indoor scene reconstruction from sets of noisy range images. *Graphical Models*, 63:304–332, 2001.

[157] H. Zhao and R. Shibasaki. Reconstructing a textured CAD model of an urban environment using vehicle-borne laser range scanners and line cameras. *Machine Vision and Applications*, 14:35–41, 2003.

[158] J. Novak and A. Miks. Modern optoelectronic methods for non-contact deformation measurement in industry. *Journal of Optics A: Pure and Applied Optics*, 4:S413–S420, 2002.

[159] E. P. Baltsavias. A comparison between photogrammetry and laser scanning. *ISPRS Journal of Photogrammetry & Remote Sensing*, 54:83–94, 1999.

[160] M. Baba, D. Narita, and K. Ohtani. 360degree shape measurement system for objects having from Lambertian to specular reflectance properties utilizing a novel rangefinder. *Journal of Optics A: Pure and Applied Optics*, 4:S295–S303, 2002.

[161] M. Baba and K. Ohtani. A new sensor system for simultaneously detecting the position and incident angle of a light spot. *Journal of Optics A: Pure and Applied Optics*, 4:S391–S399, 2002.

[162] J. M. Henderson, K. R. Smith, and R. D. Bucholz. An accurate and ergonomic method of registration for image- guided neurosurgery. *Computerized Medical Imaging and Graphics*, 18(4):273–277, 1994.

[163] A. Raabe, R. Krishnan, R. Wolff, E. Hermann, M. Zimmermann, and V. Seifert. Laser surface scanning for patient registration in intracranial image-guided surgery. *Neurosurgery*, 50(4):797–801, 2002.

[164] M. A. Audette, K. Siddiqi, and T. M. Peters. Level-set surface segmentation and fast cortical range image tracking for computing intrasurgical deformations. In *LNCS: Medical Image Computing and Computer Assisted Intervention: MICCAI '99*, volume 1679, pages 788–797. Springer-Verlag, 1999.

[165] M. A. Audette, K. Siddiqi, F. P. Ferrie, and T. M. Peters. An integrated range-sensing, segmentation and registration framework for the characterization of intra-surgical brain deformations in image-guided surgery. *Computer Vision and Image Understanding*, 89(2-3):226–251, 2003.

[166] S. Nakajima, H. Atsumi, R. Kikinis, T. M. Moriarty, D. C. Metcalf, F. A. Jolesz, and P. M. Black. Use of cortical surface vessel registration for image-guided neurosurgery. *Neurosurgery*, 40(6):1201–1208, 1997.

[167] P. J. Besl and N. D. McKay. A method for registration of 3-d shapes. *IEEE Transactions on Pattern Analysis and Machine Intelligence*, 14(2):239–256, 1992.

[168] W. M. Wells, P. Viola, H. Atsumi, S. Nakajima, and R. Kikinis. Multi-modal volume registration by maximization of mutual information. *Medical Image Analysis*, 1(1):35–51., 1996.

[169] F. Maes, A. Collignon, D. Vandermeulen, G. Marchal, and P. Seutens. Multimodality image registration by maximization of mutual information. *IEEE Transactions on Medical Imaging*, 16(2):187–198, April 1997.

[170] M. A. Audette, F. P. Ferrie, and T. M. Peters. An algorithmic overview of surface registration techniques for medical imaging. *Medical Image Analysis*, 4(3):201–217, 2000.

[171] A. E. Johnson and S. B. Kang. Registration and integration of textured 3D data. *Image and Vision Computing*, 17(2):135–147, February 1999.

[172] D. M. Cash, T. K. Sinha, W. C. Chapman, R. L. Galloway, and M. I. Miga. Fast, Accurate Surface Acquisition Using a Laser Range Scanner for Image-guided Liver Surgery. In *SPIE Medical Imaging 2002, San Diego*, volume 4681, 2002.

[173] S. J. Ahn, W. Rauh, and H. Warnecke. Least-squares orthogonal distances fitting of circle, sphere, ellipse, hyperbola, and parabola. *Pattern Recognition*, 34:2283–2303, 2001.

[174] C. Studholme, D. L. G. Hill, and D. J. Hawkes. An overlap invariant entropy measure of 3d medical image alignment. *Pattern Recognition*, 32(1):71–86, 1999.

[175] W. H. Press, S. A. Teukolsky, W. T. Vetterling, and B. P. Flannery. *Numerical Recipes in C: The Art of Scientific Computing*. Cambridge University Press, New York, 2nd edition, 1992.

[176] J. M. Fitzpatrick, D. L. G. Hill, and C. R. Maurer. Image registration. In M. Sonka and J. M. Fitzpatrick, editors, *Handbook of Medical Imaging*, volume 2, pages 447–513. SPIE Press, Bellingham, 2000.

[177] W. E. L. Grimson, G. J. Ettinger, S. J. White, T. LozanoPerez, W. M. Wells, and R. Kikinis. An automatic registration method for frameless stereotaxy, image guided surgery, and enhanced reality visualization. *IEEE Transactions on Medical Imaging*, 15(2):129–140, 1996.

[178] C. R. Maurer, R. J. Maciunas, and J. M. Fitzpatrick. Registration of head ct images to physical space using a weighted combination of points and surfaces. *IEEE Transactions on Medical Imaging*, 17(5):753–761, 1998.

[179] A. J. Herline, J. L. Herring, J. D. Stefansic, W. C. Chapman, R. L. Galloway, and B. M. Dawant. Surface registration for use in interactive image-guided liver surgery. In *LNCS: Medical Imaging Computation and Computer-Assisted Intervention: MICCAI '99*, volume 1679, pages 892–899. Springer-Verlag, 1999.

[180] P. M. Black, T. Moriarty, E. Alexander, P. Stieg, E. J. Woodard, P. L. Gleason, C. H. Martin, R. Kikinis, R. B. Schwartz, and F. A. Jolesz. Development and implementation of intraoperative magnetic resonance imaging and its neurosurgical applications. *Neurosurgery*, 41(4):831–842, 1997.

[181] W. E. L. Grimson, R. Kikinis, F. A. Jolesz, and P. M. Black. Image-guided surgery. *Scientific American*, 280(6):62–69, 1999.

[182] M. Knauth, N. Aras, C. R. Wirtz, A. Dorfler, T. Engelhorn, and K. Sartor. Surgically induced intracranial contrast enhancement: Potential source of diagnostic error in intraoperative mr imaging. *American Journal of Neuroradiology*, 20(8):1547–1553, 1999.

[183] R. Bajcsy, R. Lieberson, and M. Reivich. A computerized system for the elastic matching of deformed radiographic images to idealized atlas images. *Journal of Computer Assisted Tomography*, 7(4):618–625, 1983.

[184] J. C. Gee, D. R. Haynor, L. LeBriquer, and R. K. Bajcsy. Advances in elastic matching theory and its implementation. In *LNCS: CVRMed-MRCAS '97*, volume 1205, pages 63–72. Springer-Verlag, 1997.

[185] G. E. Christensen, R. D. Rabbitt, and M. I. Miller. 3d brain mapping using a deformable neuroanatomy. *Physics in Medicine and Biology*, 39(3):609–618, 1994.

[186] A. Hagemann, K. Rohr, H. S. Stiehl, U. Spetzger, and J. M. Gilsbach. Biomechanical modeling of the human head for physically based, nonrigid image registration. *IEEE Transactions on Medical Imaging*, 18(10):875–84., 1999.

[187] W. C. Lin, S. A. Toms, M. Motamedi, E. D. Jansen, and A. Mahadevan-Jansen. Brain tumor demarcation using optical spectroscopy; an in vitro study. *Journal of Biomedical Optics*, 5(2):214–220, 2000.

[188] W. C. Lin, S. A. Toms, M. Johnson, E. D. Jansen, and A. Mahadevan-Jansen. In vivo brain tumor demarcation using optical spectroscopy. *Photochemistry and Photobiology*, 73(4):396–402, 2001.

[189] J. Feldmar, J. Declerck, G. Malandain, and N. Ayache. Extension of the ICP algorithm to nonrigid intensity-based registration of 3D volumes. *Computer Vision and Image Understanding*, 66(2):193–206, May 1997.

[190] P. Viola and W. Wells. Alignment by Maximization of Mutual Information. *International Journal of Computer Vision*, 24(2):137–154, 1997.

[191] M.J. Clarkson, D. Rueckert, and A.P. King. Registration of video images to tomographic images by optimising mutual information using texture mapping. In *LNCS: Medical Image Computing and Computer-Assisted Intervention: MICCAI '99*, volume 1679, pages 579–588. Springer-Verlag, 1999.

[192] T. K. Sinha, D. M. Cash, R. J. Weil, R. L. Galloway, and M. I. Miga. Cortical Surface Registration Using Texture Mapped Point Clouds and Mutual Information. In *LNCS: Medical Imaging Computing and Computer Assisted Intervention: MICCAI '02*, volume 2489, page 533. Springer-Verlag, 2002.

[193] V. R. Mandava. *Three dimensional multimodal image registration using implanted markers*. PhD thesis, Vanderbilt University, December 1991.

[194] V. R. Mandava, J. M. Fitzpatrick, C. R. Maurer, and et al. Registration of multimodal volume head images via attached markers. In *Medical Imaging IV: Image Processing*, volume 1652, pages 271–282. SPIE, 1992.

[195] Bernard Rosner. *Fundamentals of Biostatistics*. Duxbury Press, 4th edition, 1995.

[196] F. Glover. Tabu Search: A Tutorial. *Interfaces*, 20(4):74–94, 1990.

[197] A. Hertz, E. Taillard, and D. de Werra. *Local Search in Combinatorial Optimization*. Wiley-Interscience series in discrete mathematics and optimization. John Wiley & Sons Ltd., 1997.

[198] D. J. Hawkes, C. Studholme, and D. L. Hill. Accuracy, precision, and robustness of fully automated 3d neuro-image registration by multi-resolution optimisation of mutual information (momi). *Radiology*, 205:111–111, 1997.

[199] C. R. Wirtz, M. M. Bonsanto, M. Knauth, V. M. Tronnier, F. K. Albert, A. Staubert, and S. Kunze. Intraoperative magnetic resonance imaging to update interactive navigation in neurosurgery: method and preliminary experience. *Computer Aided Surgery*, 2(3-4):172–9, 1997.

[200] R. L. Galloway, R. J. Macuinas, W. A. Bass, and W. Carpini. Optical localization for interactive, Image-Guided Neurosurgery. *Medical Imaging*, 2164:137–145, 1994.

[201] D. M. Cash, T. K. Sinha, W. Chapman, H. Terawaki, B. Dawant, R. L. Galloway, and M. I. Miga. Incorporation of a laser range scanner into image-guided liver surgery: surface acquisition, registration, and tracking. *Medical Physics*, 30(7):1671–1682, 2003.

[202] J. D. Foley, J. Hughes, and A. van Dam. *Computer Graphics: Principles and Practice*. Addison-Wesley Systems Programming Series. Addison-Wesley, July 1995.

[203] F. L. Bookstein. Principal warps: thin-plate splines and the decomposition of deformations. *IEEE Transactions on Pattern Analysis and Machine Intelligence*, 11(6):567–585, 1989.

[204] K.S. Arun, T.S. Huang, and S.D. Blostein. Least-squares fitting of 2 3-d point sets. *IEEE Transactions on Pattern Analysis and Machine Intelligence*, 9(5):699–700, September 1987.

[205] M. I. Miga, T. K. Sinha, D. M. Cash, R. L. Galloway, and R. J. Weil. Cortical surface registration for image-guided neurosurgery using laser range scanning. *IEEE Transactions on Medical Imaging*, 22(8):973–985, August 2003.

[206] A. Herline, J. D. Stefansic, J. Debelak, R. L. Galloway, and W. C. Chapman. Technical advances toward interactive image-guided laparoscopic surgery. *Surgical Endoscopy-Ultrasound and Interventional Techniques*, 14(7):675–679, 2000.

[207] G. Rohde, A. Aldroubi, and B.M. Dawant. The Adaptive Bases Algorithm for Intensity Based Non Rigid Image Registration. *IEEE Transactions on Medical Imaging*, 22(11):1470–1479, November 2003.

[208] M. Ferrant, A. Nabavi, B. Macq, F. A. Jolesz, R. Kikinis, and S. K. Warfield. Registration of 3-d intraoperative mr images of the brain using a finite-element biomechanical model. *IEEE Transactions on Medical Imaging*, 20(12):1384–1397, 2001.

[209] H. Chui and A. Rangarajan. A new point matching algorithm for non-rigid registration. *Computer Vision and Image Understanding*, 89:114–141, 2003.

[210] H. Chui, L. Win, R. Schultz, J. S. Duncan, and A. Rangarajan. A unified non-rigid feature registration method for brain-mapping. *Medical Image Analysis*, 7:113–130, 2003.

[211] O. Skrinjar and J. Duncan. Stereo-guided volumetric deformation recovery. In *2002 IEEE International Symposium on Biomedical Imaging*, pages 863–866, 2002.

[212] V. Duay, T.K. Sinha, P. D'Haese, M. I. Miga, and B. M. Dawant. Non-rigid registration of serial intraoperative images for automatic brain-shift estimation. In *LNCS: Biomedical Image Registration*, volume 2717, pages 61–70, New York, 2003. Springer-Verlag.

[213] Y. I. Abdel-Aziz and H. M. Karara. Direct linear transformation into object space coordinates in close-range photogrammetry. In *Symposium on Close-Range Photogrammetry*, pages 1–18, 1971.

[214] R. Hartley and A. Zisserman. *Multiple view geometry in computer vision*. Cambridge University Press, New York, New York, 2001.

[215] Paul Dierckx. *Curve and Surface Fitting with Splines*. Oxford University Press, 1993.

[216] J.M. Fitzpatrick and J.B. West. The distribution of target registration error in rigid-body point-based registration. *IEEE Transactions on Medical Imaging*, 20(9):917–927, 2001.

[217] J. B. West, J. M. Fitzpatrick, S. A. Toms, C. R. Maurer, and R. J. Maciunas. Fiducial point placement and the accuracy of point-based, rigid body registration. *Neurosurgery*, 48(4):810–816, 2001.

[218] T. K. Sinha, M. I. Miga, D. M. Cash, R. L. Galloway, and R. J. Weil. Neurosurgical procedures using laser range scanning for cortical surface characterization. *Neurosurgery*. In Submission.

[219] T. K. Sinha, B. M. Dawant, V. Duay, D. M. Cash, R. J. Weil, and M. I Miga. A method to track cortical surface deformations using a laser range scanner. *IEEE Transactions on Medical Imaging*. In submission.

[220] W. E. Lorenson and H. E. Cline. Marching Cubes: A High Resolution 3D Surface Construction Algorithm. In *SIGGRAPH '87*, volume 21, pages 163–169, 1987.

[221] C. Studholme, D. L. G. Hill, and D. J. Hawkes. Automated three-dimensional registration of magnetic resonance and positron emission tomography brain images by multiresolution optimization of voxel similarity measures. *Medical Physics*, 24(1):25–35, 1997.

[222] P. Viola. *Alignment by maximization of mutual information*. PhD thesis, Massachusetts Institute of Technology, June 1995.